

THERMAL TRANSPORT PROPERTIES OF SINGLE CRYSTAL
QUARTZ AND PORTLANDITE

Zur Erlangung des akademischen Grades eines
DOKTORS DER NATURWISSENSCHAFTEN
(Dr. rer. nat.)

von der KIT-Fakultät für
Bauingenieur-, Geo und Umweltwissenschaften des
Karlsruher Instituts für Technologie (KIT)
genehmigte

DISSERTATION

von
Simon Breuer (M.Sc.)
aus Bad Mergentheim

Tag der mündlichen Prüfung:
23.11.2020

REFERENT: Prof. Dr. Frank R. Schilling
KORREFERENT: Prof. Dr. Hauke Marquardt

Karlsruhe 2020

»*The important thing in science is not so much to obtain new facts
as to discover new ways of thinking about them.*«

— Sir William L. Bragg (1957)

In loving memory of my grandmother,
dedicated to my wonderful family

ABSTRACT

The thermal properties of materials are important physical quantities to understand a variety of processes on and inside the Earth. For example, they have a decisive influence on the way in which convection forms in the Earth's mantle and thus they directly influence the plate movements of the overlying crust. Furthermore, the thermal transport parameters of the subsurface play an important role in the efficient use of the geothermal potential. Besides the relevance for geosystems, the knowledge of thermal transport properties and the understanding of transport processes plays an important role for many practical applications. Examples are the temperature management of processors or electrical components in general, as well as the development and production of highly insulating components for buildings, and the design of mechanical components for thermally demanding applications.

To determine the thermal transport properties of a material, *i.e.* the temperature-dependent thermal diffusivity and thermal conductivity, a variety of different techniques can be applied. The method used in this thesis is the so-called flash method, which is one of the most important established techniques for the determination of the thermal transport properties of solids. Nevertheless, there are still influencing factors and interdependencies in both the measurement and the evaluation routines of flash experiments which have not yet been (sufficiently) considered. For instance, the question of what is the actual time dependency of the heat pulse that needs to be taken into account in the data processing and what is the influence of the radiative heat transport on the derived conductive thermal transport properties near phase transitions in flash measurements. These considerations are covered in this cumulative dissertation and subject to the three included studies to improve the flash technique and therewith to better understand the thermal transport properties of single crystal quartz and portlandite.

In the first study the focus lies on the further development of the measurement methodology, which is then used for the subsequent studies to derive the heat transport in quartz and portlandite single crystals. Test measurements show significant and systematic deviations between the measured data and their approximations by standard evaluation routines. Hence, it is systematically investigated how the recorded data are additionally delayed by the detector and the electronic components. It is shown that a significant time delay inheres the measured signal for the tested experimental setup for both low temperature (HgCdTe) and high temperature (InSb) infrared detectors. The influence on the measurement is comparable to the known finite pulse-time effect. This additional delay of the measured signal is the cause of systematic deviations and can lead to a significant underestimation of the heat

transport efficiency of the investigated material. For this reason, a transfer function is used to reproduce the additional time delay of the signal. In a second step, the evaluation routine is expanded to take the time delay into account. With the help of synthetic measurement curves for different sample thicknesses and thermal diffusivities it is possible to quantify the systematic errors that occur when the additional time delay reported here is not taken into account in the data evaluation. As an example, deviations from the true thermal diffusivity are $\sim 1-4\%$ for a theoretical sample with a thickness of 1 mm and a thermal diffusivity of $10 \text{ mm}^2/\text{s}$, depending on the used infrared detector and heat pulse consideration.

The second study investigates the heat transport of quartz SiO_2 single crystals. Quartz is one of the most abundant rock-forming minerals in the Earth's crust and is widely used in technical applications. However, there is still uncertainty about the details of the temperature-dependent heat transport, for example at the α - β phase transition at 573°C , and a general lack on heat transport data below room temperature. Therefore, flash measurements are carried out on quartz single crystals parallel to the crystallographic c - and a -axis in the temperature range between -120°C and 800°C . In addition to the first thermal diffusivity measurements at low temperatures (-120°C to room temperature), the raw data show that at higher temperatures towards the α - β phase transition an increasing radiation part inheres the measured signal. This requires a further customization of the evaluation procedure developed in the first study so that the radiative and phononic heat transport can be separated from each other. A detailed look at the measurement curves indicates that the origin of this radiation, which is assumed to be non-ballistic, can be assigned to the α - β phase transition. With a new approach, the evaluation routine is adapted to take into account different radiative contributions in the area below the phase transition and in the β -phase to better derive the contribution of phononic heat transport in quartz. It is shown that the α - β phase transition is not characterized by a change in the direction of the maximum thermal diffusivity (crossover) as reported in a previous study, and that the trend of the temperature-dependent thermal diffusivity is mainly correlated to the mean free path of phonons.

In the third study the thermoelastic properties of portlandite $\text{Ca}(\text{OH})_2$ single crystals are investigated, with a focus on the thermal transport properties. Portlandite is one of the main components in hydrated cement, but it is also used for flue gas treatment and is considered for future thermochemical energy storage. However, no single crystal measurements for the orientation- or temperature-dependent heat transport have been made so far – also due to the lack of sufficiently large (natural) single crystals. Here, cm-sized synthetic portlandite crystals were grown using a diffusion process crystal growth setup. The crystals were then used for flash measurements within custom sample holders. The anisotropic heat transport is measured for temperatures

between $-100\text{ }^{\circ}\text{C}$ through the dehydration of portlandite up to $700\text{ }^{\circ}\text{C}$ parallel to the crystallographic c - and a -axis. To accurately derive thermal transport properties, the approximation routine developed in the first study needs to be applied. In addition to flash measurements, the elastic properties of synthetic portlandites are determined by Brillouin spectroscopy and compared with data of natural portlandite. Similarly to the elastic properties, the evaluated heat transport properties show a strong dependence on the crystallographic orientation. This can be related to the layered structure of $\text{Ca}(\text{OH})_2$. With respect to the derived thermal transport properties, partly strong variations from the intrinsic behavior are revealed for different experimental settings (*e.g.* heating rate and sample dimensions).

KURZFASSUNG

Die thermischen Eigenschaften von Materialien sind wichtige physikalische Größen für das Verständnis einer Vielzahl von Prozessen auf und in der Erde. So haben sie beispielsweise maßgeblichen Einfluss auf die Art und Weise der sich bildenden Konvektionszonen im Erdmantel und somit auch auf die Plattenbewegungen der unmittelbar darüberliegenden Kruste. Weiterhin spielen die thermischen Materialparameter des Untergrundes eine wichtige Rolle für die effiziente Nutzung des geothermischen Potentials. Neben der Relevanz für Geosysteme spielt die Kenntnis der thermischen Eigenschaften und das Verständnis von Wärmetransportprozessen aber auch für viele praktische Anwendungen eine wichtige Rolle. Als Beispiele sind etwa das Wärmemanagement von Prozessoren oder allgemein elektrischer Bauteile zu nennen, ebenso wie die Entwicklung und Herstellung hoch-isolierender Bauelemente für Gebäude, oder auch die Bemessung von mechanischen Bauteilen für thermisch anspruchsvolle Einsatzbereiche.

Zur Bestimmung der thermischen Eigenschaften eines Materials, d.h. der temperaturabhängigen thermischen Diffusivität (Temperaturleitfähigkeit) und Wärmeleitfähigkeit, können eine Vielzahl von unterschiedlichen Verfahren eingesetzt werden. Die in dieser Arbeit verwendete sog. Flash Methode stellt dabei eines der wichtigsten etablierten Verfahren zur Bestimmung der thermischen Eigenschaften von Festkörpern dar. Dennoch gibt es sowohl bei der Messung als auch bei der Auswertung von Flash-Experimenten nach wie vor Einflussfaktoren und Zusammenhänge, die bis dato nur unzureichend berücksichtigt oder noch nicht betrachtet wurden. Zum Beispiel die Frage, was die tatsächliche in der Datenauswertung zu berücksichtigende Zeitabhängigkeit des Heiz-Pulses ist und welchen Einfluss der radiative Wärmetransport in Flash-Experimenten auf die abgeleiteten konduktiven Wärmetransporteigenschaften im Bereich einer Phasenumwandlung hat. Diese Aspekte werden in dieser kumulativen Dissertation innerhalb der drei eingebundenen Studien behandelt, mit dem Ziel, die Flash Methode weiterzuentwickeln und so das Verständnis des Wärmetransportvermögens von Quarz- und Portlandit-Einkristallen zu verbessern.

In der ersten Studie geht es um die Weiterentwicklung der Messmethodik, welche dann in den nachfolgenden Studien bei der Auswertung des Wärmetransports von Quarz- und Portlandit-Einkristallen Anwendung findet. Testmessungen zeigen signifikante und systematische Abweichungen zwischen den Messdaten und ihren Anpassungen mittels Standard-Auswerteroutinen. Aus diesem Grund wird systematisch untersucht, inwieweit eine Verzögerung der Datenerfassung durch den Detektor bzw. die elektronischen Komponenten vorliegt. Es wird gezeigt, dass dem Messsignal für das getestete experimentelle Setup so-

wohl für den verwendeten Tieftemperatur Infrarot-Detektor (HgCdTe) als auch für den Hochtemperatur Infrarot-Detektor (InSb) eine signifikante Zeitverzögerung anhaftet. Die Wirkung dieser ist vergleichbar mit der bekannten finiten Pulszeit-Verzögerung. Die zusätzliche Verzögerung des Messsignals ist die Ursache systematischer Abweichungen und kann zu einer teils signifikanten Unterschätzung des Wärmetransportvermögens des untersuchten Materials führen. Aus diesem Grund wird eine Transferfunktion angewendet, mit Hilfe derer die zusätzliche zeitliche Verzögerung des Signals am Infrarot-Detektor abgebildet werden kann. In einem zweiten Schritt wird die Auswertungsroutine unter Berücksichtigung der zeitlichen Verzögerung erweitert. Mit Hilfe von synthetischen Messkurven kann der systematische Fehler bei Nichtbeachtung der zusätzlichen zeitlichen Verzögerung für die Auswertung verschiedener Probendicken und Temperaturleitfähigkeiten quantifiziert werden. Als Beispiel ist für eine theoretische Probe von 1 mm Dicke und $10 \text{ mm}^2/\text{s}$ Temperaturleitfähigkeit die Abweichung von der tatsächlichen Temperaturleitfähigkeit, abhängig vom verwendeten Infrarot-Detektor und der Heizpuls-Berücksichtigung, $\sim 1\text{-}4 \%$.

Die zweite Studie untersucht das Wärmetransportvermögen von Quarz-Einkristallen. Quarz (SiO_2) stellt eines der häufigsten gesteinsbildenden Minerale der Erdkruste dar und kommt vielfach in technischen Anwendungen zum Einsatz. Dennoch gibt es nach wie vor Ungewissheit zum Verlauf des temperaturabhängigen Wärmetransports, etwa am α - β Phasenübergang bei $573 \text{ }^\circ\text{C}$, sowie einen generellen Mangel an Daten zum Wärmetransportvermögen unterhalb der Raumtemperatur. Aus diesem Grund werden Flash-Messungen richtungsabhängig an Quarz-Einkristallen entlang der kristallographischen c - und a -Achse im Temperaturbereich zwischen $-120 \text{ }^\circ\text{C}$ und $800 \text{ }^\circ\text{C}$ durchgeführt. Neben der erstmaligen Messung der thermischen Diffusivität bei tiefen Temperaturen ($-120 \text{ }^\circ\text{C}$ bis Raumtemperatur) wird gezeigt, dass bei höheren Temperaturen ein zum α - β Phasenübergang hin zunehmender Strahlungsanteil im Messsignal eine weitere Anpassung der in der ersten Studie entwickelten Datenauswertung erforderlich macht. Dadurch soll der radiative vom phononischen Wärmetransport getrennt werden. Eine Untersuchung der Messkurven deutet darauf hin, dass der Ursprung dieser als nicht-ballistisch angenommenen Strahlung dem α - β Phasenübergang zuzuordnen ist. Mit Hilfe eines neuen Ansatzes wird die Auswertungsroutine derart angepasst, dass im Bereich unterhalb des Phasenübergangs ebenso wie für β -Quarz unterschiedliche radiative Anteile im Flash-Signal effektiv berücksichtigt und so der phononische Beitrag zum Wärmetransport in Quarz besser ermittelt werden kann. Es zeigt sich, dass der α - β Phasenübergang nicht mit einer Änderung der Richtung des maximalen Wärmetransportvermögens einhergeht (Crossover), wie es in einer früheren Arbeit berichtet wurde, und dass der Verlauf des temperaturabhängigen Wärmetransports vorwiegend mit der Änderung der mittleren freien Weglänge der Phononen korreliert.

In der dritten Studie werden die thermoelastischen Eigenschaften von Portlandit-Einkristallen $\text{Ca}(\text{OH})_2$ untersucht, wobei der Fokus auf dessen Wärmetransportvermögen liegt. Bei Portlandit handelt es sich um einen der Hauptbestandteile in hydratisiertem Zement, außerdem kann er zur Rauchgasbehandlung verwendet werden und wird für zukünftige thermochemische Energiespeicherung in Betracht gezogen. Dennoch gibt es bislang keinerlei Einkristall-Messungen zum richtungs- oder temperaturabhängigen Wärmetransport – auch aufgrund des Mangels an hinreichend großen (natürlichen) Einkristallen. Im Rahmen dieser Arbeit wurden cm-große, synthetische Portlanditkristalle mittels eines Diffusionsverfahrens zum Kristallwachstum gezüchtet, die mit Hilfe speziell angefertigter Probenträger für Messungen mit der Flash Methode verwendet werden können. Der anisotrope Wärmetransport wird für Temperaturen zwischen -100 °C über die Dehydratation von Portlandit bis 700 °C entlang der kristallographischen c - und a -Achse gemessen. Um präzise Werte zum Wärmetransportvermögen zu erlangen, wird für die Datenauswertung die in der ersten Studie entwickelte Auswerterroutine benötigt. Neben den Flash-Messungen werden außerdem die elastischen Eigenschaften der synthetischen Portlandite mittels Brillouin-Spektroskopie ermittelt und mit den Werten eines natürlichen Portlandits verglichen. Ähnlich der elastischen Eigenschaften zeigen die ausgewerteten Messungen zum Wärmetransport eine starke Richtungsabhängigkeit. Diese kann der schichtartigen Struktur von $\text{Ca}(\text{OH})_2$ zugeordnet werden. Im Bezug auf die ermittelten Wärmetransporteigenschaften zeigen sich, abhängig von den gewählten experimentellen Bedingungen (z.B. der Heizrate oder den Probendimensionen), teils starke Abweichungen vom intrinsischen Materialverhalten.

CONTENTS

ABSTRACT	vii
KURZFASSUNG	xi
LIST OF FIGURES	xvii
LIST OF TABLES	xix
NOMENCLATURE	xxi
1 INTRODUCTION	3
1.1 Heat Transport	4
1.2 Methods to Determine Thermal Transport Properties . .	12
1.3 Objectives and Structure	18
Study 1	
2 IMPROVING THERMAL DIFFUSIVITY MEASUREMENTS BY INCLUDING DETECTOR INHERENT DELAYED RESPONSE IN LASER FLASH METHOD	25
2.1 Introduction	26
2.2 Theory	27
2.3 Experimental	31
2.4 Results	31
2.4.1 Detector Inherent Delayed Response and its Con- sideration by Transfer Function	31
2.4.2 Systematic Errors Caused by Detector Inherent Delayed Response	34
2.4.3 Impact of Delayed Detector Response on Experi- mental Data	38
2.5 Discussion	39
2.6 Conclusion	43
2.7 Acknowledgments	44
Study 2	
3 ANISOTROPIC THERMAL TRANSPORT PROPERTIES OF QUARTZ: FROM -120 °C THROUGH THE α - β PHASE TRANSITION	47
3.1 Introduction	48
3.2 Experimental	51
3.3 Results	54
3.4 Discussion	58
3.5 Conclusion	69

3.6 Acknowledgments	70
-------------------------------	----

Study 3

4 THERMOELASTIC PROPERTIES OF SYNTHETIC SINGLE CRYSTAL PORTLANDITE – TEMPERATURE-DEPENDENT THERMAL DIFFUSIVITY WITH DERIVED THERMAL CONDUCTIVITY AND ELASTIC CONSTANTS AT AMBIENT CONDITIONS	75
4.1 Introduction	76
4.2 Methods	78
4.2.1 Samples	78
4.2.2 Brillouin Scattering	81
4.2.3 Thermal Diffusivity	84
4.3 Results	87
4.3.1 Brillouin Scattering	87
4.3.2 Thermal Diffusivity and Thermal Conductivity	92
4.4 Discussion	95
4.5 Conclusion	103
4.6 Acknowledgments	105

Synthesis

5 CONCLUSION AND OUTLOOK	109
--------------------------	-----

Appendix

A	123
A.1 Appendix to Chapter 3	123
A.2 Appendix to Chapter 4	133

Back Matter

BIBLIOGRAPHY	137
AUTHOR’S PUBLICATIONS	157
ACKNOWLEDGMENTS	161
DECLARATION OF AUTHORSHIP	163

LIST OF FIGURES

Figure 1.1	Illustrating the concept of entropy by thermal energy reservoirs	5
Figure 1.2	Illustrating heat transport by conduction and ballistic process	5
Figure 1.3	Acoustic and optical lattice vibration, and the displacement of a lattice plane for a pure longitudinal and a pure transverse vibration	7
Figure 1.4	Temperature dependence of phonon mean free path, specific heat, and thermal conductivity	10
Figure 1.5	Setup of the used laser flash apparatus	17
Figure 2.1	Dimensionless rear side surface temperature history	29
Figure 2.2	Schematic construction of the used laser flash apparatus	30
Figure 2.3	Laser pulse intensity measured by integrated diode for different pump energies	30
Figure 2.4	Laser pulses detected by integrated diode vs. pulse signals measured with IR detectors	32
Figure 2.5	True thermal diffusivity vs. fitted apparent thermal diffusivity using discrete convolution	35
Figure 2.6	Systematic error vs. sample thickness for certain true thermal diffusivities	37
Figure 2.7	Measurement of POCO Graphite AXM 5Q at 24.9 °C with low temperature MCT IR detector	38
Figure 2.8	Synthetic MCT IR detector temperature response curve	40
Figure 2.9	Systematic errors potentially associated with standard reference materials for thermal diffusivity measurements	42
Figure 3.1	Signal-time curve measured at 550 °C with the laser flash apparatus using InSb IR detector	53
Figure 3.2	Measured lattice (phononic) thermal diffusivity of synthetic quartz single crystals between -120 °C and 800 °C	56
Figure 3.3	Anisotropy of the single crystal thermal diffusivity of quartz	57
Figure 3.4	Thermal diffusivity measured for a cubic quartz specimen between 400 °C and 700 °C	62
Figure 3.5	Quartz phononic mean free path length between -120 °C and 800 °C in [001] and [100] direction	63

Figure 3.6	Ratio of direct radiative heat transfer to theoretical adiabatic maximum temperature on the rear side of the specimen	66
Figure 3.7	Comparison of fit results using different model approaches to approximate the thermal diffusivity below and above the phase transition . . .	68
Figure 4.1	Crystal structure of portlandite	77
Figure 4.2	X-ray diffraction on powdered portlandite and its dehydration product	80
Figure 4.3	Schematic diagram of the experimental setup used for Brillouin scattering	82
Figure 4.4	Brillouin spectra of portlandite in the axial plane (100) and in perpendicular direction (001) (basal plane)	83
Figure 4.5	Schematic diagram of the laser flash apparatus for thermal diffusivity measurements	85
Figure 4.6	Signal-time curve of portlandite measured by laser flash method with low temperature setup (MCT IR detector) at $-60.5\text{ }^{\circ}\text{C}$	86
Figure 4.7	Measured acoustic wave velocities of single crystal portlandite	88
Figure 4.8	3D representation of the acoustic wave velocities of portlandite	89
Figure 4.9	3D representation of the Young's modulus of portlandite	90
Figure 4.10	Thermal diffusivity of single crystal portlandite in [001] and [100] direction between $-100\text{ }^{\circ}\text{C}$ through the dehydration of portlandite up to $700\text{ }^{\circ}\text{C}$	93
Figure 4.11	Anisotropy of the thermal diffusivity of single crystal portlandite between $-100\text{ }^{\circ}\text{C}$ and $400\text{ }^{\circ}\text{C}$.	94
Figure 4.12	Derived anisotropic thermal conductivity of portlandite between $-100\text{ }^{\circ}\text{C}$ and $400\text{ }^{\circ}\text{C}$	95
Figure 4.13	Influence of the experimental conditions on the dehydration and the derived thermal diffusivity of portlandite	97
Figure 4.14	Approximations for the temperature trend of the thermal diffusivity and thermal conductivity of portlandite	99
Figure 4.15	Dependence of the thermal diffusivity on the specimen thickness for single crystal portlandite in the basal plane orientation	102
Figure 4.16	Spatial distribution of elastic and thermal transport properties of portlandite for selected orientations	104
Figure 5.1	Scanning microscope photographs of glass samples coated with graphite	113

LIST OF TABLES

Table 1.1	Technical data and specifications of the laser flash apparatus LFA 457	18
Table 2.1	Transfer function coefficients for the used experimental setup	33
Table 2.2	c factors used to link true and apparent thermal diffusivities	34
Table 2.3	φ factors used for systematic error calculation for high and low temperature IR detectors	36
Table 3.1	Published data on thermal transport properties of single crystal quartz	50
Table 3.2	Specimens and measurement characteristics for low and high temperature thermal diffusivity experiments	54
Table 4.1	Elemental composition of synthetic portlandite crystals	80
Table 4.2	Synthetic portlandite single crystal elastic constants derived by Brillouin spectroscopy at ambient conditions	90
Table 4.3	Adiabatic aggregate elastic moduli and acoustic velocities for portlandite at ambient conditions	91
Table 4.4	Fit constants for thermal transport property approximations	98
Table A.1	Low temperature quartz single crystal thermal diffusivity in [001] and [100] direction	123
Table A.2	Thermal diffusivity measured across the quartz phase transition	124
Table A.3	Thermal diffusivity measured for thick quartz single crystal specimens	126
Table A.4	Specimen LT[001] ratio of direct radiative heat transfer to theoretical adiabatic maximum temperature	127
Table A.5	Specimen LT[100] ratio of direct radiative heat transfer to theoretical adiabatic maximum temperature	128
Table A.6	Specimen HT1[001] ratio of direct radiative heat transfer to theoretical adiabatic maximum temperature	129
Table A.7	Specimen HT2[001] ratio of direct radiative heat transfer to theoretical adiabatic maximum temperature	130

Table A.8	Specimen HT ₁ [100] ratio of direct radiative heat transfer to theoretical adiabatic maximum temperature	131
Table A.9	Specimen HT ₂ [100] ratio of direct radiative heat transfer to theoretical adiabatic maximum temperature	132
Table A.10	Thermal diffusivities of synthetic single crystal portlandite in [100] and [001] direction	133
Table A.11	Derived thermal conductivity tensor for single crystal portlandite	134

NOMENCLATURE

Quantity	Symbol	Dimension
Temperature	T	K (or °C)
Time	t	s
Mass	m	kg
Length/thickness	d	m
Volume	V	m ³
Density	ρ	kg/m ³
Diameter	\varnothing	m
Wavelength	λ	m
Frequency shift	$\Delta\omega$	1/s
Wave velocity	v	m/s
Electric potential	U	V, (kg m ² A ⁻¹ s ⁻³)
Heat	Q	J, (kg m ² s ⁻²)
Heat flux	q	W/m ² , (kg/s ³)
Entropy	S	J/K
Thermal conductivity	κ	W/(m K)
Thermal diffusivity	D	m ² /s
Heat capacity	$C_{V,p}$ ^a	J/K
Specific heat (capacity) ^b	$c_{V,p}$	J/kg K, J/m ³ K, J/mol K
Elastic stiffness tensor	c_{ijkl} ^c	Pa, (kg m ⁻¹ s ⁻²)
Young's modulus	E	Pa
Bulk modulus	K	Pa
Shear modulus	G	Pa
Poisson's ratio	ν	
Phonon mean free path	l_{phonon} (or l)	m
Photon mean free path	l_{photon}	m
Thermal expansion coefficient	α	1/K
Debye temperature	Θ_D	K
Angle of diffraction	θ	degree
Brillouin scattering angle	ϕ	degree
Kronecker delta	δ_{ij}	
Birefringence	n	

^a at constant volume (V) or constant pressure (p)

^b per unit mass, unit volume or per mole

^c C_{ij} in Voigt notation

»Heat, like gravity, penetrates every substance of the universe, its rays occupy all parts of space. The object of our work is to set forth the mathematical laws which this element obeys. The theory of heat will hereafter form one of the most important branches of general physics.«

— Jean Baptiste Joseph Fourier (1822)

INTRODUCTION

The first seeds of heat transport science and thermodynamics were sown by Sir Isaac Newton (*1642 †1727) in 1701 analyzing heat transport. His law of cooling states that the rate of temperature change of an object is proportional to the temperature difference between the object and its surrounding (Dixit et al. 2017). Ever since, continuous efforts paid off with a grown understanding of heat transport processes. Nowadays, heat transfer (here synonymous to heat transport) is important at almost any length scale. For example, in the sub-micron scale with nanoparticle or nanofluid applications for enhanced cooling (*e.g.* in the industrial and automotive field, Minkowycz et al. 2013), in the macroscopic millimeter to meter range *e.g.* for civil engineering to improve the thermal management of buildings (Cui et al. 2017), and in the length scale above where *e.g.* heat radiation transfers millions of kilometers and interacts with interstellar objects like the Earth (Lacis and Hansen 1974).

In geosciences, most of the geodynamic processes within our Earth are driven by heat transport originating in temperature differences, for example mantle convection and associated therewith controlling tectonic plates, volcanism, and natural seismic events (Khain and Goncharov 2006). But not only the length scales where heat transfer takes place are extensive, also its applications extent over numerous fields. In traditional areas such as energy technology with *e.g.* power stations, in aerospace engineering or classical fields like automotive and civil engineering. But, recently heat transfer became increasingly important in areas such as IT, climate research, material sciences, and waste disposal technology, just to name a few (Marek and Nitsche 2012). In the geoscientific sector, geothermal energy for *e.g.* conversion into electricity and home or district heating are important uses of naturally transferred heat (Fridleifsson 2001).

Even though principles of heat transfer and related subjects have already been described and worked with for more than three centuries, it is the growing understanding of the involved heat transport processes in combination with the use of specifically designed materials and the knowledge of precisely determined thermal transport properties that continuously opens up new applications (*e.g.* Kim et al. 2001; Keblinski et al. 2005). It is especially noteworthy that better insights into heat transport go hand in hand with the (further) development of experimental techniques and, most recently, theoretical *ab initio* calculations (Lindsay et al. 2019). As the latter approach is rather complex and requires extended computational effort, it is primarily used to increase our fundamental understanding in heat transport processes and to

resolve thermal properties of crystals in pressure-temperature regions that cannot be reached by traditional experimental methods (Xiong et al. 2019). Hence, there is a continued demand on experimental techniques for precise measurements on thermal transport properties, also to independently approve theoretical models.

For this purpose, this cumulative dissertation investigates in detail the experimental and data processing routines associated with measurements of thermal transport properties by the flash technique. This thesis presents further developments of this method that help to improve our understanding of heat transport and that enable an accurate derivation of single crystal thermal transport properties of quartz (SiO_2) and portlandite $\text{Ca}(\text{OH})_2$, two minerals of particular interest for geosciences and for technical applications.

1.1 HEAT TRANSPORT

According to the second law of thermodynamics, natural processes within a closed system are irreversible and hence can run only in one direction, which is synonymous with the prohibition of perpetual motion machines. This argumentation follows the work of Nicolas L. S. Carnot (*1796 †1832) on the operation of steam engines (1824), where he states that heat energy cannot be fully transferred into work (Dixit et al. 2017). Pivotal for the comprehension of Carnot's work was the concept of entropy S introduced by Rudolf J. E. Clausius (*1822 †1888). Accordingly, entropy characterizes the state of a system and links heat energy Q with the absolute temperature T (Clausius 1879)

$$dS = \frac{\partial Q}{T} \quad (1.1)$$

The amount of entropy in a system is either constant (reversible process) or increases (irreversible process). Fig. 1.1 illustrates two thermal energy reservoirs of different temperature in thermal contact with each other. It can be shown that the resulting change of the entropy ΔS is positive only for the case that heat (spontaneously) "flows" from the hot to the cold reservoir¹, which is in accordance with the second law of thermodynamics (Baehr and Kabelac 2016). In the general case, heat flow persists until thermal equilibrium is reached.

Heat can be transported by different mechanisms. One can distinguish between two fundamentally different principles² (Fig. 1.2) (Hofmeister 2019):

- ¹ For the case that heat would be transferred from the cold ($-\Delta Q$) to the hot ($+\Delta Q$) reservoir, it would be: $\Delta S_{\text{cold}} = -\Delta Q/T_{\text{cold}}$ and $\Delta S_{\text{hot}} = +\Delta Q/T_{\text{hot}}$ and thus $\Delta S = \Delta S_{\text{cold}} + \Delta S_{\text{hot}} = \Delta Q [(T_{\text{cold}} - T_{\text{hot}})/T_{\text{cold}}T_{\text{hot}}] < 0$. The entropy of the system would therefore decrease, which is a contradiction to the second law of thermodynamics.
- ² Convection, often named to be a third fundamental mechanism, is not considered here as it is directly related to a material transport where heat is transported with the bulk. Beyond that, convection always involves a conductive heat transfer part within the bulk and at interfaces and it may therefore not be regarded as a separate mechanism of heat transport (Nusselt 1915; Incropera et al. 2007).

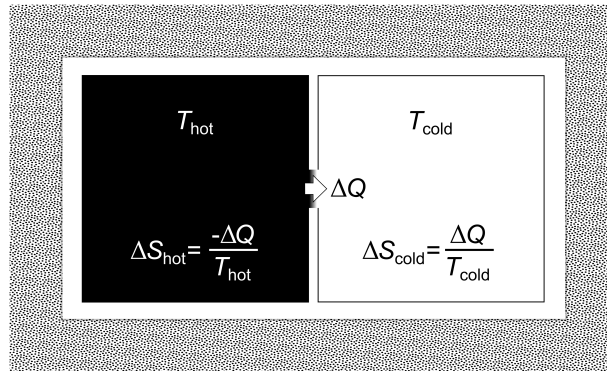


Figure 1.1: Illustrating the concept of entropy S by two thermal energy reservoirs of different temperatures in thermal contact with each other. The transferred heat between the two baths is ΔQ . The reservoirs are placed inside a perfectly isolated box. For heat transferred from the hot to the cold bath the total change of entropy is $\Delta S > 0$ and thus in accordance with the second law of thermodynamics

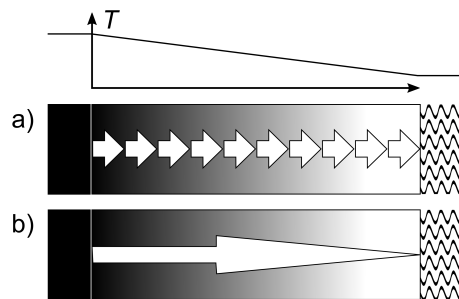


Figure 1.2: Illustrating heat transport by either a) conduction (energy diffusion) or b) ballistic process within a body heated on the left hand side (black bar). Whereas diffusion is characterized by several collisions of (quasi)particles transporting heat within the body (*e.g.* phonons), ballistic transfer takes place without the interaction of the body itself. Squiggles on the right hand side illustrate radiative heat transfer to the surrounding (modified from Hofmeister 2019)

- conduction, and
- ballistic transport.

Heat Conduction and Phonons

Conductive heat transport takes place in matter of any physical state. It always includes some particle interaction within the corresponding material (Fig. 1.2a). Generally speaking, internal energy is diffused by (quasi)particle collisions and, *e.g.* in metals, by the movement of free electrons within the corresponding body (Gurzhi 1964; Issi 1999). The dominating heat conduction part in insulating (dielectric) crystalline solids can be assigned to phonons (Horai 1971). In quantum mechanical terms, the latter are quasiparticles of lattice vibrational

energy due to oscillating atoms. Because of the three-dimensionally ordered repeating structure of a crystal and the thermal vibrations of atoms being limited to certain energies (quantization), only discrete coupled oscillations can occur (Ziman 1960). In principal, one can distinguish between two different types of phonons: 1) so-called acoustic lattice waves are characterized by in-phase oscillation of neighboring atoms (Fig. 1.3a). Depending on the atoms vibrating parallel or perpendicular to the direction of propagation, the corresponding waves are termed longitudinal (v_p) and transverse (v_{s1}, v_{s2}) acoustic phonons (Fig. 1.3c&d), respectively. 2) Higher frequency optical phonons are characterized by neighboring atoms oscillating anti-phase (Fig. 1.3b). In general, in a crystalline solid three acoustic and $3r-3$ different optical phonon modes exist, whereas r is the number of atoms in the primitive cell (*e.g.* Ziman 1960; Kittel 2005; Gross and Marx 2014). It was previously assumed that acoustic phonons are the primary heat carriers in insulating solids even at elevated temperatures (Slack 1965; Slack and Oliver 1971; Roufosse and Klemens 1974), but studies in the recent past indicate that optical phonons may significantly contribute to heat conduction too (Hofmeister 1999; Hofmeister 2006; Esfarjani et al. 2011). The number of phonons increases at elevated temperatures as well as higher frequency optical modes are increasingly occupied. Relating thereto, phonon-phonon interactions such as three-phonon “umklapp” processes increase (Peierls 1929) and the average distance phonons travel without interactions l_{phonon} (or l , mean free path) decreases (Kittel 2005). The thermal resistance of a material is directly linked to these umklapp processes and thus to the mean free path (Gurzhi 1964). Hence, for insulating crystalline solids with conductive heat transfer mainly related to phonons than to electrons or photons a general decrease of the heat transport efficiency with an increase of the temperature can be expected.

Ballistic Heat Transfer

In contrast to conductive heat transport, ballistic heat transfer is characterized by energy crossing material without or with negligible participation of the same (Fig. 1.2) (Hofmeister 2019). Ballistic heat transfer is often equated to radiative transfer. This is valid as long as the mean free path of the photons l_{photon} is of the order of the respective object or larger. Otherwise, *i.e.* l_{photon} is significantly smaller than the dimension of the probed material, the underlying mechanism of radiative heat transfer is conduction as it involves interactions in the form of absorption and re-emission within the material (Höfer and Schilling 2002; Böer and Pohl 2018; Hofmeister 2019). For the latter case, the radiative heat transfer within a solid has a strong temperature dependence $\propto T^3$ for an ideal gray body (Clark 1957; Shankland 1970; Beck et al. 1978) and thus becomes important at higher temperatures usually above several hundred degrees for most minerals (Clauser and Huenges 1995).

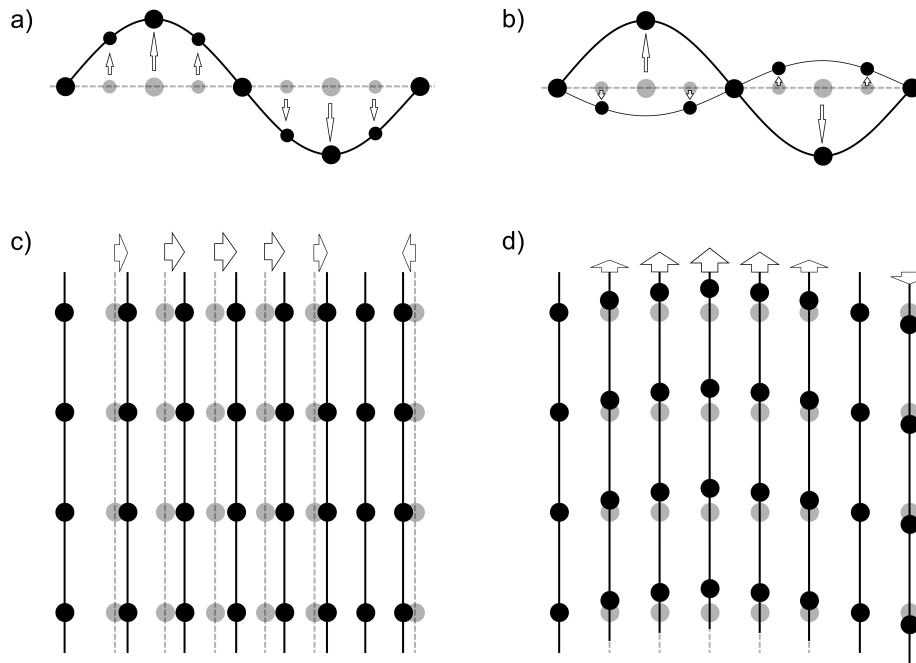


Figure 1.3: Sketch illustrating an acoustic (a) and optical (b) transverse lattice vibration of a one-dimensional system with two types of atoms of different mass. The displacement of a lattice plane is shown in c) for a pure longitudinal vibration with the direction of wave propagation (left to right) and particle displacement equal each other and in d) for a pure transverse lattice vibration, where the direction of displacement and propagation form an angle of 90° . Dashed lines and gray atoms correspond to equilibrium positions, arrows indicate the displacement (modified from Gross and Marx 2014)

But as the mean free path of photons is of the order of some millimeters for minerals (*e.g.* Höfer and Schilling 2002; Gibert et al. 2005), sample dimensions need to be of the order of at least some centimeters to observe intrinsic (conductive) heat transfer by radiation. Such sample dimensions are not reached for the measurements presented within the studies of this thesis. Therefore, conductive heat diffusion in the examined insulated single crystals is primarily associated with phononic (lattice) processes.

Representation of Thermal Transport Properties

The starting point of modern quantitative heat flow analysis through a material was set by the pioneering work of Jean Baptiste Joseph Fourier (*1768 †1830). His finding that heat transfer is a time-dependent phenomenon with his formulated differential equation of heat flow within a body still is the basis of almost any heat flow related issue in the present time. After his initial work on heat transport and conductivity was rejected in 1807, Fourier published his monograph in 1822 containing the law of heat conduction:

$$q = -\kappa \nabla T \quad (1.2)$$

with heat flux q (energy per time per area), thermal conductivity κ and temperature gradient ∇T . In a more general case and for homogeneous bodies, allowing the thermal conductivity κ to depend on the temperature and by conserving energy it is

$$\rho c_p \frac{\partial T}{\partial t} = \nabla \cdot \kappa \nabla T \quad (1.3)$$

with the density ρ and isobaric specific heat c_p per unit mass (Hofmeister 2019). With the thermal diffusivity D describing the rate of temperature spread and the relation

$$\kappa = D \rho c_p \quad (1.4)$$

Eq. 1.3 can be written in the form

$$\frac{\partial T}{\partial t} = D \nabla^2 T \quad (1.5)$$

for the assumption that κ and D are independent of T . Eq. 1.5 is often denoted as the heat equation. The thermal diffusivity D and thermal conductivity κ are orientation-dependent (anisotropic) properties for single crystals and can be described by second rank tensors D_{ij} and κ_{ij} (Nye 1985).

One major aspect to understand thermal transport properties has all along been the temperature dependence of heat transport processes.

As aforementioned, heat transport in dielectric solids can be primarily assigned to phonons. Treating these lattice excitations as particles, heat diffusion can be expressed according to the kinetic gas theory as (e.g. Debye 1914; Ziman 1960; Berman 1976; Kittel 2005)

$$\kappa = \frac{1}{3} c_V v l \quad (1.6)$$

(c_V : isochoric specific heat per unit volume, v : average phonon velocity, l : phonon mean free path). Hence, the temperature dependence of the thermal conductivity $\kappa(T)$ (and thermal diffusivity $D(T)$, cf. Eqs. 1.4&1.6³) depends on the temperature variation of the respective variables in Eq. 1.6. As a consequence of energy quantization of lattice vibrations, the temperature-dependent thermal conductivity and thereto related quantities strongly differ for the case that

- all lattice vibrations (modes) are excited at high temperatures ($T \gg \Theta_D$) and
- phonon modes “freeze out” at low temperatures ($T \ll \Theta_D$)

where Θ_D is the so-called Debye temperature (Gross and Marx 2014). In the following, the variation of the average phonon velocity with temperature is neglected as it is marginal compared to the temperature variations of the specific heat and the phonon mean free path, respectively (Roufosse and Klemens 1974; Böer and Pohl 2018).

The specific heat tends to zero at the absolute zero. Above 0 K but below Θ_D one observes a dependence $\propto T^3$, known as the Debye T^3 approximation (Kittel 2005). At high temperatures (i.e. $T \gg \Theta_D$) the specific heat approaches the so-called limit of Dulong-Petit ($c_V = 3r'R$, r' number of atoms in the unit cell, R ideal gas constant) (Gross and Marx 2014), Fig. 1.4.

The mean free path of phonons varies inversely with the temperature for $T > \Theta_D$ (Peierls 1929) as the number of phonons and thus three-phonon umklapp processes increases $\propto T$. Towards lower temperatures (i.e. $T < \Theta_D$) the number of phonons available for scattering processes reduces and thus the mean free path is expected to increase ($\propto \exp^{\Theta_D/T}$ according to the Debye model). For very low temperatures ($T \ll \Theta_D$) the mean free path cannot increase arbitrarily. It is limited by approximately temperature-independent scattering processes at lattice imperfections, but may also be limited by the specimen dimensions for large mean free paths (comparable with a ballistic transport). In addition, the mean free path and thus the thermal conductivity can vary due to crystal purity (Ziman 1960; Berman 1976; Kittel 2005; Gross and Marx 2014; Böer and Pohl 2018). The theoretical temperature trend

³ In a harmonic approximation the heat capacity at constant pressure C_p [J/K] equals the heat capacity at constant volume C_V as a result of the volumetric thermal expansion coefficient $\alpha_V = 0 \text{ K}^{-1}$. Thus, $c_V \left[\frac{\text{J}}{\text{m}^3 \text{K}} \right] = \rho c_p \left[\frac{\text{kg}}{\text{m}^3} \frac{\text{J}}{\text{kgK}} \right]$. Otherwise, $C_p = C_V + \alpha_V^2 V T K_T$ with the volume V , the absolute temperature T and the isothermal bulk modulus K_T (Berman and Brown 1985; Gross and Marx 2014).

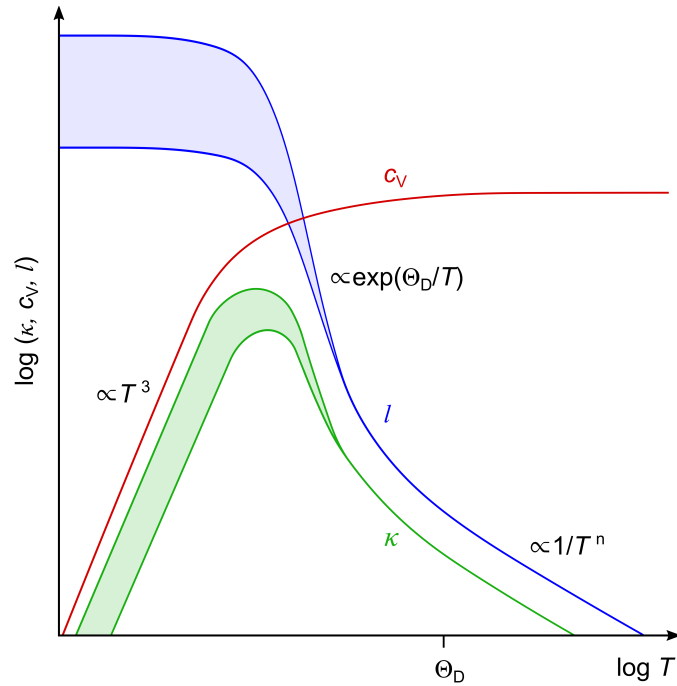


Figure 1.4: Illustrating the relative trend of the temperature dependence of the phononic mean free path l (blue), the molar specific heat c_V (red), and thereof derived thermal conductivity κ (green) on a double-log scale. The greenish and blueish areas represent possible variations due to lattice imperfections, crystal size and purity (the latter might affect the heat transport at even higher temperatures than shown here, Kittel 2005). For details, see text (modified from Böer and Pohl 2018)

of the thermal conductivity is illustrated in Fig. 1.4, including the individual effects of the specific heat and the mean free path, respectively. For the thermal diffusivity the temperature trend is expected to follow that of the mean free path according to Eqs. 1.4&1.6.

By far the most temperature-dependent measurements of the thermal transport properties of minerals and rocks are performed at and above room temperature. In this temperature region the thermal conductivity of insulated solids is expected to show a $\propto 1/T^n$ behavior, even up to the melting point (Leibfried and Schlömann 1954; Roufosse and Klemens 1974; Hofmeister 2006). Depending on the theoretical approach, n varies from ~ 1 -2. Preceding theoretical considerations, this temperature dependency was first time observed by Eucken (1911). To approximate the measured temperature trend of the heat transport capability in the temperature range around and above the Debye temperature, numerous models have been proposed within the last century.

With his work about the kinetic theory of heat conduction in crystals Peierls (1929) derived the temperature dependence of the thermal conductivity in accordance with Eucken's empirical observations as

$$\kappa(T) = \frac{A}{T} \quad (1.7)$$

Based on a series of measurements on thermal transport properties of crustal rocks at elevated temperatures, Cermák and Rybach (1982) proposed a more versatile correlation of $\kappa(T)$:

$$\kappa(T) = \frac{1}{A + BT} \quad (1.8)$$

This form found manifold use to approximate the thermal transport measured in crystals and rocks (*e.g.* Seipold 1992; Cohen 1998; Höfer and Schilling 2002; Gibert et al. 2005). At very high temperatures thermal conductivities approximated by Eqs. 1.7&1.8 approach $0.0 \text{ W m}^{-1} \text{ K}^{-1}$. But with respect to heat transport in solids mainly provided by lattice vibrations, theoretical considerations on the mean free path l of phonons indicate that l cannot become arbitrarily short (*i.e.* below inter-atomic distances, Ray et al. 2006) for very high temperatures (Ziman 1960; Spitzer 1970; Slack 1979). Accordingly, the thermal conductivity reaches a lower limit κ_0 for high temperatures (so-called Einstein limit, Cahill et al. 1992). Considering the contribution of different phonon frequencies to κ in Eq. 1.6, Roufosse and Klemens (1974) derived (rearranged for κ_0)

$$\kappa(T) = \frac{A}{T^{3/2}} + \kappa_0 \quad (1.9)$$

Thereto comparable, Zoth and Haenel (1988) proposed an empirical correlation to describe the temperature-dependent thermal conductivity in the form

$$\kappa(T) = \frac{A}{B + T} + \kappa_0 \quad (1.10)$$

As the heat capacity is almost constant for $T > \Theta_D$ (*cf.* Fig. 1.4), these approximations for $\kappa(T)$ can similarly be expected for the thermal diffusivity $D(T)$ (with the lower limit D_0 instead of κ_0) (Hofmeister 2006). In the recent past, Hofmeister et al. (2014) proposed a model of bulk phonon-polaritons for the thermal diffusivity of insulating single-crystals:

$$D(T) = \frac{A}{T^n} + HT \quad (1.11)$$

with $n = 0.25\text{-}2$ for most crystals. The proposed temperature trend (may be applied to $\kappa(T)$ too) includes an optional high temperature term

HT that can either reproduce a lower limit in thermal diffusivity or describe an increase in heat transport towards very high temperatures. The latter is often attributed to the contribution of radiation to heat transport and considered in the form of a CT^3 -term in Eqs. 1.7-1.10 (*e.g.* Höfer and Schilling 2002; Gibert et al. 2005; Ray et al. 2006). A , B , H , n , and κ_0 in Eqs. 1.7-1.11 are fitting constants while using absolute temperature.

The outlined correlations to approximate the temperature-dependent thermal transport properties are in general assumed to lose their applicability for the case that the probed matter undergoes any sort of phase changes or chemical reactions (including *e.g.* dehydration). This is due to the fact that phase changes are accompanied by *e.g.* modifications of the crystal structure, chemical compound, and volume (density), but also by changes of the elastic behavior and thereto related properties such as acoustic wave velocities (Carpenter 2006; Klumbach 2015). This means that phase transitions involve changes in the phonon spectrum that are in turn directly related to changes in the mean free path and specific heat (Böer and Pohl 2018). As a consequence, phase changes result in partly radical changes of the thermal conductivity and thermal diffusivity (*e.g.* Zhang and Luo 2013).

The knowledge about heat transport properties around phase transitions plays an important role not only in the geoscientific field (*e.g.* Schubert et al. 1975; Steinbach and Yuen 1992) but also for *e.g.* taking advantage of phase transitions for thermochemical energy storage (Schmidt 2017). Therefore, a precise determination of the thermal conductivity and thermal diffusivity through phase transitions is of interest. Due to the numerous variations of physical properties and other factors influencing chemical reactions (*e.g.* specimen size \longleftrightarrow dehydration) it seems reasonable that measurements of thermal transport properties and their data evaluations require particular care. This may also be the reason why accurate data on thermal transport properties around phase transitions are scarce and often inaccurate or even inconsistent (Chen et al. 2018).

1.2 METHODS TO DETERMINE THERMAL TRANSPORT PROPERTIES

Measurements on thermal transport properties, namely thermal conductivity and thermal diffusivity, cannot be performed directly but indirectly through some form of temperature recordings over time and/or space (Hofmeister 2019). Measurement techniques and methods to determine the thermal transport properties of matter are diverse and some have established as standard methods. But even though their origin often lies far back, there is still an ongoing and continuous further development of the methods to widen their range of application and to increase the quality of the resulting data to ultimately understand the nature of heat transport better (Reif-Acherman 2014). In general, the question of which method is best suited depends on

several factors, for example on the physical state of the material, on the size of the samples that can be prepared from the corresponding material as well as on the (expected) quantity of the thermal transport property (Zhao et al. 2016). But the choice of the measurement technique is also affected by the temperatures or rather the temperature range to be investigated and by the required resultant property being either the thermal conductivity or thermal diffusivity (even though conversions from κ to D and vice versa can be performed according to Eq. 1.4, this requires precise and reliable information on the density and specific heat of the probed material, which is often not available).

With respect to frequently used methods to determine thermal conductivity and thermal diffusivity, three different measurement approaches can be distinguished:

1) Steady-state methods. Measurements of this type are performed under conditions of thermal equilibrium, *i.e.* no temperature change exists over time within the sample during each measurement (Baehr and Kabelac 2016). The main advantages of these techniques are the straightforward operation and data analysis (Kerschbaumer et al. 2019). Two established steady-state methods are the guarded hot plate (Poensgen 1912) and the radial heat flow method (Angell 1911), both providing the thermal conductivity of the probed material.

2) Transient methods. Measurements under transient or transitory conditions are time-dependent and thus fundamentally different to steady-state methods. The basis of measurements under transient conditions is the record of a temperature evolution over time either of the test specimen itself or of the used heat source, *e.g.* a wire. Compared to steady-state methods, transient techniques in principle have the advantage to perform measurements within a short period of time (Zhao et al. 2016). Furthermore, by measuring the thermal evolution over time the heat transfer mechanisms involved may be distinguished (Hofmeister 2019). But due to the dynamic nature of transient methods, the evaluation of thermal transport properties is more complex and less straightforward. Important transitory methods are the (laser) flash method (Parker et al. 1961) providing the thermal diffusivity and the transient plane source (hot disk) method (Gustafsson 1991) measuring the thermal conductivity and thermal diffusivity. To measure the thermal transport properties of drill core rock samples the optical scanning method by Popov et al. (1985) is frequently applied.

3) Periodic (transient) methods. These types of methods are a special case of transient methods. A heat source generates a periodically oscillating signal and similarly the probed matter exhibits a cyclic temperature response. But in contrast to non-periodic transient methods that measure the temperature change over time, periodic methods record and compare the oscillating heat source signal and the thermal response replied by the probed sample (Hofmeister 2019). In the recent past, periodic methods became increasingly important especially in the field of measuring thermal transport properties of thin films

(Zhao et al. 2016). Frequently used periodic transient methods are *e.g.* the Ångström's (1861), the 3ω (Cahill and Pohl 1987), and the thermoreflectance method (Paddock and Eesley 1986).

Among the numerous different existing methods to derive thermal transport properties, the transient flash method combines several favorable features (see below) so that it became a standard technique to measure the thermal diffusivity of solids and liquids (Vozár and Hohenauer 2003).

In the following, a brief overview of this method with some major further developments is given, whereas more detailed operating principles are given within the reprinted studies of this cumulative dissertation (in particular, see chapter 2).

The Flash Method

Up to the early 1960s, methods to determine thermal transport properties mostly suffered from different shortcomings limiting their applicability and accuracy. For instance, they required big sample dimensions, needed to know absolute temperatures and temperature gradients, or required information on the quantity of heat input, whereas the latter two are in particular challenging to be determined precisely (Zawilski et al. 2001; Zhao et al. 2016). In addition, early methods often needed long measurement times and contact heat losses to *e.g.* heat sources or thermocouples were ever-present (Zhao et al. 2016; Hofmeister 2019). Furthermore, using the existing steady-state methods it was difficult to extend measurements to high temperatures (Reif-Acherman 2014) and thus the precise knowledge of material properties in temperature regions important for *e.g.* computational geosciences and engineering was limited. These drawbacks and difficulties could be overcome by the pioneering work of Parker et al. in 1961 entitled "*Flash Method of Determining Thermal Diffusivity, Heat Capacity, and Thermal Conductivity*".

The flash method was intentionally designed for the needs of the Navy Bureau of Aeronautics to measure metals, ceramics, alloys and composites (Reif-Acherman 2014). Based on the work of Carslaw and Jaeger (1959), W. J. Parker with his colleagues R. J. Jenkins, C. P. Butler and G. L. Abbott developed a transient method to derive the thermal diffusivity D of a solid under the assumption of adiabatic conditions. For an instantaneous radiant pulse absorbed on one side of a solid of uniform thickness d the history of the typically small temperature rise on the opposite rear surface is used to evaluate the thermal diffusivity of the probed matter. It seems noteworthy that the temperature rise is not required to be recorded in absolute values but only relatively (dimensionless, *cf.* Eq. 1.12) with respect to the initial sample temperature. It furthermore follows that the amount of initial heat energy radiated onto and absorbed by the sample does not need to be known. Thus, the flash method only requires the measuring of time and relative change of temperature, both of which can be determined

precisely. The sample's rear surface dimensionless temperature history is given as (Parker et al. 1961)

$$V(t) = 1 + 2 \sum_{n=1}^{\infty} (-1)^n \exp\left(-n^2 \frac{\pi^2 D t}{d^2}\right) \quad (1.12)$$

With this novel approach, high or low temperature measurements can be performed by simply heating or cooling the sample within a furnace or cooler. Neither the radiant source nor the detector, *e.g.* an infrared (IR) detector, need to be placed within the heated or cooled chamber. Therefore, flash measurements can be performed contactless, *i.e.* free of thermal contact resistances at the interfaces (Parker et al. 1961). Typical sample thicknesses are in the range of some millimeters, resulting in measurements usually lasting fractions of a second up to a few seconds. The advantages of this new method were quickly recognized and marked the starting point of numerous further developments in this field that are still ongoing.

Due to the fact that the proposed method initially assumes adiabatic conditions and therefore doesn't consider heat transfer from the sample to the surrounding, thereof derived thermal diffusivities from flash experiments can be well overestimated (Cape and Lehman 1963; Clark III and Taylor 1975). Therefore, in 1963 Cowan and also Cape and Lehman gave some first analytical solutions for energy "losses" of the sample surfaces. Further studies dealing with heat losses in flash experiments are, among others, Watt (1966), Heckman (1973), and Clark III and Taylor (1975). The consideration of heat transfer to the surrounding is particularly important for measurements at high temperatures but also at ambient conditions for poor-conducting matter due to the required longer measurement times (Vozár and Hohenauer 2003).

Another important improvement to the evaluation of flash method measurements deals with Parker et al.'s initial simplification of an instantaneous radiant source heating the specimen. Due to the fact that in flash technique experiments the radiant heat, provided by *e.g.* flash lamps or laser pulses, extends over a short but non-instantaneous period of time, the data evaluation needs to take the temporal change of the power of the energy pulse into account. This so-called "finite pulse-time effect" can have a significant influence on the thermal diffusivity evaluation of thin samples and highly diffusive materials. It was first considered by Cowan and also Cape and Lehman in 1963 for energy pulses approximated by a rectangular and a saw-tooth shape, respectively. In the meanwhile, a number of different studies proposed evaluation routines to consider energy pulses of different shape (*e.g.* Taylor and Cape 1964; Dusza 1995; Lim et al. 2009), using the center of gravity (Azumi and Takahashi 1981) as well as taking account for finite pulse-time effect by empirical corrections (Schoderböck et al. 2009).

Moreover, additional contributions led to further significant improvements of the flash method (excerpt):

- (semi)transparent specimens need to be coated in order to absorb the energy pulse at the front surface and to adequately emit radiation to the detector at the rear surface. This additional layer being *e.g.* sprayed onto the specimen influences the rear side temperature history. Studies by *e.g.* Cernuschi et al. (2002) and Lim et al. (2009) described and analyzed this effect and thus contributed to a better understanding of possible dependencies influencing flash method measurements.
- Lee (1975) extended the flash method to layered materials. Such measurements are not only important in the field of *e.g.* thermal barrier coatings in gas turbines (Blumm et al. 2003b), but are also a necessary prerequisite to measure thermal transport properties of liquids with the flash apparatus. Cernuschi et al. (2002) used the approach of a multi-layer system to take account of the influence of graphite coated specimens on the evaluation of the thermal diffusivity of the substrate.
- Most of the common standard data evaluation routines for flash measurements assume the heating energy pulse to be uniformly distributed (and uniformly absorbed) across the heated surface of the sample. Effects on the temperature history for nonuniform pulses have been analyzed by *e.g.* Watt (1966), Schriempf (1972) and McKay and Schriempf (1976), Baba et al. (1993) and Baba and Ono (2001). Accordingly, systematic errors associated with nonuniform heating pulses can reach several percents and therefore effects of nonuniform heating need to be carefully taken into account.

These and other contributions over the past decades made the flash technique to the method of choice for many applications not only in the scientific environment but also in the industry and helped to significantly improve our understanding of heat transport. Together with the consideration of heat loss effects in (laser) flash method measurements the corrections made in connection with the finite pulse-time effect were most important. Nevertheless, there is the need for further investigations and developments in the context of the flash method to derive accurate thermal transport properties, which is the subject of this thesis (see also 1.3 Objectives and Structure). These considerations include issues *e.g.* related to questions of what is the actual time dependency of the heat pulse that needs to be taken into account in the data processing and what is the influence of the radiative heat transport on the derived conductive thermal transport properties near phase transitions in flash measurements.

The apparatus used for the measurements presented within the studies of this thesis is a table-top laser flash apparatus (LFA) model 457 MicroFlash[®] from Netzsch-Gerätebau (Germany). The key technical data given by Netzsch-Gerätebau are listed in Tab. 1.1 and the device setup is shown in Fig. 1.5.



Figure 1.5: Basic setup of the laser flash apparatus (LFA) MicroFlash[®] 457 (Netzsch-Gerätebau) to measure thermal transport properties. 1) furnace power unit 2) purge gas flow meter 3) InSb IR detector (or optional low T HgCdTe (MCT) IR detector, not shown) 4) laser flash apparatus 5) liquid cooling system 6) laser power unit 7) LFA control unit (top) and liquid N_2 cooling controller for low T measurements (bottom) 8) PC control. Inset (opened furnace chamber): 9) sample thermocouple 10) sample and sample holder 11) high T furnace (not shown: optional low T cooler with attached liquid N_2 vessel) 12) radiation shielding

Table 1.1: Technical data and specifications of the used laser flash apparatus 457 by Netzsch-Gerätebau

Temperature range	-125 °C to 1100 °C
Furnace	low T : -125 °C to 500 °C high T : 20 °C to 1100 °C
IR detectors	low T : HgCdTe (MCT), liquid N ₂ -cooled high T : InSb, liquid N ₂ -cooled
Laser	Nd:YAG (1064 nm), max. 18 J/pulse (adjustable)
Pulse width	~ 0.3 ms
Measurement atmosphere	inert, oxidizing, vacuum ($< 10^{-2}$ mbar)
Sample area	cross section: 6×6, 8×8, 10×10 mm diameter: 0.5", 1.0", 6, 8, 10 mm
Sample thickness	~ 0.1-14 mm
Thermal diffusivity range	~ 0.01 mm ² /s to 1000 mm ² /s

1.3 OBJECTIVES AND STRUCTURE

Objectives

To get an insight into heat transport and to understand the underlying processes not only a wide temperature range needs to be investigated, it is at least equally important to be able to accurately and reliably measure the corresponding transport quantities as this is the precondition for all following interpretations.

Therefore, the overarching objective of this dissertation is the improvement of the flash method to accurately derive heat transport data and thereby to gain a better understanding of the thermal transport properties of single crystal quartz SiO₂ and portlandite Ca(OH)₂. This subject is handled within three self-contained publications. The investigations and implications for the flash technique made in the corresponding studies may be transferred to other experimental setups and hence help to increase the range of application of laser flash measurements and the reliability of such measurements in general.

- The first study (chapter 2) focuses on the finite pulse-time effect. The objective is to figure out whether there is an additional signal retardation inhering the temperature history measured at the IR detectors, its possible consequences for standard data reduction routines, and the development of an approach which allows to consider a further retarded signal in data processing. This approach can then be applied to derive thermal transport properties of quartz and portlandite in the subsequent studies.

- In the second study (chapter 3) the temperature-dependent thermal transport properties of quartz are investigated. The primary objective is to measure low temperature thermal diffusivities and to clarify the temperature dependence of the heat transport around the α - β phase transition. In this context, the influence of phase transitions on measurements of thermal transport properties by the flash technique is investigated. There is evidence that standard data reduction routines cannot be used to approximate the temperature history in the vicinity of phase transitions (Branlund and Hofmeister 2007) and thus an adapted data processing (based on the approach of the first study) is required.
- The objective of the third study (chapter 4) is to, for the first-time, measure the thermal transport properties of single crystal portlandite over a wide temperature range including the dehydration of $\text{Ca}(\text{OH})_2$ to $\text{CaO} + \text{H}_2\text{O}$. Therefore, single crystals needed to be synthesized and custom sample holders have been designed to be able to take up the crystal platelets for flash method measurements. A closer look at the dehydration reaction (kinetics) at elevated temperatures investigates the influence of sample dimensions on the derived thermal transport properties.

Both studies on quartz and portlandite furthermore examine thickness dependencies in flash method thermal diffusivity measurements for the probed specimens. The inclusion of single crystal elastic properties (separately derived by Brillouin spectroscopy for the synthesized portlandite crystals) is used to resolve links between the elastic and thermal transport properties.

The accurate knowledge of the physical properties, including the thermal transport properties, of the two mineral species investigated here is of geoscientific and technical interest and of considerable importance for a variety of applications:

- Quartz is one of the Earth's crust most abundant minerals. Its thermal transport properties help for our understanding of the Earth's crustal structure and dynamic behavior (*e.g.* Götze 2009). In particular, assuming that the lower part of thick continental crusts can reach temperatures where the α - β phase transition takes place (*e.g.* Jeanloz and Morris 1986; Zandt et al. 1996; Mechie et al. 2004; Klumbach 2015), a precise knowledge of heat transport within this temperature region is of particular interest and can affect *e.g.* modelings of dynamic tectonic processes. Beyond that, synthetic quartz has a wide range of technical applications – not only but also – due to its piezoelectric property, *e.g.* as quartz crystal microbalance (Deakin and Buttry 1989).
- Portlandite is a layered mineral and isostructural to brucite $\text{Mg}(\text{OH})_2$. In terms of their structure, they rank among the most simple hydroxides available (Kruger et al. 1989), which explains a

fundamental interest in their elastic and thermal transport properties. From a geological point of view, the knowledge of physical properties of hydrous minerals allows for a better understanding of the dynamics in oceanic crust and the uppermost mantle, also because the possibility to release water due to dehydration may trigger seismic events (Nagai et al. 2000). Furthermore, portlandite is an essential mineral in the context of civil engineering as it is a major phase in hydrated cement (*e.g.* Aïtcin 2016). The elastic and thermal transport properties of Ca(OH)_2 affect the properties of hydrated cement based composites (Speziale et al. 2008b) and therefore a detailed understanding of the thermoelastic properties may allow to better customize composites. Beyond that, the de- and rehydration of portlandite is seen as a promising reaction for thermochemical energy storage (Schmidt 2017) and may therefore substantially contribute to future challenges of an energy transition towards sustainable energy systems.

Whereas the vast majority of studies on minerals' thermal transport properties cover their behavior around ambient conditions or examine the temperature range between room temperature and a few hundred degrees Celsius, measurements presented in this thesis aimed to be carried out over a wider temperature range between at least $-100\text{ }^\circ\text{C}$ and $700\text{ }^\circ\text{C}$. With such an extended temperature range, a better understanding of heat transport and the underlying processes shall be reached. For instance, recently proposed models to approximate the temperature dependence of thermal transport properties, *e.g.* by Hofmeister et al. (2014), need to be validated for their applicability in the low temperature region. Beyond that, measurements in the low temperature region (*i.e.* $T < 20\text{ }^\circ\text{C}$) may reveal thermal transport properties of particular interest for new applications *e.g.* in the field of information technology and engineering.

Structure

This dissertation is prepared as a cumulative dissertation consisting of three self-contained studies. The first study on detector inherent delayed response in LFA measurements (chapter 2) has been peer-reviewed and published in the Springer Journal *International Journal of Thermophysics* (Breuer and Schilling 2019). The third study on thermoelastic properties of portlandite (chapter 4) has been peer-reviewed and published in the Elsevier Journal *Cement and Concrete Research* (Breuer et al. 2020). The study on the anisotropic thermal transport properties of quartz (chapter 3) is under review for publication in the *European Journal of Mineralogy* (Copernicus Publications, Breuer and Schilling 2020) at the time of the completion of this thesis. These studies are reprinted within the following three chapters 2, 3 & 4. As they all deal with thermal diffusivity measurements by the flash method, some repetitions appear especially in the theory, methods, and experimental

parts. The findings of these studies are summarized in the last chapter 5 and the contribution of the results to the understanding of thermal transport processes and to measurements using the flash method are discussed. Beyond that, perspectives for future research are pointed out.

STUDY 1

This study is published in the Springer Journal

International Journal of Thermophysics.

The following chapter is a reprint of:

Breuer, S., & Schilling, F. R. (2019). Improving Thermal Diffusivity Measurements by Including Detector Inherent Delayed Response in Laser Flash Method. *International Journal of Thermophysics*, 40(10), 95. doi:10.1007/s10765-019-2562-9

IMPROVING THERMAL DIFFUSIVITY MEASUREMENTS BY INCLUDING DETECTOR INHERENT DELAYED RESPONSE IN LASER FLASH METHOD

ABSTRACT

Laser flash experiments are a widely used to determine thermal diffusivity of matter. Especially for thin samples or high diffusive materials, the laser pulse-time delay and its shape may become crucial for precise measurements (“finite pulse-time effect”). An additional delayed response and modification of the shape of the signal can be caused by time delays of detectors and electronic components (*e.g.*, electronic filters) and may be inherent to Laser Flash Apparatuses (LFA). Similar to the correction of the finite pulse-time effect, this detector system inherent delayed response needs to be taken into account, especially for thin or high diffusive materials. To correct for this additional delay, detector signals of direct laser pulses were measured and for correction of this systematic errors a transfer function is derived. It reproduces the detector signal using the pulse shape measured by a diode within the apparatus and thus takes into account the actual laser pulse shape and detector behavior. For the used experimental setup, systematic errors caused by this effect are in the same range than the often considered finite pulse-time effect. As the detector-related time delay is system inherent, the developed transfer function can be used to effectively eliminate both, the finite pulse-time delay and the detector inherent delayed response. Besides experimental determinations, synthetic temperature response data are used to quantify the systematic errors related to the additional detector inherent retardation for various thermal diffusivities and sample thicknesses. By not taking the additional delay into account systematic errors $> 10\%$ may arise for both, high and low temperature detectors, indium antimonide (InSb) and MCT (HgCdTe), respectively.

KEYWORDS

Finite pulse-time effect · Laser flash method · Thermal diffusivity · Uncertainty

2.1 INTRODUCTION

Precise thermal transport properties are crucial in earth (Čermák and Haenel 1982) and material sciences (*e.g.*, Turner and Taylor 1991). The knowledge of thermal transport properties is necessary to develop and test theoretical models (Siegesmund 1996) and to study the behavior of materials such as single crystals (Horai and Simmons 1969), glasses (Chui and Gardon 1969), ceramics (Tong 1994), or rocks (Seipold 1992). To model the temperature distribution within the Earth, precise information on the thermal transport properties of rocks are essential (Buntebarth 1984).

Since Parker et al. (1961) introduced the transient laser flash method, this technique got continuously improved and is nowadays widely used to determine temperature-dependent thermal diffusivity of solids, powders, and liquids (Blumm and Opfermann 2002; Cernuschi et al. 2002). A short-duration high-intense radiant source (laser pulse, flash lamp) is absorbed on one side of a typically disk-shaped and millimeter-thick sample and the temperature history is detected by an infrared (IR) detector on the opposite rear side of the sample (Swank and Windes 2014). This method can be considered as contact free and hence, no thermal contact resistances need to be taken into account for the evaluation of the observed response curve. As the relative time-depending temperature evolution is determined, no calibrations or absolute temperature recordings are needed (Hofmeister 2004; Abdulagatov et al. 2015). However, numerous factors have been identified affecting the temperature response and such the determined thermal diffusivity, *e.g.*, the influence of the thickness of sample coatings to obtain an optimized absorption and emission behavior (Araki et al. 1992; Albers et al. 2001; Cernuschi et al. 2002; Lim et al. 2009; Schoderböck et al. 2009), nonuniform surface heating (Schriempf 1972; McKay and Schriempf 1976; Baba et al. 1993; Baba and Ono 2001), and heat loss effects (*e.g.*, Cape and Lehman 1963; Cowan 1963; Watt 1966; Heckman 1973; Clark III and Taylor 1975), just to name a few. By quantitatively including the mentioned shortcomings an increase in accuracy can be obtained. The improved evaluation procedures allowed to widen the range of application of laser flash method (micron-sized sample thicknesses (Kehoe et al. 1998), multilayer specimens (Lee 1975), sample coating thermal diffusivity determinations (*e.g.*, Akoshima et al. 2013b; Stryczniewicz and Panas 2015; Stryczniewicz et al. 2017), *etc.*). This also includes the retardation of the temperature response due to a short finite time-lasting laser pulse known as the “finite pulse-time effect” (Cape and Lehman 1963). Except for a minority of experimental setups, the laser pulse cannot be approximated by a Dirac delta (δ) function (Dirac 1967) without having a noticeable influence on the accuracy of the determination of the thermal diffusivity (Heckman 1973). Thus, several attempts were carried out to consider the pulse shape in thermal diffusivity data evaluation, including *e.g.*, saw-tooth (Cape and Lehman

1963), triangular (Taylor and Cape 1964; Taylor and Clark III 1974), square (Cowan 1963; Watt 1966), and exponential (Larson and Koyama 1967; Xue et al. 1993; Lim et al. 2009) pulse shape approximations as well as trapezoidal (Dusza 1995) and empirical (Schoderböck et al. 2009) corrections. But, to better account for the finite pulse-time effect, the actual pulse shape has to be considered in every single thermal diffusivity data evaluation (Lim et al. 2009). In this case, the pulse shape is usually determined using a diode collecting scattered light of the laser for each measurement.

Laser flash measurements on thin and high diffusive materials have shown significant misfits using common data evaluation routines. It seems plausible that the temperature response signal can be additionally affected by detector- and device-specific electronic components (*e.g.*, electronic filters). Thus, we tested the hypothesis that a detector-specific signal retardation has to be taken into account to reduce systematic errors in LFA measurements. The present work therefore covers the questions: 1) is there a detector-sided time delay in temperature recordings, 2) how significant is this systematic error for various sample geometries (*i.e.*, thicknesses), and 3) how can this effect be taken into account in data evaluation routines? The shape of the temperature response curve and thus the approximated thermal diffusivity is affected by numerous additional effects (Vozár and Hohenauer 2003; ASTM E1461 2013). Therefore, to be able to determine the net effect of a possible detector-specific signal retardation, we focus on synthetic curves without any influence of *e.g.*, sample coatings (Araki et al. 1992; Albers et al. 2001; Cernuschi et al. 2002; Lim et al. 2009; Schoderböck et al. 2009), radiation heat losses (Cape and Lehman 1963; Cowan 1963; Watt 1966; Heckman 1973; Clark III and Taylor 1975), *etc.*

2.2 THEORY

The temperature distribution $T(x, t)$ of a thermally insulated solid of uniform thickness d at any time $t > 0$ is given by (Carslaw and Jaeger 1959)

$$T(x, t) = \frac{1}{d} \int_0^d T(x, 0) dx + \frac{2}{d} \sum_{n=1}^{\infty} \exp\left(\frac{-n^2 \pi^2 D t}{d^2}\right) \times \cos \frac{n \pi x}{d} \int_0^d T(x, 0) \cos \frac{n \pi x}{d} dx \quad (2.1)$$

where D is the thermal diffusivity. Based on Eq. 2.1, Parker et al. (1961) gave the analytical solution (adiabatic) for flash method thermal diffusivity measurements. The rear side ($x = d$) surface temperature of

a specimen heated at the front face by a short radiant energy pulse is given as (Parker et al. 1961)

$$T(d, t) = \frac{Q}{\rho c_p d} \left[1 + 2 \sum_{n=1}^{\infty} (-1)^n \exp\left(\frac{-n^2 \pi^2 D t}{d^2}\right) \right] \quad (2.2)$$

with Q the heat pulse energy absorbed per unit area, ρ the density, and c_p the specific heat capacity of the sample. Equation 2.2 can be rewritten as (Parker et al. 1961)

$$V(\omega) = 1 + 2 \sum_{n=1}^{\infty} (-1)^n \exp(-n^2 \omega) \quad (2.3)$$

with the dimensionless parameters for temperature evolution

$$V(d, t) = \frac{T(d, t)}{T_{max}} \quad (2.4)$$

$$\omega(t) = \frac{\pi^2 D t}{d^2} \quad (2.5)$$

and $T_{max} = Q/(\rho c_p d)$ the maximum temperature at the rear side specimen surface at infinite time. As the measured detector signal is not normalized to 1, an additional prefactor is used to scale the fitted curve. For $V = 0.5$ the thermal diffusivity is given as (Parker et al. 1961)

$$D \cong 1.370 \frac{d^2}{\pi^2 t_{1/2}} \cong 0.1388 \frac{d^2}{t_{1/2}} \quad (2.6)$$

where $t_{1/2}$ is the time of the rear side surface history to reach half of its maximum temperature (Fig. 2.1).

Nowadays the evaluation of the thermal diffusivity is typically done by nonlinear least-square curve approximations (Koski 1981) using the entire measured time domain and Eq. 2.3 or modified versions instead of the less robust half time $t_{1/2}$ method (McMasters and Dinwiddie 2010). In this study, fitting is performed for the full curve up to $t_{lim} = 10 t_{1/2}$ (ISO 18755 2005). To determine thermal diffusivity values from measured or synthetic temperature-time curves, a Levenberg-Marquardt algorithm (Levenberg 1944; Marquardt 1963) is used. The analytical solution (Eq. 2.2ff.) assumes (Parker et al. 1961; Baba and Ono 2001; Vozár and Hohenauer 2003):

- Instantaneous and uniform absorption of the heat pulse on the front face
- Specimen nontransparent to the used radiant heat source and thermal radiation

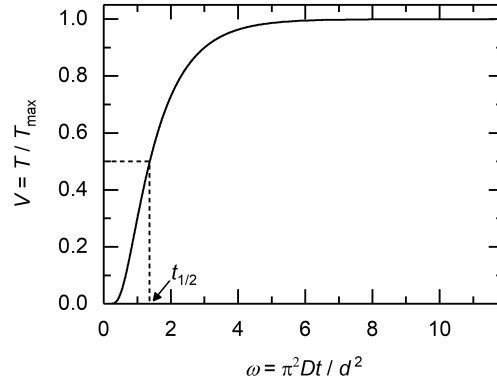


Figure 2.1: Dimensionless rear side surface temperature history

- No heat loss to the surrounding (adiabatic conditions)
- Uniform (geometry), homogeneous sample and that thermophysical properties and density are constant during the experiment.

Depending on the experimental setup and sample characteristics, these assumptions are often not sufficiently met and may therefore require further considerations. Regarding high diffusive and/or thin samples, the heating pulse cannot be assumed as instantaneous (ASTM E1461 2013), causing a significant error in the evaluation of the thermal diffusivity. These uncertainties arising with finite pulse-time effects are often highly underestimated, *e.g.*, Vozár and Hohenauer (2005).

For linear partial differential equations like the heat equation, the principle of superposition can be applied (*e.g.*, Shizawa and Mase 1991). The temperature history on the rear side sample surface can therefore be considered as the sum of individual stimuli with weighting pursuant to the laser power supply. Hence, the solution by Parker et al. (1961) can be applied to any complex source term problem in laser flash experiments considering the appearing laser pulse shape and a possible detector inherent delayed response. The superimposed rear side surface temperature history $V_S(t)$ is mathematically expressed as the convolution of a pulse shape function $g(t)$ and the adiabatic solution $V(t)$ (Azumi and Takahashi 1981; Dusza 1996):

$$V_S(t) = (g * V)(t) = \int_{t'=0}^t g(t') V(t-t') dt' \quad (2.7)$$

For not taking pulse-time effects into account, $g(t)$ is given by the Dirac δ function for an ideally instantaneous pulse, thus $V_S(t)$ equals the solution given by Parker et al. (1961). In case of a time-discrete convolution the integral is replaced by a summation.

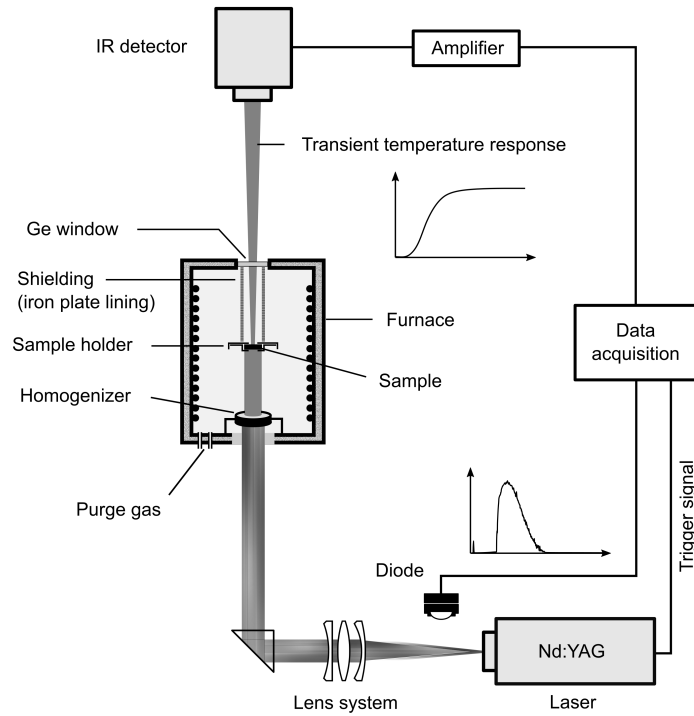


Figure 2.2: Simplified schematic construction of the laser flash apparatus for thermal diffusivity measurements. In addition to the manufacturer setup, an optical homogenizer is placed beneath the sample to reduce a possible nonuniform front surface heating. A thin iron plate lining is employed between the sample and the Ge window to block disturbing sideways radiation to the detector

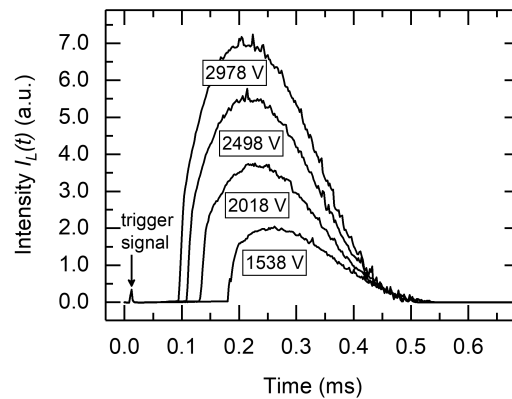


Figure 2.3: Laser pulse intensity $I_L(t)$ measured by integrated diode for different pump energies given as electric potential U in voltage. The asymmetric shape is characterized by a rapid rise followed by a slow collapse in radiant intensity. The onset of stimulated radiation emission is reduced in time as well as the full width at half maximum (FWHM) is increased with increasing pump energy ($\propto U$)

2.3 EXPERIMENTAL

The laser flash apparatus used is a LFA 457 MicroFlash[®] from Netzsch-Gerätebau, Germany. A sketch of the used modified laser flash setup is shown in Fig. 2.2.

The LFA is either equipped with a MCT (HgCdTe) “low temperature” detector (-125 °C to 500 °C) or an indium antimonide (InSb) “high temperature” detector (room temperature to 1100 °C). The minimum time resolution of the detectors is 4 μs. The radiant pulse energy is supplied by a Nd:YAG laser (IR Sources Inc.). It emits light at 1064 nm wavelength with an adjustable power output of up to 18.5 J, controlled by electric potential from $U_{min} = 1538$ V to $U_{max} = 2978$ V. Even though the main spectral response of the IR detectors is situated at slightly higher wavelengths than the actual laser emits, the high-intense pulse can nevertheless be measured at the detector. This holds true as long as a low but not negligible detector efficiency is taken into account.

To prevent the detector measuring sideways scattering irradiation, the beam path between the sample and the germanium window is additionally shielded by an iron rolled plate lining for this study (Fig. 2.2).

Test measurements have shown that a slightly nonuniform heating occurs, which might lead to systematic errors according to *e.g.* Schriempf (1972) and Baba and Ono (2001). Thus, to further reduce heating inhomogeneity a custom 1” diameter areal laser homogenizer RD 203 by Holo/Or Ltd. (Israel) is installed beneath the sample (Fig. 2.2).

The shape of each individual laser pulse is measured from scattered laser light as a function of time using an integrated diode located near the source of emission (Fig. 2.3). To reduce uncertainties arising from the nonlinearity of the temperature dependence on the spectral radiance (Planck’s equation) (Baba and Ono 2001), U_{min} is used unless otherwise stated (ISO 18755 2005).

To detect the direct laser pulse at the IR detector the sample holder is equipped with a custom plate of 12.7 mm in diameter. It is made of Macor glass ceramic (Schröder Spezialglas, Germany) and has a centric pinhole with $\varnothing = 0.5$ mm to avoid an overdrive of the detector. To prevent any laser radiation passing the 3 mm thick semitransparent ceramic plate, pure gold of some μm thickness (according to the deposition rates given by the manufacturer) is sputtered on both sides of the plate using a Denton Vacuum LLC (USA) Desk V.

2.4 RESULTS

2.4.1 *Detector Inherent Delayed Response and its Consideration by Transfer Function*

The finite pulse-time effect can be considered by a heat source term approximating the pulse shape (Fig. 2.3, $g(t)$ in Eq. 2.7) in the solution

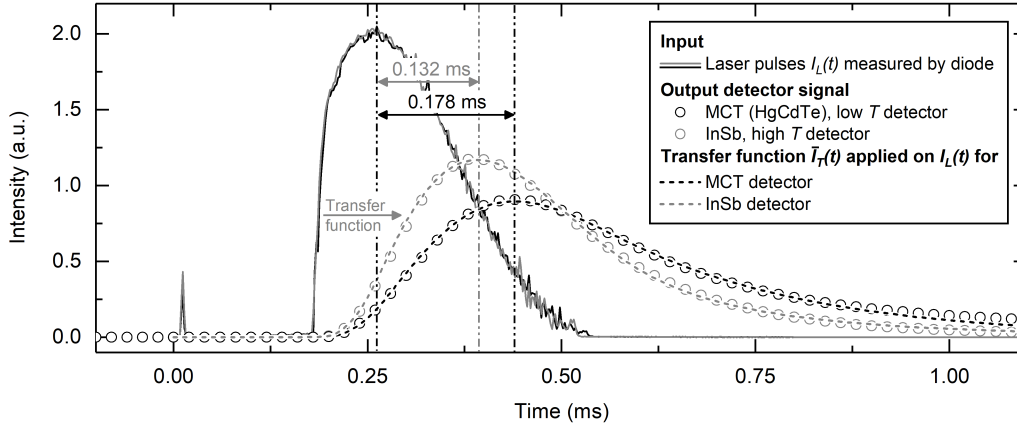


Figure 2.4: Laser pulses $I_L(t)$ ($U = 1538$ V) detected by integrated diode (solid lines) and pulse signals measured with high temperature InSb (\circ gray) and low temperature MCT (\circ black) IR detectors using direct beam (for details see text). Transfer function is applied on the input laser pulses $I_L(t)$ giving $\bar{I}_T(t)$ and shown as dashed lines to reproduce the corresponding detectors' signals. The high reproducibility of the shape of the laser pulse is shown by the gray and black solid lines lying on top of each other. The spike at ~ 0.01 ms corresponds to the trigger signal for the laser

of the unsteady heat conduction equation (*e.g.*, Cape and Lehman 1963). To spot whether there is an additional detector-sided time delay in the data, the direct laser pulse irradiation with applied beam size reducing custom plate is measured with the high and low temperature IR detectors. The results are shown in Fig. 2.4.

It appears that an additional time delay at the two different detectors is present causing the input laser pulses $I_L(t)$ to be further delayed with a pronounced tailing. This effect is more distinct for the low temperature (MCT) than for the high temperature (InSb) detector. The additional retardation by the detector inherent delayed response is of comparable size as the finite pulse-time effect for the measured setup. Thus, thermal diffusivity data evaluation using $g(t) = I_L(t)$ (Eq. 2.7), which considers the finite pulse-time effect according to quasi-simultaneously measured laser pulse (Fig. 2.3), results in an underestimation of apparent thermal diffusivities D_a as the retardation by the detector is not considered sufficiently. The systematic errors made by using the Dirac δ function for the data evaluation are even bigger, as in addition to the detector inherent delay the finite pulse-time effect needs to be taken into account.

To apply a more accurate pulse description, an empirical transfer function is developed in the style of an *e.g.*, electronic filter, linking the pulse shape measured by integrated diode with the retarded pulse measured at the IR detector with respect to the trigger pulse at $t = 0$ s. It is found that the intensity $I_T(t)$ of the transferred laser pulse over time t (η diode time resolution) is well approximated by

Table 2.1: Transfer function coefficients for Eqs. 2.8&2.9 determined for the used experimental setup

Detector	MCT (HgCdTe, low T)	InSb (high T)
η	2 μ s	2 μ s
A_1	1.40×10^{-1}	4.97×10^{-2}
A_2	9.767×10^{-1}	1.256
ε	0.048 ms	0.044 ms
r	7.554×10^{-3}	35.103×10^{-3}
n	19	17

$$I_T(t) = \begin{cases} 0.0 & 0 \leq t \leq \varepsilon \\ I_L(t - \varepsilon) \frac{A_1}{I_{L,max}} & t > \varepsilon \wedge I_T(t - \eta) \leq 0.0 \\ I_T(t - \eta) - (|I_T(t - \eta)| r)^{A_2} & t > \varepsilon \wedge I_T(t - \eta) > 0.0 \\ + I_L(t - \varepsilon) \frac{A_1}{I_{L,max}} & \end{cases} \quad (2.8)$$

with detector type dependent constants, controlling the scaling (A_1), the post-maximum curve shape (A_2), the time delay (ε), and the detector recovery factor (r) (Tab. 2.1), based on $I_L(t)$ the pulse intensity measured by the integrated diode. To smooth the transferred pulse shape measured by diode (*cf.* Fig. 2.3), a central moving average is applied:

$$\bar{I}_T(t) = \frac{1}{2n+1} \sum_{i=-n}^n I_T(t + i\eta) \quad (2.9)$$

The laser pulse shape measured by diode is used to predict a detector signal using Eqs. 2.8&2.9. The as predicted curves $\bar{I}_T(t)$ (Fig. 2.4, dashed lines) are compared to measured ones (Fig. 2.4, circles) for low and high temperature detectors. It is shown that the laser pulse shape measured at both IR detectors is well reproduced by applying the developed transfer function on the laser pulse measured by integrated diode.

Around ~ 0.01 ms a spike is observed (Figs. 2.3&2.4), which corresponds to the trigger signal for the laser. The origin of the spike is either an optical or electrical (more likely) impulse to trigger the depopulation of excited states in the laser medium. Some tests were performed with and without suppressing this spike for the thermal diffusivity D determination. No differences in the evaluated D value for fits with or without the trigger spike are observed. The spike at ~ 0.01 ms is suppressed for the application of the transfer function. Due to the pronounced fading of the detector data, particularly for the

Table 2.2: c factors used in Eq. 2.10 to link true and apparent thermal diffusivities

Detector type	MCT (HgCdTe)	MCT (HgCdTe)	InSb	InSb
Pulse shape	Dirac δ	$I_L(t)$	Dirac δ	$I_L(t)$
c (s)	-0.00385	-0.00187	-0.00337	-0.00138

MCT detector, the coefficients for the transfer function are set so that at $t = 2.0$ ms, \bar{I}_T is < 0.01 and for $t > 2.0$ ms the intensity is $\bar{I}_T = 0.0$. Tests reveal that the same transfer function with its constants shown in Tab. 2.1 can be used for different laser outputs.

2.4.2 Systematic Errors Caused by Detector Inherent Delayed Response

To quantify the influence of the detector retardation effect on the determination of thermal diffusivities and to avoid experimental uncertainties, thickness-dependent synthetic rear side surface temperature response curves $V_S(t)$ are generated using predefined thermal diffusivities D_0 (here named true diffusivity) in Eqs. 2.3&2.7 and the actual retarded laser pulses (Fig. 2.4, dashed lines) as pulse shape functions $g(t)$ (*cf.* Eq. 2.7) for both detectors. No heat losses are used in the models to avoid further complications (adiabatic boundary condition). To quantify the related systematic errors, apparent thermal diffusivities D_a are determined using either $I_L(t)$ pulse shape (finite pulse-time effect, Fig. 2.3) or the Dirac δ function. Figure 2.5 shows true thermal diffusivities D_0 vs. apparent ones D_a for different sample thicknesses between 0.1 mm and 10 mm with an operating laser pulse voltage of $U = 1538$ V for low (left) and high temperature detectors (right). Results using Dirac δ function and $I_L(t)$ laser pulse shape are presented at the top and bottom, respectively. The uncertainties for the fit procedure itself are < 0.001 %.

As the effect of the detector-sided retardation is less distinct for the high temperature indium antimonide detector (*cf.* Fig. 2.4), D_0 vs. D_a lines lie closer to the diagonal (Fig. 2.5c&d), which represents an ideal match between true and apparent thermal diffusivities $D_0 = D_a$. With an increasing sample thickness the deviation of D_a from the true value D_0 decreases as the temperature response and thus $t_{1/2}$ gets large with respect to the laser pulse duration and detector retardation effect. Deviations from the true thermal diffusivities D_0 are slightly smaller using higher laser power outputs as the onset of stimulated laser light emission starts earlier after the trigger pulse (*cf.* Figure 2.3). However, if the samples show a distinct temperature dependence of the thermal diffusivity, *e.g.*, $\propto 1/T$, a higher laser pulse may lead to additional experimental uncertainties (Schilling 1999).

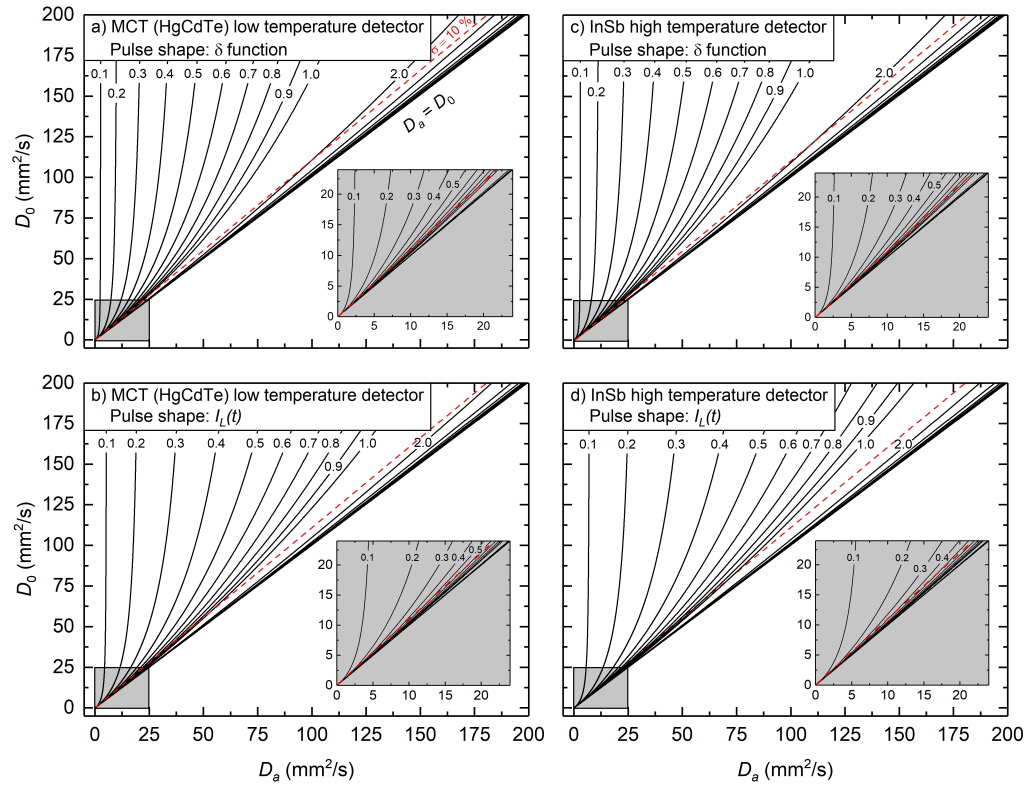


Figure 2.5: True thermal diffusivity D_0 vs. fitted apparent thermal diffusivity D_a using discrete convolution (Eq. 2.7) with $g(t)$ either the Dirac δ (a, c) or $I_L(t)$ pulse shape function (b, d) for the two different IR detectors for low (MCT) (a, b) and high (InSb) (c, d) temperatures. Numbers inside the plot correspond to different sample thicknesses given in millimeters. Dashed red lines correspond to a systematic error of D_a of $\sigma = 10\%$, which increases with decreasing sample thickness

Table 2.3: φ factor used for systematic error calculation in Eq. 2.12 for thermal diffusivity data evaluation using Dirac δ and $I_L(t)$ pulse shapes for high and low temperature detectors

Detector type	MCT (HgCdTe)	MCT (HgCdTe)	InSb	InSb
Pulse shape	Dirac δ	$I_L(t)$	Dirac δ	$I_L(t)$
φ (s ⁻¹)	2.5979	5.3585	2.9712	7.2537

As indicated in Fig. 2.5, there is a systematic correlation between the apparent and true thermal diffusivity values and the sample thicknesses. This relation of D_0 with respect to the appearing D_a is represented as

$$D_0 = \frac{D_a}{1 + \left(\frac{c}{d^2}\right) D_a} \quad (2.10)$$

for $(c/d^2) D_a < 1.0$ and c factors given in Tab. 2.2. For $c = 0.0$ s it is $D_a = D_0$ and $g(t) = I_T(t)$, which is equivalent to the consideration of the additional detector-sided retardation.

If the deviation of the thermal diffusivity is expressed as

$$\sigma = \frac{D_0 - D_a}{D_a} \times 100\% \quad (2.11)$$

then the systemic error of the apparent thermal diffusivity D_a plotted vs. the sample thickness d becomes linear in double logarithmic scale (Fig. 2.6).

Considering the dependence of the sample thickness d , systematic errors displayed in Fig. 2.6 are expressed as

$$\sigma(d) = \frac{D_0}{\varphi d^2} \quad (2.12)$$

with σ in percent and φ shown in Tab. 2.3. In case thermal diffusivities are fitted using a Dirac δ or $I_L(t)$ pulse shape, Eqs. 2.10-2.12 allow for corrections of systematic errors in laser flash measurements for the used experimental setup.

The systematic errors made by an instantaneous pulse approximation (Dirac δ function, Fig. 2.6a&c) are roughly twice as big as including the pulse shape $I_L(t)$ measured by integrated diode (Fig. 2.6b&d) compared to the true value of the thermal diffusivity D_0 by considering the detector-sided retardation. Systematic errors of apparent thermal diffusivities are increasing with a decrease of sample thickness d . For a moderate thickness of $d = 0.5$ mm, a thermal diffusivity of $D_0 = 5.0$ mm²/s, and $I_L(t)$ pulse shape correction, the apparent thermal diffusivity for the low temperature MCT detector is $D_a \cong 4.82$ mm²/s.

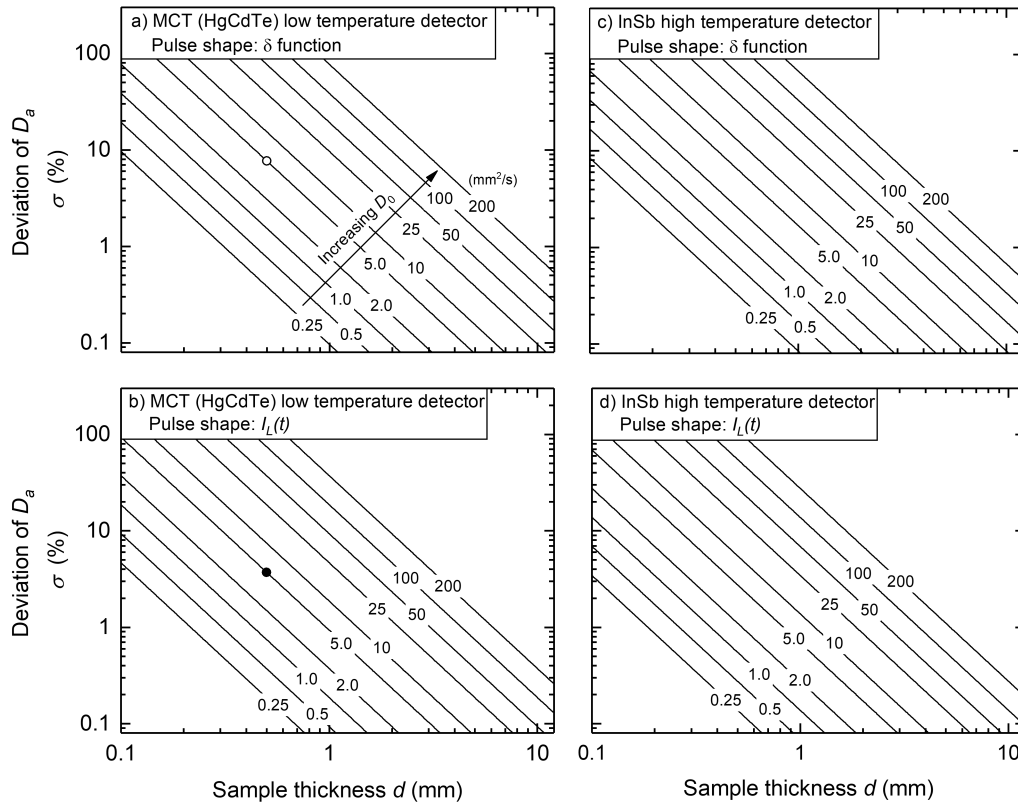


Figure 2.6: Systematic error σ (deviation of apparent thermal diffusivity D_a) vs. sample thickness d for certain true thermal diffusivities D_0 from $0.25 \text{ mm}^2/\text{s}$ to $200 \text{ mm}^2/\text{s}$ for a Dirac δ pulse (a, c) and $I_L(t)$ pulse shape function (b, d) for the low (a, b) and high (c, d) temperature IR detector, respectively. \bullet and \circ are examples which are discussed in more detail in the text

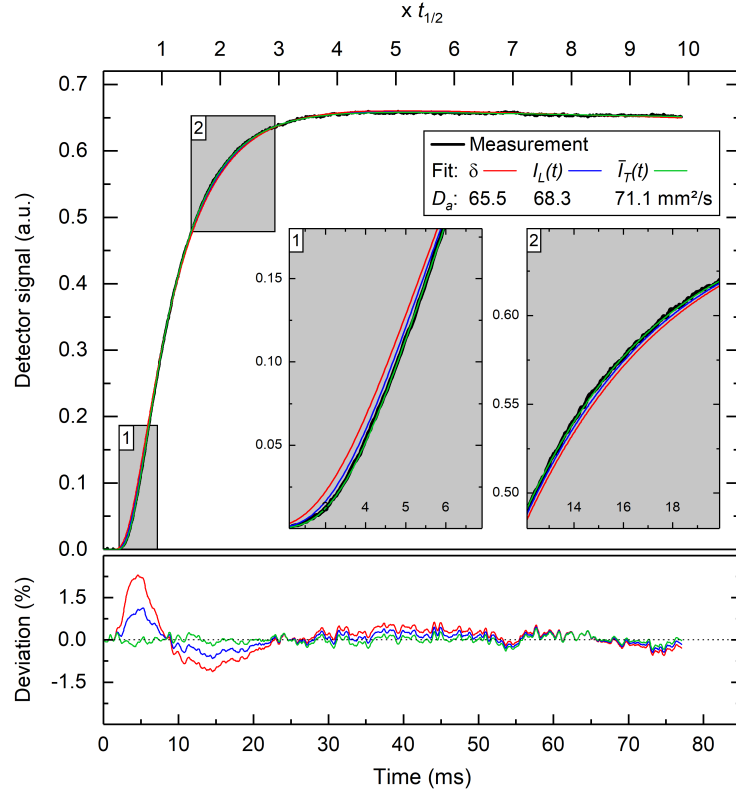


Figure 2.7: Measurement of POCO Graphite AXM 5Q ($d = 1.992(3)$ mm) at 24.9 °C with low temperature MCT (HgCdTe) detector and 1538 V laser voltage output. For the data evaluation three pulse shape functions are considered: Dirac δ function (red), laser pulse-time corrected $I_L(t)$ (blue) and laser pulse shape including detector retardation $\bar{I}_T(t)$ (green). The deviation is referred to the maximum intensity $I_{max} \sim 0.66$ of the detector signal

Thus, although including the finite pulse-time effect the systematic error is about 3.7 % (filled circle, Fig. 2.6b) or without considering any pulse-time effect (Dirac δ function) $D_a \cong 4.64$ mm²/s and $\sigma \approx 7.8$ % (open circle, Fig. 2.6a).

2.4.3 Impact of Delayed Detector Response on Experimental Data

Figure 2.7 shows a LFA measurement of a standard sample (10×10 mm, POCO Graphite AXM 5Q, NIST SRM 8426 series) at 24.9 °C without a coating applied. The corresponding data fit according to Eq. 2.7 for three laser pulse shape functions (Dirac δ pulse, laser pulse corrected $I_L(t)$, detector retardation corrected $\bar{I}_T(t)$) are plotted into the same diagram. The fits include a custom heat loss model proportional to the detector signal (linear heat loss approximation).

Most important for the thermal diffusivity fit procedure is the region of the actual temperature rise. For POCO Graphite, in this area of fast temperature response ($t \leq 25$ ms) the deviations of the three

different fits (Fig. 2.7, lower part) show significant differences with serious misfits for data evaluations using Dirac δ (Fig. 2.7, red) and $I_L(t)$ (Fig. 2.7, blue) pulse shape functions. With respect to insets 1 and 2, fits using the latter heat source terms have their slope onsets too early and less steeply ascending slopes compared to the measured detector signal.

The fit using the detector retardation transfer function provides the best match (green curve in Fig. 2.7) and is for comparison defined as $D_0 = 71.1(1) \text{ mm}^2/\text{s}^4$. Deviations σ from D_0 are 8.5 % and 4.1 % while using the Dirac δ pulse and $I_L(t)$ pulse shape for data evaluation, respectively. For comparison, systematic errors arising from synthetic curve calculations according to Eq. 2.12 (see also Figs. 2.5&2.6) result in slightly smaller errors $\sigma = 6.9 \%$ and 3.3% . This might be due to the fact that in the synthetic temperature history curves no heat losses were assumed. As a consequence, the derived uncertainties shown in Figs. 2.5&2.6 may be regarded as a minimum.

2.5 DISCUSSION

Systematic errors related to finite pulse-time effects can be crucial for the accuracy of thermal diffusivity data evaluation. Standard fit routines consider the finite pulse-time effect by different mathematical representations (*e.g.*, saw-tooth (Cape and Lehman 1963), *etc.*). They lead to a much better approximation of thermal diffusivity compared to an idealized Dirac δ pulse shape (Lim et al. 2009; McMasters and Dinwiddie 2010). However, these corrections are often not sufficient as the retardation caused by detector inherent delay can affect the temperature history curve resulting in apparent thermal diffusivities being significantly too small (*cf.* Figs. 2.7&2.8). As described, if the transfer function for the detector inherent retardation is determined for a specific configuration, it is possible to correct this systematic error if the shape (*e.g.*, measured with an integrated diode) and retardation of the laser pulse is known (*e.g.*, through a transfer function).

If the time delay of detector and electronic components is not (correctly) implemented in thermal diffusivity fitting routine, a misfit of the temperature response and the approximated curve as shown in Fig. 2.8 (*cf.* Fig. 2.7) will arise. Due to the effect of detector-sided retardation the temperature rise on the rear side surface of the sample is recorded later than the heat physically arrives there and hence the measured slope is noticeable steeper compared to fittings using Dirac δ or $I_L(t)$ pulse functions. The magnitude of such misfits using δ or $I_T(t)$ pulse shapes correlates with the thermal transport properties and the thickness d of the specimen.

⁴ A comparison of thermal transport properties of POCO Graphite AXM 5Q with literature values would be misleading and expedient as the thermal diffusivity at a given temperature of different specimens may strongly vary (*e.g.*, Hust 1984; Baba and Cezairliyan 1994; Sheindlin et al. 1998; Akoshima and Baba 2005).

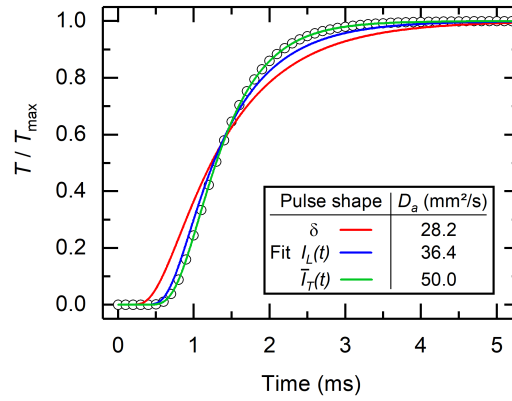


Figure 2.8: Synthetic MCT detector temperature response curve (\circ) for a sample with true thermal diffusivity $D_0 = 50 \text{ mm}^2/\text{s}$ and $d = 0.5 \text{ mm}$. Full pattern fits with corresponding apparent thermal diffusivities D_a for: Dirac δ pulse shape (red – as derived $D_a = 28.2 \text{ mm}^2/\text{s}$), finite pulse-time effect ($I_L(t)$, blue – as derived $D_a = 36.4 \text{ mm}^2/\text{s}$) and finite pulse-time effect including detector-sided retardation ($\bar{I}_T(t)$, green – as derived $D_a = 50.0 \text{ mm}^2/\text{s}$)

Comparable steep rear side temperature response curves with modeling misfits can originate from other effects too. Therefore, the shape of the misfit can usually not directly be linked to the different processes. Wherever possible, these effects should be minimized experimentally (*e.g.*, using an optical homogenizer within the beam path of the laser to reduce the nonuniform sample heating, Fig. 2.2), as any interacting effects make it complex to either separate or understand one of those sufficiently (*e.g.*, sample surface graphite coating mixed with the finite pulse-time effect, Schoderböck et al. 2009). An insufficient consideration of sample surface radiation heat losses may result in approximated temperature response curves too flat too (ASTM E1461 2013). Furthermore, any kind of nonhomogeneous sample surface heating (nonuniform beam profile or heterogeneous surface absorption due to insufficient coating) affects the slope in temperature rise (*e.g.*, Schriempf 1972; McKay and Schriempf 1976; Baba et al. 1993; Baba and Ono 2001) and may be mixed up with previously mentioned effects. Similarly, semitransparent materials may affect the temperature-time curve in a comparable manner (Mehling et al. 1998). These examples rudimentarily show the variability of usually not wanted (or ignored) influences on the temperature-time curve in flash experiments and reveal the importance of separating the different curve shape influencing factors. However, as the transfer function for the detector inherent retardation can be determined independently for any specific configuration, it is possible to correct for this systematic error independently of the other effects.

To avoid that the laser directly irradiates the IR detector, a protecting Ge window is placed between the sample rear side and the detector (*cf.* Fig. 2.2). In a first approximation, one might assume that the ger-

manium window entirely blocks the laser radiation and thus that the retarded laser signal is not caused by the detector itself but is the result of *e.g.*, a heating of the Ge window (and/or its antireflection coating). Following this, measurements performed with (thin) samples of high thermal diffusivity should be well fitted while applying standard finite pulse-time effect corrections. But the presented measurement (POCO Graphite, *cf.* Fig. 2.7) shows that the finite pulse-time correction alone does not sufficiently describe the observed temperature-time curve, especially up to $t = 25$ ms (Fig. 2.7, blue curve). The deviation from the fitted curve is far above the experimental uncertainties. However, if the described detector inherent delay is additionally taken into account, a much better match between the approximated and observed curves is achieved (Fig. 2.7, green curve). Furthermore, if the Ge window would cause the observed retarded pulse signals only, both detectors should show a similar behavior, which is not observed in Fig. 2.4. Both observations strongly support the hypothesis that the laser pulse retardation originates from the IR detector and its electronic components. Accordingly, it seems reasonable that even though the transmittance of the Ge window is very low for the laser radiation wavelength, due to its high intensity the laser still transmits radiation to the detector to a certain amount. According to this, we conclude that 1) the detector inherent delay needs to be taken into account for the used setup and 2) that the presented experimental scheme to determine the transfer function and evaluation procedure helps to improve the accuracy of LFA experiments.

The delayed detector response described here and the evaluation routine based on the principle of superposition enables to account for the actual pulse shape in intrinsic thermal diffusivity determinations. As shown for the standard sample POCO Graphite (*cf.* Fig. 2.7), systematic errors are several percent for common thermal diffusivity fitting procedure using $I_L(t)$ pulses and even higher for a Dirac δ pulse shape function. These systematic errors for synthetic temperature response curves are able to exceed the overall laser flash method standard uncertainty estimation of ~ 4.0 % (coverage factor $k = 2$) (Vozár and Hohenauer 2005; Akoshima and Baba 2006). Referring to Fig. 2.9, if one demands the systematic error originating in pulse-time effects to be $\sigma \leq 0.5$ % using $I_L(t)$ (Dirac δ) pulse shape function, the sample thickness is required to be $d \geq 5.2$ mm, \blacklozenge in Fig. 2.9 (7.4 mm, \diamond in Fig. 2.9) and thus at least ~ 2.5 (3.7) times bigger than the actual sample dimension of used standard POCO Graphite ($D_0 = 71.1$ mm²/s, \square in Fig. 2.9). Regarding standard (reference) materials used for thermal diffusivity measurements (Baba and Ono 2001; Ogawa et al. 2001; Blumm et al. 2003a; Akoshima and Baba 2005; Salmon et al. 2010; Akoshima et al. 2015), it shows that especially the few high diffusive solids (IG-110/CRM 5804 and POCO Graphite, *cf.* Fig. 2.9) are far in the region of not negligible systematic errors $\sigma \gg 0.5$ %.

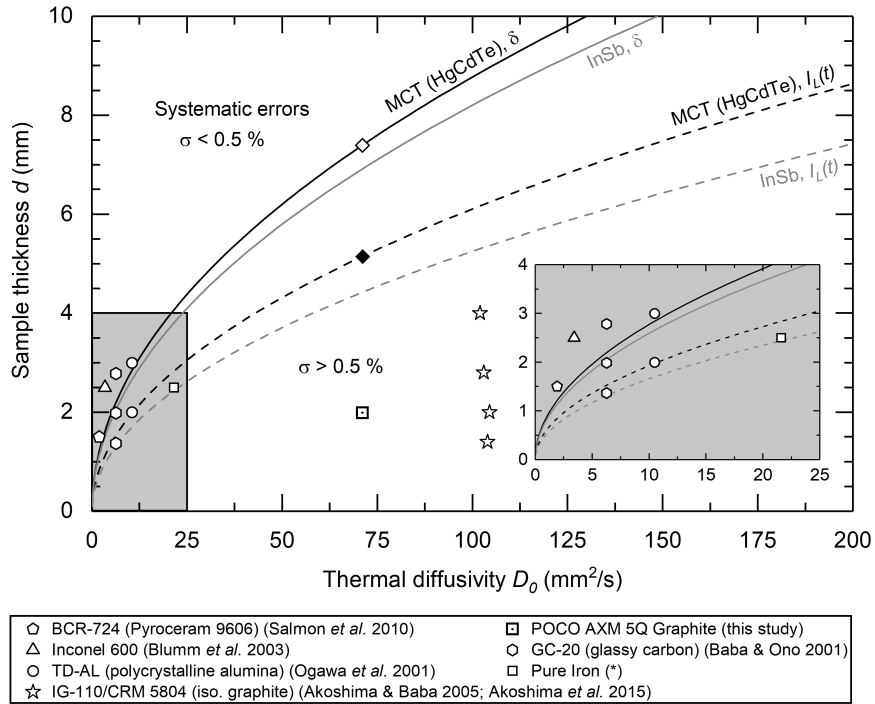


Figure 2.9: Lines representing systematic error thresholds $\sigma = 0.5\%$ for high (gray) and low (black) temperature detectors and for Dirac δ (solid) and $I_L(t)$ (dashed) pulse shape functions, respectively. Above (below) each line the systematic errors are $\sigma < 0.5\%$ ($> 0.5\%$) for the shown sample thicknesses d and thermal diffusivities D_0 . ♦ and ◇ see explanations given in the text. (*) unpublished, from: Netzsch manufacturer's certification – reference sample set (serial #4835)

To trace possible systematic errors in laser flash thermal diffusivity data, a variation of sample thicknesses can be used. An insufficient heating pulse shape consideration manifests in apparent thermal diffusivities increasing with the sample thickness. As in parallel sample coating effects (Lim et al. 2009) and changes in the laser power used may also affect the thermal diffusivity (Akoshima et al. 2013a), samples with varying thickness could be measured without or with at least very thin and similar coating and at constant low laser power to reduce other above mentioned effects and to obtain thermal diffusivity values with a higher precision. But even for measurements with constant heat pulse energy the apparent thermal diffusivity D_a can be a function of the thickness as samples undergo different absolute temperature rises during the experiment (*cf.* T dependence of D) and effects of detector nonlinearity may result in an underestimation of thermal diffusivity (*e.g.*, Groot 1989; Hasselman and Merkel 1989; Hasselman and Donaldson 1990; Akoshima et al. 2013a). Anyway, a variation in sample thickness may be difficult due to rarely accessible (natural) materials (*e.g.*, geological single crystals) or due to heterogeneity of the probed material. In such cases, a data evaluation routine accounting for the actual laser pulse shape including detector retardation effects is a viable option which can help to significantly reduce this systematic error.

2.6 CONCLUSION

As the shape of the sample rear side temperature response curve in thermal diffusivity measurements is diverse and affected by numerous factors, a separation of those effects is inevitable for measurements with high accuracy. It has been shown that even though a finite pulse-time effect correcting algorithm is applied, thermal diffusivities may still contain large systematic errors due to a further time delay possibly caused by the detector and electronic components. By not accounting for this additional retardation, systematic errors can be of the same order of magnitude as the finite pulse-time effect itself and a consideration is necessary, especially for thin specimens and materials of high thermal diffusivity. The presented experimental scheme allows for the determination of a transfer function while using a specifically designed sample with a pinhole. It is shown that the as determined device-specific transfer function applied to the heating laser pulse (detected by diode) takes account for the delayed response of the used InSb and HgCdTe infrared detectors. The modified data evaluation procedure based on principles of superposition shows that using a standard sample of POCO Graphite (AXM 5Q) systematic errors in LFA experiments are effectively reduced.

2.7 ACKNOWLEDGMENTS

This work was made possible by a foundation of Dr. M. Herrenknecht. The authors want to thank Dr. B.I.R. Müller, Dr. G. de la Flor, and H. Fuchs for constructive discussions and the reviewers for their comments which helped to improve the manuscript.

STUDY 2

This study is under review in Copernicus Publications

European Journal of Mineralogy.

The following chapter is a reprint of:

Breuer, S., & Schilling, F. R. (2020). Anisotropic Thermal Transport Properties of Quartz: From -120 °C Through the α - β Phase Transition. *European Journal of Mineralogy*, (under review)

ANISOTROPIC THERMAL TRANSPORT PROPERTIES OF QUARTZ: FROM -120 °C THROUGH THE α - β PHASE TRANSITION

ABSTRACT

Thermal diffusivities of synthetic quartz single crystals have been measured between -120 °C and 800 °C using laser flash method. At -120 °C the lattice thermal diffusivities are $D_{[001]} = 15.7(8)$ mm²/s and $D_{[100]} = 8.0(4)$ mm²/s in [001] and [100] direction, respectively. Between -80 °C and 560 °C the temperature dependence is well approximated by a $D(T) = 1/T^n$ dependency (with $n = 1.824(29)$ and $n = 1.590(21)$ for [001] and [100] direction), whereas for lower temperatures measured thermal diffusivities show smaller values. The anisotropy of the thermal diffusivity $D_{[001]}/D_{[100]}$ decreases linearly over T in α - and β -quartz, with a discontinuity at the α - β phase transition at $T_{\alpha,\beta} = 573$ °C. In the measured signal-time curves of α -quartz an unusual radiative heat transfer is observed, which can be linked to the phase transition. However, the effect is already observed far below the actual transition temperature. The standard evaluation procedure insufficiently describes the behavior and leads to an underestimation of the thermal diffusivity of ≥ 20 %. Applying a new semi-empirical model of radiation absorption and re-emission reproduces well the observed radiative heat transfer originating in the phase transition. In the β -quartz region the radiative heat transfer is not influenced by the phase transition effect observed in α -quartz and for the thermal diffusivity evaluation common models for (semi)transparent samples can be used.

KEYWORDS

Thermal diffusivity · Quartz · α - β phase transition · Laser flash method

3.1 INTRODUCTION

Thermal transport properties such as thermal conductivity κ and thermal diffusivity D play an important role in understanding Earth's crust and mantle dynamics and their underlying processes (Čermák 1982; Lenardic and Kaula 1995). Furthermore, growing attention is given to a precise knowledge of heat transport in material sciences as well as in engineering (Taylor and Kelsic 1986; Turner and Taylor 1991). According to Fourier's law the heat flux q is equal to the thermal conductivity κ of a material times the negative temperature gradient $\partial T/\partial x$ in one dimension:

$$q = -\kappa \frac{\partial T}{\partial x} \quad (3.1)$$

The thermal conductivity quantifies the heat flow through a material. Comparable to chemical concentration equilibration through diffusion, thermal diffusivity D quantifies the temperature equilibration capability.

$$\frac{\partial T}{\partial t} = D \frac{\partial^2 T}{\partial x^2} \quad (3.2)$$

Thermal conductivity and thermal diffusivity are interrelated through the isobaric specific heat capacity c_p and density ρ :

$$\kappa = D\rho c_p \quad (3.3)$$

Comparable to the concept of diffusion in the kinetic gas theory, phononic (lattice) heat diffusion in solids is often approximated by (Debye 1914; Berman 1976; Kittel 2005)

$$D = \frac{1}{3} vl \quad (3.4)$$

with the mean velocity of phonons v and their mean free path length l . Regarding insulated solids, phononic heat transport dominates at low temperatures (*e.g.* Shankland et al. 1979; Schilling 1999; Gibert et al. 2005). In earlier studies, heat transfer was often solely related to acoustic phonons (Slack 1965; Slack and Oliver 1971; Roufosse and Klemens 1974), whereas recent studies show that longitudinal and transverse optical phonons need to be taken into account (Hofmeister 1999; Hofmeister 2006; Esfarjani et al. 2011). With increasing temperature and number of phonons the phonon-phonon interactions, *e.g.* three-phonon umklapp processes, increase (Peierls 1929; Ross et al. 1984; Kittel 2005), resulting in a temperature dependence of the thermal diffusivity frequently being approximated by (*e.g.* Eucken 1911; Zoth and Haenel 1988; Seipold 1992; Clauser and Huenges 1995):

$$D \propto \frac{1}{T} \quad (3.5)$$

Even though Fourier's law presumes length independence, heat transport can vary with specimen thicknesses *e.g.* due to radiative transport mechanism for optically non-thick conditions (Hofmeister 2019) and mode mixing effects (Hofmeister et al. 2007; Hofmeister 2007). Thermal conductivity and thermal diffusivity of crystalline solids are directional, *i.e.* anisotropic, material properties (except for the cubic system) and can be described by a symmetric tensor of 2nd rank (Nye 1985).

Quartz is one of the most abundant rock-forming minerals in the Earth's crust (Ronov and Yaroshevsky 1969; Yaroshevsky and Bulakh 1994). High geothermal gradients in the uppermost tenth kilometers (Birch 1955) demand a detailed knowledge about the thermal transport properties of its constituents (Buntebarth 1984; Siegesmund 1996). Thus, quartz plays an important role in developing and testing thermal transport models (Höfer and Schilling 2002) and detailed information on the single crystal thermal transport properties are required (Touloukian et al. 1973). In terms of its significance, also for technical applications, single crystal thermal diffusivity data on quartz are still scarce and restricted to temperatures above 0 °C (Tab. 3.1). For higher temperatures formerly reported thermal transport properties (Höfer and Schilling 2002; Kanamori et al. 1968) contain both contact losses and spurious radiative gains as has been shown by Branlund and Hofmeister (2007).

At ambient pressure, α -quartz ($P3_221$) undergoes a displacive phase transition to β -quartz ($P6_222$) at $T_{\alpha,\beta} = 573$ °C (*e.g.* Le Chatelier 1890; Bragg and Gibbs 1925; Dolino 1990). In the vicinity of the phase transition an incommensurate phase is observed (Dolino 1990). Already above ~ 540 °C, *i.e.* > 30 K below the phase transition, apparent changes of anelastic (thermal expansion) and elastic properties (*e.g.* elastic constants and therewith acoustic wave velocities) are observed (Raz et al. 2002; Klumbach and Schilling 2014)

To the best of the authors' knowledge, no thermal diffusivity data of quartz below 0 °C have been published so far. Measurements in [001] and $[\bar{0}01]$ direction crossing the α - β phase transition were reported by different authors: Kanamori et al. (1968), Höfer and Schilling (2002), and Branlund and Hofmeister (2007). The trend of the thermal diffusivity around the α - β phase transition remains uncertain, as a crossover in the direction of maximum thermal diffusivity was reported by Höfer and Schilling (2002). Branlund and Hofmeister (2007) considered this behavior to be possibly caused by specimen size (thickness) effects. The only data set not being potentially associated with known shortcomings of contact methods, *e.g.* thermal contact resistance effects (Lee and Hasselman 1985; Hofmeister 2007; Abdulagatov et al. 2015), is the one by Branlund and Hofmeister (2007). But with respect to that, Branlund and Hofmeister noted that the used "*model of Mehling et al. (1998) fails to fit the measured signal-time curves near the transition*". The

Table 3.1: Published data on thermal transport properties of single crystal quartz in [001] and [100] direction

Reference	Method	Crystal type	Temperature range (°C)
Berthier (1965) ^a	radial heat flow	natural	50-700 ^b
Kanamori et al. (1968)	Ånström ^c (modified)	natural	40-860
Beck et al. (1978)	radial heat flow ^d	natural	0-350
Höfer and Schilling (2002)	transient method ^e	synthetic	20-800
Branlund and Hofmeister (2007)	laser flash method ^f	natural and synthetic	20-1000
This study ^g	laser flash method ^f	synthetic	-120-800

^aCited by Touloukian et al. (1973)

^bOnly direction \perp [001] measured over the α - β phase transition up to 700 °C

^cCarslaw and Jaeger (1959)

^dExtrapolated from 1.95 GPa (multi anvil press), converted to D

^eSchilling (1999)

^fParker et al. (1961)

thermal diffusivity behavior around the α - β phase transition therefore remains unclear.

Phononic heat transport decreases with increasing temperature, approximated by Eq. 3.5 for the case that all phonon modes are excited. However, this assumption is only valid for high temperatures. At low temperatures, phonon modes freeze out and affect the heat transport properties of the solid (Kittel 2005). Thus, low temperature data are of fundamental interest.

The aims of this study are: 1) Present low temperature behavior of the heat transport in quartz. 2) Better understand the thermal diffusivity behavior through the α - β phase transition (including a possible crossover occurrence, Höfer and Schilling 2002, and size effects, Hofmeister 2019). This requires a new approach to approximate the signal-time data for α -quartz measurements below the α - β phase transition compared to the model used by Branlund and Hofmeister (2007). 3) Review a proposed (Höfer and Schilling 2002) strong correlation of the phonon velocity and the temperature dependence of the thermal diffusivity. Therefore, thermal diffusivity laser flash data on synthetic quartz single crystals have been collected between -120 °C and 800 °C in different crystallographic directions and at different sample thicknesses (2-10 mm, 10×10 mm cross section). The measurements furthermore allow to better distinguish between phononic and radiative heat transfer.

3.2 EXPERIMENTAL

Experimental setup

The thermal diffusivity is measured by laser flash method (Parker et al. 1961) using a Netzsch-Gerätebau MicroFlash[®] LFA 457. A short (~ 0.3 ms) laser pulse (0.5" diameter, approx. ~ 1 J power output, 1064 nm, IR Sources Inc.) heats up one side of the specimen with thickness d and the resulting (relative) temperature history is recorded on the opposite (rear) side using an infrared (IR) detector. For low temperature measurements ($T = -120$ to 400 °C) a HgCdTe (MCT) IR detector is used, for high T measurements between room temperature (RT) and 800 °C an indium antimonide (InSb) detector is installed. Furnace temperatures are measured close to the specimen using a type K thermocouple (class 1, DIN EN/IEC 60584-1). The chamber is continuously flushed with gaseous N_2 (99.99 %) with a flow rate of 50 ml/min. The temperature increase ΔT of the specimen rear side during one measurements is ≤ 1 K and thermophysical properties (D , κ , c_p) and density ρ are assumed to be constant within ΔT for each diffusivity determination. The used laser flash setup presumes the IR detector voltage outputs to be linear to the temperature increase during one measurement.

In laser flash (LFA) experiments on (semi)transparent insulating solids three major processes influence the detected signal-time curve:

adiabatic lattice (phononic) heat transport, fast radiative transport and heat loss to the surrounding (1-3 in Fig. 3.1). To isolate the phononic contribution to thermal transport, the signal-time curves (black line, Fig. 3.1) are approximated by a combination of the adiabatic model given by Parker et al. (1961) (dashed blue line, Fig. 3.1)

$$T(d, t) = \frac{Q}{\rho c_p d} \left[1 + 2 \sum_{n=1}^{\infty} (-1)^n \exp\left(\frac{-n^2 \pi^2 D t}{d^2}\right) \right] \quad (3.6)$$

(Q absorbed heat pulse energy per unit area) with a custom heat loss model and a fast radiative portion (dotted orange and dash-dotted red line, Fig. 3.1). Heat loss from the surfaces of the specimen is approximated by subtracting a proportional temperature difference $dT_{i, \text{heat loss}}$ from the temperature T_i for each time interval Δt (Schilling 1998; Höfer and Schilling 2002)

$$dT_{i, \text{heat loss}} = h T_i \Delta t \quad (3.7)$$

with fitting constant h as only free parameter. This approximation assumes 1D heat flow and hence mainly heat losses from the front and rear surfaces. This approximation is well fulfilled for thin platelets. For thicker samples 2D effects may occur, *e.g.* if heat losses perpendicular to the assumed 1D heat flow influence the observed signal.

Fitting fast direct radiative heat transfer is different for measurements at temperatures below and above the α - β phase transition (*cf.* Fig. 3.2c&d). For $T \leq 573$ °C an absorption/re-emission approximation for semitransparent samples is applied. For $T > 573$ °C the ballistic (boundary to boundary) transfer is defined as portion of the fast temperature decrease of the specimen's front surface instantaneously heated by the laser. The corresponding temperature distribution is given in Parker et al. (1961) and in a good approximation represented by $\propto 1/\sqrt{t}$.

$$T_{i, \text{rad}} = \begin{cases} T_0 \tau^i + b, & T \leq 573 \text{ °C}, i \in \mathbb{N}_0 \\ \frac{T_0}{\sqrt{t_i}} + b, & T > 573 \text{ °C}, i \in \mathbb{N} \end{cases} \quad (3.8)$$

(t_i : time steps). Constants approximated during the fit process are: T_0 characterizing the initial height of the radiative portion (*cf.* inset Fig. 3.1), τ controlling the magnitude of the temperature decrease and b an optional shift of the derived relative T signal. For measurements at temperatures below 150 °C the radiative heat transfer is negligible (Fig. 3.2b).

Depending on the individual raw data, the signal-time curve is fitted to $5\text{-}10 \times t_{1/2}$ (with $t_{1/2} = 0.1388 d^2/D$, Parker et al. 1961) by inhouse software using least-squares Levenberg-Marquardt algorithm (Levenberg 1944; Marquardt 1963). A pulse-time correction according to Breuer

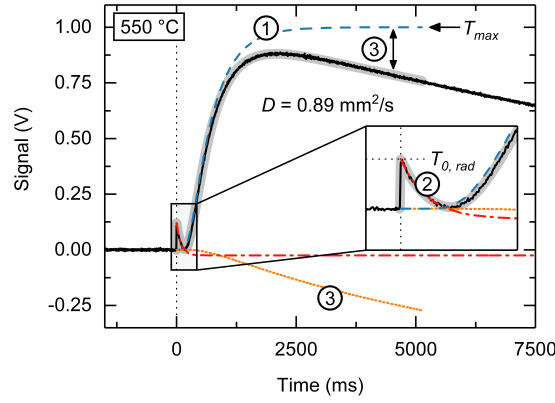


Figure 3.1: Signal-time curve (black line) measured at 550 °C in the laser flash apparatus using InSb infrared detector. The detector signal (V) is assumed to scale linearly to the temperature. The fitted curve (thick gray line) is the result of a least-squares approximation of the adiabatic model by Parker et al. (1961) (1, dashed blue line) with a fast radiative portion (2, dash-dotted red line, Eq. 3.8, $T \leq 573$ °C) and subtracting heat loss from the specimen surface (3, dotted orange). Vertical dotted line denotes the release of the heating laser pulse. $T_{0,rad}$ corresponds to the direct radiative heat transfer at $t = 0.0$ ms (Eq. 3.8). T_{max} is referred to as the theoretical adiabatic maximum temperature of the specimen rear side by lattice (phononic) heat transfer (*i.e.* excluding heat losses of the sample)

and Schilling (2019) is applied to each approximation. Thickness corrections with increasing T are applied using linear thermal expansion coefficients $\alpha_L(T)$ for [001] and [100] direction as given by Klumbach (2015) (based on Raz et al. 2002). Reported thermal diffusivities are the average of three independent measurements at the corresponding temperature. The experimental reproducibility is 2-3 % while the accuracy is 5 %, confirmed by measurements on Pyroceram 9606, Inconel 600 and Stainless Steel 310 standard samples. Uncertainties can be higher in the vicinity of phase transitions, *e.g.* due to a pronounced distortion of the signal-time curves (overlap of different heat transport processes) or by using very small (McMasters et al. 2017) and/or thick sample dimensions (Swank and Windes 2014).

The temperature dependence of the thermal diffusivity $D(T)$ of quartz below 550 °C is fitted using the empirical model proposed by Hofmeister et al. (2014) (T in K):

$$D(T) = FT^{-G} + HT \quad (3.9)$$

where the FT^{-G} term describes the contribution of lattice phonons to heat transport and the rear high T term (HT) represents a contribution of bulk infrared phonon-polaritons. Fitting constants are $F, G (> 0)$, and $H (\geq 0)$.

Table 3.2: Specimens and measurement characteristics for the low and high temperature thermal diffusivity experiments

Specimen	Thickness (mm)	Detector	Temperature (°C)
LT _[100]	2.010(3) ^a	HgCdTe	-119-400
LT _[001]	2.064(3)	HgCdTe	-119-400
HT1 _[100]	1.986(3)	InSb	26-775
HT2 _[100]	4.022(4)	InSb	25-725
HT1 _[001]	1.999(3)	InSb	26-800
HT2 _[001]	4.706(4)	InSb	25-640

^anumbers in parentheses are 1σ standard deviation of the last digits

Samples

For the thermal diffusivity measurements six 10×10 mm platelets with various thicknesses were prepared from one synthetic quartz single crystal in gem quality supplied by Maicom Quarz (in accordance with DIN EN/IEC 60758). The specimens were cut so that the perpendicular to the surface corresponds to the crystallographic [100] (*i.e.* a -axis) and [001] (*i.e.* c -axis) direction (Tab. 3.2), respectively. The angular deviations of the samples were proven by ultrasonic sound velocity measurements and are $< 1^\circ$. The tabulated thicknesses were measured using a micrometer, the deviation from parallelism is $\leq 1^\circ$. To reduce radiative heat transfer in LFA measurements (Hasselmann and Merkel 1989), all platelets were sputter coated with Au (99.99 %) using a Denton Vacuum LLC Desk V to $\sim 0.1 \mu\text{m}$ (according to the deposition rates given by the manufacturer). To ensure consistent laser pulse absorption (Cernuschi et al. 2002; Stryczniewicz et al. 2017) and to buffer oxygen fugacity at high T (Pertermann et al. 2008), specimens were coated with graphite spray (CRC Industries) of about $\sim 15 \mu\text{m}$ thickness per side. Platelet surfaces were slightly roughened to mitigate possible non-uniformity of the laser pulse absorption and to increase the adhesion of the coatings (Branlund and Hofmeister 2007).

3.3 RESULTS

The as derived single crystal thermal diffusivity data of quartz are shown in Fig. 3.2a as a function of temperature for the main directions [001] and [100] (data in Appendix A.1, Tab. A.1&A.2).

The data of high and low temperature measurements show a distinct $D(T)$ evolution nearly proportional to $1/T$ between -80°C and $\sim 550^\circ\text{C}$ for both crystallographic orientations as expected for *e.g.* three-phonon umklapp processes (Peierls 1929; Kittel 2005). The direction of faster temperature equilibration coincides with the 3-fold axis

in [001] direction. In the vicinity of the α - β phase transition thermal diffusivities stop following the trend of $D \propto 1/T$. The data show a further distinct decrease in lattice thermal diffusivity, starting at $T \sim 560$ °C and reaching its minimum of $D_{[100]} \sim 0.56$ mm²/s and $D_{[001]} \sim 0.60$ mm²/s at the α - β phase transition temperature (HT2_[001]) or slightly above ($T_{D,min} = 575.6$ °C for HT1_[001] and 578.0 °C for HT1_[100] and HT2_[100]). After the phase transition D values sharply increase and stay more or less constant up to 800 °C at $D_{[001]} \sim 0.98$ mm²/s and $D_{[100]} \sim 0.86$ mm²/s. Thermal diffusivities in hexagonal β quartz are about 15 % and 21 % higher for [001] and [100] direction compared to fitted D values of α -quartz extrapolated to $T_{\alpha,\beta} = 573$ °C (black lines, Fig. 3.2a). In the β phase the c -axis is still the direction of maximum thermal diffusivity. Green and blue areas in Fig. 3.2a correspond to thermal diffusivity variations (effect of impurities) of quartz single crystals measured by Branlund and Hofmeister (2007). Data of this study lie close to the lower end of these variations and slightly below the thermal diffusivities reported by Kanamori et al. (1968) (leftwards triangles) and Höfer and Schilling (2002) (stars). Data fits (least-square minimization) according to Eq. 3.9 for $-120 \leq T \leq 550$ °C are presented as black lines for the [001] and [100] direction in Fig. 3.2a (drawn up to $T_{\alpha,\beta} = 573$ °C for illustration). The resultant fit parameters are (D in mm²/s, T in K): $D_{[001]}(T) = 1.86(30) \times 10^5 T^{-1.824(29)}$ ($R^2 = 0.990$) for [001] direction and $D_{[100]}(T) = 2.71(31) \times 10^4 T^{-1.590(21)} + 7.8(29) \times 10^{-5} T$ ($R^2 = 0.996$) for [100] direction, respectively. Fitting the [100] direction data benefit from including the HT term (*cf.* Eq. 3.9) whereas for the c -axis data the fitting gives $H = 0.0 (\pm 5 \times 10^{-5})$. Thus, no improvement of the fit quality is achieved including the high temperature term for the latter. For $T < -80$ °C the measured thermal diffusivities are lower than the data approximations after Eq. 3.9, especially for the higher diffusive [001] direction.

The front parts of raw data signal-time curves are exemplarily shown in Fig. 3.2b-d for different furnace temperatures. For measurements at low temperatures (Fig. 3.2b), direct radiative heat transfer is effectively suppressed by the sputtered gold layer and data fittings are independent of Eq. 3.8. Furthermore, heat losses are marginal within the short time span of low temperature LFA experiments. For measurements above $T \sim 150$ -200 °C fast radiative heat transfer is explicitly visible in all signal-time curves and increases with temperature (Fig. 3.2c). The shape of the radiative heat transfer portion in raw data signal-time curves shows a different behavior for $T \leq 573$ °C and $T > 573$ °C, which is considered in the applied approximation procedure, Eq. 3.8 (thick gray in Fig. 3.2c&d). Within the α -quartz phase the intensities of the radiative heat transfer in signal-time curves decrease only slowly and are characterized by an almost linear decline with t (Fig. 3.2c). The origin of this radiation is considered in the quartz sample itself. This type of intrinsic radiation cannot be (effectively) suppressed by the gold layer sputtered on the back side of the specimen.

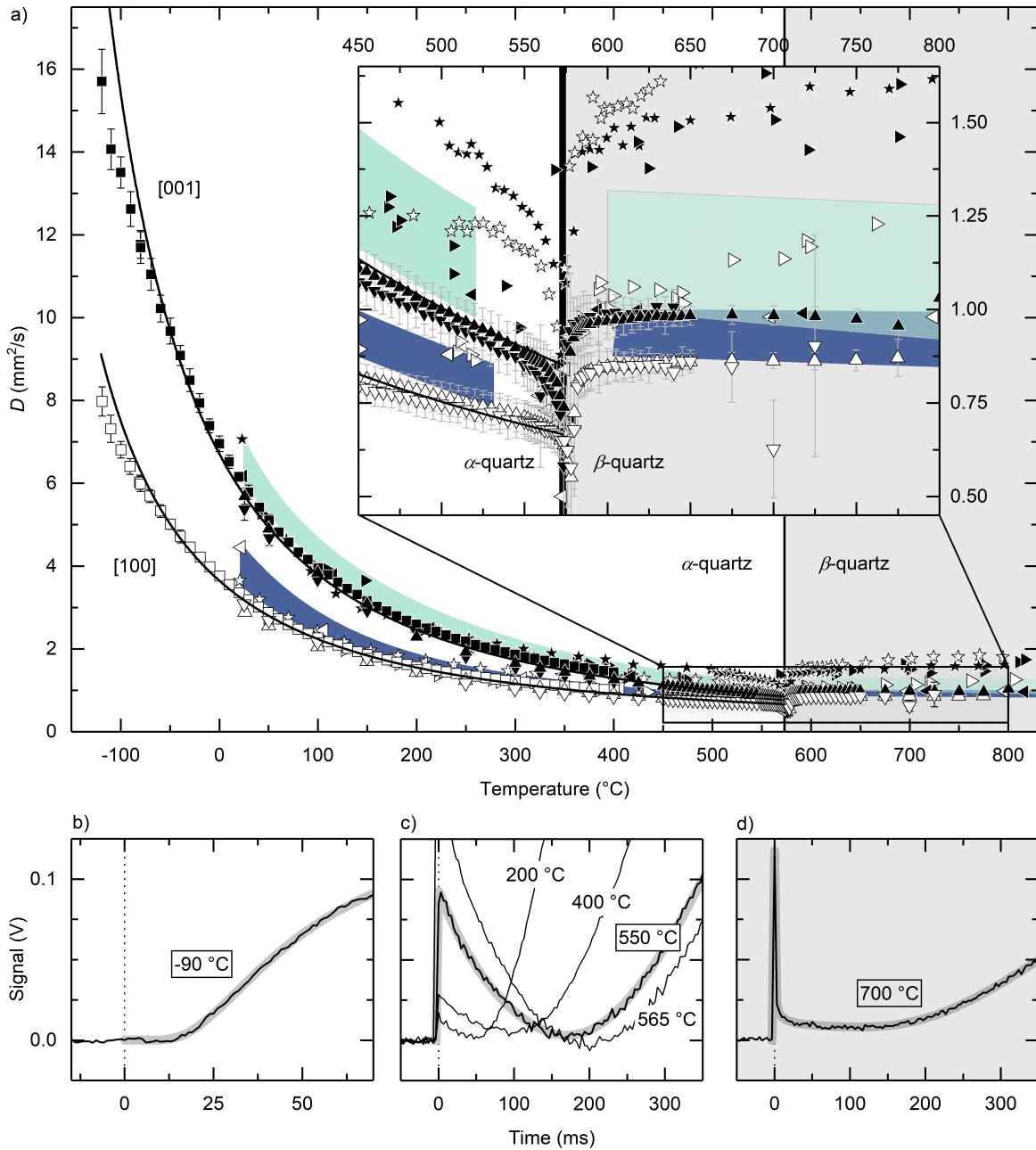


Figure 3.2: a) Measured lattice (phononic) thermal diffusivity D of synthetic quartz single crystals between -120 °C and 800 °C over the α - β phase transition at $T_{\alpha,\beta} = 573$ °C. Low temperature data (squares) are shown for [001] (black filling) and [100] direction (white filling). High temperature data are shown between 25 °C and 800 °C for specimens HT1 (upwards triangles) and HT2 (downwards triangles). $D(T)$ data fits (black line) after Eq. 3.9 for $T \leq 550$ °C in [001] and [100] direction are shown up to the phase transition at 573 °C. Literature data are shown as rightwards triangles – Kanamori et al. (1968), stars – Höfer and Schilling (2002), and leftwards triangles – Branlund and Hofmeister (2007) (“SynQ” specimen). Green and blue areas correspond to the variations of measured D values given by Branlund and Hofmeister (2007) for [001] and [100] direction. Front sections of specimen HT1_[001] raw data signal-time curves (black lines) and data fits (thick gray) are shown for temperatures b) $T = -90$ °C c) 550 °C (with additional raw data shown for 200 °C, 400 °C and 565 °C) and d) 700 °C. Fits of the latter two include a fast radiative heat transfer portion according to Eq. 3.8 with $T_i \propto \tau^i$ (c) and $T_i \propto 1/\sqrt{t_i}$ (d), respectively. For details see text

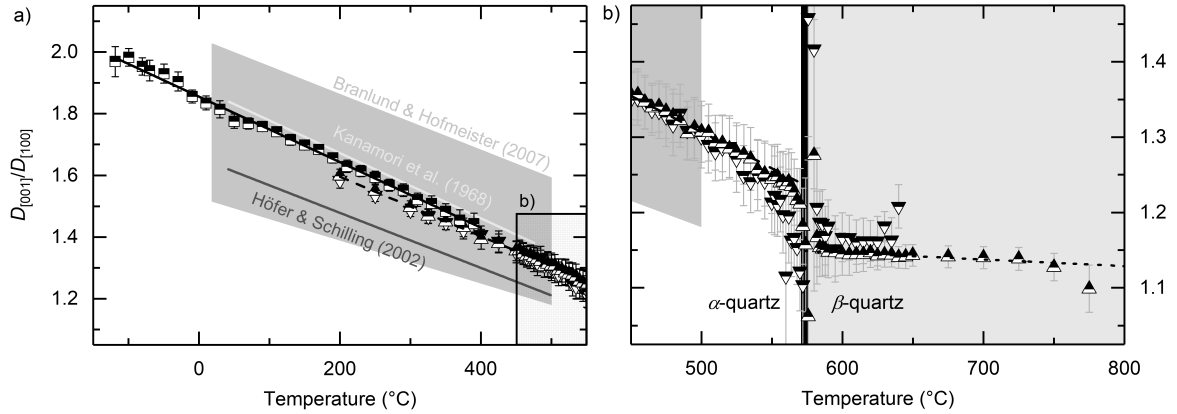


Figure 3.3: Anisotropy of the single crystal thermal diffusivity of quartz shown as ratio $D_{[001]}/D_{[100]}$ for measurements at low (squares, a) and high temperatures (upwards triangles for specimens HT₁, downwards triangles for HT₂, for $T \geq 200$ °C). The α - β phase transition zone is shown enlarged in b). Black solid and dashed lines represent linear fits to α phase data for $T \leq 510$ °C and to β phase for $T = 585$ - 750 °C (b, dotted black line)

In contrast, at temperatures above the phase transition this radiative contributions vanishes. Instead, in the β phase region the radiative heat transfer shows a rapid drop in intensity well described by a $\propto 1/\sqrt{t}$ dependence (Fig. 3.2d) in accordance to a standard boundary to boundary (ballistic) transfer. Even though radiative heat transfer is noticeable for temperatures as low as $T \sim 150$ - 200 °C, the evaluated lattice (phononic) α -quartz thermal diffusivity is consistently unaffected by the radiative transport and well described by Eq. 3.9 until a stronger decrease in thermal diffusivity starts at ~ 560 °C (Fig. 3.2a).

The anisotropy of the single crystal thermal diffusivity of quartz is shown in Fig. 3.3 as $D_{[001]}/D_{[100]}$. The anisotropy ratios are well approximated by linear fits in the α - as well as in the β -quartz region (solid and dashed black lines in Fig. 3.3). The fit to the ratio of LT specimens gives (T in Celsius) $D_{[001]}/D_{[100]}(T) = -1.060(11) \times 10^{-3} T + 1.856(2)$ (solid black line, Fig. 3.3a) and for specimens HT₁ and HT₂ $D_{[001]}/D_{[100]}(T) = -0.963(12) \times 10^{-3} T + 1.788(5)$ (dashed black line, Fig. 3.3a&b, $T \geq 200$ °C). LT as well as HT_{1/2} anisotropy ratios fit well to the data on anisotropy given by Branlund and Hofmeister (2007) on various quartz samples (gray area, Fig. 3.3) and data reported by Kanamori et al. (1968) within $25 \leq T \leq 500$ °C. The data on $D_{[001]}/D_{[100]}$ by Höfer and Schilling (2002) are within the shown anisotropy range (Branlund and Hofmeister 2007) but up to ~ 10 % lower than the data reported in this study. At the phase transition the anisotropy $D_{[001]}/D_{[100]}$ rapidly decreases by about 7 % but stays above 1.0 at all temperatures. Thus, in [001] direction the highest thermal diffusivity is observed over the whole temperature range and no crossover is observed for any probed specimen with thicknesses $d \sim 2.0$ - 4.7 mm (*cf.* Tab. 3.2). The

slope of the linear fit to the anisotropy ratio $D_{[001]}/D_{[100]}$ in the β -quartz phase is significantly flatter than for the α phase and gives $D_{[001]}/D_{[100]} = -0.088(13) \times 10^{-3} T + 1.200(8)$ (dotted black line, Fig. 3.3b).

3.4 DISCUSSION

The presented data for low temperature α -quartz thermal diffusivity fit well into the trend of already published data (*cf.* Tab. 3.1) at and above room temperature (Fig. 3.2a). A small systematic offset can be recognized for the data measured with the low and the high temperature setup. As the preparation was kept the same for all samples, this offset might be caused by different characteristics (nonlinearity, sensitivity) of the two IR detectors and thus reflects the accuracy of the experiment.

It is noticeable that for low temperature measurements $T < -80$ °C the thermal diffusivities are significantly and systematically lower than the data fits according to Eq. 3.9 (using all data between -120 °C and 550 °C), especially for the higher diffusive c -axis direction. To better understand the origin of this deviation, different considerations are discussed: A) This behavior can be caused by the effect of IR detector nonlinearity leading to an underestimation of thermal diffusivity (Hasselmann and Donaldson 1990; Baba and Ono 2001). Negative impacts assuming a linear detector voltage to temperature output are high especially at the lower end of the IR detectors' operating T range and significant even for low absolute temperature rises ΔT during each measurement (Hasselmann and Merkel 1989; Hoefler and Taylor 1990). This could also explain the deviation between measurements with low and high temperature IR detectors as observed in Fig. 3.2a, where thermal diffusivities measured with the high T InSb detector (at its low temperature limit) depict to lower values. B) Specimens measured at low temperatures have a higher ΔT due to smaller heat capacity c_p of α -quartz compared to measurements performed at high temperatures (assuming similar pulse energy absorption) (Lord and Morrow 1957; Akaogi et al. 1995; Chase 1998). As a consequence of higher ΔT , thermal diffusivity values of α -quartz at very low T are quite possibly too low as they reflect the property at higher temperatures (*e.g.*, see Akoshima et al. 2013a). This effect is more pronounced if a strong temperature dependence of thermal diffusivity D is present, as it is the case for α -quartz at very low temperatures (*cf.* Fig. 3.2a). But deviations of measured and fitted thermal diffusivities of up to 20 % are very unlikely to be solely caused by detector nonlinearity and effects of an increase in ΔT due to changes in heat capacity at low temperatures. The used model to fit temperature-dependent thermal diffusivities (Eq. 3.9) is originally tested for $T \geq 25$ °C (Hofmeister et al. 2014). But this approximation seems to be inappropriate at very low temperatures, *i.e.* at $T < -80$ °C for α -quartz. C) At low temperatures, where an increased portion of the phonon modes is frozen out, the temperature dependence of the heat capacity strongly increases

($\propto T^3$ at low T) and likewise the thermal conductivity increases before it reaches a maximum followed by a decrease $\propto e^{\Theta_D/T}$ (Casimir 1938; Lord and Morrow 1957; Zeller and Pohl 1971; Gross and Marx 2014). Furthermore, with an increasing mean free path length l due to a reduction in phonon-phonon interactions at low temperatures, lattice imperfections and geometrical effects become more and more dominant (de Haas and Biermasz 1935; Blakemore 1974; Kittel 2005). It seems therefore reasonable for the intrinsic $D(T)$ trend to deviate from a $D \propto 1/T^G$ behavior for measurements at low temperatures. Hence, we conclude that the observed behavior is not the result of experimental uncertainties alone and that the mentioned deviations to the data fits are in part a manifestation of the intrinsic behavior of α -quartz as a reduced amount of phonon modes are excited and the scattering of phonons at 1D and 2D defects becomes more dominant at lower temperatures.

With the above exception, fits covering low and high temperature measurements up to 550 °C are well approximated by the model proposed by Hofmeister et al. (2014) (*cf.* black lines, Fig. 3.2a). The presented high temperature data have the highest conformity to laser flash data presented by Branlund and Hofmeister (2007) for phonon-dominated heat transfer processes. In contrast, contact methods used by Höfer and Schilling (2002) and Kanamori et al. (1968) only have a good agreement with the data of this study in the lower temperature range (RT to ~ 200 °C) and show a less pronounced decrease of $D(T)$ towards higher temperatures. This is most likely due to direct radiative heat transfer not (sufficiently) being taken into account in these data sets (Andre and Degiovanni 1995; Mehling et al. 1998; Branlund and Hofmeister 2007). A mix of radiative and phononic transfer seems to lead to a positive slope in thermal diffusivities at temperatures above the phase transition, whereas the presented data on lattice thermal diffusivities in this study are in accordance with the data by Branlund and Hofmeister (2007), which indicate $D(T)$ being roughly constant at $T > 600$ °C. The thermal diffusivities for α -quartz samples (this study) are up to ~ 12 % smaller than the D range of various quartz samples presented by Branlund and Hofmeister (2007) (*cf.* green and blue areas, Fig. 3.2a). Above 573 °C the differences are less distinct and the thermal diffusivities lie at the lower limits of published β -quartz laser flash data. A small but noticeable negative influence, *i.e.* lowering thermal diffusivity, of the applied graphite coating on the specimens is conceivable (*e.g.* Albers et al. 2001; Lim et al. 2009) but unable to explain the observed differences alone. Therefore, low(er) thermal diffusivity data of quartz measurements in this study might be caused by low amounts of interstitial ions and the occurrence of phonon scattering at hydroxyls (OH), both decreasing the thermal diffusivity (Branlund and Hofmeister 2007). This interpretation is further supported by the low temperature behavior ($T < -80$ °C), where part of the deviation to the applied $1/T^n$ approximation is probably caused by defects.

D(T) around the α - β phase transition

The two recent publications on thermal diffusivity of single crystal α - β -quartz (*i.e.* studies by Höfer and Schilling 2002 and Branlund and Hofmeister 2007) show a different behavior for the crystallographic direction of the maximum thermal diffusivity at elevated temperatures. Branlund and Hofmeister (2007) confirmed measurements by Kanamori et al. (1968) and found that the direction of maximum thermal diffusivity does not change through the phase transition, whereas Höfer and Schilling (2002) presented data where a crossover (*i.e.* a change in the crystallographic direction of maximum thermal diffusivity) is described.

In this study, measurements on both specimens HT1 and HT2 show no crossover in the $D(T)$ data at any temperature (Fig. 3.2a). After Branlund and Hofmeister (2007), the crossover observed in measurements by Höfer and Schilling (2002) can be explained by the specimen dimensions used by the latter. Accordingly, mixing of longitudinal optic (LO) and transverse optic (TO) modes can cause an inflation of D parallel to [100] and thus the observed crossover occurs (Hofmeister 2007; Hofmeister et al. 2007; Hofmeister 2019). In order to test this hypothesis of a sample thickness dependence of the crossover, an additional thick quartz sample has been measured over the phase transition using laser flash method with an increased laser pulse power output of ~ 5 J (Fig. 3.4, data in Appendix A.1, Tab. A.3). This cubed sample has an edge length of ~ 10 mm (10×10 mm cross section), exceeding the thinnest specimens measured by Höfer and Schilling (2002).

In general, thermal diffusivities presented in Fig. 3.4a show a large variation in $D(T)$, which is due to different measurement techniques and specimens used. Relative trends show that thin specimens measured in this study (*e.g.* HT1, Fig. 3.4a) inhere no crossover in the crystallographic direction of maximum thermal diffusivity between α - and β -quartz, similar to the data presented by Kanamori et al. (1968) and Branlund and Hofmeister (2007) (not shown in Fig. 3.4). The derived anisotropy $D_{[001]}/D_{[100]}$ is > 1.0 at all temperatures (Fig. 3.4b). For specimens with $d = 8.5$ -20 mm measured by Höfer and Schilling (2002) and for the quartz cube ($d \sim 10$ mm, this study, Fig. 3.4a) $D(T)$ data show a crossover around the phase transition with $D_{[100]}$ getting the direction of maximum thermal diffusivity in the β phase. The corresponding anisotropy $D_{[001]}/D_{[100]}$ is characterized by a drop just under 1.0 for the cubic specimen (Fig. 3.4b). Thus, increasing the specimen thickness reproduces the crossover formerly being observed. These results are in accordance with the interpretation by Branlund and Hofmeister (2007) that TO-LO mixing significantly affects thermal diffusivity measurements. It should be clarified that for such thick specimens (~ 10 mm) measured by LFA method the reproducibility and accuracy of the diffusivity determination is much lower compared to appropriate thin specimens and at the resolution limit of the ex-

periment for the used setup. This is due to the very small rear side temperature increase for thick samples, synonymous with a low signal-noise ratio for the data measured at the IR detector. For the thick samples modifications of the used simplified 1D evaluation procedure would be necessary to take 2D effects into account.

After Hofmeister (2007), limiting the thickness-to-diameter ratio to $d/\varnothing = 0.1$ gives intrinsic thermal diffusivities without or at least negligible influence of mode mixing. In this study, all specimens exceed this ratio and have $d/\varnothing \sim 0.2-0.5$ (cf. Swank and Windes 2014 and ASTM E1461 2013). As the results in this study show good agreement with the thermal diffusivity data of single crystal quartz presented by e.g. Branlund and Hofmeister (2007), it is concluded that a possible influence of mode mixing on thermal diffusivity LFA measurements is still negligible for quartz specimens at $d < 5.0$ mm with the used experimental setup.

Data fits show that the lowest measured thermal diffusivities lie up to ~ 5 K above the actual phase transition temperature of $T_{\alpha,\beta} = 573$ °C (except HT2_[001]; thermocouple tolerance is ≈ 2.3 °C at 573 °C, DIN EN/IEC 60584-1). As the temperature is recorded close to but not directly at the sample surface, the observed temperature of the thermocouple may record a slightly higher temperature. However, such observation has also been made by Branlund and Hofmeister (2007). The highest amount of direct radiative heat transfer, linked with a maximum distortion in signal-time curves (reducing the accuracy of the derived data), can be assigned to measurements of minimum thermal diffusivity. The observed shift in minimum thermal diffusivity could therefore be linked to the formation of an incommensurate (inc) phase between ~ 573 °C and ~ 574.3 °C (Bachheimer 1980; Dolino et al. 1983; Dolino 1990; Klumbach 2015). Due to the experimental setup with 2 K temperature steps, thermocouple uncertainties and most notably the specimen temperature increase ΔT within each measurement, it is not possible to clearly discriminate such variations and hence processes within this narrow temperature range. In addition, the phase transition temperature could be affected by e.g. impurities and defects in the crystal.

What controls thermal diffusivity of quartz

The crossover in v_{mean} at the α - β phase transition of quartz led Höfer and Schilling (2002) conclude that their observed crossover in the thermal diffusivity behavior of the used thick samples is the result of a direct correlation of the thermal diffusivity D and the elastic behavior (i.e. sound velocities). The single crystal platelets used in this study are much thinner, satisfying 1D heat transport. Therefore, the observation made by Höfer and Schilling (2002), that the as derived v_{mean} is the main factor controlling the $D(T)$ behavior at high temperatures, is verified here.

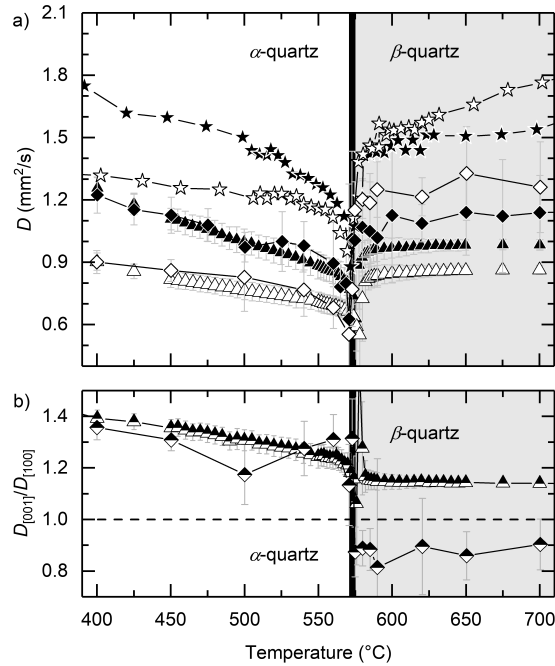


Figure 3.4: a) Thermal diffusivities in [001] (black filling) and [100] direction (white filling) measured for a cubic quartz specimen with thickness $d \sim 10$ mm (diamonds) in comparison to HT1 data (upwards triangles, this study) and measurements given by Höfer and Schilling (2002) (stars). A crossover in the crystallographic direction of the maximum thermal diffusivity is observed for the thick cubic specimen as it was measured for tall cylinders measured by Höfer and Schilling (2002). b) Anisotropy of the thermal diffusivity shown for HT1 (upwards triangles) compared to data of the cubic quartz specimen (diamonds). The crossover in the thermal diffusivity D at the phase transition (a) is represented by a decrease of the anisotropy $D_{[001]}/D_{[100]}$ below 1.0 (dashed line), whereas specimen's HT1 anisotropy stays above 1.0 at all temperatures. As indicated by the error bars, the data showing the observed crossover for the thick cubic sample are at the limit of the experimental resolution

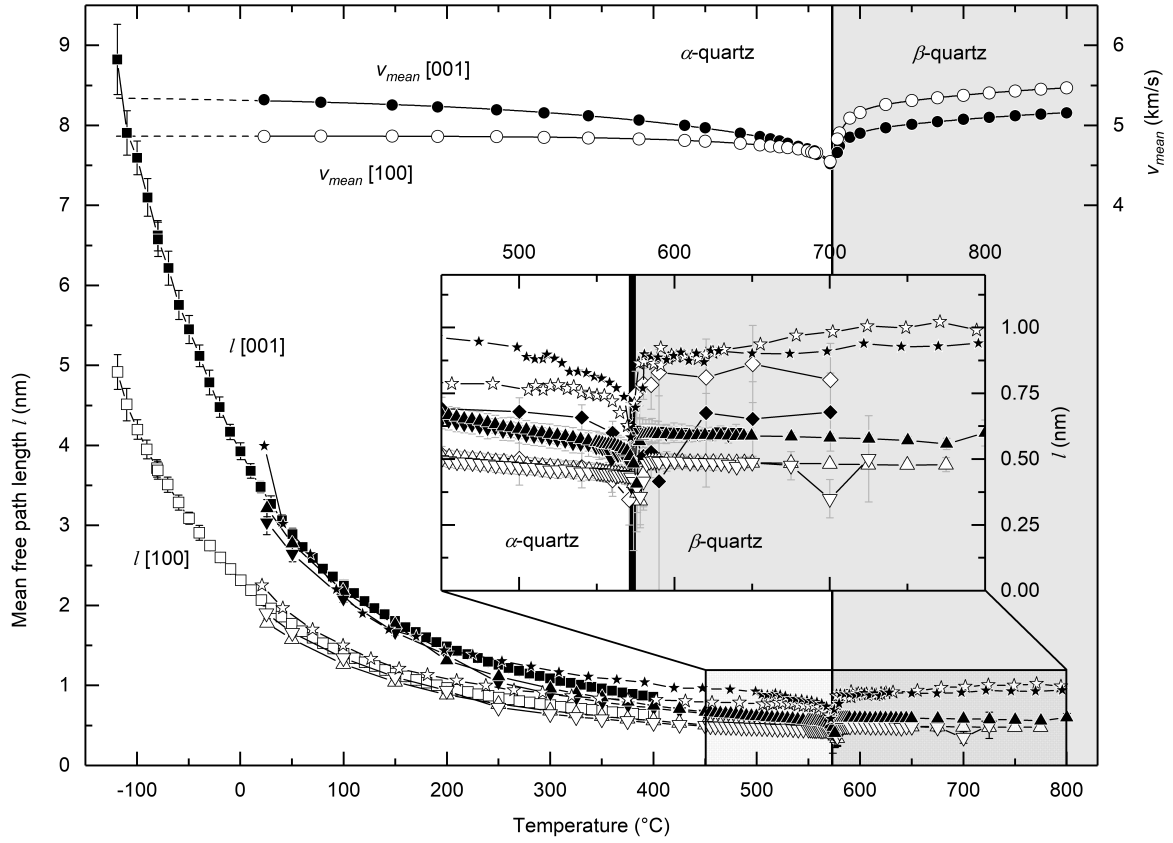


Figure 3.5: Phononic mean free path length l between $-120\text{ }^{\circ}\text{C}$ and $800\text{ }^{\circ}\text{C}$ for $[001]$ (black filling) and $[100]$ direction (white filling) and different specimens: LT (squares), HT1 (upwards triangles) and HT2 (downwards triangles). Calculated after Eq. 3.4 with v_{mean} (circles) derived from elastic constants given by Kammer et al. (1948), Zubov and Firsova (1962), and Ohno (1995). Averaged sound velocities are extrapolated to $-120\text{ }^{\circ}\text{C}$ (dashed black line). Data given by Höfer and Schilling (2002) are shown as stars for comparison. The mean free path length l of the thick cubic specimen (this study, cf. Fig. 3.4a) is given as diamonds (inset)

To derive the mean free path lengths l of quartz in [100] and [001] direction, Eq. 3.4 is used as a first approximation. For the mean velocities v_{mean} the quadratic mean of the directional v_P and both v_{S1} and v_{S2} sound velocities are used ($v_{mean} = \sqrt{(v_P^2 + v_{S1}^2 + v_{S2}^2)/3}$) based on the elastic constants of single crystal quartz (Kammer et al. 1948; Zubov and Firsova 1962; Ohno 1995). For temperatures between -120 °C and 20 °C the sound velocities are extrapolated using an exponential fit which leads to the solid lines for v_{mean} of α -quartz shown in Fig. 3.5. The crossover in v_{mean} at the phase transition temperature (Fig. 3.5) is the result of v_P and v_{S1} , v_{S2} velocities in [100] direction exceeding the sound velocities in [001] direction (which in turn expresses a change in elastic constants with T).

The trend of $l(T)$ (Fig. 3.5) mainly follows that of $D(T)$ (cf. Fig. 3.2a). In contrast to the strong variation of the mean free path length $l(T)$ from 8.8 nm (in [001], 4.9 nm in [100] direction) to ~ 0.5 nm, the mean sound velocities vary only ~ 20 % over the entire temperature range (Fig. 3.5). Thus, it follows that the influence of v_{mean} on $D(T)$ is much less distinct than that of $l(T)$ over the investigated temperature range (including the behavior during the α - β phase transition). The changes in the sound velocities v_{mean} in quartz are not directly correlated to the mean free path length in thin samples (this study) as deduced by Höfer and Schilling (2002) for thick samples. As a consequence, the thermal diffusivity is mainly related to the mean free path length with minor contribution of the mean phonon sound velocity, assuming 1D heat transport.

The discussion of Höfer and Schilling (2002) is based on the assumption that acoustic phonons dominate thermal diffusivity of quartz and the mean free path length is strongly dependent on the phonon wavelength. However, the possible size dependence of the measured thermal diffusivities and the missing direct correlation between the sound velocities and the mean free path length can be seen as an indication for 2D heat transport effects and that longitudinal and transverse optical phonons (especially at elevated temperatures) need to be taken into account to better describe the observed behavior. This would be in agreement with independent density functional theory calculations and observed phonon lifetimes for other oxides such as MgO (Dekura and Tsuchiya 2017; Giura et al. 2019). Together with the deviation of the thermal diffusivity from a simple $1/T^n$ dependence at low temperatures ($T < -80$ °C) and the comparison to data presented by Branlund and Hofmeister (2007), one can conclude that the main portion of the temperature dependence of quartz at elevated temperatures is the result of phonon-phonon interactions whereas the absolute thermal diffusivity and the low temperature behavior indicates a significant influence of 1D/2D defects and inclusions and that the minor variations in the elastic properties have a subordinate influence on the thermal transport behavior.

Direct radiative heat transfer

The influence of direct heat transfer by radiation on the raw data signal-time curve in laser flash experiments of (semi)transparent materials is well known (*e.g.* Andre and Degiovanni 1995; Mehling et al. 1998). But for materials undergoing phase transitions within the temperature range of thermal diffusivity measurements, it seems likely that underlying processes of radiative heat transfer can be different to those of common ballistic transfer in transparent or semitransparent media. Branlund and Hofmeister (2007) noticed in their study that direct radiative heat transfer exceedingly rises close to the α - β phase transition, unable to get fitted by Mehling et al.'s (1998) model. But this finding wasn't considered in their evaluation routine and it is shown here how a separate evaluation procedure can be applied (Fig. 3.2c&d, Fig. 3.7c). Direct radiative heat declines within a few degrees above the phase transition. Branlund and Hofmeister (2007) assume that the laser pulse triggers an α to β phase transition (in portion) of the sample at and close to the heated surface already at $T < 573$ °C. The following β - α inversion is coupled with a release of latent heat observable through a non-ballistic radiative contribution in LFA measurements. This process lasts longer (Fig. 3.2c, Eq. 3.8, $T \leq 573$ °C) than common ballistic direct radiative heat transfer (Fig. 3.2d, Eq. 3.8, $T > 573$ °C), which represents fast cooling of the specimen front surface after the heating by the laser pulse.

To visualize and better understand the change of heat transfer by radiation in $D(T)$ measurements, the ratio of the direct radiative portion $T_{0,rad}$ (Eq. 3.8, *cf.* inset Fig. 3.1) to the theoretical adiabatic maximum temperature T_{max} on the specimen rear side (*cf.* Fig. 3.1) is shown in Fig. 3.6 in logarithmic scale (data in Appendix A.1, Tab. A.4-A.9). Scattering of the data in the low temperature region is the result of experimental uncertainties (*i.e.* approaching resolution limit of the detector, $T_{0,rad}$ very small and close to 0 V), exaggerated by the logarithmic scaling.

The normalized radiation ratio $T_{0,rad}/T_{max}$ shows a first strong increase with T up to the phase transition at $T_{\alpha,\beta} = 573$ °C. This trend is described by $T_{0,rad}/T_{max} = 9.9(4) \times 10^{-3} / (1 - 1.7(1) \times 10^{-3} T) \times 100$ % (solid line, Fig. 3.6, T in Celsius). No difference can be seen for specimens measured in [100] (white filling) and [001] direction (black filling) or for measurements on thinner (upwards triangles) and thicker specimens (downwards triangles). The ratios of the data measured with the HgCdTe IR detector for low temperatures (squares) lie slightly above the data measured by InSb detector for $T > 150$ °C, which is likely due to different detector characteristics (*e.g.* sensitivity, nonlinearity). At the α - β phase transition the radiative contribution $T_{0,rad}/T_{max}$ reaches its maximum followed by a sharp and distinct decrease within a few Kelvin. In the β -quartz phase, the ratio $T_{0,rad}/T_{max}$ again shows a strong increase with T but a dependence on specimen thicknesses

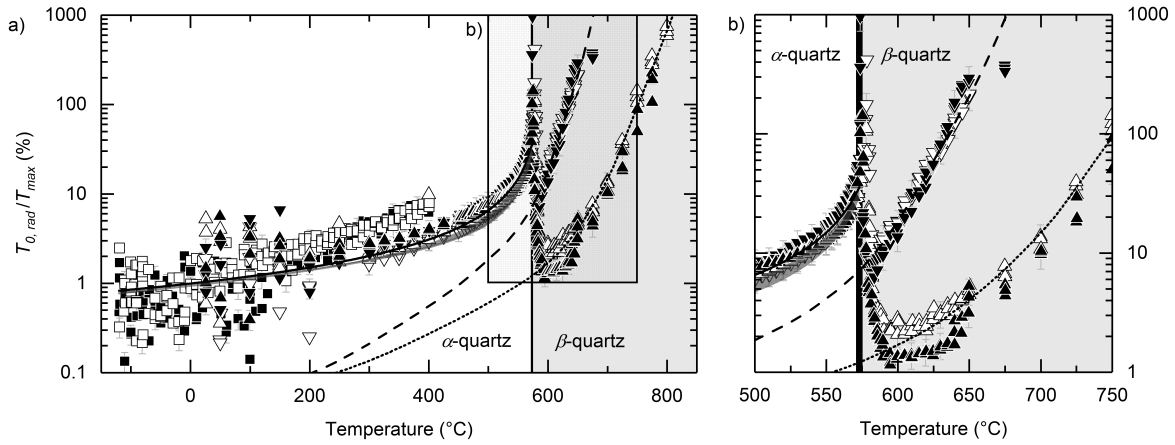


Figure 3.6: a) Ratio of the direct radiative heat transfer ($T_{0,rad}$, cf. Eq. 3.8 and inset Fig. 3.1) to the theoretical adiabatic maximum temperature on the specimen rear side T_{max} (cf. Fig. 3.1) for [001] (black filling) and [100] direction (white filling) and specimens LT (squares), HT1 (upwards triangles) and HT2 (downwards triangles). The solid line represents a reciprocal fit for $T \leq 573$ °C, dashed and dotted lines are splines to guide the eyes for direct radiative ballistic (boundary to boundary) heat transfer (details see text). For the dark gray thick line the effect of direct ballistic heat transport is subtracted from the deduced direct radiative heat transfer. The gray line thus represents the net effect of a non-ballistic radiative heat transfer for α -quartz. The behavior in the vicinity of the α - β phase transition region is shown in detail in b)

(upwards/downwards triangles) becomes apparent. Thicker HT2 specimens have a higher onset and stronger increase with T as thinner HT1 specimens, while again no significant differences for different crystallographic directions [001] and [100] are present. To guide the eyes, the temperature development of $T_{0,rad}/T_{max}$ in the β phase is shown by dashed (HT2) and dotted (HT1) lines (Fig. 3.6) for ~ 2 mm and ~ 4 -4.7 mm thick samples.

The observed strong decrease in the radiation ratio directly after passing the phase transition at 573 °C indicates that at least two different mechanisms influence the radiative heat transfer in LFA measurements through the phase transition, also noticeable through the different shapes of the radiative heat transfer portion in the signal-time data comparing Fig. 3.2c ($T < 573$ °C) and Fig. 3.2d ($T > 573$ °C), first 200 ms. This is further supported by the fact that there is no $T_{0,rad}/T_{max}$ dependence on sample thickness d below 573 °C but above. The radiation below the transition is supposed to be primarily caused by the phase change itself within the sample and non-ballistic (release of latent heat, see above and Branlund and Hofmeister 2007). This affects laser flash measurements as low as $T \sim 150$ -200 °C (cf. Fig. 3.2c, Fig. 3.6), which is well conceivable as the absolute temperatures at the front surface of the specimen initially rise to high values (Parker et al. 1961) well above the phase transition temperature due to the short duration of the laser

pulse. That the gold layer on the back side of the specimen cannot suppress this radiative heat generated within the sample below the phase transition might be explained by a decreased Au reflectance for the wavelength of this non-ballistic radiation. However, the effectively suppressed ballistic contribution around 600 °C is a clear evidence that the thickness of the gold coating is sufficient and that this non-ballistic contribution is not the result of the coating. The net effect of radiative heat transfer originating from the phase transition is approximated by subtracting the ballistic radiative heat transfer (dashed and dotted line, Fig. 3.6) from the assumed non-ballistic portion (dark gray in Fig. 3.6). If this is taken into account (Eq. 3.8), $D(T)$ data fits according to Eq. 3.9 describe well the measured data in both crystallographic directions [001] and [100] up to $T \sim 560$ °C (*cf.* black lines Fig. 3.2a). This indicates that the used semi-empirical approach to consider the radiative heat transfer for $T < 573$ °C (Eq. 3.8) is well suited to describe the measured data while taking latent heat effects into account. In contrast, at higher temperatures $T > 573$ °C where $T_{0,rad}/T_{max}$ shows a sample thickness dependence (Fig. 3.6), the radiation is inferred to be the common boundary to boundary (ballistic) radiative heat transfer. This is also supported by the fact that standard evaluation routines accounting for ballistic radiative transfer (Eq. 3.8 for $T > 573$ °C and Mehling et al. 1998) fit well the observed signal-time data (*cf.* Fig. 3.2d, Fig. 3.7d). This direct ballistic radiative heat transfer increasingly inheres the signal-time data towards higher temperatures (around the α - β phase transition and above, dashed and dotted lines in Fig. 3.6), which is explained by a reduced reflectance of the sputtered Au layer at high temperatures (Loebich 1972). As the thermal diffusivity $D(T)$ in the β phase shows no specimen thickness dependence but the ratio $T_{0,rad}/T_{max}$ does, this supports the fact that the model chosen here is well suited to approximate the signal-time curves for thermal diffusivity determinations at temperatures above 573 °C (*cf.* Fig. 3.2d, Fig. 3.7b&d). A further increase in fit quality may be achieved by mixing the two radiative heat transfer models (Eq. 3.8) in the temperature range ~ 400 -573 °C as indicated by $T_{0,rad}/T_{max}$ in Fig. 3.6.

Against the background of having two different effects contributing to the radiative heat transfer portion in the signal-time curves, measured HT1 data have been re-evaluated using the most frequently used standard fit procedure for (semi)transparent specimens after Mehling et al. (1998). This way, systematic errors for not taking into account the non-ballistic radiative transfer in the data evaluation routine below 573 °C can be estimated. The derived differences ΔD between the two model approaches are given as percentage in Fig. 3.7a&b. For measurements up to ~ 200 -250 °C the data fits show no significant differences independent of the used fit routine and $\Delta D \leq \pm 2$ % (Fig. 3.7a). At higher temperatures up to 573 °C (coinciding with the first rise of radiation ratio $T_{0,rad}/T_{max}$, Fig. 3.6a), differences in the fitted thermal diffusivities are increasing, exceeding 5 % at $T \sim 500$ °C and the max-

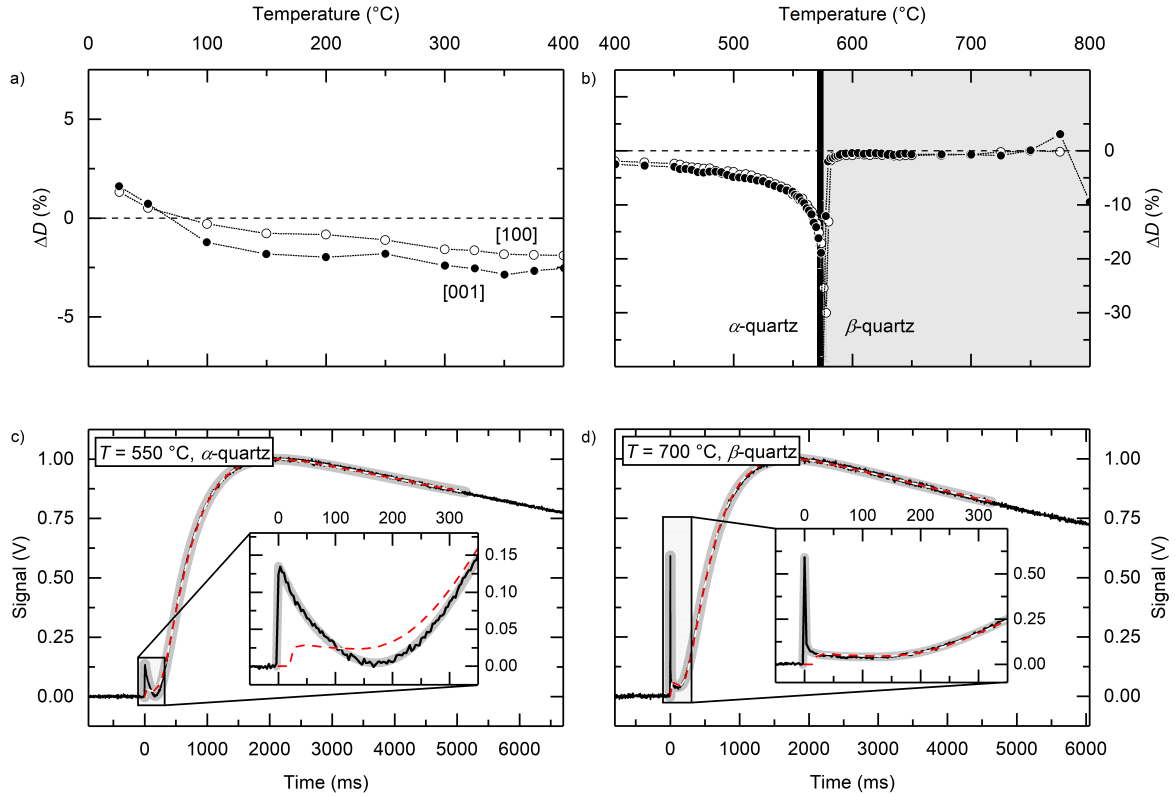


Figure 3.7: Comparison of the fit results using different model approaches to approximate HT1 data below and above the α - β phase transition. a) and b) illustrate the differences ΔD between thermal diffusivities evaluated by the approximation approach proposed in this study (*i.e.* accounting for direct radiative heat transfer differently for $T \leq 573$ °C and $T > 573$ °C) and the model for (semi)transparent specimens by Mehling et al. (1998) (as implemented in the manufacturer's software). Exemplary data fits to measurements along the c -axis direction at $T = 550$ °C and $T = 700$ °C are shown in c) and d), respectively. The measured IR detector signal-time curves are given as black lines. Data fits to $8 \times t_{1/2}$ are given as thick gray (this study) and dashed red lines (after Mehling et al. 1998). The front part of the fast radiative heat transfer is shown enlarged in the insets. Corresponding thermal diffusivities are: c) $D = 0.89(3)$ mm²/s (this study), $D = 0.82(5)$ mm²/s (Mehling et al. 1998) d) $D = 0.98(3)$ mm²/s (this study) and $D = 0.97(4)$ mm²/s (Mehling et al. 1998)

imum is reached at the phase transition with $\Delta D \geq 20\%$ (Fig. 3.7b). Negative differences mean that the data approximations of this study (accounting for non-ballistic and ballistic transfer) yield higher thermal diffusivities than fits using the model by Mehling et al. (1998) only accounting for standard ballistic radiative transfer. Exemplary signal-time data fits for the two different evaluation routines are presented in Fig. 3.7c for $T = 550\text{ }^\circ\text{C}$. It shows that the front part of fast radiative heat transfer (inset) is well approximated by the non-ballistic absorption/re-emission model proposed in this study (thick gray line Fig. 3.7c) and that the standard model for (semi)transparent specimens improperly approximates the observed behavior within the first few hundred microseconds (dashed red line, Fig. 3.7c). The resulting derived thermal diffusivities are in this example $D = 0.89(3)\text{ mm}^2/\text{s}$ (this study) and $D = 0.82(5)\text{ mm}^2/\text{s}$ (fit after Mehling et al. 1998) and thus $\Delta D \sim 8\%$. Above the phase transition temperature, the derived thermal diffusivity becomes independent of the used fitting procedure for both crystallographic directions. At $T = 700\text{ }^\circ\text{C}$ the fitted signal-time data shown in Fig. 3.7d reveal that both approximations accounting for ballistic radiative heat transport (Eq. 3.8 for $T > 573\text{ }^\circ\text{C}$ and Mehling et al. 1998) are comparably well with a minor exception for the very first few ten milliseconds of the model by Mehling et al. (1998). Consequently, there is no significant difference in the deduced diffusivity values independently of the used fitting routine with $D = 0.98(3)\text{ mm}^2/\text{s}$ (this study) and $D = 0.97(4)\text{ mm}^2/\text{s}$ (after Mehling et al. 1998), respectively.

In view of the direct radiative heat transfer it is concluded that laser flash measurements of (semi)transparent specimens can be significantly influenced by phase transitions already far away from the phase transition temperature (*i.e.* several hundred degrees Celsius) in flash technique measurements. In this case, direct radiative heat transfer in signal-time data has its origin (in parts) in the phase transition itself and is thus supposed to be non-ballistic (*e.g.* release of latent heat due to inversion of phase transition, Branlund and Hofmeister 2007, strong variation in heat capacity). This process results in radiative heat transfer signal-time data differently shaped compared to regular boundary to boundary (ballistic) radiative heat transfer. Hence, standard fit algorithms are inappropriate and signal-time data affected by phase transitions need to be specifically evaluated using appropriate fit procedures for (semi)transparent specimens.

3.5 CONCLUSION

Laser flash thermal diffusivity measurements were performed on quartz synthetic single crystals between $-120\text{ }^\circ\text{C}$ and $800\text{ }^\circ\text{C}$. The temperature dependence of the thermal diffusivity D between $-80\text{ }^\circ\text{C}$ and $560\text{ }^\circ\text{C}$ can be approximated by the model of bulk phonon-polaritons given by Hofmeister et al. (2014). Low temperature data show that an extrapolation to lower temperatures of previously measured thermal

diffusivity values (at and above room temperature) leads to an over-estimation of thermal diffusivity values, especially for temperatures below $-80\text{ }^{\circ}\text{C}$. The $[001]$ direction (c -axis) shows the maximum thermal diffusivity at all temperatures for samples with thicknesses $d \lesssim 5\text{ mm}$ (cross section $10 \times 10\text{ mm}$). The anisotropy of the thermal diffusivity $D_{[001]}/D_{[100]}$ decreases linearly over the measured temperature range with a discontinuity around the α - β phase transition at $573\text{ }^{\circ}\text{C}$. The latter is linked to a change in the crystallographic direction of maximum averaged sound velocities (crossover), reflecting changes in elastic constants over the phase transition.

A sample thickness dependency of the thermal diffusivity is observed above the phase transition. No crossover in the direction of the maximum thermal diffusivity is observed for sample thicknesses $d \lesssim 5\text{ mm}$ in laser flash measurements. However, while using a centimeter-sized sample (cross section $10 \times 10\text{ mm}$), a crossover in thermal diffusivity over the α - β phase transition is observed but at the limit of the experimental resolution.

Direct radiative heat transfer in signal-time curves is fundamentally different in flash measurements for $T \leq 573\text{ }^{\circ}\text{C}$ and $T > 573\text{ }^{\circ}\text{C}$. It was shown that the phase transition has 1) a significant influence on signal-time curves 2) already at temperatures far below the actual phase change. This is not only supported by the difference in shape of the direct radiation transfer in the raw data, but also by a sharp drop of radiative heat transfer intensities just above the phase transition. In the β phase the intensities of direct radiative heat transfer increase and can be described by common ballistic (boundary to boundary) transfer. A comparison of data fits shows that a frequently used model only accounting for boundary to boundary radiative heat transport in (semi)transparent specimens is insufficient to adequately consider the supposed non-ballistic radiative heat transfer for $T \leq 573\text{ }^{\circ}\text{C}$ originating in the phase transition. An absorption/re-emission approach introduced approximates well the observed fast radiative heat transfer in signal-time curves at temperatures below $573\text{ }^{\circ}\text{C}$.

These findings that radiative heat transport in quartz flash technique raw data is caused by different effects give rise to the assumption that flash method thermal diffusivity measurements on (semi)transparent matter undergoing phase changes are affected in a similar manner even though temperatures are several hundred degrees away from the actual phase transition. This can result in a strong underestimation of the thermal diffusivities when using standard fit routines that cannot separate the different radiative heat transport mechanisms effectively.

3.6 ACKNOWLEDGMENTS

This work was made possible by a foundation of Dr. M. Herrenknecht. The authors thank J. Späthe, R. Stemmler and D. Guth for their help in performing the laser flash measurements and Dr. G. de la Flor for com-

ments on an early version of the manuscript. The authors gratefully acknowledge the unknown reviewers for their in-depth, constructive, and helpful comments on an earlier version of this manuscript. Further acknowledge to the support by the KIT-Publication Fund of the Karlsruhe Institute of Technology.

STUDY 3

This study is published in the Elsevier Journal

Cement and Concrete Research.

The following chapter is a reprint of:

Breuer, S., Schwotzer, M., Speziale, S., & Schilling, F. R. (2020). Thermoelastic Properties of Synthetic Single Crystal Portlandite $\text{Ca}(\text{OH})_2$ - Temperature-Dependent Thermal Diffusivity with Derived Thermal Conductivity and Elastic Constants at Ambient Conditions. *Cement and Concrete Research*, 137, 106199. doi:10.1016/j.cemconres.2020.106199

THERMOELASTIC PROPERTIES OF SYNTHETIC
SINGLE CRYSTAL PORTLANDITE –
TEMPERATURE-DEPENDENT THERMAL
DIFFUSIVITY WITH DERIVED THERMAL
CONDUCTIVITY AND ELASTIC CONSTANTS AT
AMBIENT CONDITIONS

ABSTRACT

Synthetic portlandite single crystals were used to measure thermal diffusivity and elastic constants. The full tensor of elastic constants c_{ijkl} is derived by Brillouin spectroscopy at ambient conditions. The resultant aggregate bulk and shear moduli are $K_{S,VRH} = 32.2(3)$ GPa and $G_{VRH} = 21.2(2)$ GPa, respectively. The thermal diffusivity D was measured between -100 °C and 700 °C parallel $[001]$ and perpendicular $[100]$ to the crystallographic c -axis using laser flash method. The dehydration of the crystals influences the thermal diffusivity determination depending on sample size, orientation and heating rate. Thermal diffusivity and the derived thermal conductivity show a pronounced anisotropy with a maximum perpendicular to the c -axis, *i.e.* in the plane of the $[\text{CaO}_6]$ octahedral layers. In the same direction the highest sound velocities (v_P and v_{mean}) and longest mean free path length of phonons are determined. The thermal diffusivity as well as the derived thermal conductivity show a distinct temperature dependence.

KEYWORDS

Thermal diffusivity · Thermal conductivity · Elastic constants · Portlandite $\text{Ca}(\text{OH})_2$ · Laser flash method

4.1 INTRODUCTION

Thermoelastic properties such as thermal diffusivity, thermal conductivity, elastic constants as well as dynamic elastic response (*e.g.* sound velocities) are a prerequisite to better understand and predict the behavior of composite materials (Meade and Jeanloz 1990). The knowledge of thermoelastic properties of portlandite $\text{Ca}(\text{OH})_2$ as one of the major phases (ca. 20 wt%, Birchall et al. 1978; Aïtcin 2016) in hydrated portland cement based composites is of fundamental importance, affecting the properties of buildings to a great extent (Speziale et al. 2008b). Furthermore, $\text{Ca}(\text{OH})_2$ is used as a reaction medium, especially in the context of numerous process variants for flue gas cleaning in combustion technology (Bigham et al. 2005). With regard to the further development of these technologies, many studies have addressed the reactivity of portlandite both with SO_2 (*e.g.* Liu and Shih 2006; Wang et al. 2018) and with CO_2 (*e.g.* Shih et al. 1999). Reaction mechanisms and influencing factors are important in view of the variety of technical implementations, which also cover a wide range of temperature conditions (Fernández et al. 1998; Li et al. 1999; Renedo et al. 2013). It is common practice to assess the reaction kinetics and take into account mineralogical/chemical changes. However, thermal properties resulting from the crystal physics of the relevant compounds, *e.g.* $\text{Ca}(\text{OH})_2$, have not yet been integrated into such considerations. Beyond that, in the topical field of thermochemical energy storage the reversible dehydration of portlandite is considered as a promising reaction and could play a leading role providing large storage capacities for intermittent renewable energy production in the future (Schmidt 2017). For ongoing numerical and experimental research a detailed knowledge about the thermal transport properties of the reactants is crucial and still lacking particularly for portlandite (Ranjha et al. 2016).

Portlandite $\text{Ca}(\text{OH})_2$ is a trigonal hydroxide crystallizing in space group $P\bar{3}m1$ and is isostructural to brucite $\text{Mg}(\text{OH})_2$. The structure is characterized by nearly close-packed oxides forming distorted edge-sharing $[\text{CaO}_6]$ octahedral layers perpendicular to the 3-fold crystallographic c -axis (Holuj and Kwan 1975; Kruger et al. 1989; Desgranges et al. 1996; Nagai et al. 2000) (Fig. 4.1). H is pointing up- and downwards into the interlayer space, expanding the structure in $[001]$ direction. H is displaced from the trigonal symmetry axis and disordered around the 3-fold rotation axis with maximum probability density parallel to the c -axis (Desgranges et al. 1993; Desgranges et al. 1996). Whereas ionic bonding is dominant within the $[\text{CaO}_6]$ layers, hydrogen bonds connect the opposing octahedral layers (Kruger et al. 1989; Desgranges et al. 1996). As a result, portlandite shows a perfect cleavage parallel to (001) .

Apart from theoretical calculations by Laugesen (2005) and Ulian and Valdrè (2019), measured full sets of elastic constants c_{ijkl} of portlandite have been reported only by Holuj et al. (1985) and Speziale

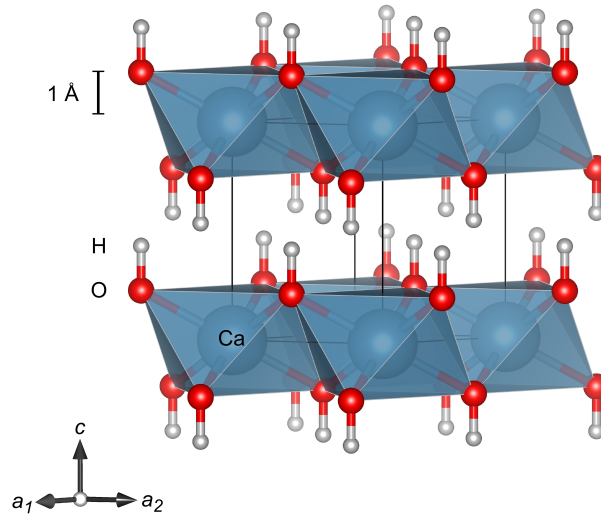


Figure 4.1: Crystal structure of portlandite $\text{Ca}(\text{OH})_2$. Edge-sharing $[\text{CaO}_6]$ octahedra (blue, oxygen in red) form layers stacked parallel to the 3-fold c -axis. H atoms (gray) are pointing into the interlayer space and are disordered around the 3-fold axis. Black lines correspond to the edges of one unit cell (drawn using *VESTA*, Momma and Izumi 2011, modified)

et al. (2008b). In contrast, thermal transport properties such as the thermal diffusivity and thermal conductivity seem to be still lacking especially as a function of temperature and in particular for single crystal portlandites. This is most likely due to its rare natural occurrence in general and in particular due to missing single crystals in a sufficient size to perform *e.g.* laser flash measurements.

The aim of this contribution is to enhance our profound knowledge about the thermoelastic properties of portlandite with a focus on the thermal transport properties. Therefore, large single crystal portlandites were grown by diffusion experiments. These are used to derive the full set of elastic stiffness constants c_{ijkl} by Brillouin scattering experiments at ambient conditions. The results on the elastic behavior of synthetic $\text{Ca}(\text{OH})_2$ crystals are compared to published experimental data on portlandite (Holuj et al. 1985; Speziale et al. 2008b). Thermal transport properties are collected by means of laser flash measurements to derive the thermal diffusivity D in the temperature range between -100 °C over the dehydration temperature of portlandite up to 700 °C. For the temperature range of portlandite stability between -100 °C and ~ 400 °C, the full set of thermal diffusivity tensor components D_{ij} is obtained. Related thereto, the thermal conductivity tensor components κ_{ij} are derived using tabulated data for the isobaric heat capacity and density. Additionally, averaged (Voigt, Reuss, Hill) elastic moduli and thermal diffusivity and thermal conductivity data are also given.

4.2 METHODS

For this study, centimeter-sized portlandite single crystals have been grown and characterized to determine the thermal diffusivity and elastic properties while using a laser flash apparatus (LFA) and a Brillouin spectrometer, respectively.

4.2.1 Samples

Portlandite single crystals were grown by diffusion process proposed by Johnston (1914) and adapted by Ashton and Wilson (1927) and Johnstone and Glasser (1992). Two plastic bottles (260 ml) were placed ~ 10 cm apart from each other in a large desiccator (DURAN DN250) and deionized water was filled up to a few centimeters over the open top of the bottles (total volume approximately 5 l). One bottle was filled with a 1.6 molal solution of sodium hydroxide (NaOH, $\geq 99\%$), the other bottle with a 0.8 molal solution of calcium chloride (CaCl_2 , $\geq 99\%$) through slow injection (approximately 150-200 ml) at the bottom of the bottles using a syringe. The atmosphere in the sealed, vibration-damped desiccator was pure N_2 . The desiccator was placed in a dark surrounding at a constant temperature of $T \approx 23^\circ\text{C}$. The growth of portlandite single crystals took place at the inner rim on the top of the two bottles over several months. Sodium hydroxide and calcium chloride were re-injected 5-8 times (in a 4-6 weeks' interval) into the respective bottles (~ 100 ml solution) whenever no detectable crystal growth was observed over 7-14 days.

For the characterization small parts of the synthesized single crystals were used.

Inductively coupled plasma mass spectroscopy (ICP-MS, X-Series2, Thermo Scientific) was used to determine the content on 22 cations (Tab. 4.1, without Ca). Portlandite was pulverized (agate mortar) for acid digestion in HNO_3 (65 %, subboiled), HF (40 %, suprapur) and HClO_4 (65 %, normatom). The accuracy of ICP-MS analysis was tested by the certified standard CRM-TMDW (High Purity Standards).

Contents of carbon and sulfur (Tab. 4.1) were measured using a carbon-sulfur-analyzer (CSA) (CS-2000, Eltra). The powdered portlandite ($m \sim 150$ mg) was heated to $T \approx 2000^\circ\text{C}$. A fragment of the steel chip reference standard 92400-3050 (Eltra) was used for accuracy evaluation.

Anions were analyzed using an ion chromatography (IC) system (ICS-1000, Dionex) (Tab. 4.1). Fine powdered $\text{Ca}(\text{OH})_2$ ($m = 115.3$ mg) was mixed with 10 ml deionized water for ~ 5 min before filtering and instantaneously measuring the solution. The certified reference material CRM-LGC6020 (river anions, LGC Standards) was used for accuracy validation.

Thermogravimetric (TG) analysis was carried out using a TGA 2 (Mettler Toledo) system (Fig. 4.10b). A powdered $\text{Ca}(\text{OH})_2$ sample

($m = 37.6$ mg) was placed in an aluminum oxide crucible and the mass loss was recorded at a heating rate (HR) of 5 K/min over the temperature range between 30 °C and 1000 °C under N₂ atmosphere (99.99 %).

For differential scanning calorimetry (DSC) plane single crystal platelets (001) were placed in aluminum pans (empty reference pan) in a DSC apparatus DSC822e (Mettler Toledo). Two independent measurements were carried out under N₂ atmosphere (99.99 %) at different temperature ranges and heating rates (Fig. 4.10b): 1) T between -100 °C and 550 °C (liquid N₂-cooled, HR 10 K/min, specimen cross section ~ 3.3 mm, ~ 0.5 mm thick, $m \approx 8.0$ mg) and 2) T between 300 °C and 575 °C at a reduced heating rate of 2 K/min (~ 3.6 mm cross section, ~ 0.5 mm thickness, $m \approx 9.5$ mg).

Powder X-ray diffraction (XRD) measurements (D8 Discover, Bruker) (Fig. 4.2) were carried out on portlandite as well as on the dehydration product directly after performing laser flash measurements. Patterns were taken from 10° to 80° (2θ) in steps of 0.02° with incident Cu K α radiation (40 kV, 40 mA).

The grown Ca(OH)₂ single crystals are transparent and free of visible inclusions or foreign phases under the light microscope. The crystals are idiomorphic/hypidiomorphic and exhibit elongated (parallel to the crystallographic c -axis) pseudo-hexagonal prisms of up to 1.5 cm length and ~ 7 mm in cross section, respectively. The elemental composition is presented in Tab. 4.1. No significant changes in element concentrations for single crystals originating in different batches were found nor could any spatial variation in composition (mineral zoning) be detected by sampling different states of growth. Except for carbon, chlorine, sulfate and nitrate (all ≤ 0.05 %), foreign ion contents are in the low ppm range.

The results of the powder XRD measurements are shown in Fig. 4.2. The diffraction pattern solely shows portlandite reflections for the measured powdered single crystal. After high temperature LFA measurements were carried out, the XRD pattern of the powdered sample shows mainly reflections of CaO, *i.e.* the dehydration product of portlandite (gray, Fig. 4.2). Only few portlandite reflections are present, *e.g.* at $2\theta \sim 18^\circ$ (001), $2\theta \sim 34^\circ$ {101} and $2\theta \sim 64^\circ$ (2 $\bar{1}$ 2) and {103} and low in intensity. The pattern of the dehydrated portlandite shows significant bigger full widths at half maximum (FWHM) compared to the pre-heated portlandite powder XRD. As during LFA measurements the temperatures reached 700 °C, it is evident that portlandite single crystals completely dehydrate. Thus, Ca(OH)₂ reflections in the post-heated specimen (gray, Fig. 4.2) are most likely originating from a rehydration of CaO (Maciel-Camacho et al. 1997). The unit cell parameters of the synthesized portlandite crystals determined by Rietveld refinement (Topas, Bruker) are $a_1 = 3.594(1)$ Å, $c = 4.910(1)$ Å, $V = 54.93(3)$ Å³ ($T = 20$ °C) and the thereof calculated density is $\rho = 2.240(2)$ g/cm³, all

Table 4.1: Elemental composition of synthetic portlandite crystals analyzed by ICP-MS (without Ca), IC and CSA (in ppm wt)

ICP-MS										
Na	Mg	P	K	Ti	Cr	Mn	Fe	Co	Ni	Cu
bdl ^a	23.4(1) ^b	4.0(5)	28.2(7)	0.5(1)	0.2(1)	1.0(1)	4.2(2)	bdl	0.5(1)	0.1(1)
ICP-MS										
Zn	As	Rb	Sr	Y	Mo	Ag	Cd	Ba	Pb	
1.0(2)	1.5(1)	bdl	bdl	bdl	0.1(1)	0.1(1)	bdl	bdl	bdl	
IC						CSA				
F ⁻	Cl ⁻	Br ⁻	(NO ₃) ⁻	(PO ₄) ³⁻	(SO ₄) ²⁻	C		S		
bdl	481(2)	bdl	81(3)	bdl	208(2)	511(5)		7.0(1)		

^a bdl below detection limit (Na: 3 ppm, others: ≤ 0.1 ppm)

^b numbers in parentheses are 1σ standard deviation of the last digits

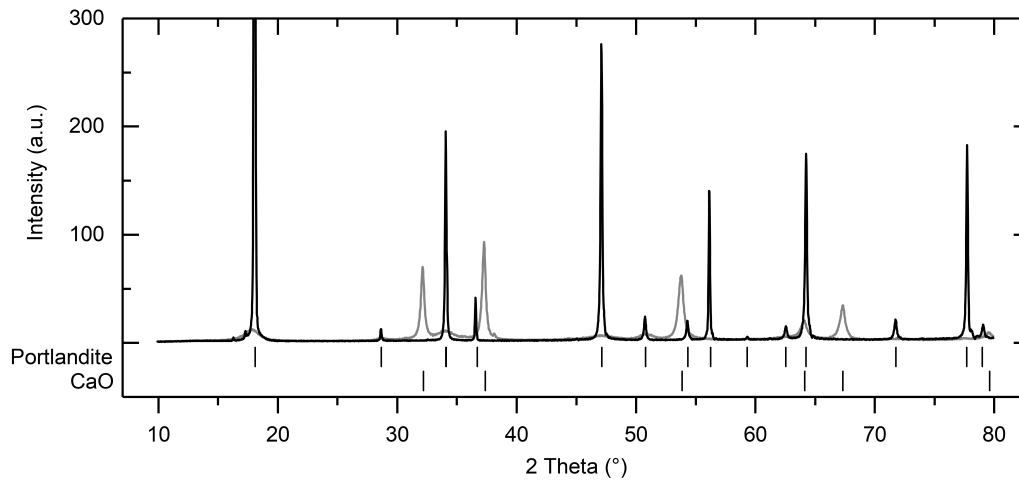


Figure 4.2: X-ray diffraction on powdered portlandite (black) and its dehydration product (gray) after thermal diffusivity measurements were carried out up to $T = 700$ °C (phase identification: portlandite - ICDD PDF 04-0733, CaO - ICDD PDF 04-0777)

of which are well in agreement with published data, *e.g.* Pavese et al. (1997), Nagai et al. (2000), and Speziale et al. (2008b).

4.2.2 Brillouin Scattering

Acoustic wave velocities and hence elastic properties of samples can be derived by Brillouin scattering using inelastic scattering of light by thermally activated vibrations (phonons) (Brillouin 1922; Mandelstam 1926; Gross 1930). For transparent single crystal specimens the full elastic (stiffness) tensor c_{ijkl} can be resolved. For a detailed review on Brillouin scattering see, *e.g.*, Vacher and Boyer (1972) and Speziale et al. (2014).

For the experiments in this study the incident light for scattering was produced by a solid state Nd:YVO₄ laser (Verdi Series, Coherent) emitting at $\lambda_0 = 532.15$ nm with a power of approximately 100 mW. With the use of a symmetric forward scattering geometry, knowledge of the refractive index of the specimen is not required (Whitfield et al. 1976). The external (outside of the specimen) scattering angle (angle between the incoming and scattered beam) was set to $\phi = 60^\circ$. Scattered light was analyzed by a six-pass tandem Fabry-Perot interferometer (TFP-1, JRS Scientific Instruments) (Sandercock 1982). The interferometer mirror spacing was set to 10 mm, corresponding to a spectral range of 14.99 GHz. The finesse is ~ 75 . A solid state single-photon counter tube (Count-10B, Laser Components) with low dark counts and high quantum efficiency $> 65\%$ (at 532 nm) was used to detect the signal. A simplified schematic construction of the Brillouin scattering experimental setup is shown in Fig. 4.3.

For Brillouin scattering experiments two single crystal orientations have been prepared. One platelet parallel to the perfect cleavage along (001) (so-called “basal”) and one platelet in perpendicular direction (100), referred to as “axial”. The opposing crystal faces have been ground and polished to plane-parallelism (deviation $< 1^\circ$) down to 1 μm grit size. The specimens were attached to a thin polycrystalline diamond platelet on a goniometer head and set in the center of the Eulerian cradle (Fig. 4.3) in the focus of the incident laser beam.

Inelastic scattering of light manifests in a Doppler shift in frequency (Gammon et al. 1983), which results in a spectrum symmetric to the unshifted line (Fig. 4.4). The frequency shifts $\Delta\omega$ in Brillouin spectra are linked to the acoustic sound velocities v (*e.g.* Whitfield et al. 1976):

$$v_{p,s} = \frac{\Delta\omega_{p,s}\lambda_0}{2\sin(\phi/2)} \quad (4.1)$$

with incident wavelength λ_0 , external scattering angle ϕ and subscripts p and s denote the quasi-longitudinal and quasi-transverse acoustic modes, respectively. For ideal elastic bodies (Hooke’s law behavior) the relation of acoustic wave velocities and stiffness tensor c_{ijkl} is described

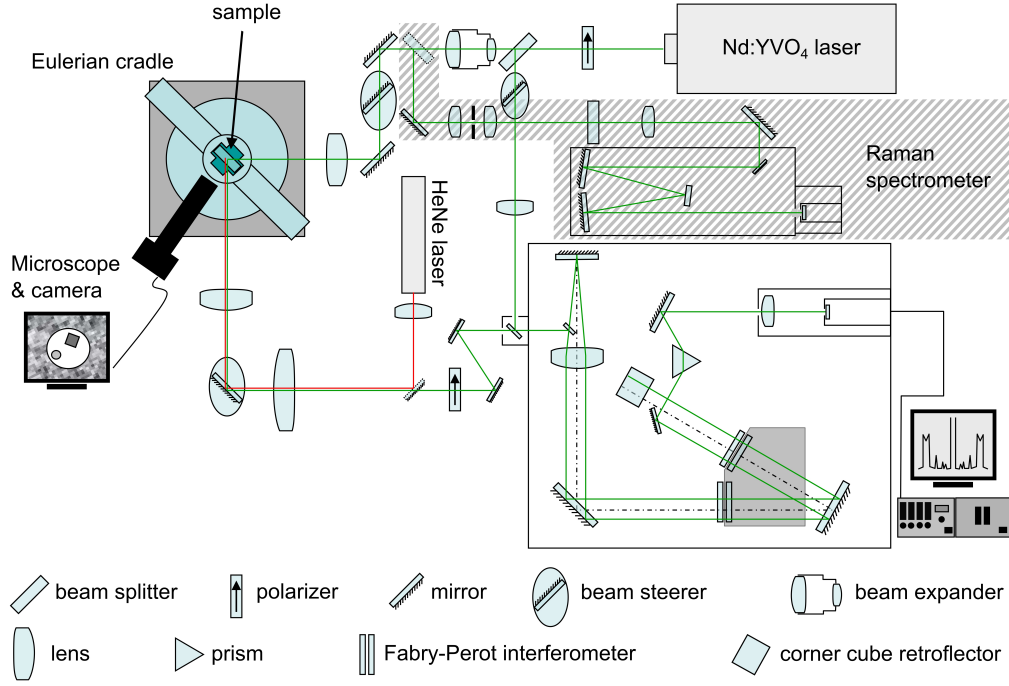


Figure 4.3: Schematic diagram of the experimental setup used for Brillouin scattering with attached Raman spectrometer (hatched gray). The HeNe laser is used for sample placement and alignment of the experimental setup (modified from Speziale and Duffy 2002)

by an equation of motion (atomic displacements). The solution for plane waves is given by the Christoffel's equation (Cummins and Schoen 1972; Every 1980)

$$(\Gamma_{ik} - \rho v^2 \delta_{ik}) u_k = 0 \quad (4.2)$$

with the Christoffel matrix $\Gamma_{ik} = c_{ijkl} n_j n_l$, where n_j and n_l are the direction cosines of the phonon propagation vector, ρv^2 is the eigenvalue (with ρ the density and v the wave velocity), u_j gives the polarization of the corresponding phonon (eigenvector), and δ_{ij} is the Kronecker delta. 36 directions have been measured on each of two different specimen platelets. The elastic tensor of portlandite consists of a total of six independent coefficients (e.g. Nye 1985). The Christoffel's equation is thus over-determined and solved for c_{ijkl} using an inhouse software with least-square Levenberg-Marquardt algorithm (Levenberg 1944; Marquardt 1963). Together with the fit of the components of the stiffness tensor c_{ijkl} , the crystallographic orientations of used specimen platelets were refined as well. For the data evaluation, portlandite has been treated as optically isotropic material (birefringence $n_{max} = 0.027$, Holuj et al. 1985; Rumble et al. 2018). The errors involved with this simplification are small and well within the reproducibility of the experiment (Chen et al. 2001; Speziale et al. 2008b).

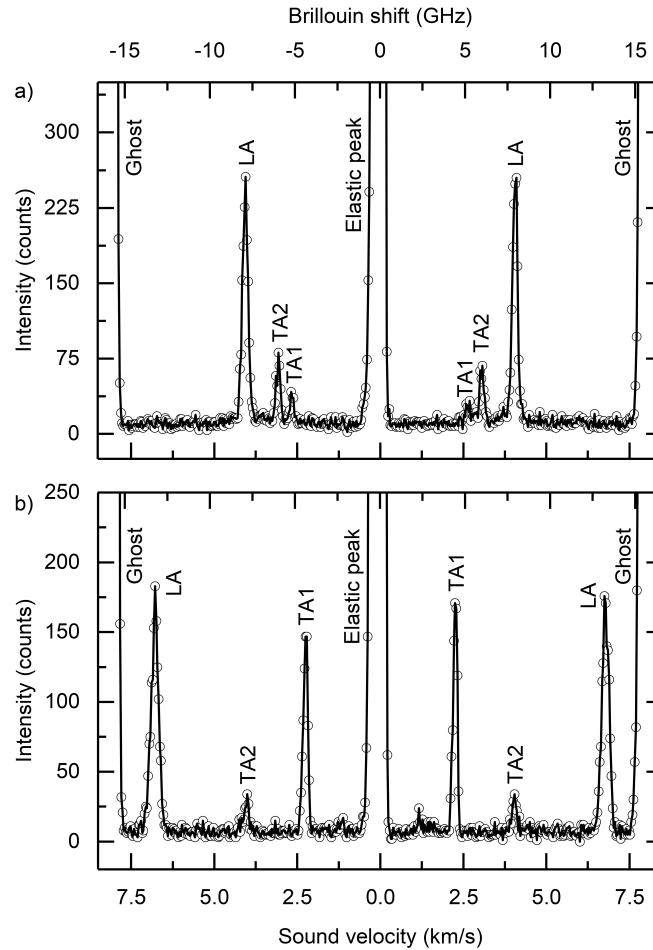


Figure 4.4: Brillouin spectra of portlandite a) in the axial plane (100) and b) in perpendicular direction (001) (basal plane). LA: quasi-longitudinal acoustic wave (v_p), TA₁ and TA₂: slow (v_{s2}) and fast (v_{s1}) quasi-transverse acoustic wave. Ghost peaks correspond to higher order elastically scattered incident light

Periodically repeated single-crystal MgO measurements at ambient conditions over a period of several years yield to a reproducibility of $\sim 0.5\%$ for the used setup while the accuracy is $\sim 1.0\%$.

4.2.3 Thermal Diffusivity

Measurements on the lattice thermal diffusivity D of single crystal portlandite have been carried out by transient laser flash method (Parker et al. 1961) using a Netzsch-Gerätebau MicroFlash[®] LFA 457 system. A short duration laser pulse heats up the front of a plate-like specimen and the resulting time-dependent temperature change is recorded on the opposite back side. A brief overview of the method is given by, *e.g.*, Vozár and Hohenauer (2003).

The radiant source used for the measurements is a Nd:YAG laser emitting at 1064 nm (IR Sources Inc.). It produces a short duration (~ 0.3 ms) 0.5" enlarged pulse with a maximum power output of 18.5 J, operated at approx. 4 J. The specimens were placed inside a furnace continuously flushed with N₂ purge gas (99.99 %, 50 ml/min). For the placement of the specimens inside the furnace custom ceramic sample holders were made of Macor glass ceramic (Schröder Spezialglas). The temperatures were measured close to the specimens using a type K thermocouple (class 1, DIN EN/IEC 60584-1 2013). For measurements at low temperatures (-100 °C to 100 °C) a HgCdTe (MCT) infrared (IR) detector was installed, for measurements from ambient conditions up to $T = 700$ °C an InSb detector was used. To reduce a possible laser profile non-uniformity, a custom 1" laser homogenizer (RD 203, Holo/Or Ltd.) was installed beneath the sample for the low temperature setup. The heating rate (HR) between each temperature step was set to 3 K/min and the specimens were held for ~ 0.5 h at each temperature step. The temperature increase of the specimens is approximated to be $\Delta T \leq 1$ K within each measurement. The IR detector output is assumed to be linear to the temperature and the thermophysical properties and density ρ of Ca(OH)₂ are assumed to be constant within ΔT of each independent measurement at a predefined temperature. A schematic diagram of the used laser flash setup for thermal diffusivity measurements is shown in Fig. 4.5.

For the LFA experiments five basal (D measured in [001] direction) and six axial ($D \perp c$ -axis) portlandite platelets have been prepared. A total of over 1100 independent thermal diffusivity measurements were performed for axial or basal orientations. The reported thermal diffusivities are an average of at least three independent measurements at the corresponding temperature per specimen and the mean of five basal and six axial platelets, respectively. The crystallographic orientations of the axial platelets have been determined by single crystal X-ray diffraction (SC-XRD, D8 Quest, Bruker, Mo K _{α} microfocus source $I\mu$ S 3.0, 50 kV, 1.4 mA) while the basal specimens perfectly cleaved in (001) platelets. The out-of-plane angles of the principal crystallographic

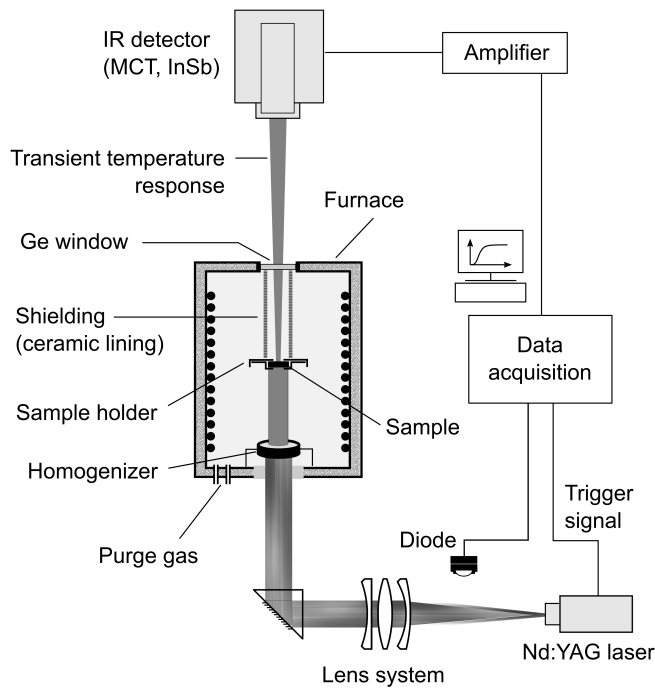


Figure 4.5: Schematic diagram of the used laser flash apparatus for measurements of the thermal diffusivity (adapted from Breuer and Schilling 2019)

axial plane orientations (100) are less than 1.0° for all specimens. This misorientation of the specimens for LFA measurements led to a systematic error of $\leq 0.05\%$ for the thermal diffusivity values, far below the reproducibility of the laser flash apparatus and is therefore neglected for the description of the thermal diffusivity D_{ij} and thermal conductivity κ_{ij} tensor. All specimens have been ground to plane-parallelism (deviation $< 1^\circ$) and the surfaces were slightly roughened for a better adhesion of the coatings and to attenuate a possible non-uniformity of the laser (Branlund and Hofmeister 2007). $\text{Ca}(\text{OH})_2$ platelets as well as the sample holders were sputter-coated with Au (99.99%) to $\sim 0.1\ \mu\text{m}$ (108 manual, Cressington) to reduce a direct radiative heat transfer. The specimens were additionally coated with graphite spray (Graphit 33, CRC Industries) to $\sim 10\ \mu\text{m}$ thickness per side to achieve a uniform and consistent laser pulse absorption (Cernuschi et al. 2002; Stryczniewicz et al. 2017). The thicknesses d reached from 0.5 mm to 1.3 mm for the basal cut and from 1.0 mm to 1.7 mm for the axial orientation. The cross sections varied from 3 mm to 7 mm. Thicknesses were corrected according to linear thermal expansion coefficients given by Xu et al. (2007) for portlandite (extrapolated from $35\ ^\circ\text{C}$ to $-100\ ^\circ\text{C}$ and from $370\ ^\circ\text{C}$ to $520\ ^\circ\text{C}$) and by Fiquet et al. (1999) for CaO. For the transition region $T = 450\text{-}520\ ^\circ\text{C}$ an altering linear mixture of both expansion coefficients was applied.

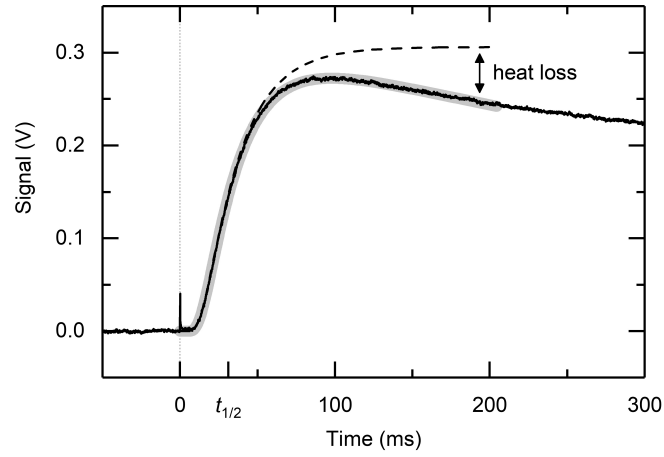


Figure 4.6: Signal-time curve (solid black) of portlandite (basal plane, $d = 0.505(3)$ mm) measured by the laser flash method with the low temperature setup (MCT IR detector) at $T = -60.5$ °C. The adiabatic temperature evolution (*cf.* Eq. 4.6) is shown as dashed black line, the approximated curve including finite pulse-time correction and heat loss to the surroundings is shown as thick gray line. The dotted vertical line (gray) corresponds to the release of the laser pulse used to heat up the front surface of the specimen. The time at half maximum is given as $t_{1/2} = 0.1388 d^2 / D$

According to Fourier's law, one-dimensional conductive heat flow is described by

$$q = -\kappa \frac{\partial T}{\partial x} \quad (4.3)$$

with heat flux q , constant temperature gradient $-\partial T / \partial x$ and thermal conductivity κ (2nd rank tensor for anisotropic solids). The temperature equilibration in a homogeneous solid is described by Carslaw and Jaeger (1959)

$$\frac{\partial T}{\partial t} = D \frac{\partial^2 T}{\partial x^2} \quad (4.4)$$

With the known lattice thermal diffusivity D of a solid, the thermal conductivity κ can be derived using the isobaric heat capacity c_p and density ρ :

$$\kappa = D\rho c_p \quad (4.5)$$

For thermal diffusivity measurements by the laser flash method a short-duration heat pulse is absorbed by the specimen's front surface and the resulting temperature change over time t at the back side is given as (Parker et al. 1961)

$$T(d, t) = \frac{Q}{\rho c_p d} \left[1 + 2 \sum_{n=1}^{\infty} (-1)^n \exp\left(\frac{-n^2 \pi^2 D t}{d^2}\right) \right] \quad (4.6)$$

assuming adiabatic conditions, with Q the heat pulse energy absorbed per unit area and the specimen thickness d . The evaluation of the thermal diffusivity D is performed by an inhouse software using least-square Levenberg-Marquardt algorithm on the basis of Eq. 4.6 including a custom heat loss model and a finite pulse-time correction (for details, see Breuer and Schilling 2019) (Fig. 4.6). The temperature-time history was fitted to $4\text{-}8 \times t_{1/2}$ (with $t_{1/2} = 0.1388 d^2 / D$, Parker et al. 1961). The reproducibility of the laser flash thermal diffusivity measurements is $\sim 2\text{-}3\%$. The accuracy was tested in the corresponding temperature range using standard samples (Pyroceram 9606, Inconel 600, Stainless Steel 310) and is $\sim 5\%$.

Comparable to the calculation of aggregate elastic moduli, the 2nd rank thermal diffusivity tensor D_{ij} (and similarly κ_{ij}) may be averaged in a Voigt- (Voigt 1928) and Reuss-like (Reuss 1929) behavior as

$$D_V = \frac{1}{3} \sum_{i=1}^3 D_{ii} \quad (4.7)$$

and

$$\frac{1}{D_R} = \frac{1}{3} \sum_{i=1}^3 \frac{1}{D_{ii}} \quad (4.8)$$

The Voigt-Reuss-Hill (Hill 1952) average is determined as the arithmetic mean of D_V and D_R .

4.3 RESULTS

4.3.1 Brillouin Scattering

The acoustic wave velocities determined in axial and basal planes are shown in Fig. 4.7. The refined specimen orientations, given as rotation axes of the surface normal of the platelets, are $89.3^\circ/89.1^\circ$ (azimuth/pole distance) for the axial plane and $-9.6^\circ/1.1^\circ$ for the basal plane, respectively. This includes both sample preparation and sample mounting on the goniometer head. Standard deviations 1σ of the refined orientations are $\sim 1.0^\circ$. The elastic constants have been approximated by applying Eq. 4.2 to a total of 216 determined quasi-longitudinal or quasi-transverse acoustic wave velocities in the axial or basal plane orientation. The resultant components of the stiffness tensor C_{ij} (Voigt notation) are given in Tab. 4.2. Using these, the calculated velocities (black lines) fitted to the measured data (circles) are shown in Fig. 4.7. The acoustic wave velocities show a distinct anisotropy between the crystallographic c -axis (*i.e.* $[001]$) and a_1 -axis ($=a_2=a_3, \langle 100 \rangle$). The highest velocities and a maximum shear wave splitting are measured in the direction perpendicular to the c -axis with

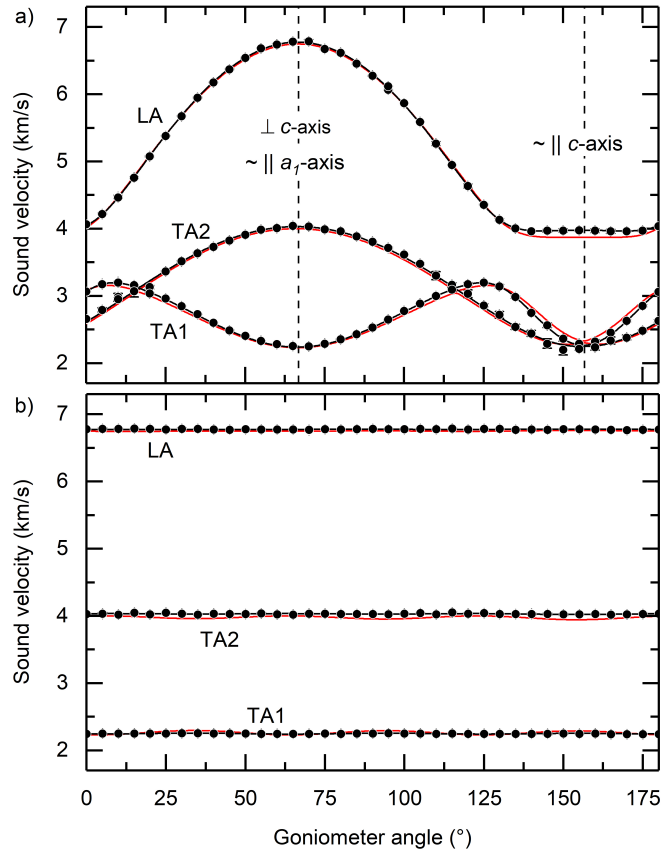


Figure 4.7: Measured (circles) acoustic wave velocities of synthetic single crystal portlandite in a) axial plane and b) basal plane. Solid black lines correspond to calculated velocities based on the elastic constants determined in this study (Eq. 4.2). Red solid lines correspond to calculated acoustic velocities using the elastic constants of natural portlandite determined by Speziale et al. (2008b) (*cf.* Tab. 4.2). LA: quasi-longitudinal acoustic wave (v_P), TA1 and TA2: slow (v_{S2}) and fast (v_{S1}) quasi-transverse acoustic wave, respectively

$v_P = 6.8(1)$ km/s, $v_{S1} = 4.0(1)$ km/s, and $v_{S2} = 2.3(1)$ km/s. The variations of acoustic velocities within the a_1 - a_2 - a_3 plane (001) are < 15 m/s and show a sixfold symmetry.

Representing surfaces for the acoustic wave velocities and for the Young's modulus (*e.g.* see Nye 1985) are shown in Fig. 4.8a, c, e and Fig. 4.9a, respectively. They show well the trigonal symmetry of portlandite. Selected cuts are shown on the right hand side of Figs. 4.8&4.9: azimuth = 30° (black) crossing the minimum and opposing maximum (rotoinversion) of the corresponding property and the basal plane (001) (gray). The anisotropic Young's modulus E shows a large variation with $E_{max}/E_{min} \sim 3$. It is smallest at a pole angle of $145^\circ/325^\circ$ (azimuth = 30°) with $E_{min} = 29.6(2)$ GPa (Fig. 4.9b). The Young's modulus features a small local maximum $E_{[001]} = 34.3(2)$ GPa perpendicular to the layered structure of $\text{Ca}(\text{OH})_2$, *i.e.* in c -axis direction. Its overall maximum lies at a pole angle $88^\circ/268^\circ$ (azimuth = 30°)

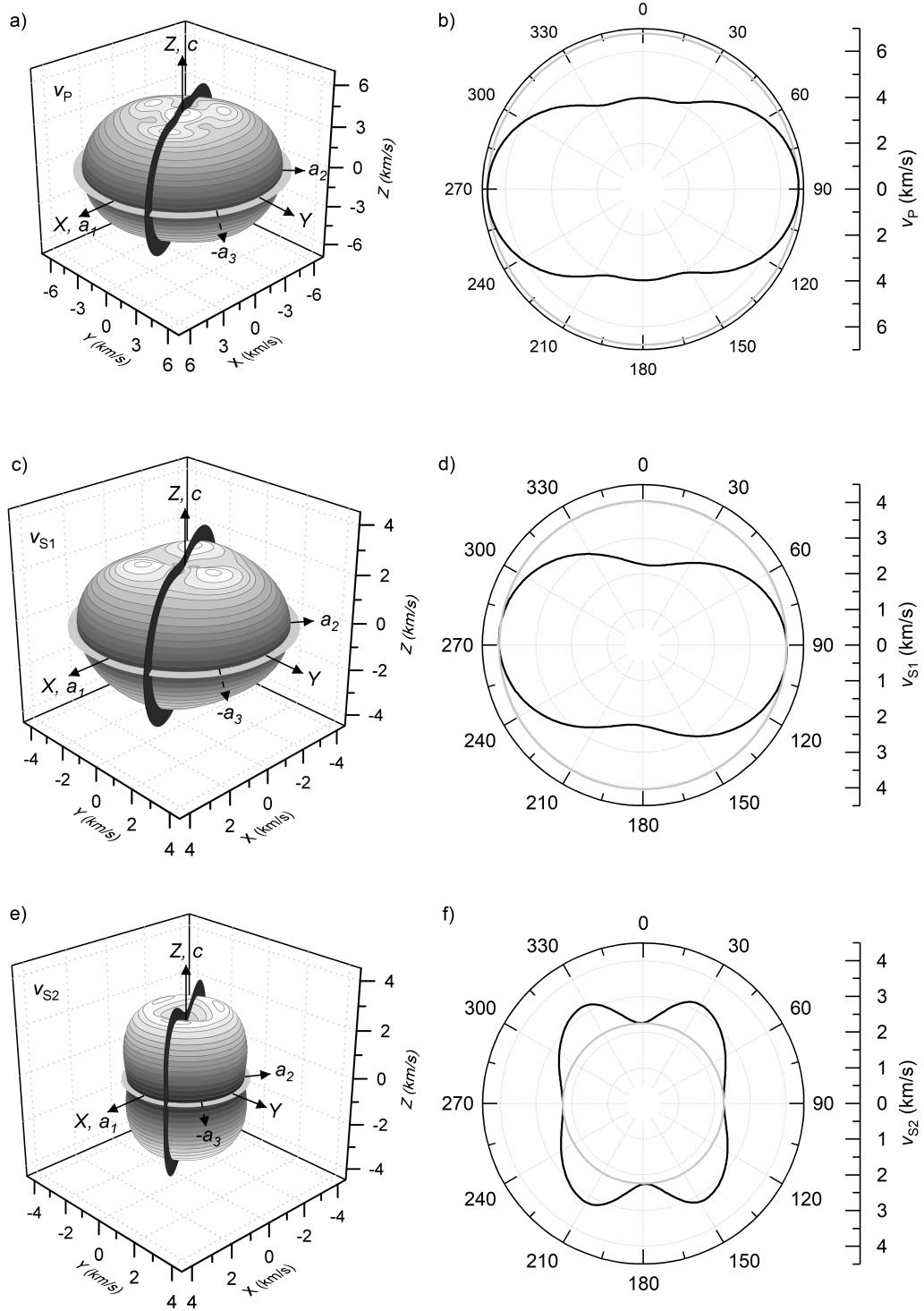


Figure 4.8: 3D representation of the acoustic wave velocities v_P (a), v_{S1} (c) and v_{S2} (e) of portlandite. Two selected cuts, azimuth = 30° (black) and basal plane (001) (gray), are shown in b), d) and f)

Table 4.2: Synthetic portlandite single crystal elastic constants C_{ij} (Voigt notation) derived by Brillouin spectroscopy at ambient conditions. For comparison, literature data on synthetic and natural $\text{Ca}(\text{OH})_2$ are shown. Components in GPa

	Speziale et al. (2008b) (natural $\text{Ca}(\text{OH})_2$)	Holuj et al. (1985) (synthetic $\text{Ca}(\text{OH})_2$)	This study
C_{11}	102.0(20)	99.3(15)	102.8(8)
C_{12}	32.0(10)	36.2(20)	30.2(5)
C_{13}	8.4(4)	29.7(150)	8.9(5)
C_{14}	4.5(2)	0.0 ^a	2.1(4)
C_{33}	33.6(7)	32.6(20)	35.4(4)
C_{44}	12.0(3)	9.8(20)	11.4(2)
C_{66}^b	35.0(11)	31.6(15)	36.3(5)

^a assumed

^b $C_{66} = (C_{11} - C_{12})/2$

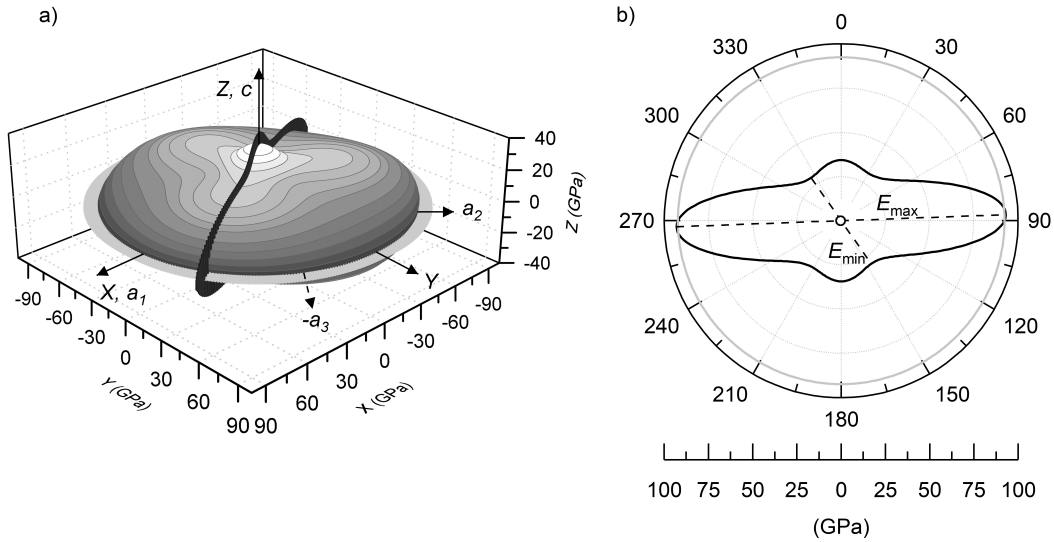


Figure 4.9: Young's modulus E of synthetic portlandite as three-dimensional representation (a) and b) two selected cuts along azimuth = 30° (black) with E_{min} and E_{max} and the basal plane (001) (gray)

Table 4.3: Adiabatic aggregate elastic moduli and acoustic velocities for portlandite at ambient conditions. Elastic moduli K_S , G , E in GPa, wave velocities v in km/s

	Speziale et al. (2008b) (natural Ca(OH) ₂)	This study (synthetic Ca(OH) ₂)
$K_{S,V}$	37.3(4)	37.4(3)
$K_{S,R}$	26.0(3)	27.0(3)
$K_{S,VRH}$	31.6(3)	32.2(3)
G_V	24.4(3)	24.7(2)
G_R	17.5(4)	17.7(2)
G_{VRH}	20.9(3)	21.2(2)
E_V	60.0(8)	60.7(5)
E_R	42.8(10)	43.6(4)
E_{VRH}	51.4(10)	52.2(4)
ν_V	0.23(1)	0.23(1)
ν_R	0.23(1)	0.23(1)
ν_{VRH}	0.23(2)	0.23(1)
$v_{P,VRH}$	5.15(2)	5.20(2)
$v_{S,VRH}$	3.05(2)	3.08(1)
$v_{mean,[001]}$	2.93(2)	2.95(1)
$v_{mean,[100]}$	4.71(2)	4.73(2)

V Voigt (1928), R Reuss (1929) and VRH Voigt-Reuss-Hill (Hill 1952) average elastic moduli (e.g. den Toonder et al. 1999; Pabst and Gregorová 2004)

ν Poisson's ratio

$$v_{P,VRH} = K_{S,VRH} + 4/3G_{VRH} \text{ and } v_{S,VRH} = \sqrt{G_{VRH}/\rho}$$

$$v_{mean} = \sqrt{(v_P^2 + v_{S1}^2 + v_{S2}^2)/3}, \text{ (Schilling 1998)}$$

with $E_{max} = 93.1(4)$ GPa (Fig. 4.9b). In the basal plane (pole = 90°) the Young's modulus is slightly reduced with $E_{[100]} = 92.2(3)$ GPa.

The adiabatic aggregate elastic moduli and velocities for an isotropic polycrystalline material calculated on the basis of the measured C_{ij} for synthetic $\text{Ca}(\text{OH})_2$ are shown in Tab. 4.3 together with the elastic moduli calculated for natural portlandite after Speziale et al. (2008b). Except for the Reuss bound adiabatic bulk modulus ($K_{S,R}$), differences of the aggregate elastic moduli and velocities for synthetic and natural portlandite are $\leq 2\%$.

4.3.2 Thermal Diffusivity and Thermal Conductivity

The results of laser flash thermal diffusivity D measurements on synthetic single crystal portlandites in basal (*i.e.* D in $[001]$ direction, tensor component D_{33}) and axial plane ($D \perp c$ -axis, D_{11}) orientations are presented in Fig. 4.10 (tabulated values see Appendix A.2, Tab. A.10) together with the results of TG and DSC measurements.

The thermal diffusivity decreases with increasing temperature over the entire portlandite stability field for both directions investigated. The temperature diffuses much faster in the plane of the $[\text{CaO}_6]$ octahedral layers $\perp c$ -axis ($D_{11} = D_{22} = 6.1(2)$ mm^2/s at 25°C) than parallel to the c -axis ($D_{33} = 0.73(2)$ mm^2/s). The pronounced anisotropy of thermal diffusivity can be calculated as $D_{[100]}/D_{[001]}$ and is shown in Fig. 4.11 up to the beginning of the dehydration of portlandite. At $T = -100^\circ\text{C}$ the thermal diffusivity is almost ten times higher in $[100]$ (axial plane) than in the perpendicular $[001]$ direction (basal plane). The anisotropy gradually reduces to $D_{[100]}/D_{[001]} \sim 8.3(3)$ at ambient conditions and stays roughly constant up to the beginning dehydration.

With the components of D_{ij} measured by laser flash method, the Voigt- (Eq. 4.7) and Reuss-like (Eq. 4.8) averaged thermal diffusivities for single crystal portlandite are shown in Fig. 4.10a together with the Voigt-Reuss-Hill average. At ambient conditions it is derived: $D_V = 4.31(13)$ mm^2/s , $D_R = 1.78(3)$ mm^2/s , and $D_{VRH} = 3.04(7)$ mm^2/s . However, due to the layered structure of $\text{Ca}(\text{OH})_2$ it is worth mentioning that an actual bulk thermal diffusivity of a general polycrystalline aggregate of portlandite is strongly depending on the texture (Seipold 1998) and porosity (Woodside and Messmer 1961).

Regarding the DSC curves in Fig. 4.10b, no significant heat flow can be seen for the low temperature measurement starting at -100°C (dashed gray, shown up to 300°C , HR 10 K/min). Above room temperature, one reaction can be identified for both TG (black) and DSC (solid gray, HR 2 K/min) curves, *i.e.* the dehydration of $\text{Ca}(\text{OH})_2$ to CaO (*cf.* Fig. 4.2). For the selected experimental conditions, the release of H_2O takes place between 386°C and 514°C . The TG measurement on powdered $\text{Ca}(\text{OH})_2$ shows a total mass loss of ~ 23.6 wt% for the dehydration reaction while the DSC characterizes this dehydration as endothermic reaction (Fig. 4.10b).

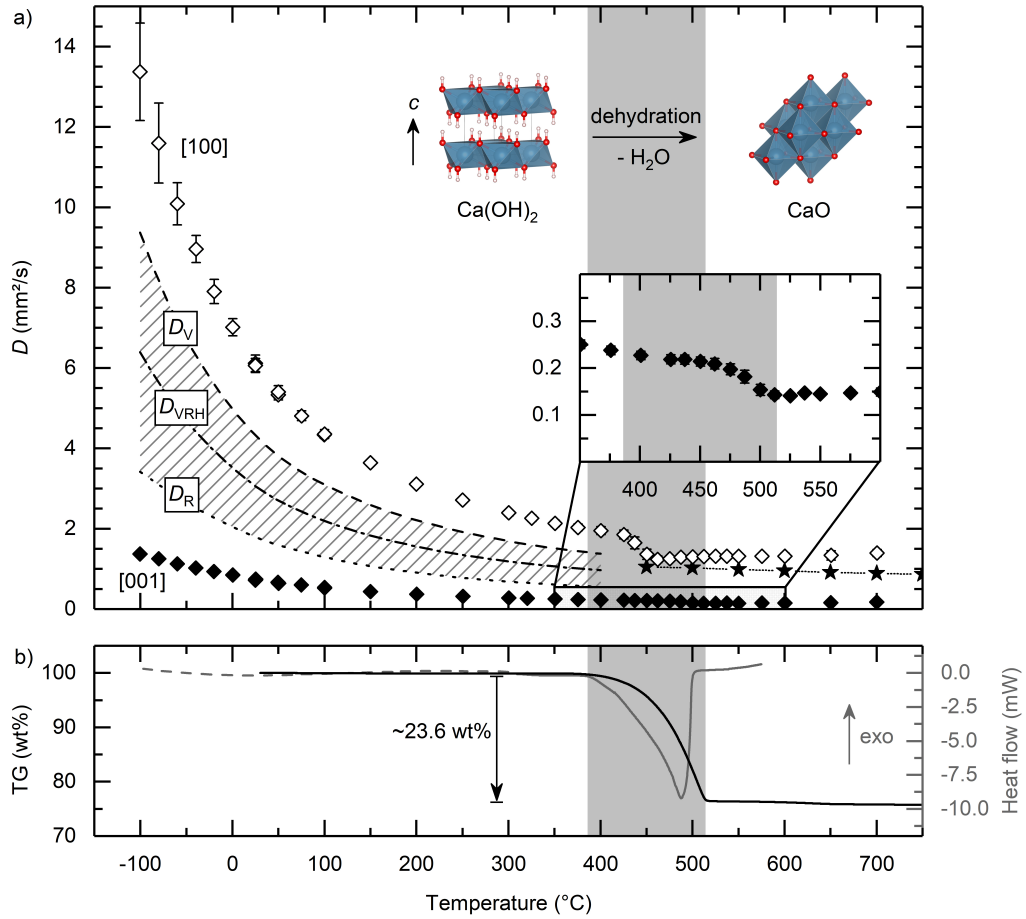


Figure 4.10: a) Thermal diffusivity measured by laser flash method for synthetic single crystal portlandite in [001] (basal plane, solid diamonds, = D_{33}) and [100] direction (axial plane, open diamonds, = D_{11}) between -100 °C through the dehydration of portlandite (gray shaded) up to 700 °C. D_V and D_R correspond to Voigt and Reuss-like averaged thermal diffusivities, D_{VRH} denotes the Voigt-Reuss-Hill average. Stars correspond to thermal diffusivity measurements of burnt lime (CaO) by Yur'ev and Spirin (2012). b) Results of thermogravimetric (TG, black) and differential scanning calorimetric (DSC, gray) measurements on Ca(OH)_2 . For details, see text

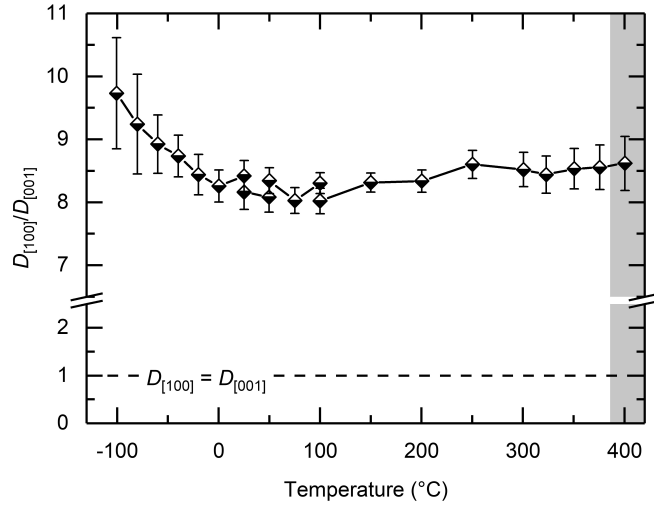


Figure 4.11: Anisotropy of the thermal diffusivity $D_{[100]}/D_{[001]}$ of synthetic single crystal portlandite

With respect to the measured thermal diffusivity in this temperature range, a further distinct decrease of nearly 40 % for both directions [100] and [001] is shown. Above 514 °C the thermal diffusivity stays roughly constant at $D_{[001]} \approx 0.15(1) \text{ mm}^2/\text{s}$ and $D_{[100]} \approx 1.32(5) \text{ mm}^2/\text{s}$. Thus, the thermal diffusivities of CaO from dehydrated $\text{Ca}(\text{OH})_2$ single crystal platelets exhibit an anisotropy and lie above ([100]) and below ([001]) the measured D values for CaO after decarbonation of polycrystalline limestone ($D \sim 0.95 \text{ mm}^2/\text{s}$, stars in Fig. 4.10a, Yur'ev and Spirin 2012). An apparent slight trend to increasing D values for high temperatures $T > 550 \text{ °C}$ might be caused by the degradation of sputtered Au on the sample holders, which resulted in an increasing transparency of the used ceramic.

The thermal conductivity κ for single crystal portlandite is derived according to Eq. 4.5 using the thermal diffusivities measured by laser flash method (this study, Fig. 4.10a). The density is $\rho = 2.240(2) \text{ g/cm}^3$ (20 °C, see 4.2.1) and adjusted in consideration of the thermal expansion coefficients given by Xu et al. (2007). For the isobaric heat capacity tabulated quantities according to Chase (1998) (based on Kobayashi 1950 (cited by Chase 1998) and Hatton et al. 1959) are used. The resulting tensor components κ_{11} and κ_{33} (tabulated values see Appendix A.2, Tab. A.11) together with averaged thermal conductivities (*cf.* Eqs. 4.7&4.8) are shown in Fig. 4.12. The thermal conductivity is decreasing over the whole temperature range. For temperatures above room temperature, a trend roughly proportional to $1/T$ (Eucken's law, Eucken 1911) can be recognized while for temperatures below 25 °C the slope of $\kappa(T)$ decreases slightly. Comparable to the thermal diffusivity, heat diffuses ~ 8 -10 times more effectively perpendicular to the 3-fold c -axis than parallel to [001]. At ambient conditions, the 2nd rank thermal conductivity tensor components for single crystal portlandite are $\kappa_{11} = 16.1(6) \text{ W m}^{-1} \text{ K}^{-1}$ and $\kappa_{33} = 1.94(6) \text{ W m}^{-1} \text{ K}^{-1}$. The

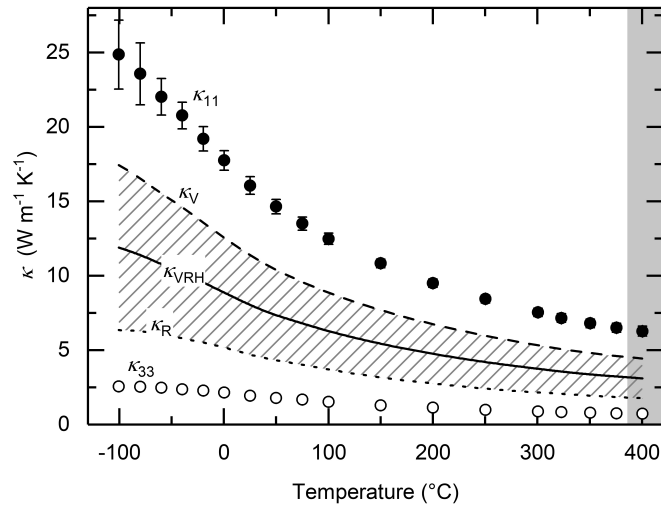


Figure 4.12: Derived thermal conductivity κ of portlandite (Eq. 4.5): tensor components κ_{11} (\perp c -axis, solid circles) and κ_{33} (\parallel c -axis, open circles) and Voigt- and Reuss-like averaged quantities with the Voigt-Reuss-Hill average ($_{VRH}$) (Eqs. 4.7&4.8)

averaged thermal conductivities at 25 °C are $\kappa_V = 11.4(4)$ $\text{W m}^{-1} \text{K}^{-1}$, $\kappa_R = 4.69(13)$ $\text{W m}^{-1} \text{K}^{-1}$, and $\kappa_{VRH} = 8.02(25)$ $\text{W m}^{-1} \text{K}^{-1}$, respectively. As noted with respect to the thermal diffusivity, the effective thermal conductivity of a bulk of polycrystalline portlandite strongly depends on its texture and porosity.

4.4 DISCUSSION

The spatial dispersion of acoustic wave velocities measured in this study agrees well with the velocities derived on the basis of natural portlandite elastic constants measured by Speziale et al. (2008b) (*cf.* Fig. 4.7, red line). Thus, it can be stated that at least for this kind of measurements adequate specimens comparable to natural $\text{Ca}(\text{OH})_2$ crystals were grown in the laboratory. The stiffness constants C_{ij} show only marginal differences to the components measured for natural portlandite (Tab. 4.2). An exception is C_{14} , which is a measure for the anisotropy within the basal plane (Ulian and Valdrè 2019). It is less than half (this study) compared to data reported by Speziale et al. (2008b). It is assumed that the difference is mostly due to the different spatial distribution of the sets of directions probed in the two studies. The combination of an axial plane with a truly basal one and a better quality of the signal in the new set of measurements suggest the value of C_{14} presented in this study is more accurate than that of Speziale et al. (2008b). In any case, such differences of individual elastic constants mostly vanish when calculating the averaged elastic moduli for a hypothetical isotropic polycrystal, *cf.* Tab. 4.3 (Zha et al. 1996). Significant differences in the elastic components determined in this study and by Speziale et al. (2008b) for natural $\text{Ca}(\text{OH})_2$ exist

with respect to Brillouin data on synthetic portlandite measured by Holuj et al. (1985). Especially the component C_{13} differs $> 200\%$, but also C_{12} is reported $\sim 20\%$ higher than measured in this study (Tab. 4.2). These deviations are likely caused by the small number of crystal orientations measured by Holuj et al. (1985) compared to the large number of velocities determined in this study and by Speziale et al. (2008b).

The kinetics of the dehydration of hydrates such as portlandite and of minerals containing water in their crystal structure depends on numerous different factors (Galwey 2003). Due to that, data on dehydration kinetics, *i.e.* above all the temperature of dehydration/decomposition, can vary quite significantly often resulting in a wide temperature range (*e.g.* Jozewicz and Gullett 1995; Schaube et al. 2012; Lager et al. 2018). To give an estimation on how strong the thermal diffusivity can vary with the dehydration of single crystal portlandite due to selected experimental conditions, two major influencing factors are considered: 1) the heating rate (HR) and 2) the influence of the particle/crystal size. For the former, two specimens (basal plane) of comparable size ($d \sim 0.7$ mm, ~ 4.5 mm cross section) were measured by the laser flash method with ~ 3 h isothermal segments per temperature step (representing $\lim_{HR \rightarrow 0}$) on the one hand and a high heating rate of ~ 10 K/min on the other hand. The resulting effect of heating rates on the measured thermal diffusivity around the dehydration of portlandite crystal platelets is shown Fig. 4.13a. For the influence of the particle/crystal size, two axial plane specimens markedly different in size (see Fig. 4.13b for details) were measured by the laser flash method (all other conditions being equal). Comparing the two heating rate boundaries shown for the example of the basal plane orientation (Fig. 4.13a), significant differences in the temperature dependence of the thermal diffusivity become apparent. While the release of water is completed at a temperature of around ~ 390 °C for $\lim_{HR \rightarrow 0}$ and the thermal diffusivity decreases to $D_{[001]} = 0.15(1)$ mm²/s, D values for high heating rates lie up to ~ 60 - 65% above at about $D_{[001]} \approx 0.24$ - $0.25(2)$ mm²/s ($T = 400$ - 475 °C). This discrepancy may originate from a non-homogeneous temperature distribution within the platelet subject to heating at high HR and thus reflect the thermal diffusivity of an effective lower temperature than measured by the thermocouple just next to the specimen. Due to the lacking ability of specimen temperature equilibration, high heating rates lead to a dehydration reaction extended over a wide temperature range visible at ~ 475 °C reaching up to ~ 575 °C (Fig. 4.13a), *i.e.* up to ~ 185 °C above the dehydration temperature approximated for $\lim_{HR \rightarrow 0}$ with the laser flash method. Another factor influencing the dehydration temperature and correspondingly the thermal diffusivities is the specimen size. Fig. 4.13b shows that for the smaller crystal platelet the onset of dehydration at $T = 425$ °C is ~ 25 °C below that of the bigger specimen. In general, it can be seen that the evolution of the thermal diffusivity with temper-

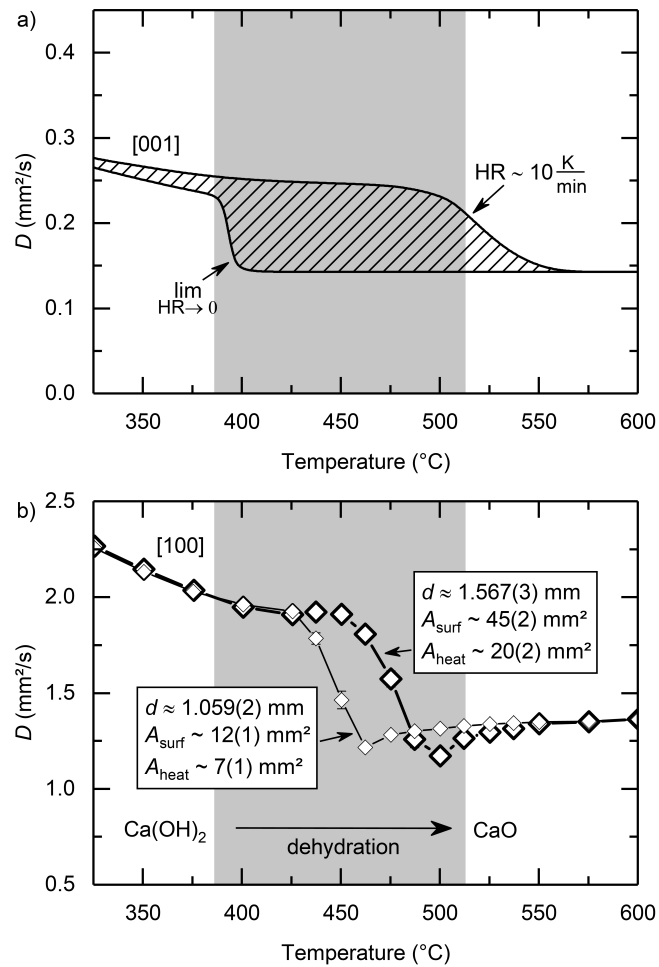


Figure 4.13: Influence of the experimental conditions on the dehydration and thermal diffusivity D of portlandite. a) Boundary conditions for heating rates (HR) $\lim_{\text{HR} \rightarrow 0}$ and $\text{HR} \sim 10 \text{ K/min}$, shown for the basal plane orientation. b) Influence of the specimen dimensions on D ($\perp c$ -axis, axial plane) measured by laser flash method (axial plane, $\text{HR} \sim 3 \text{ K/min}$). A_{surf} is the platelets' surface area, A_{heat} is the area heated by the laser pulse. The gray shaded area corresponds to the dehydration temperature according to TG & DSC measurements (see 4.2.1&4.3.2, Fig. 4.10b)

Table 4.4: Parameters for data approximations shown in Fig. 4.14 for the thermal diffusivity D and thermal conductivity κ , respectively. T in K, R^2 is ≥ 0.98 for all fits

	$D(T) = AT^{-B}$ (mm ² /s)	$D(T) = T_D T^{-3/2} + D_0$ (mm ² /s)	$\kappa(T) = T_\kappa T^{-3/2} + \kappa_0$ (W/mK)
[100]	$24.0(31) \times 10^3 T^{-1.45(2)}$	$29.4(2) \times 10^3 T^{-3/2+0.37(1)}$	$80.7(11) \times 10^3 T^{-3/2+1.35(6)}$
[001]	$2.03(69) \times 10^3 T^{-1.39(6)}$	$3.14(6) \times 10^3 T^{-3/2+0.09(1)}$	$8.2(2) \times 10^3 T^{-3/2+0.34(2)}$

ature is shifted by $\sim 25\text{-}30$ °C comparing both specimen dimensions shown in Fig. 4.13b. These observed differences are expected to be even stronger for greater crystal size differences and might be transferred to powdered samples as well as to components of *e.g.* hydrated cements. In Fig. 4.13 it is shown that the sample dimensions and experimental conditions can impact the determination of thermal transport properties. Accordingly, studies on *e.g.* portlandite for thermochemical storage systems need to carefully take into account such influencing factors as they may significantly bias the results.

The thermal diffusivity data of portlandite show a temperature dependence roughly proportional to $1/T$ for both directions [001] and [100] up to ~ 400 °C as being expected for three-phonon umklapp processes (Peierls 1929; Kittel 2005). The trend might be described by a modified Eucken's law $D(T) = AT^{-B}$ (T in K, after Seipold 1998, see also Hofmeister et al. 2014) for the contribution of lattice phonons to heat transport. Fits between -100 °C and 380 °C describe well the measured thermal diffusivity data (dashed black lines Fig. 4.14a&c, shown up to $T = 650$ °C for illustration, fit parameters are shown in Tab. 4.4).

For the high temperature region, approximations $\propto T^{-B}$ lead to a thermal diffusivity vanishing for $\lim_{T \rightarrow \infty}$. But, with respect to the thermal diffusivity D (and conductivity κ) provided by lattice phonons, it seems to be more appropriate that D (and κ) reaches the so-called Einstein limit with D_0 (κ_0) > 0.0 mm²/s (W m⁻¹ K⁻¹) (Cahill et al. 1992) as the mean free path length l cannot become arbitrarily short (*e.g.* Spitzer 1970; Roufosse and Klemens 1974; Berman 1976). An approximation for the temperature dependence of D (and κ) including a lower limit for high temperatures was proposed by Roufosse and Klemens (1974). Rearranged for D_0 and κ_0 , it is

$$\begin{aligned} D(T) &= T_D T^{-3/2} + D_0 \\ \kappa(T) &= T_\kappa T^{-3/2} + \kappa_0 \end{aligned} \quad (4.9)$$

with T_D and T_κ fitting constants and T in Kelvin. In a first approximation, the Einstein limit of the thermal diffusivity D_0 and thermal conductivity κ_0 can be predefined using the directional minimum bond

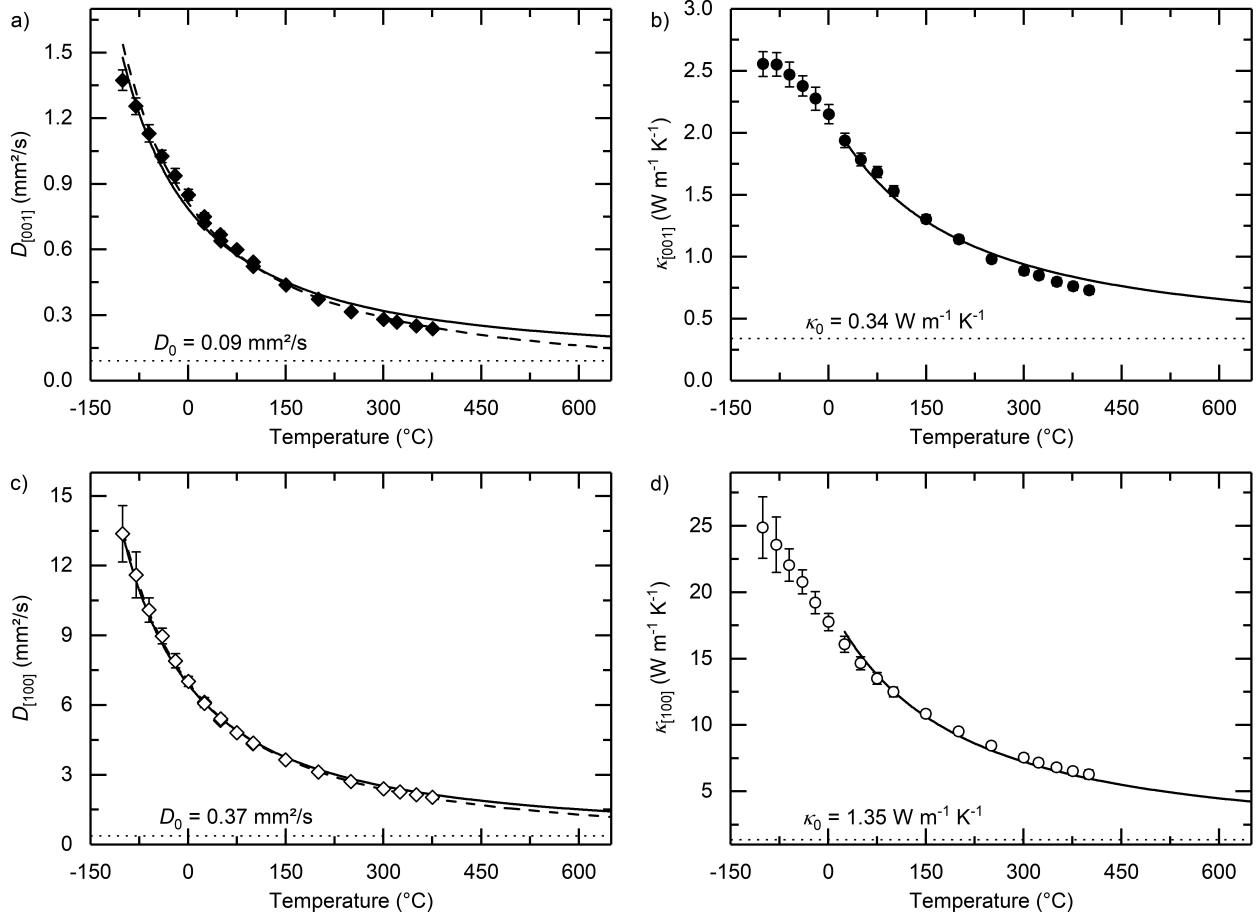


Figure 4.14: Data approximation for the temperature dependence of portlandite thermal diffusivity (a, c) and thermal conductivity (b, d) in $[001]$ (top) and $[100]$ (bottom) direction. Dashed lines (a, c) represent fits according to $D(T) = AT^{-B}$ (after Seipold 1998). Solid lines represent data fits including predefined high temperature limits D_0 and κ_0 (dotted lines, Eq. 4.10) after Roufosse and Klemens (1974) (Eq. 4.9). Fit parameters are shown in Tab. 4.4. For details, see text

length (l_0) inside the unit cell as the lower limit of mean free path length l . In c -axis direction [001], $l_0 \approx 0.96 \text{ \AA}$ for the O-H bond, whereas in [100] direction $l_0 \approx 2.37 \text{ \AA}$ for the Ca-O bond of the octahedral layer (after Xu et al. 2007). Using (e.g. Ziman 1960; Berman 1976; Kittel 2005)

$$\begin{aligned} D_0 &= 1/3 v l_0 \\ \kappa_0 &= 1/3 \rho c_p v l_0 \end{aligned} \quad (4.10)$$

with v phononic velocity approx. by $v_{mean} = \sqrt{(v_p^2 + v_{s1}^2 + v_{s2}^2)}/3$, the lower limit in thermal diffusivity D_0 is 0.09(1) mm^2/s and 0.37(1) mm^2/s in [001] and [100] direction, respectively. For the thermal conductivity, $\kappa_0 = 0.34(2) \text{ W m}^{-1} \text{ K}^{-1}$ in [001] direction and 1.35(6) $\text{W m}^{-1} \text{ K}^{-1}$ in [100] direction (high T approximation $\rho c_p = 3.6 \times 10^6 \text{ J m}^{-3} \text{ K}^{-1}$). The resultant approximations for the temperature dependence of the thermal diffusivity (and thermal conductivity, for $T > 298 \text{ K}$) only depend on a single parameter T_D (T_κ) and are shown in Fig. 4.14, the corresponding fit parameters are given in Tab. 4.4. Data fits for thermal diffusivity (Fig. 4.14, left) and thermal conductivity (right) are of comparable quality for respective directions. It shows that for the axial plane orientation the fits are of slightly better quality. Compared to the previously mentioned two-parameter model $D(T) = AT^{-B}$ (after Seipold 1998, dashed black lines Fig. 4.14a&c), the one-parameter (with fixed D_0, κ_0) approximations using Eq. 4.9 are of only marginally lower quality. Hence, using a minimum in crystal bond length as the lower limit for the mean free path length l in combination with the model proposed by Roufousse and Klemens (1974) fits well the observed data. This suggests that the main structural element controlling heat diffusion in single crystal portlandite in [001] direction at least at high temperatures is the hydroxyl group and thus the hydrated interlayer (series circuit of low conducting hydroxyl group interlayers and higher conducting $[\text{CaO}_6]$ octahedral layers). In contrast, heat diffusion perpendicular to the c -axis can be well described if the $[\text{CaO}_6]$ octahedral layers dominate the heat transport in this direction, comparable to a parallel circuit.

The thermal conductivity κ at low temperatures cannot be well described by a model $\propto 1/T$ (cf. Fig. 4.14b&d). This is likely due to the strong temperature dependence of the heat capacity c_p as it evolves towards a $\propto T^3$ behavior in the lower temperature region (i.e. well below the Debye temperature $\Theta_D \sim 100 \text{ }^\circ\text{C}$, Desgranges et al. 1994) as a consequence of phonon modes “freezing out” (e.g. Gross and Marx 2014).

Commonly, thermal diffusivity measurements by the laser flash method on single crystalline matter are presumed to be independent of the probed specimen thickness d . This holds true as long as optically thick conditions exist. According to Hofmeister (2019), specimen thicknesses ordinarily measured using laser flash method can be optically thick for fundamental IR modes but optically thin for overtone modes.

Thus, depending on the particular material a thickness dependence of the thermal diffusivity can exist (*'intrinsic length dependence'*). To approximate this effect, Hofmeister (2019) suggests:

$$D(d) = D_{\infty} [1 - \exp(-\gamma d)] \quad (4.11)$$

with a fitting constant γ and the thermal diffusivity D_{∞} for a material of infinite thickness. To assess the single crystal portlandite thermal diffusivity data collected in this study, basal plane specimens with varying thicknesses from $d \approx 0.14$ mm to $d \approx 1.25$ mm were measured at $T = -100$ °C, -40 °C, 25 °C and 100 °C. The results show a pronounced dependence on the thickness d of the measured thermal diffusivity at all temperatures considered (Fig. 4.15). To approximate this trend, Eq. 4.11 is adapted by adding the Einstein limit for minimum thermal diffusivity D_0 ($= 0.09(1)$ mm²/s in [001], see above). This is for the case that $\lim_{d \rightarrow 0}$, taking into account that the mean free path length l cannot fall below the minimum lattice bond distance (≈ 0.96 Å, O-H bond in [001] direction, see above):

$$D(d) = D_{\infty} [1 - \exp(-\gamma d)] + D_0 \quad (4.12)$$

(note: the thermal diffusivity limit for an infinite thick specimen is in this case $D_{\infty} + D_0$). Using Eq. 4.12 with γ being equal for all temperatures, the observed trend is well approximated (black lines, Fig. 4.15). But, transparent specimens need to be coated for laser pulse absorption in LFA measurements (see 4.2.3) and it is known that applied coatings can affect the thermal diffusivity measurements (e.g. Cernuschi et al. 2002; Lim et al. 2009; Schoderböck et al. 2009). Therefore, it seems reasonable to evaluate whether the observed $D(d)$ dependence (Fig. 4.15) could also be explained by a coating-related influence for different specimen thicknesses. Even though including coating effects in thermal diffusivity evaluation routines is non-trivial (Araki et al. 1992; Hartmann et al. 1993), in a first approximation $D(d)$ is fitted using

$$D(d) = 0.1388 \frac{d^2}{t_{1/2} + \Delta t} \quad (4.13)$$

where $t_{1/2} = 0.1388 d^2 / D_{\infty}$ and Δt represents the additional time needed for heat to travel through the applied coating. The resultant fits (Fig. 4.15, gray lines) represent well the observed trend of a decreasing apparent thermal diffusivity with decreasing specimen thickness and are of comparable quality to approximations using Eq. 4.12. For thicknesses $d \geq 0.5$ mm the thermal diffusivities $D_{[001]}$ approach a constant value. The increase of D for $d \geq 0.5$ mm is small and within the experimental uncertainties independent of the chosen approximation.

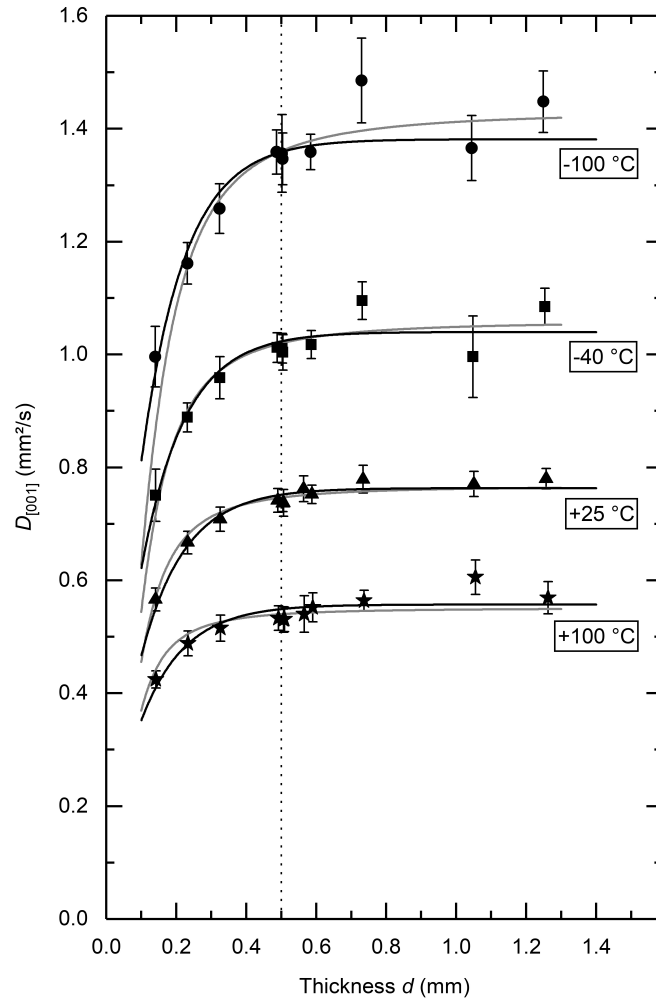


Figure 4.15: Dependence of the thermal diffusivity D on the specimen thickness d for single crystal portlandite in basal plane orientation. Black lines: least-square fits using a model proposed by Hofmeister (2019) adapted by adding $D_0 = 0.09(1)$ mm²/s (cf. Eq. 4.12). Comparable results are obtained using an approach that takes into account the influence of the applied graphite coating in signal-time curves of measured thermal diffusivity of portlandite (gray, Eq. 4.13). The dotted line corresponds to the minimum specimen thickness used for the results presented in 4.3.2

Our specimens for collecting thermal transport data (*i.e.* tensor components D_{ij} , derived κ_{ij} and its temperature dependencies, see 4.3.2) have a minimum thickness of $d = 0.5$ mm for the basal plane. Thus, it can be stated that at least for $D_{[001]}$ the specimen thicknesses have no significant influence on the measured thermal diffusivities and derived conductivities. In direction $\perp c$ -axis, thermal diffusivities are considerably higher (*cf.* Figs. 4.10&4.11) associated with a reduced $t_{1/2}$. The applied coating will thus have a stronger influence on the thermal diffusivity and D_∞ for an infinite thick sample would be reached for higher thicknesses d . On the other hand, measured axial plane specimens are thicker ($d = 1.0$ to 1.7 mm) than basal plane platelets, counteracting the thickness influence on thermal diffusivity. In conclusion, it cannot be excluded that for the thermal transport properties in the axial plane direction $[100]$ reported here (4.3.2, *e.g.* Fig. 4.10, Appendix A.2, Tab. A.10&A.11) a (significant) thickness dependence inheres the data. Thus, intrinsic heat transport and temperature equilibration $\perp c$ -axis as well as the derived anisotropies $D_{[100]}/D_{[001]}$ and $\kappa_{[100]}/\kappa_{[001]}$ might be even higher than reported. In other words, the presented values are rather lower bounds for the heat transport properties as well as for the anisotropy.

In Fig. 4.16 acoustic sound velocities are shown together with the thermal diffusivity D and the derived mean free path length $l (= 3D/v$, *cf.* Eq. 4.10) over three distinct crystallographic directions. The elastic properties such as v_{mean} (and also Young's modulus, see Fig. 4.9) and the thermal transport properties run parallel showing a pronounced anisotropy. With respect to the thermal diffusivity D at $T = -100$ °C, 25 °C and 375 °C (black and gray, Fig. 4.16), the strong temperature dependence of thermal transport properties is presented as an example. The maximum in thermal transport properties coincides with the direction $\perp c$ -axis reflecting the important role of the $[\text{CaO}_6]$ octahedral layers in contrast to the 3-fold axis $[001]$ direction with strong bonds of octahedral layers in alternation with weak interlayer bonding. The thermal transport properties thus greatly correlate with the crystal structure of portlandite (*cf.* Fig 4.1).

4.5 CONCLUSION

Thermoelastic properties of synthetic portlandite $\text{Ca}(\text{OH})_2$ single crystals have been studied in detail.

Both the elastic and thermal transport data show a pronounced anisotropy with faster acoustic wave velocities, larger Young's modulus and higher thermal diffusivity and thermal conductivity in the direction perpendicular to the 3-fold c -axis. The spatial distribution of these properties correlates with the layered structure of $\text{Ca}(\text{OH})_2$.

A series of measurements with different specimen thicknesses reveals a distinct thickness dependency of the thermal diffusivity, which could be related to the influence of the applied specimen coating. In a

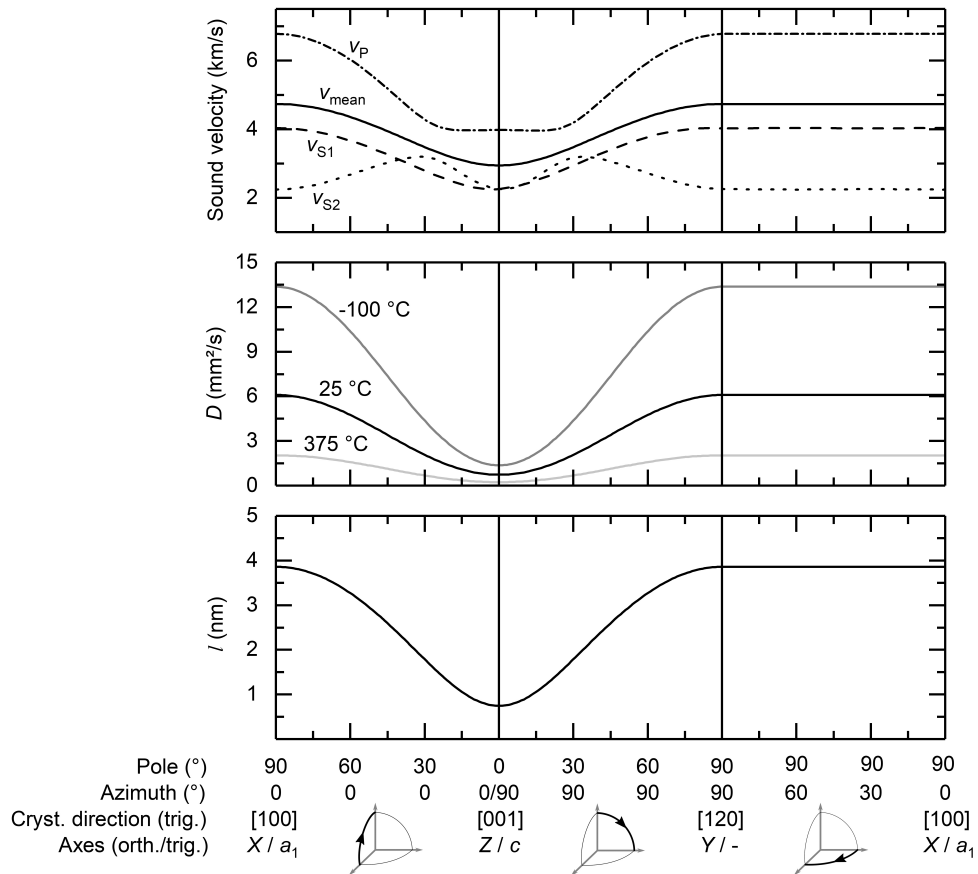


Figure 4.16: Spatial distribution of elastic (acoustic sound velocities at ambient conditions) and thermal transport properties (thermal diffusivity D) of portlandite for selected orientations. Mean free path length derived as $l = 3D/v$ (cf. Eq. 4.10, v approximated by $v_{mean} = \sqrt{(v_p^2 + v_{s1}^2 + v_{s2}^2)}/3$ at ambient conditions). The thermal diffusivity is shown for $T = -100\text{ °C}$, 25 °C and 375 °C illustrating the temperature dependence of thermoelastic properties

comparable manner, the dehydration of $\text{Ca}(\text{OH})_2$ to $\text{CaO} + \text{H}_2\text{O}$ is strongly dependent on the experimental conditions and particularly affected by the crystal/specimen size and the chosen heating rate. This has a significant impact on the measured thermal diffusivities within the temperature range of portlandite dehydration and thus should be taken into account for prospective investigations.

The strong temperature dependence and high anisotropy of the thermoelastic properties of single crystal portlandite measured in this study holds potential for further developments of innovative applications. As an example in civil engineering, in case of a controllable growth direction of portlandite (and also ettringite, see Speziale et al. 2008a) crystals during the hydration of cement pastes, intended anisotropic components for constructions are certainly conceivable. With respect to future use of portlandite in flue gas cleaning combustion technology, the detailed knowledge of the thermal conductivity and thermal diffusivity provides a basis for new system designs and for refining modeling approaches related to technical processes. In particular the relationship between the temperature-dependent thermal transport properties and the crystallographic orientations could contribute to innovations concerning the process design. Lastly, numerical studies on portlandite for thermochemical storage systems often assume constant and orientation-independent (*i.e.* isotropic) thermal transport properties. But, measurements shown here reveal not only a high temperature variation but also strong orientation-dependent thermal transport properties for portlandite. Thus, assumptions on thermal transport properties being isotropic and constant over a wide temperature range seem to be inappropriate. The data collected in this study therefore contribute to better and more meaningful numerical studies of technical processes based on portlandite as reactive medium.

4.6 ACKNOWLEDGMENTS

This study was made possible by a Dr. M. Herrenknecht foundation. The authors want to thank R.M. Danisi for developing a SC-XRD routine to measure angular misorientations of the portlandite platelets and A. Wunsch and D. Seiler for their initial experiments of portlandite crystal growth. Thanks to B. Oetzel, E. Eiche and M. Denker for performing ICP-MS, XRD, CSA and IC measurements. The authors furthermore acknowledge F. Krause for help performing TG and DSC measurements and L. Pennacchioni for help performing Brillouin scattering measurements. We moreover want to thank the anonymous reviewers for their effort and helpful comments on the manuscript.

SYNTHESIS

CONCLUSION AND OUTLOOK

The knowledge and understanding of thermal transport properties of solids is of fundamental importance for material sciences and engineering applications as well as to comprehend the system Earth. It is not only of academic interest to reveal the underlying processes of heat transfer as it forms a basis for *e.g.* various fields of prospective energy transition (developing novel heat storage systems, large scale realization of zero-emission buildings, *etc.*) and the design of customized materials. Against this background, the overarching objective of this thesis is the improvement of the flash method including the further development of data evaluation for a fundamental improvement of the data basis of crystals relevant to a variety of technical applications – quartz and portlandite.

One of the major further developments of the flash method presented by Parker et al. (1961) was the consideration of a time-dependent and thus non-instantaneous heat source in data processing (“finite pulse-time effect”). Thereby, the accuracy of flash method measurements was significantly improved (Larson and Koyama 1967). In the first study (chapter 2) of this thesis it was shown that a systematic mismatch can exist between the measured and approximated temperature histories, although the finite pulse-time effect is taken into account. Analyzing the misfits revealed an additional delay of the signal due to the IR detector and electronic components. It was shown that this can be such a pronounced effect that its consideration is required for an accurate data evaluation. Therefore, a transfer function was developed reproducing the signal of the retarded heat pulse on the basis of the heat source measured by an integrated diode. The transferred radiant source signal is used in a specifically developed data reduction routine to approximate the measured signal-time curve. The results have shown that not only thin specimens or high thermal diffusive materials are strongly affected (with systematic errors exceeding 10 % for standard data processing), but also specimens with moderate thicknesses (millimeter range) or thermal diffusivities can inhere systematic errors ≥ 1 -2 %. This result is substantial to understand and classify the reliability of flash method measurements and it is opposed to an often over-optimistic view on the accuracy (2-3 %) of flash method data (*e.g.* Abdulagatov et al. 2015). It could be furthermore shown that even for materials used as reference samples, the provided thicknesses for flash method measurements might be too low to evaluate their intrinsic thermal transport properties by applying standard evaluation routines. In other words, it could be demonstrated that higher diffusive reference materials (*e.g.* POCO or isotropic graphite) are required at

significantly bigger specimen thicknesses to avoid misinterpretations associated with different data reduction routines used.

With these findings the data processing and thus the quality of the resultant thermal transport properties is significantly improved for widespread flash method.

The fact that this kind of signal retardation inhering flash method raw data was still unnoticed might have several reasons: First and foremost, it is not just uncommon but also not recommended to directly irradiate the IR detector by a high-intense short-duration laser pulse. Then, depending on the used model to approximate the measured temperature history, systematic misfits might remain unrecognized as the often numerous fit parameters usually somehow give a sufficiently well data approximation. This is even more the case if proprietary software with marginal knowledge of the underlying equations and limited access to adjustments is used. In addition, indications for systematic misfits using standard evaluation routines are primarily visible for measurements on thin and high thermal diffusive specimens and could be first identified here on test measurements of silicon wafers. The fact that flash method measurements are not only affected by the finite pulse-time effect but several other factors complicates the interpretation of the measured temperature-time curves too. On the one hand, these influencing factors can have consequences for the measured raw data different in sign (*e.g.* nonuniform hot center flash heating, Baba and Ono 2001, vs. retarded pulse-time, Breuer and Schilling 2019), on the other hand, not enough attention seems to be paid on what affects flash method data in general. In the view of the author, the latter is very crucial as the quality of the measured and processed thermal transport data can only be as good as the apparatus' operator and round robin tests that could remedy this fact are scarce. As a consequence, the often as a general statement claimed accuracy of the method of $\sim 3\%$ or even better (Hofmeister 2006; Reif-Acherman 2014; Abdulagatov et al. 2015) is at least questionable.

To increase the accuracy and reliability of future thermal transport properties measured by the flash method, at least the following aspects ought to be concerned:

- Referring to chapter 2, an additional signal retardation inheres measured flash method raw data and affects the data evaluation in the same order of magnitude as the frequently considered finite pulse-time effect. Neglecting this influencing factor can result in systematic errors easily exceeding 10 %. But as these findings were gathered with a single flash method setup, this kind of signal retardation in the temperature history needs to be evaluated with other experimental setups too (whether commercial or custom constructions), and if necessary, adaptations have to be made to either the experimental setup or the evaluation routines.

- As already mentioned, the knowledge about the details of applied approximation routines is often limited. This might be – mainly but not solely – due to the fact that commercial systems and their proprietary software solutions are (or have to be) used. But especially with a view to non-standard measurements (*e.g.* very thin or thick dimensions, custom sample holders, various coatings, *etc.*), it seems to be advantageous to have access to the underlying code of the used evaluation routines, which could also help to verify whether or not certain models can be applied to process flash method data in a given case. It might therefore be appropriate to set up custom evaluation routines for specific demands.
- The additional time delay considered in the first study presents only one influencing factor in flash method measurements. Over the past decades, several more factors limiting the accuracy of flash data have been identified. Among those are the influence of the homogeneity of the heat source on the temperature history and the influence of the (commonly used) simplification that the transient spectral radiance equals the transient temperature change on the specimen's rear side. It is known that each of these two effects can have a significant influence (*i.e.* in the percent range) on the accuracy of flash method measurements (Baba and Ono 2001). But at the same time, prospects to handle and account for the mentioned influencing factors have been pointed out, involving considerable effort and expense: for example, transmitting the radiant beam through optical fibers (or at least installing additional homogenizers in the beam path), applying data processing routines that take into account a (radial symmetric) nonuniform surface heating, and linking the spectral radiance with the temperature for a given experimental setup (*e.g.* Schriempf 1972; McKay and Schriempf 1976; Hasselman and Donaldson 1990; Hoefler and Taylor 1990; Baba et al. 1993; Baba and Ono 2001). In the author's opinion, these influencing factors are addressed in certain studies, but neither (sufficiently) concerned nor integrated in many experimental flash method setups and therefore reduce the overall accuracy of the resultant thermal transport properties far below the potential of the method.

With the results presented in the first study the standard flash method could be significantly improved in terms of data evaluation to more accurately derive the thermal transport properties especially of thin and high diffusive solids. But besides the just aforementioned aspects to be considered for further improvements of the method, additional investigations are needed in the field of sample coatings. They are used – especially but not solely – for (semi)transparent samples to improve the heat pulse absorption and to reduce the direct irradiation of the IR detector. Coatings therefore ensure a good signal and proper tempera-

ture history. Nevertheless, these coatings need to be taken into account as they act as additional layers (*e.g.*, coating—sample—coating) and it seems that only under specific circumstances the influence of these coatings to derived thermal diffusivity values can be neglected. In other words, flash method raw data are in many cases (significantly) affected by the applied coatings, as it was also shown within the third study on portlandite thermal transport properties (*cf.* chapter 4, Fig. 4.15). Some of the underlying processes and mechanisms have already been addressed by the investigations of *e.g.* Araki et al. (1992), Albers et al. (2001), Cernuschi et al. (2002), Lim et al. (2009), and Schoderböck et al. (2009). These studies help to understand the problematic nature of applying additional layers on a solid prior to measure its thermal transport properties. But even though they make approaches to better account for the influence of coatings in flash methods, they generally suffer from a limited applicability and practicability. For example, Cernuschi et al. (2002) and Lim et al. (2009) proposed to handle applied graphite coatings (which are by far the most commonly used coatings) as separate layers and thus consider the investigated specimen as a multi-layer object for the subsequent data processing. Therefore, physical properties such as the thickness, but also the density, the specific heat, and the thermal conductivity (or diffusivity) of the coating have to be precisely known and of constant quality. But investigations show that the sprayed graphite coatings are in general not enough consistent in their appearance and depend on *e.g.* the used graphite, the operator, the specimen's surface conditions, the filling level of the spray can, *etc.* As a consequence, an accurate knowledge of the physical properties of these layers is limited. This is exemplarily shown in Fig. 5.1. It presents scanning electron microscope (SEM) images of standard highly porous graphite coatings (CRC Kontakt Chemie, Graphit 33) applied on glass platelets (light gray). It becomes apparent that the thickness is nonuniform with an uneven surface of the unpolished coating (Fig. 5.1a&b). Even though the thickness is reduced and the uniformity is increased by polishing (c), the surface of the coatings can be easily damaged (d). For this reason, accounting for coatings using multi-layer data evaluation routines is limited by the coating quality and reproducibility. Other techniques to apply coatings, such as sputtering, suffer from shortcomings that sub-micron coatings are often optically not thick enough to absorb the intense laser pulse and the sputtered coatings tend to easily peel off after very few measurements, especially when applied on specimens with very smooth or glassy surfaces. To conclude, (graphite) coatings applied on (semi)transparent specimens are essential and common practice to perform flash method measurements. Even though the influence of applied coatings on the resultant temperature history can be assigned in theory in data processing routines, its practical applicability is limited due to the lacking consistency of the applied coatings and thus unknown physical properties. Hence, the effects of sprayed (graphite) coatings on the resulting flash data still

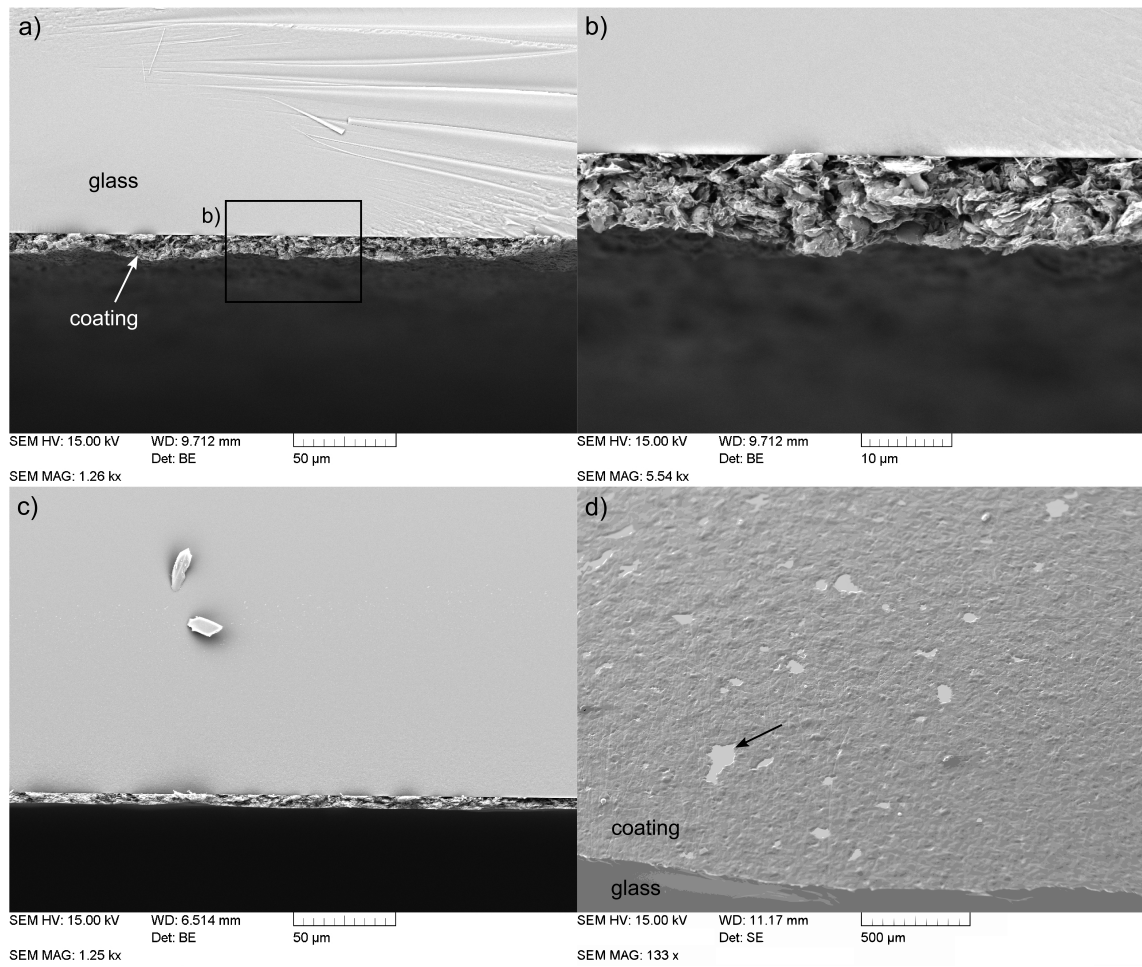


Figure 5.1: Scanning microscope photographs (SEM) of glass platelets (light gray) coated with graphite (CRC Kontakt Chemie, Graphit 33) without any further treatment (a, b) and with polished graphite surface (c, d) in a sideways (a-c) and top down view (d). The arrow in d) exemplarily indicates one of recurrent small breakouts of the coating due to the mechanical polishing (images by I. Woll)

cannot be considered with a sufficient accuracy and require a more systematic consideration. Appropriate alternatives (high thermal diffusivity, easy to apply as uniform and micron-thin layer, high absorption and emission coefficient, cost-effective) for flash method coatings are still missing. This needs to be subject to future research.

The second study presented in this thesis (chapter 3) focuses on quartz (SiO_2). It is important as rock-forming mineral in the geoscientific field and also essential for numerous technical applications due to its *e.g.* piezoelectric property. Measured by its significance it is somewhat surprising that an extensive knowledge of the thermal transport properties of single crystal quartz remains absent. Thermal transport properties are lacking especially below room temperature and contradictory results of thermal diffusivity measurements have been presented at elevated temperatures around the α - β phase transition at $573\text{ }^\circ\text{C}$ (*e.g.* Höfer 2003, and Branlund and Hofmeister 2007).

With a detailed investigation of the time-dependent temperature history it could be shown that, apart from the known ballistic radiative heat transfer, another type of radiative portion inheres the data below the α - β phase transition. As this assumed non-ballistic radiative heat transfer cannot be approximated by standard data approximations (*e.g.* by the model proposed by Mehling et al. 1998, as noted by Branlund and Hofmeister 2007), the evaluation routine developed in the first study was modified. This way, the different heat transport mechanisms could be effectively separated and accurate thermal transport properties were obtained in the region below the phase transition. It could be shown that this adapted data processing approach needs to be applied even in the wider vicinity below the phase transition as the observed non-ballistic heat transfer affects the measured temperature-time history already far below the phase transition. It became apparent that this customized approximation routine significantly increases the fit quality and the resultant thermal transport properties are therefore more accurate compared to results provided by standard models. Even though these findings were obtained for single crystal quartz, it can be reasonably assumed that other (semi)transparent crystals undergoing phase transitions show a similar behavior and, as a consequence, data processing subsequent to flash method measurements needs to consider non-ballistic radiative heat transfer. Therefore, future measurements need to be carried out on different types of (semi)transparent single crystals to check whether the observed radiation phenomenon appears and, if so, whether the proposed evaluation routine for the assumed non-ballistic radiative heat transfer can be applied. A potential crystal to investigate the temperature history in the vicinity of a phase transition in flash measurements could be, for example, BaTiO_3 with its displacive phase transitions around $-71\text{ }^\circ\text{C}$, $8\text{ }^\circ\text{C}$ and $125\text{ }^\circ\text{C}$ (Dove 1997; Ma et al. 2017).

With respect to the measured quartz single crystals it could be shown that no crossover in the crystallographic direction of the maximum

thermal diffusivity occurs by crossing the α - β phase transition at 573 °C as formerly reported by Höfer and Schilling (2002) and Höfer (2003). From a theoretical point of view, the specific heat and the average acoustic phonon velocity only have a minor impact on the heat transport at high temperatures as they are almost temperature-independent (e.g. Roufosse and Klemens 1974; Böer and Pohl 2018). In the vicinity of the α - β phase transition the elastic properties and thereto related acoustic phonon velocities show a significant change with a crossover of the direction of the maximum (average) phonon velocity (cf. Fig. 3.5). With the clarified trend of the temperature-dependent thermal diffusivity around the phase transition (no crossover) it could thus be concluded that the elastic properties, namely the average acoustic wave velocities, have a smaller impact on the heat transport as formerly assumed by Höfer and Schilling (2002). In a comparable manner and with respect to the spatial distribution of the elastic and thermal transport properties of portlandite, it could be illustrated that the heat transfer is primarily related to the phononic mean free path and less to the contribution of the acoustic sound velocities (cf. chapter 4, Fig. 4.16).

Furthermore, in the second study first time thermal diffusivity data of α -quartz were reported below room temperature down to -120 °C. The temperature trend of the thermal diffusivity was approximated by a model solely describing a dependency $D(T) \propto 1/T^n$ (three-phonon scattering processes, cf. section 1.1). It was found that the data approximation is of low quality and the resulting diffusivities are too high compared to the measured data, especially at very low temperatures (i.e. < -80 °C, cf. Fig. 3.2a). In a comparable manner the derived thermal conductivity of portlandite clearly stops to follow a $1/T^n$ trend in the low temperature region, as could be shown within the third study (chapter 4, Fig. 4.12). These findings indicate that hitherto used approximations to describe the temperature dependence of the thermal transport properties are inappropriate for data collected at low temperatures. This is most probably due to phonon modes freezing out below the Debye temperature as proposed by theory (Debye 1914; Peierls 1929, section 1.1, cf. Fig. 1.4). In this context, measurements on crystals' thermal transport properties at very low temperatures are of particular interest. In general, only few thermal transport data by the flash method exist in the low temperature region down to -100 °C or even below (e.g. Hemberger et al. 2010; Göbel et al. 2011; Göbel et al. 2013). But with respect to our understanding of heat transport processes and for the potential discovery of thermal transport properties of solids beneficial for e.g. the IT industry, more low temperature measurements are mandatory. However, such measurements are challenging to realize for a number of reasons, for instance: 1) according to the Stefan-Boltzmann law, the power radiated from an object at very low temperatures is dramatically reduced and shifted towards higher wavelengths (Wien's displacement law). As a consequence, contactless flash technique measurements with IR detectors seem to be hardly

possible at very low temperatures. 2) In addition, the construction of a flash method apparatus to measure at temperatures down to the boiling point of *e.g.* liquid helium at ~ -269 °C places new challenging demands on materials for example used for the sample chamber. 3) In addition it is remarked that measurements at such low temperatures may require considerably bigger sample dimensions (which is challenging for certain materials) compared to ordinary (sub)millimeter-thick specimens to derive the intrinsic phononic heat transport by conduction. This is due to an expected increase of the free path of phonons at very low temperatures (*cf.* section 1.1).

The third study focuses on the thermoelastic properties of portlandite (chapter 4). Even though materials containing portlandite are extensively used *e.g.* in civil engineering, the knowledge on its elastic and especially its thermal transport properties is rather scarce and limited to (compressed) powders of $\text{Ca}(\text{OH})_2$ (*e.g.*, see Schaube 2013; Ranjha et al. 2016). This fact poses certain risks, *e.g.* for modelings including the reaction $\text{Ca}(\text{OH})_2 \rightleftharpoons \text{CaO} + \text{H}_2\text{O}$, as the lacking information on (temperature-dependent) thermal transport properties can dramatically limit the significance of the results. Hence, the main objective was to create the missing data basis of the anisotropic thermoelastic properties of single crystal portlandite to eventually improve the understanding of the underlying processes and mechanisms of the thermoelastic properties of *e.g.* cured concrete. Therefore, in a first step, idiomorphic millimeter to centimeter-sized single crystals were grown by adapting a diffusion technique. Then, measurements with the flash method apparatus were performed in the temperature range between -100 °C and 700 °C using custom-designed sample holders. To derive accurate thermal transport properties, the use of the approximation routine developed within the first study of this dissertation is a necessity. This is due to the fact that the synthesized portlandite crystals could only be prepared at relatively small sample thicknesses down to ~ 0.5 mm for the flash measurements. With respect to Fig. 2.6b (see also Eq. 2.12 with Tab.2.3), systematic errors would reach up to ~ 10 % for the derived thermal diffusivities of portlandite (for $d \sim 0.5$ mm and $D \sim 13$ mm²/s at low temperatures, *cf.* Fig. 4.10) by not taking into account the detector inherent delay.

The determined thermal transport properties reveal a high degree of anisotropy. Along the [001] and [100] direction the efficiency to transfer heat differs by a factor of almost one order of magnitude (*cf.* Figs. 4.10-4.12). This behavior could be directly linked to the internal structure of portlandite. Parallel to the *c*-axis the stacked $[\text{CaO}_6]$ octahedral layers with the OH interlayers can be seen as a series circuit of high conducting octahedral and low conducting hydroxyl group layers. In contrast, a parallel circuit-like behavior can be assumed for the perpendicular direction (\perp *c*-axis), where the heat is supposed to be primarily transferred across the edge-sharing $[\text{CaO}_6]$ octahedral layers. A comparable high anisotropy was also determined by Brillouin spectroscopy for

the elastic properties of the synthetic portlandite crystals at ambient conditions. It could be shown that at least the elastic properties of synthetic and natural Ca(OH)_2 crystals are in very good agreement with each other (within the precision of the experiments). With these findings it seems possible that future applications take advantage of the high anisotropy of portlandite, *e.g.* by specifically designing materials with ordered crystallites to significantly increase (or decrease) thermoelastic properties in specific directions compared to a component with randomly orientated Ca(OH)_2 crystals. It furthermore might be interesting to investigate the chemical reactivity of portlandite in terms of orientation dependencies. Anisotropies of comparable extent to the thermoelastic properties might be advantageous for the application in thermochemical energy storage systems but also for flue gas cleaning systems.

With respect to the release of water and the formation of calcium oxide from portlandite it could be shown that the experimental conditions, namely the heating rate and the chosen specimen dimensions, can have a significant impact on the measured temperature-dependent thermal transport properties in the vicinity of the dehydration. The results furthermore indicate that the kinetics of the dehydration exhibits a strong direction dependency. It is conceivable that other material reactions that include a change of the chemical composition exhibit such a behavior in a comparable manner. Here, besides the phase change itself the porosity and micrograin development is expected to influence the observed thermal transport behavior too. These results with portlandite show that factors influencing the measurements of thermal transport properties have to be carefully thought of and it can be assumed that such influences may indirectly have a significant impact on subsequent data processing, *e.g.* in the case of portlandite, when using thermophysical properties for the development of large thermochemical energy storage systems.

Following the principle of diffusion in the kinetic gas theory, the thermal conductivity through phonons can be described in a comparable manner (*cf.* section 1.1, Eq. 1.6). Accordingly, heat transport depends on the specific heat, the average phonon velocity, and the mean free path. This raises the question whether or not there is one of the parameters dominating the heat transport. It could be revealed that at low temperatures the thermal conductivity of portlandite shows a plateau for the $[001]$ direction at around $-100\text{ }^\circ\text{C}$ and the perpendicular direction $[100]$ shows a significant flattening of the thermal conductivity towards low temperatures (*cf.* chapter 4, Fig. 4.14b&d). As the measured thermal diffusivities still follow a $\propto 1/T^n$ trend in this temperature region (Fig. 4.14a&c), the low temperature behavior of the thermal conductivity can be directly related to the strongly decreasing specific heat towards low temperatures⁵ (*cf.* Appendix A.2,

⁵ Assuming that the average phonon velocity does not vary significantly in the corresponding temperature range

Tab. A.11). As already remarked, measurements of thermal transport properties down to a few Kelvin would be of considerable interest here, in particular when performed by the flash technique to be able to distinguish between different heat transport mechanisms (Hofmeister 2019). However, it is questionable whether the (sub)millimeter-sized portlandite specimens are thick enough to investigate intrinsic heat conduction by phonons at very low temperatures. To conclude, the measurements support theoretical considerations that 1) at low temperatures the thermal conductivity is closely related to the trend of the specific heat of the corresponding material and that 2) at higher temperatures the mean free path of phonons dominates the behavior of a decreasing thermal transport efficiency for dielectric solids. The latter is even valid in the region of the α - β phase transition of quartz as shown in chapter 3.

This thesis had one focus on the further improvement of the flash technique to derive accurate thermal transport properties of single crystals of geoscientific and technical interest. Within the presented three studies improvements to the data evaluation procedures of the flash method were developed. Additional time delays of the detectors and electronic components in the used flash method apparatus were investigated and implemented into a specifically set up data reduction routine. This way, systematic errors related to flash method measurements are reduced and the reliability of the resultant thermal transport properties is increased. With measurements conducted across phase transitions it was demonstrated that the collected data can be strongly affected thereby. It was shown that an assumed non-ballistic radiative heat transfer part inheres and affects the signal of single crystal quartz measurements already far below the actual phase transition. With a new approach developed here its consideration in an adapted data reduction was demonstrated and may be applied to other flash technique measurements with materials undergoing phase transitions. Measurement series on the thermal transport properties of quartz and portlandite indicate that by no means the results of a single specimen measurement should be overinterpreted in terms of its reliability. This is because it was shown that various factors influence the flash method signal-time history (specimen dimensions, coatings, data processing routines, heating rates, *etc.*) and therefore can significantly distort the resultant (apparent) thermal transport properties.

With these further developments and observations in the field of the flash method the data basis could be improved and expanded for single crystal α - and β -quartz and could be set up for the first time for single crystal portlandite.

Future research should more consistently incorporate improvements proposed for flash technique apparatuses (beam uniformity, spectral radiance vs. temperature, *etc.*) for a continuing progress of the method. Furthermore, in the view of the author it is necessary that alternative coating solutions for (semi)transparent specimens are found as

commonly used coatings (graphite sprays) still pose a major issue limiting the accuracy of the flash method. At the same time it is essential that collected flash data are thoroughly validated and checked for influencing factors. These two points have a direct impact on our understanding of heat transport as dealing with non-intrinsic data complicates our ambition to attain a deeper insight into heat transfer processes.

APPENDIX

Appendix A.1 was submitted as supplementary material to the study presented in chapter 3.

Appendix A.2 is published as appendix to the study presented in chapter 4.

A.1 APPENDIX TO CHAPTER 3

Table A.1: Low temperature α -quartz single crystal thermal diffusivity D in [001] (c -axis) and [100] (a -axis) direction (averages of three independent measurements per T). Thicknesses: $d_{\text{LT}[001]} = 2.064(3)$ mm, $d_{\text{LT}[100]} = 2.010(3)$ mm. Measured with HgCdTe IR detector

LT [001]		LT [001]		LT [100]		LT [100]	
T	D	T	D	T	D	T	D
(°C)	(mm ² /s)	(°C)	(mm ² /s)	(°C)	(mm ² /s)	(°C)	(mm ² /s)
-119.2	15.70(78) ^a	129.7	3.46(7)	-118.9	7.97(35)	150.3	1.86(3)
-109.8	14.07(49)	139.7	3.32(7)	-110.0	7.32(33)	160.3	1.80(4)
-100.0	13.51(38)	149.8	3.16(6)	-99.6	6.81(20)	170.2	1.73(3)
-89.8	12.62(42)	159.8	3.03(7)	-90.6	6.41(19)	180.3	1.68(3)
-79.9	11.77(33)	169.7	2.92(5)	-80.9	6.02(17)	190.3	1.62(3)
-79.8	11.69(38)	179.8	2.80(6)	-80.1	5.98(18)	200.2	1.57(3)
-69.5	11.04(38)	189.8	2.69(5)	-70.3	5.69(15)	210.2	1.53(3)
-59.4	10.22(32)	199.8	2.60(6)	-59.6	5.33(15)	220.2	1.49(3)
-49.6	9.67(31)	209.8	2.50(6)	-49.7	5.01(12)	230.1	1.44(3)
-39.6	9.09(24)	219.8	2.42(6)	-39.7	4.72(15)	240.2	1.41(3)
-30.0	8.49(27)	229.8	2.33(5)	-29.5	4.46(10)	250.2	1.37(4)
-20.0	7.94(22)	239.8	2.25(5)	-19.3	4.22(10)	260.1	1.34(3)
-9.9	7.39(17)	249.8	2.18(5)	-9.5	3.98(9)	270.2	1.30(3)
0.0	6.95(19)	259.8	2.11(5)	0.5	3.76(10)	280.2	1.27(3)
10.0	6.52(16)	269.8	2.04(5)	10.2	3.55(8)	290.2	1.24(3)
19.7	6.16(12)	279.9	1.98(5)	20.3	3.35(7)	300.2	1.22(3)
29.7	5.78(18)	289.9	1.93(5)	29.8	3.19(7)	310.2	1.19(3)
40.5	5.42(12)	299.9	1.87(5)	39.8	3.01(6)	320.2	1.16(3)
50.4	5.10(13)	309.9	1.81(5)	49.6	2.87(7)	330.2	1.14(4)
60.3	4.82(9)	319.9	1.77(6)	59.8	2.72(8)	340.3	1.12(5)
70.3	4.57(9)	329.9	1.72(5)	69.9	2.59(5)	350.3	1.10(4)
80.1	4.33(10)	339.9	1.67(6)	79.9	2.48(4)	360.3	1.08(4)
89.6	4.17(7)	349.9	1.63(5)	90.0	2.37(4)	370.2	1.06(5)
89.7	4.16(8)	359.9	1.58(6)	100.0	2.26(5)	380.5	1.04(4)
100.1	3.97(11)	369.9	1.54(6)	110.7	2.18(4)	390.3	1.02(4)
100.2	3.95(8)	379.9	1.51(6)	120.2	2.09(3)	400.3	1.01(4)
110.1	3.79(7)	389.9	1.47(7)	130.2	2.01(3)		
120.1	3.61(7)	399.9	1.44(7)	140.3	1.93(4)		

^anumbers in parentheses are 2σ standard deviations of the last digits

Table A.2: Thermal diffusivity D measured across the α - β phase transition (averages of three independent measurements per T). Thicknesses: $d_{\text{HT1}[001]} = 1.999(3)$ mm, $d_{\text{HT2}[001]} = 4.706(4)$ mm, $d_{\text{HT1}[100]} = 1.986(3)$ mm and $d_{\text{HT2}[100]} = 4.022(4)$ mm. Measured with InSb IR detector

HT1 [001]		HT2 [001]		HT1 [100]		HT2 [100]	
T	D	T	D	T	D	T	D
(°C)	(mm ² /s)						
25.9	5.69(19)	25.6	5.37(27)	25.9	2.89(8)	25.4	3.08(15)
50.1	4.90(14)	50.6	4.68(18)	50.0	2.56(7)	50.1	2.69(7)
99.6	3.84(11)	99.7	3.67(7)	99.8	2.05(4)	99.7	2.18(5)
149.8	3.09(9)	149.9	2.92(7)	149.8	1.70(3)	149.7	1.79(3)
199.9	2.29(6)	200.0	2.40(8)	199.8	1.43(3)	199.7	1.52(4)
250.1	1.92(5)	250.0	1.80(5)	249.9	1.24(3)	249.8	1.17(3)
300.2	1.65(5)	300.3	1.54(4)	299.9	1.10(3)	299.9	1.04(3)
325.3	1.54(5)	325.3	1.44(5)	325.0	1.05(3)	325.0	0.98(3)
350.3	1.45(5)	350.4	1.35(4)	350.0	1.00(3)	350.0	0.93(3)
375.5	1.35(5)	375.3	1.27(5)	375.0	0.94(4)	375.0	0.89(3)
400.4	1.26(5)	400.3	1.20(5)	400.0	0.90(4)	400.0	0.85(3)
425.1	1.18(5)	425.2	1.13(5)	425.0	0.86(4)	425.1	0.82(4)
450.2	1.11(5)	450.2	1.07(6)	450.0	0.82(4)	450.1	0.79(4)
454.7	1.10(5)	454.7	1.07(6)	455.0	0.81(4)	455.0	0.79(4)
459.7	1.09(6)	459.7	1.05(5)	460.0	0.81(4)	460.0	0.78(4)
464.7	1.08(5)	464.7	1.04(5)	465.0	0.80(4)	465.0	0.78(4)
469.7	1.07(5)	469.7	1.03(6)	470.0	0.80(4)	470.0	0.78(4)
474.7	1.06(6)	474.7	1.02(6)	475.0	0.79(4)	475.0	0.77(4)
479.7	1.05(6)	479.7	1.01(6)	480.0	0.79(4)	480.0	0.77(4)
484.7	1.03(6)	484.7	1.01(6)	485.0	0.78(4)	485.0	0.76(4)
489.8	1.02(5)	489.7	0.99(6)	490.1	0.78(4)	490.0	0.75(4)
494.7	1.01(6)	494.7	0.98(6)	495.2	0.77(4)	495.0	0.75(5)
499.7	1.00(6)	499.7	0.97(6)	500.1	0.76(4)	500.0	0.75(5)
504.7	0.99(6)	504.7	0.96(6)	505.2	0.76(4)	505.0	0.74(4)
509.7	0.98(5)	509.7	0.95(6)	510.1	0.75(4)	510.0	0.74(4)
514.7	0.97(6)	514.7	0.94(6)	515.0	0.75(4)	515.0	0.73(5)
519.7	0.96(6)	519.6	0.93(6)	520.1	0.74(4)	520.0	0.72(4)
524.7	0.95(6)	524.7	0.92(5)	525.0	0.74(4)	525.0	0.72(5)
529.8	0.94(6)	529.7	0.91(6)	530.1	0.73(4)	530.1	0.73(5)
534.6	0.93(6)	534.6	0.89(6)	535.1	0.73(5)	535.0	0.72(5)
539.6	0.91(6)	539.7	0.88(6)	540.0	0.72(4)	540.0	0.71(5)
544.6	0.90(6)	544.7	0.87(7)	545.0	0.72(4)	545.0	0.70(5)
549.7	0.89(6)	549.7	0.85(6)	550.0	0.71(4)	550.0	0.70(5)
551.6	0.88(6)	551.6	0.85(7)	552.0	0.71(5)	552.1	0.70(5)
553.6	0.87(6)	553.6	0.84(6)	554.0	0.70(4)	554.0	0.70(5)
555.5	0.87(6)	555.6	0.84(6)	556.1	0.70(5)	556.1	0.69(5)
557.6	0.86(6)	557.6	0.83(7)	558.0	0.70(5)	558.0	0.69(5)

(continued)

HT1 [001]		HT2 [001]		HT1 [100]		HT2 [100]	
<i>T</i>	<i>D</i>	<i>T</i>	<i>D</i>	<i>T</i>	<i>D</i>	<i>T</i>	<i>D</i>
(°C)	(mm ² /s)						
559.6	0.86(6)	559.6	0.77(19)	560.0	0.69(5)	560.0	0.69(4)
561.6	0.86(6)	561.6	0.81(8)	562.0	0.69(4)	562.0	0.68(5)
563.6	0.84(6)	563.6	0.79(6)	564.0	0.68(4)	564.0	0.68(5)
565.6	0.83(6)	565.6	0.79(6)	566.0	0.68(4)	566.0	0.68(5)
567.6	0.82(6)	567.6	0.77(7)	568.0	0.67(4)	568.0	0.67(5)
569.6	0.80(6)	569.6	0.75(7)	570.0	0.66(4)	570.0	0.66(5)
571.6	0.77(7)	571.7	0.72(14)	572.0	0.65(5)	572.0	0.65(4)
573.7	0.74(11)	573.6	0.58(35)	574.0	0.64(6)	574.0	0.65(5)
575.6	0.63(28)	575.7	0.91(24)	576.0	0.59(12)	575.9	0.62(6)
577.6	0.89(21)	577.6	0.94(8)	578.0	0.55(17)	578.0	0.58(17)
579.6	0.93(7)	579.6	0.96(7)	580.0	0.73(20)	580.0	0.68(18)
581.6	0.94(6)	581.6	0.96(7)	582.0	0.81(8)	582.0	0.79(10)
583.6	0.95(6)	583.6	0.97(7)	584.0	0.82(6)	584.0	0.82(5)
585.6	0.95(6)	585.6	0.98(7)	586.0	0.83(5)	586.0	0.82(5)
587.6	0.96(6)	587.6	0.97(6)	588.0	0.83(5)	588.1	0.83(5)
589.6	0.96(6)	589.5	0.98(6)	590.0	0.84(5)	590.1	0.83(5)
594.7	0.97(5)	594.6	0.97(6)	595.0	0.84(5)	595.0	0.84(6)
599.7	0.97(5)	599.7	0.99(5)	600.0	0.85(4)	600.0	0.85(5)
604.7	0.97(5)	604.6	0.99(5)	605.0	0.85(4)	605.1	0.85(4)
609.7	0.97(4)	609.6	0.98(5)	610.0	0.85(3)	610.0	0.85(4)
614.7	0.97(4)	614.7	0.99(4)	615.0	0.85(3)	615.0	0.85(4)
619.7	0.98(3)	619.7	0.99(3)	620.0	0.85(3)	620.0	0.85(4)
624.7	0.98(3)	624.7	0.99(4)	625.0	0.86(3)	625.0	0.85(5)
629.8	0.98(3)	629.7	1.01(3)	629.9	0.86(2)	630.0	0.85(2)
634.7	0.98(3)	634.6	0.98(5)	634.9	0.86(2)	635.0	0.85(3)
639.7	0.98(2)	639.7	1.01(5)	639.9	0.86(2)	640.0	0.83(3)
644.7	0.98(3)			645.0	0.86(2)	645.0	0.86(4)
649.7	0.98(2)			650.0	0.86(2)	650.0	0.86(3)
675.1	0.99(3)			675.0	0.86(2)	675.0	0.85(9)
700.1	0.98(3)			699.9	0.86(2)	700.0	0.63(13)
725.2	0.98(3)			724.9	0.86(2)	724.9	0.90(30)
750.1	0.97(3)			749.8	0.86(3)		
775.1	0.96(4)			774.8	0.87(5)		
800.1	1.03(9)						

Table A.3: Thermal diffusivity D measured for thick ($d_{[001]} = 9.965(5)$ mm, $d_{[100]} = 11.089(6)$ mm) quartz single crystal specimens over the α - β phase transition (averages of three independent measurements per T). Measured with InSb IR detector

[001]		[100]	
T (°C)	D (mm ² /s)	T (°C)	D (mm ² /s)
400.1	1.22(9)	399.9	0.90(6)
425.1	1.15(7)	450.2	0.86(5)
450.3	1.13(9)	500.0	0.83(16)
475.2	1.08(8)	540.3	0.77(13)
500.3	0.97(7)	560.2	0.68(10)
525.5	1.00(14)	570.8	0.55(15)
540.3	0.98(12)	572.9	0.77(18)
560.2	0.89(20)	574.9	1.15(14)
565.0	0.78(12)	580.0	1.20(9)
568.9	0.80(15)	585.0	1.19(14)
570.8	0.63(65)	589.9	1.25(13)
572.9	1.01(42)	620.4	1.21(9)
574.9	1.01(22)	650.6	1.33(23)
579.9	1.07(23)	700.6	1.26(22)
585.0	1.05(24)		
590.0	1.02(24)		
600.0	1.13(33)		
620.3	1.09(9)		
650.1	1.14(21)		
675.0	1.12(27)		
700.2	1.14(18)		
725.0	1.14(35)		

Table A.4: $LT_{[001]}$ ratio of direct radiative heat transfer $T_{0,rad}$ to theoretical adiabatic maximum temperature T_{max}

T (°C)	$\frac{T_{0,rad}}{T_{max}}$ (%)	T (°C)	$\frac{T_{0,rad}}{T_{max}}$ (%)	T (°C)	$\frac{T_{0,rad}}{T_{max}}$ (%)	T (°C)	$\frac{T_{0,rad}}{T_{max}}$ (%)
-120.0	0.5(1)	-20.1	0.4(1)	119.9	0.5(1)	270.0	4.1(10)
-119.2	1.1(3)	-20.1	0.2(1)	129.6	0.8(2)	279.8	4.3(11)
-119.1	1.7(4)	-19.8	0.5(1)	149.7	1.3(3)	279.8	4.0(10)
-118.6	0.6(1)	-10.1	2.0(5)	149.7	1.8(4)	280.0	3.4(8)
-110.6	0.1(0)	-10.0	0.3(1)	150.1	1.5(4)	289.8	4.6(12)
-110.1	1.0(3)	-9.6	1.5(4)	159.7	1.6(4)	289.8	4.1(10)
-109.7	0.8(2)	-0.2	0.9(2)	159.7	2.6(6)	290.0	5.0(12)
-109.7	0.6(1)	-0.1	0.9(2)	160.0	2.0(5)	299.8	3.8(10)
-100.2	0.3(1)	0.4	1.4(3)	169.6	1.9(5)	299.8	4.8(12)
-99.9	1.2(3)	9.8	0.4(1)	169.7	1.8(5)	300.0	4.9(12)
-99.9	0.8(2)	9.8	0.7(2)	169.9	2.1(5)	309.8	4.9(12)
-99.9	0.3(1)	10.3	0.4(1)	179.6	1.7(4)	309.8	4.5(11)
-99.8	0.4(1)	19.6	1.7(4)	179.7	2.2(5)	310.0	4.3(11)
-90.1	0.7(2)	20.1	0.5(1)	180.0	1.6(4)	319.8	3.6(9)
-90.0	0.4(1)	29.6	1.3(3)	189.6	2.2(6)	319.8	3.9(10)
-89.9	1.4(3)	29.7	0.9(2)	189.7	2.3(6)	320.0	5.0(12)
-89.9	1.2(3)	29.9	0.9(2)	190.0	2.0(5)	329.8	5.4(13)
-89.6	0.8(2)	40.1	1.3(3)	199.7	2.3(6)	329.8	5.1(13)
-89.5	0.6(2)	40.4	1.8(4)	199.7	2.7(7)	330.0	4.3(11)
-80.7	0.8(2)	40.9	1.4(4)	200.0	3.0(7)	339.8	6.2(15)
-80.4	0.6(1)	50.3	0.7(2)	209.7	2.7(7)	339.8	6.3(16)
-80.0	0.2(1)	50.9	0.5(1)	209.7	1.9(5)	340.0	6.0(15)
-79.8	0.8(2)	59.9	0.3(1)	210.0	3.0(7)	349.8	5.7(14)
-79.8	0.6(2)	60.8	0.3(1)	219.7	2.9(7)	349.8	6.0(15)
-79.5	0.0(3)	69.7	0.9(2)	219.7	2.9(7)	350.0	6.7(17)
-79.2	0.4(1)	70.3	0.9(2)	220.0	2.6(7)	359.8	5.0(13)
-69.7	0.8(2)	70.8	1.0(2)	229.7	2.1(5)	359.8	5.1(13)
-69.5	0.2(1)	79.8	0.4(1)	229.7	3.3(8)	360.1	5.3(13)
-69.3	0.8(2)	89.1	1.0(3)	230.0	1.8(4)	369.8	6.6(17)
-59.7	1.2(3)	89.6	1.0(3)	239.7	3.3(8)	369.8	7.4(18)
-59.4	0.5(1)	89.6	1.1(3)	239.7	3.1(8)	370.1	6.8(17)
-59.2	0.6(2)	89.9	0.9(2)	240.0	2.4(6)	379.8	6.1(15)
-49.8	0.5(1)	90.0	0.3(1)	249.7	2.7(7)	379.8	6.4(16)
-49.6	0.4(1)	99.6	0.7(2)	249.7	3.5(9)	380.0	6.6(17)
-49.4	0.4(1)	99.6	0.1(0)	250.0	3.5(9)	389.8	7.7(19)
-40.2	1.0(3)	100.0	1.6(4)	259.7	3.2(8)	389.9	7.7(19)
-39.6	0.4(1)	100.8	0.8(2)	259.7	3.4(8)	390.1	7.7(19)
-39.0	1.1(3)	100.9	1.6(4)	260.0	3.9(10)	399.8	8.1(20)
-30.0	0.7(2)	109.6	0.5(1)	269.7	3.2(8)	399.9	6.2(15)
-29.9	0.6(1)	119.6	1.2(3)	269.8	4.2(10)	400.0	6.3(16)

Table A.5: $LT_{[100]}$ ratio of direct radiative heat transfer $T_{0,rad}$ to theoretical adiabatic maximum temperature T_{max}

T (°C)	$\frac{T_{0,rad}}{T_{max}}$ (%)	T (°C)	$\frac{T_{0,rad}}{T_{max}}$ (%)	T (°C)	$\frac{T_{0,rad}}{T_{max}}$ (%)	T (°C)	$\frac{T_{0,rad}}{T_{max}}$ (%)
-119.0	0.3(1)	-9.9	0.4(1)	130.1	1.8(5)	270.6	2.7(7)
-119.0	2.5(6)	-9.6	0.5(1)	130.7	2.2(5)	279.9	3.8(9)
-118.9	0.1(0)	-9.1	0.9(2)	139.8	2.3(6)	280.1	3.9(10)
-111.8	0.5(1)	0.1	1.8(4)	140.2	2.3(6)	280.6	2.9(7)
-110.5	1.1(3)	0.4	1.0(2)	140.8	2.6(6)	289.9	3.3(8)
-110.2	1.0(2)	0.9	0.9(2)	149.9	1.9(5)	290.1	4.2(10)
-109.1	0.6(2)	10.1	1.9(5)	150.2	2.8(7)	290.6	4.4(11)
-100.3	1.7(4)	10.1	1.0(2)	150.8	1.7(4)	299.9	4.5(11)
-100.2	0.8(2)	10.4	0.7(2)	159.9	2.4(6)	300.1	3.8(9)
-99.6	1.3(3)	19.9	0.7(2)	160.2	1.1(3)	300.6	4.5(11)
-99.6	0.6(2)	20.2	1.8(4)	160.8	2.0(5)	309.9	4.4(11)
-99.4	0.9(2)	20.8	0.9(2)	169.8	2.7(7)	310.1	4.8(12)
-98.4	0.6(2)	29.6	1.2(3)	170.1	2.0(5)	310.7	4.9(12)
-91.9	1.6(4)	29.7	0.8(2)	170.7	1.4(3)	319.9	4.3(11)
-91.2	0.6(2)	30.2	1.7(4)	179.9	2.0(5)	320.1	4.2(10)
-90.5	0.6(2)	39.2	1.2(3)	180.2	2.1(5)	320.7	4.2(10)
-90.2	0.2(1)	39.9	1.0(3)	180.8	2.7(7)	329.9	4.9(12)
-90.1	0.6(2)	40.3	1.4(4)	189.9	2.8(7)	330.1	5.1(13)
-89.9	1.6(4)	49.5	0.8(2)	190.2	3.2(8)	330.7	4.8(12)
-81.1	1.8(4)	49.7	1.7(4)	190.8	2.3(6)	339.9	4.8(12)
-80.8	0.2(1)	49.7	1.5(4)	199.9	3.3(8)	340.2	4.4(11)
-80.7	1.2(3)	59.6	1.7(4)	200.1	3.1(8)	340.7	5.1(13)
-80.5	1.0(3)	59.7	1.3(3)	200.6	2.4(6)	350.0	5.3(13)
-80.0	1.5(4)	60.0	2.8(7)	209.9	2.3(6)	350.2	6.4(16)
-80.0	0.9(2)	69.7	1.7(4)	210.1	2.9(7)	350.7	5.4(13)
-79.9	0.3(1)	69.8	1.4(4)	210.6	3.4(9)	360.0	4.8(12)
-70.3	1.4(4)	70.2	1.1(3)	219.9	3.1(8)	360.2	6.5(16)
-69.8	0.5(1)	79.7	1.1(3)	220.1	2.5(6)	360.8	4.5(11)
-59.8	0.7(2)	79.8	0.9(2)	220.6	3.0(7)	369.9	6.8(17)
-59.6	0.4(1)	80.3	1.2(3)	229.9	2.7(7)	370.1	5.9(15)
-59.5	0.4(1)	89.7	1.3(3)	230.0	2.9(7)	370.7	5.3(13)
-49.9	0.4(1)	89.9	2.4(6)	230.5	3.3(8)	380.2	6.7(17)
-49.6	0.9(2)	90.4	2.1(5)	239.9	3.6(9)	380.6	7.4(19)
-49.5	0.4(1)	99.7	1.9(5)	240.1	2.9(7)	380.8	5.9(15)
-39.9	0.7(2)	99.9	1.8(4)	240.6	3.3(8)	390.0	6.7(17)
-39.6	0.7(2)	100.4	1.2(3)	249.9	3.9(10)	390.2	7.6(19)
-39.5	0.5(1)	110.4	1.6(4)	250.1	3.1(8)	390.8	7.7(19)
-29.7	1.1(3)	110.8	2.4(6)	250.6	3.7(9)	400.0	7.5(19)
-29.4	0.6(1)	110.8	2.2(5)	259.9	4.1(10)	400.2	7.2(18)
-29.3	0.4(1)	119.8	2.0(5)	260.0	3.7(9)	400.8	8.0(20)
-19.6	0.4(1)	120.1	2.8(7)	260.5	3.9(10)		
-19.3	0.2(1)	120.8	1.6(4)	269.9	4.0(10)		
-19.1	1.2(3)	129.8	2.1(5)	270.1	3.8(9)		

Table A.6: $HT_{1[001]}$ ratio of direct radiative heat transfer $T_{0,rad}$ to theoretical adiabatic maximum temperature T_{max}

T (°C)	$\frac{T_{0,rad}}{T_{max}}$ (%)	T (°C)	$\frac{T_{0,rad}}{T_{max}}$ (%)	T (°C)	$\frac{T_{0,rad}}{T_{max}}$ (%)	T (°C)	$\frac{T_{0,rad}}{T_{max}}$ (%)
25.8	1.5(4)	474.8	6.3(16)	553.8	13.9(35)	589.7	1.8(5)
25.9	1.0(3)	479.6	6.3(16)	555.2	15.2(38)	589.8	1.3(3)
25.9	0.0(2)	479.8	6.1(15)	555.7	14.2(35)	594.4	1.4(4)
49.6	5.6(14)	479.8	6.1(15)	555.7	14.9(37)	594.8	1.2(3)
49.9	3.4(8)	484.6	6.4(16)	557.2	15.8(40)	594.8	1.2(3)
50.8	0.7(2)	484.8	6.4(16)	557.7	15.2(38)	599.4	1.3(3)
99.4	0.4(1)	484.8	6.3(16)	557.8	15.3(38)	599.8	1.4(3)
99.6	3.3(8)	489.7	7.1(18)	559.2	16.9(42)	599.8	1.4(3)
99.8	2.1(5)	489.8	6.8(17)	559.7	16.2(41)	604.5	1.4(4)
149.6	1.9(5)	489.8	6.9(17)	559.8	16.2(40)	604.8	1.4(3)
149.7	3.2(8)	494.6	7.2(18)	561.2	18.3(46)	604.8	1.4(3)
150.0	2.6(7)	494.8	7.2(18)	561.7	17.1(43)	609.5	1.4(4)
199.8	2.0(5)	494.8	6.7(17)	561.8	17.4(44)	609.8	1.3(3)
199.8	1.9(5)	499.6	7.4(19)	563.2	19.1(48)	609.8	1.3(3)
200.2	1.9(5)	499.8	7.4(18)	563.7	18.9(47)	614.5	1.5(4)
249.8	2.8(7)	499.8	7.4(19)	563.8	18.3(46)	614.8	1.4(4)
249.9	2.0(5)	504.6	7.5(19)	565.2	21.6(54)	614.8	1.4(4)
250.5	2.3(6)	504.8	7.6(19)	565.7	21.0(53)	619.5	1.5(4)
299.9	2.8(7)	504.8	7.7(19)	565.8	20.4(51)	619.8	1.4(4)
300.0	2.9(7)	509.5	8.3(21)	567.2	24.9(62)	619.8	1.5(4)
300.7	2.8(7)	509.7	8.1(20)	567.7	24.5(61)	624.5	1.4(3)
324.9	3.0(8)	509.8	8.2(20)	567.8	24.6(62)	624.8	1.4(3)
325.1	2.9(7)	514.6	8.5(21)	569.2	29.2(73)	624.8	1.5(4)
325.8	3.0(7)	514.8	8.4(21)	569.7	29.2(73)	629.7	1.7(4)
349.9	3.1(8)	514.8	8.4(21)	569.8	29.3(73)	629.8	1.5(4)
350.2	3.2(8)	519.6	8.9(22)	571.2	36.8(92)	629.8	1.6(4)
350.8	3.2(8)	519.8	9.0(23)	571.7	37.8(94)	634.6	1.6(4)
375.0	3.6(9)	519.8	8.8(22)	571.8	38.8(97)	634.8	1.7(4)
375.4	3.6(9)	524.6	9.2(23)	573.5	47.9(120)	634.8	1.7(4)
376.0	3.6(9)	524.8	9.1(23)	573.7	102.5(256)	639.6	2.2(5)
400.0	4.0(10)	524.8	9.0(23)	573.8	136.9(342)	639.8	1.7(4)
400.3	3.9(10)	529.7	9.8(25)	575.3	142.1(355)	639.8	2.7(7)
400.9	4.0(10)	529.8	9.6(24)	575.8	58.1(145)	644.5	2.1(5)
424.8	4.6(11)	529.8	9.9(25)	575.8	63.9(160)	644.8	2.9(7)
425.1	4.4(11)	534.2	10.3(26)	577.3	14.4(36)	644.8	2.9(7)
425.5	4.7(12)	534.8	10.6(27)	577.7	11.2(28)	649.6	3.1(8)
449.9	5.1(13)	534.8	10.2(26)	577.8	10.9(27)	649.8	5.3(13)
450.1	5.3(13)	539.2	11.4(29)	579.2	5.6(14)	649.8	4.3(11)
450.5	5.1(13)	539.8	10.9(27)	579.7	4.7(12)	675.0	5.4(14)
454.6	5.4(13)	539.8	11.2(28)	579.8	5.0(13)	675.2	4.4(11)
454.8	5.0(13)	544.3	12.4(31)	581.2	3.8(9)	675.2	4.9(12)
454.8	5.5(14)	544.8	12.0(30)	581.7	4.6(12)	700.0	9.7(24)
459.6	5.5(14)	544.8	11.8(29)	581.8	4.5(11)	700.2	10.1(25)
459.8	5.7(14)	549.3	13.3(33)	583.3	3.1(8)	700.2	10.4(26)
459.8	5.6(14)	549.8	12.5(31)	583.7	2.7(7)	725.0	18.3(46)
464.6	5.8(14)	549.8	12.7(32)	583.8	2.9(7)	725.2	29.6(74)
464.8	5.6(14)	549.8	12.7(32)	585.3	2.3(6)	725.3	19.6(49)
464.8	5.9(15)	549.9	13.3(33)	585.7	2.2(6)	749.9	50.1(125)
469.6	5.8(14)	551.2	14.0(35)	585.8	2.0(5)	750.2	92.3(231)
469.8	5.9(15)	551.7	13.3(33)	587.3	1.8(5)	750.2	88.7(222)
469.8	5.7(14)	551.8	13.4(34)	587.7	1.9(5)	775.0	105.9(265)
474.6	5.9(15)	553.2	14.7(37)	587.8	1.6(4)	775.1	227.6(569)
474.8	5.8(14)	553.7	13.9(35)	589.3	1.7(4)	775.3	190.1(475)

Table A.7: HT₂_[001] ratio of direct radiative heat transfer $T_{0,rad}$ to theoretical adiabatic maximum temperature T_{max}

T (°C)	$\frac{T_{0,rad}}{T_{max}}$ (%)	T (°C)	$\frac{T_{0,rad}}{T_{max}}$ (%)	T (°C)	$\frac{T_{0,rad}}{T_{max}}$ (%)	T (°C)	$\frac{T_{0,rad}}{T_{max}}$ (%)
25.5	2.5(6)	469.8	6.1(15)	551.7	17.1(43)	585.3	8.5(21)
25.6	0.8(2)	474.5	6.6(17)	551.7	17.6(44)	585.7	7.2(18)
25.6	1.3(3)	474.7	6.9(17)	553.3	18.5(46)	585.7	9.1(23)
50.1	0.5(1)	474.8	6.9(17)	553.7	18.8(47)	587.3	9.6(24)
50.8	1.6(4)	479.5	7.2(18)	553.7	18.7(47)	587.7	9.7(24)
50.8	2.7(7)	479.8	7.0(17)	555.3	20.1(50)	587.7	9.4(24)
99.5	0.8(2)	479.8	7.4(18)	555.7	20.0(50)	589.3	11.1(28)
99.7	4.4(11)	484.5	7.0(18)	555.8	20.2(51)	589.6	10.6(26)
99.9	5.3(13)	484.7	7.1(18)	557.3	20.5(51)	589.7	9.6(24)
149.7	1.1(3)	484.8	7.3(18)	557.7	21.1(53)	594.4	12.0(30)
149.7	1.1(3)	489.5	7.6(19)	557.7	20.8(52)	594.7	13.9(35)
150.2	6.6(17)	489.7	7.6(19)	559.4	-3.9(-10)	594.8	14.4(36)
199.8	1.8(5)	489.8	7.7(19)	559.7	23.2(58)	599.5	14.8(37)
199.8	1.5(4)	494.5	8.2(20)	559.8	22.9(57)	599.7	16.7(42)
200.3	0.8(2)	494.7	7.9(20)	561.3	24.2(61)	599.8	13.7(34)
249.8	1.7(4)	494.8	8.1(20)	561.7	25.0(63)	604.4	21.6(54)
249.9	2.1(5)	499.5	8.4(21)	561.8	24.9(62)	604.7	19.1(48)
250.2	2.3(6)	499.7	8.1(20)	563.4	27.8(69)	604.8	19.9(50)
299.9	2.3(6)	499.8	8.5(21)	563.7	28.2(70)	609.5	22.3(56)
300.1	2.2(6)	504.5	8.2(20)	563.7	27.9(70)	609.7	30.4(76)
300.8	2.2(5)	504.7	8.0(20)	565.3	30.2(75)	609.7	32.3(81)
324.9	2.4(6)	504.8	8.5(21)	565.7	31.6(79)	614.6	32.7(82)
325.3	2.5(6)	509.5	8.1(20)	565.7	30.8(77)	614.7	33.1(83)
325.8	2.8(7)	509.7	8.7(22)	567.3	34.0(85)	614.8	30.2(76)
350.0	3.0(7)	509.8	8.8(22)	567.7	35.4(88)	619.5	35.6(89)
350.3	2.8(7)	514.5	9.1(23)	567.7	35.1(88)	619.8	41.8(104)
350.9	2.8(7)	514.7	9.6(24)	569.3	39.8(99)	619.8	47.7(119)
375.0	3.4(8)	514.8	9.0(23)	569.7	41.6(104)	624.5	51.7(129)
375.2	3.4(9)	519.5	10.0(25)	569.7	41.8(105)	624.7	53.4(134)
375.7	3.7(9)	519.7	10.1(25)	571.5	48.6(122)	624.8	55.5(139)
400.0	4.0(10)	519.7	10.2(25)	571.7	52.1(130)	629.5	73.9(185)
400.2	4.0(10)	524.5	10.3(26)	571.8	54.1(135)	629.7	77.0(193)
400.6	3.9(10)	524.7	11.0(27)	573.3	121.1(303)	629.8	81.9(205)
424.9	4.6(12)	524.8	11.4(29)	573.7	361.4(903)	634.4	99.9(250)
425.2	4.9(12)	529.5	11.6(29)	573.8	967.1(2418)	634.7	100.5(251)
425.5	4.8(12)	529.7	11.9(30)	575.6	21.8(54)	634.8	114.6(287)
449.9	5.1(13)	529.8	12.2(31)	575.7	20.1(50)	639.6	161.9(405)
450.1	5.5(14)	534.5	12.7(32)	575.8	18.6(47)	639.8	169.4(424)
450.5	5.2(13)	534.7	13.0(32)	577.3	10.2(25)	639.8	184.6(461)
454.5	5.4(13)	534.7	13.1(33)	577.7	9.3(23)	644.7	228.4(571)
454.8	5.3(13)	539.5	13.8(34)	577.7	9.9(25)	644.8	259.1(648)
454.8	5.3(13)	539.7	13.6(34)	579.3	7.3(18)	644.8	251.6(629)
459.5	6.0(15)	539.8	13.8(35)	579.7	8.3(21)	649.7	286.5(716)
459.8	6.0(15)	544.5	15.2(38)	579.7	8.8(22)	649.8	270.0(675)
459.8	5.8(14)	544.7	15.3(38)	581.3	8.3(21)	649.8	293.2(733)
464.5	6.2(15)	544.8	15.3(38)	581.7	6.9(17)	674.8	376.9(942)
464.8	6.0(15)	549.5	16.9(42)	581.8	6.4(16)	674.9	355.5(889)
464.8	5.6(14)	549.7	16.4(41)	583.3	8.5(21)	675.0	333.5(834)
469.5	6.4(16)	549.8	17.2(43)	583.7	8.3(21)		
469.8	6.3(16)	551.4	17.2(43)	583.7	6.3(16)		

Table A.8: $HT_{1[100]}$ ratio of direct radiative heat transfer $T_{0,rad}$ to theoretical adiabatic maximum temperature T_{max}

T (°C)	$\frac{T_{0,rad}}{T_{max}}$ (%)	T (°C)	$\frac{T_{0,rad}}{T_{max}}$ (%)	T (°C)	$\frac{T_{0,rad}}{T_{max}}$ (%)	T (°C)	$\frac{T_{0,rad}}{T_{max}}$ (%)
25.9	0.6(1)	479.8	5.4(13)	557.8	15.6(39)	599.8	2.1(5)
25.9	5.3(13)	479.9	5.5(14)	557.9	15.8(39)	599.9	2.8(7)
26.0	3.7(9)	480.2	5.4(13)	558.3	16.1(40)	600.3	2.6(7)
49.7	0.4(1)	484.8	6.4(16)	559.8	16.7(42)	604.8	2.2(5)
49.9	4.0(10)	484.9	5.7(14)	559.9	16.7(42)	604.9	2.1(5)
50.5	2.9(7)	485.2	6.6(17)	560.3	17.2(43)	605.3	2.2(6)
99.6	4.3(11)	489.8	5.8(14)	561.8	18.0(45)	609.8	2.5(6)
99.6	3.5(9)	490.0	5.9(15)	561.9	18.0(45)	609.9	2.2(6)
100.2	3.2(8)	490.6	6.1(15)	562.3	18.6(46)	610.2	2.7(7)
149.6	1.7(4)	494.9	6.4(16)	563.8	19.1(48)	614.8	2.7(7)
149.7	1.6(4)	495.0	6.3(16)	563.9	19.1(48)	614.9	2.7(7)
150.0	1.5(4)	495.7	6.2(15)	564.3	19.7(49)	615.2	2.4(6)
199.7	1.7(4)	499.8	6.4(16)	565.8	20.8(52)	619.8	2.2(6)
199.8	1.6(4)	500.0	6.5(16)	565.9	20.9(52)	619.9	2.7(7)
200.0	2.1(5)	500.6	6.8(17)	566.3	21.6(54)	620.2	2.4(6)
249.8	4.6(12)	505.0	6.8(17)	567.8	22.9(57)	624.9	2.8(7)
249.8	1.7(4)	505.0	6.8(17)	567.9	23.3(58)	624.9	3.1(8)
250.1	2.0(5)	505.6	7.2(18)	568.3	23.8(59)	625.2	3.5(9)
299.8	2.2(5)	509.8	7.0(17)	569.8	25.3(63)	629.8	3.1(8)
299.8	1.9(5)	510.0	7.2(18)	569.9	25.2(63)	629.9	3.2(8)
300.1	2.0(5)	510.6	7.2(18)	570.3	26.1(65)	630.1	3.0(7)
324.8	2.2(5)	514.8	7.6(19)	571.8	29.1(73)	634.8	3.7(9)
324.9	2.5(6)	514.9	7.4(19)	571.9	29.3(73)	634.9	3.0(7)
325.2	2.3(6)	515.4	7.6(19)	572.2	31.5(79)	635.1	3.4(9)
349.8	2.3(6)	519.8	8.0(20)	573.8	42.1(105)	639.8	3.5(9)
349.9	2.5(6)	519.9	8.1(20)	573.9	39.2(98)	639.9	4.0(10)
350.2	2.5(6)	520.5	8.1(20)	574.3	42.3(106)	640.1	3.3(8)
374.8	2.8(7)	524.8	8.5(21)	575.8	52.9(132)	644.8	4.0(10)
374.9	2.7(7)	524.9	8.6(21)	575.9	53.7(134)	644.9	4.1(10)
375.3	3.6(9)	525.4	8.6(21)	576.4	139.6(349)	645.2	4.2(10)
399.8	3.1(8)	529.8	9.3(23)	577.8	105.9(265)	649.8	4.8(12)
399.9	9.8(25)	530.0	9.1(23)	577.9	111.1(278)	649.9	4.5(11)
400.3	3.1(8)	530.5	9.3(23)	578.3	70.0(175)	650.2	5.3(13)
424.8	4.4(11)	534.8	10.0(25)	579.8	23.8(60)	674.9	6.7(17)
424.9	3.7(9)	534.9	10.0(25)	579.9	22.5(56)	674.9	7.7(19)
425.3	3.8(9)	535.5	10.4(26)	580.2	16.5(41)	675.1	6.3(16)
449.9	4.5(11)	539.8	10.7(27)	581.8	6.3(16)	699.8	13.8(34)
449.9	4.8(12)	539.9	10.6(27)	581.9	6.5(16)	699.9	13.2(33)
450.3	5.2(13)	540.4	10.7(27)	582.2	5.0(13)	700.1	10.8(27)
454.8	4.6(12)	544.8	11.5(29)	583.8	3.8(10)	724.8	36.7(92)
454.9	4.5(11)	544.9	11.7(29)	583.9	3.7(9)	724.8	39.6(99)
455.3	5.4(13)	545.3	11.7(29)	584.3	3.3(8)	725.0	30.9(77)
459.8	4.7(12)	549.8	12.8(32)	585.8	3.2(8)	749.8	122.2(306)
459.9	4.7(12)	549.9	12.9(32)	585.9	3.4(8)	749.8	143.2(358)
460.3	4.8(12)	550.4	12.9(32)	586.3	2.8(7)	749.9	106.1(265)
464.8	4.8(12)	551.8	13.6(34)	587.8	2.6(7)	774.8	302.8(757)
464.9	4.9(12)	551.9	14.1(35)	587.9	3.2(8)	774.8	351.0(877)
465.2	4.9(12)	552.4	13.6(34)	588.3	3.0(7)	774.9	282.1(705)
469.8	5.4(13)	553.8	14.1(35)	589.8	2.4(6)	799.8	594.9(1487)
469.9	5.6(14)	553.9	14.3(36)	589.9	2.8(7)	799.8	660.7(1652)
470.2	5.1(13)	554.4	14.4(36)	590.3	2.2(6)	799.8	752.5(1881)
474.8	5.1(13)	555.8	14.8(37)	594.8	2.4(6)		
474.9	5.2(13)	556.0	15.7(39)	594.9	2.3(6)		
475.2	5.0(12)	556.4	15.1(38)	595.3	2.2(6)		

Table A.9: HT₂_[100] ratio of direct radiative heat transfer $T_{0,rad}$ to theoretical adiabatic maximum temperature T_{max}

T (°C)	$\frac{T_{0,rad}}{T_{max}}$ (%)	T (°C)	$\frac{T_{0,rad}}{T_{max}}$ (%)	T (°C)	$\frac{T_{0,rad}}{T_{max}}$ (%)	T (°C)	$\frac{T_{0,rad}}{T_{max}}$ (%)
25.3	0.0(4)	469.9	4.7(12)	550.3	12.7(32)	583.8	11.3(28)
25.4	1.3(3)	470.3	4.7(12)	551.9	13.3(33)	584.0	9.1(23)
25.4	1.9(5)	474.8	5.0(12)	552.0	13.3(33)	584.3	9.5(24)
49.6	0.2(1)	474.9	4.7(12)	552.3	13.7(34)	585.9	10.2(25)
49.9	0.2(1)	475.3	5.0(12)	553.8	14.1(35)	585.9	10.1(25)
50.9	0.5(1)	479.8	5.3(13)	554.0	14.4(36)	586.3	9.1(23)
99.5	1.9(5)	479.9	5.2(13)	554.3	14.1(35)	587.9	10.8(27)
99.6	1.0(2)	480.3	5.1(13)	555.9	14.8(37)	588.0	13.0(33)
99.9	4.3(11)	484.8	5.5(14)	556.0	14.9(37)	588.3	11.0(28)
149.5	0.0(0)	484.9	5.4(13)	556.3	15.2(38)	589.9	13.0(33)
149.7	0.5(1)	485.3	5.6(14)	557.8	15.2(38)	590.0	13.6(34)
149.9	1.2(3)	489.8	5.5(14)	557.9	15.9(40)	590.3	12.9(32)
199.7	0.9(2)	489.9	5.5(14)	558.2	15.7(39)	594.8	16.7(42)
199.7	0.3(1)	490.3	5.9(15)	559.8	16.4(41)	595.0	17.0(43)
199.8	0.9(2)	494.8	6.0(15)	560.0	16.7(42)	595.3	15.6(39)
249.7	0.0(0)	494.9	5.8(15)	560.3	16.9(42)	599.8	18.4(46)
249.8	0.0(1)	495.3	6.0(15)	561.8	17.6(44)	600.0	18.2(46)
249.9	0.0(1)	499.8	6.3(16)	562.0	18.4(46)	600.3	17.9(45)
299.8	1.6(4)	499.9	6.1(15)	562.3	18.5(46)	604.9	24.5(61)
299.8	0.0(2)	500.3	6.1(15)	563.8	18.8(47)	605.0	27.4(69)
300.2	0.0(10)	504.8	6.5(16)	563.9	19.0(48)	605.3	24.6(62)
324.8	2.0(5)	504.9	6.9(17)	564.2	19.6(49)	609.9	29.4(74)
324.9	2.0(5)	505.3	6.6(16)	565.8	20.8(52)	609.9	32.3(81)
325.2	1.9(5)	509.8	6.7(17)	566.0	21.0(53)	610.3	30.1(75)
349.8	2.3(6)	509.9	6.9(17)	566.3	21.3(53)	614.8	42.6(106)
349.9	1.9(5)	510.3	6.7(17)	567.8	22.3(56)	614.9	38.0(95)
350.3	2.2(5)	514.8	7.7(19)	568.0	22.5(56)	615.3	43.3(108)
374.8	2.5(6)	514.9	7.1(18)	568.3	22.6(57)	619.8	55.2(138)
374.9	2.5(6)	515.3	7.2(18)	569.8	25.5(64)	619.9	48.8(122)
375.3	2.7(7)	519.8	8.1(20)	569.8	24.9(62)	620.2	46.8(117)
399.8	3.1(8)	519.9	7.8(19)	570.3	26.0(65)	624.8	60.0(150)
399.9	2.9(7)	520.4	8.0(20)	571.8	29.2(73)	624.9	70.0(175)
400.3	2.9(7)	524.8	8.5(21)	571.9	28.5(71)	625.2	54.9(137)
424.8	3.4(8)	524.9	8.7(22)	572.3	29.3(73)	629.8	76.2(191)
425.0	3.3(8)	525.3	8.3(21)	573.8	61.2(153)	630.0	74.2(186)
425.4	3.6(9)	529.9	9.0(23)	573.9	60.8(152)	630.3	69.8(174)
449.9	3.9(10)	530.0	9.0(23)	574.2	60.8(152)	634.9	96.9(242)
450.0	3.9(10)	530.3	8.9(22)	575.8	70.3(176)	634.9	109(273)
450.3	3.9(10)	534.9	9.6(24)	575.9	71.7(179)	635.3	89.6(224)
454.8	5.8(14)	535.0	9.7(24)	576.1	76.9(192)	639.8	135.3(338)
454.9	4.3(11)	535.2	9.8(24)	577.8	132.0(330)	639.9	122.0(305)
455.3	4.0(10)	539.8	10.8(27)	577.9	175.1(438)	640.2	126.2(315)
459.8	5.1(13)	539.9	10.5(26)	578.3	415.2(1038)	644.8	166.3(416)
459.9	4.8(12)	540.3	10.1(25)	579.8	73.8(184)	644.9	165.8(414)
460.3	4.2(10)	544.9	12.0(30)	579.9	64.1(160)	645.2	152.1(380)
464.8	4.3(11)	544.9	11.4(29)	580.2	45.7(114)	649.8	214.9(537)
464.9	4.7(12)	545.3	11.5(29)	581.8	14.3(36)	649.9	208.4(521)
465.3	4.4(11)	549.8	13.1(33)	581.9	12.5(31)	650.2	215.4(538)
469.8	4.6(12)	549.9	12.9(32)	582.3	11.2(28)		

A.2 APPENDIX TO CHAPTER 4

Table A.10: Thermal diffusivities D of synthetic single crystal portlandite in [100] (axial plane) and [001] (basal plane) direction measured by laser flash method. The data are the averages of five basal and six axial specimens with at least three independent measurements per temperature step and specimen. Data between $-100\text{ }^{\circ}\text{C}$ and $100\text{ }^{\circ}\text{C}$ were measured by low T HgCdTe (MCT) IR detector, between $25\text{ }^{\circ}\text{C}$ and $700\text{ }^{\circ}\text{C}$ by high T setup with the InSb IR detector

T ($^{\circ}\text{C}$)	$D_{[100]}$ ($= D_{11}, D_{22}$) (mm^2/s)	T ($^{\circ}\text{C}$)	$D_{[001]}$ ($= D_{33}$) (mm^2/s)
-100.6	13.4(12)	-100.5	1.37(5)
-80.0	11.6(10)	-80.2	1.25(4)
-59.8	10.1(5)	-60.0	1.13(4)
-39.6	9.0(3)	-40.0	1.03(3)
-19.6	7.9(3)	-19.9	0.94(3)
0.3	7.0(2)	0.2	0.85(3)
25.0	6.1(2) ^a	25.1	0.75(2) ^a
25.1	6.1(2)	25.1	0.72(2)
50.0	5.4(2) ^a	49.7	0.67(1) ^a
49.0	5.3(1)	50.1	0.64(1)
75.0	4.81(12) ^a	75.0	0.60(1) ^a
99.8	4.34(9)	100.0	0.52(1)
100.1	4.36(11) ^a	100.1	0.54(1) ^a
149.9	3.64(7)	150.2	0.44(1)
199.9	3.11(6)	200.3	0.37(1)
250.1	2.71(7)	250.4	0.32(1)
300.4	2.39(8)	300.4	0.28(1)
325.4	2.26(8)	320.5	0.27(1)
350.5	2.14(8)	350.5	0.25(1)
375.5	2.04(8)	375.6	0.24(1)
400.4	1.96(10)	400.6	0.23(1)
425.4	1.86(11)	425.5	0.22(1)
437.3	1.65(15)	437.3	0.22(1)
450.3	1.37(13)	450.3	0.21(1)
462.3	1.24(8)	462.1	0.21(1)
475.3	1.25(7)	475.3	0.20(1)
487.3	1.30(7)	487.2	0.18(1)
500.3	1.30(6)	500.3	0.15(1)
512.2	1.31(5)	512.2	0.14(1)
525.3	1.31(5)	525.2	0.14(1)
537.2	1.32(4)	537.2	0.15(1)
550.2	1.32(5)	550.2	0.14(1)
575.4	1.32(6)	575.3	0.15(1)
600.4	1.32(8)	600.3	0.15(1)
650.4	1.34(11)	650.3	0.15(1)
700.3	1.39(9)	700.2	0.17(1)

^a thermal diffusivity values measured by HgCdTe (MCT) IR detector in the overlapping T region between $25\text{ }^{\circ}\text{C}$ and $100\text{ }^{\circ}\text{C}$

Table A.11: Thermal conductivity tensor κ_{ij} for single crystal portlandite derived using Eq. 4.5 in [100] ($=\kappa_{11}=\kappa_{22}$) and in perpendicular c -axis direction [001] ($=\kappa_{33}$)

T (°C)	κ_{11} (W/mK)	κ_{33} (W/mK)	ρ (g/cm ³)	c_p (J/kg K)
-100.6	24.9(23)	2.55(10)	2.261	823
-80.1	23.6(21)	2.55(9)	2.257	901
-59.9	22.0(12)	2.47(10)	2.254	969
-39.8	20.8(9)	2.38(8)	2.250	1030
-19.8	19.2(8)	2.28(9)	2.247	1081
0.2	17.8(7)	2.15(8)	2.243	1128
25.1	16.1(6)	1.94(6)	2.239	1178
49.9	14.6(5)	1.78(5)	2.235	1221
75.0	13.5(4)	1.68(4)	2.231	1258
100.0	12.5(4)	1.53(4)	2.226	1290
150.0	10.8(3)	1.30(3)	2.218	1343
200.1	9.5(3)	1.14(3)	2.210	1382
250.3	8.4(3)	0.98(3)	2.201	1413
300.4	7.5(3)	0.89(3)	2.193	1438
322.9	7.2(3)	0.85(3)	2.189	1447
350.5	6.8(3)	0.80(3)	2.185	1459
375.6	6.5(3)	0.76(3)	2.181	1467
400.5	6.3(3)	0.73(3)	2.176	1476

The temperature-dependent densities ρ are approximated on the basis of the density measured by XRD at 20 °C ($\rho = 2.240(2)$ g/cm³, see chapter 4, section 4.2.1) using linear thermal expansion coefficients α_L for portlandite given by Xu et al. (2007) extrapolated for the given temperature range between -100 °C and 400 °C: a_1 -axis $\alpha_{L,a} = 1.1759 \times 10^{-5}$ K⁻¹ and c -axis $\alpha_{L,c} = 5.2548 \times 10^{-5}$ K⁻¹.

Listed isobaric heat capacities c_p for portlandite are taken from Chase (1998) (based on Kobayashi 1950 (cited by Chase 1998) and Hatton et al. 1959, 1 σ assumed as 2 %) and $M_{\text{Ca}(\text{OH})_2} = 74.093$ g/mol was used for calculations.

BACK MATTER

BIBLIOGRAPHY

- Abdulagatov, I. M., Abdulagatova, Z. Z., Kallaev, S. N., Bakmaev, A. G., & Ranjith, P. G. (2015). Thermal-Diffusivity and Heat-Capacity Measurements of Sandstone at High Temperatures Using Laser Flash and DSC Methods. *International Journal of Thermophysics*, 35. doi:10.1007/s10765-014-1829-4
- Aïtcin, P.-C. (2016). Portland Cement. In P.-C. Aïtcin & R. J. Flatt (Eds.), *Science and Technology of Concrete Admixtures* (pp. 27–51). Woodhead Publishing.
- Akaogi, M., Yusa, H., Shiraishi, K., & Suzuki, T. (1995). Thermodynamic Properties of α -Quartz, Coesite, and Stishovite and Equilibrium Phase Relations at High Pressures and High Temperatures. *Journal of Geophysical Research: Solid Earth*, 100(B11), 22337–22347. doi:10.1029/95JB02395
- Akoshima, M., Abe, H., & Baba, T. (2015). Development of Reference Materials for Thermal-Diffusivity Measurements by the Flash Method. *International Journal of Thermophysics*, 36(12), 3272–3287. doi:10.1007/s10765-015-1996-y
- Akoshima, M., & Baba, T. (2005). Thermal Diffusivity Measurements of Candidate Reference Materials by the Laser Flash Method. *International Journal of Thermophysics*, 26(1), 151–163. doi:10.1007/s10765-005-2361-3
- Akoshima, M., & Baba, T. (2006). Study on a Thermal-Diffusivity Standard for Laser Flash Method Measurements. *International Journal of Thermophysics*, 27(4), 1189–1203. doi:10.1007/s10765-006-0091-9
- Akoshima, M., Hay, B., Neda, M., & Grelard, M. (2013a). Experimental Verification to Obtain Intrinsic Thermal Diffusivity by Laser-Flash Method. *International Journal of Thermophysics*, 34(5), 778–791. doi:10.1007/s10765-013-1470-7
- Akoshima, M., Neda, M., & Baba, T. (2013b). Quantitative Evaluation of the Effect of Black-Coating for Laser Flash Measurement. In L. I. Kiss, I. T. C. Conference, & I. T. E. Symposium (Eds.), *Thermal conductivity 31, thermal expansion 19: Proceedings of the thirty-first International Thermal Conductivity Conference; proceedings of the Nineteenth International Thermal Expansion Symposium*. Lancaster: DEStech Publications.
- Albers, A. P., Restivo, T., Pagano, L., & Baldo, J. (2001). Effect of Testing Conditions on the Laser Flash Thermal Diffusivity Measurements of Ceramics. *Thermochimica Acta*, 370, 111–118.
- Andre, S., & Degiovanni, A. (1995). A Theoretical Study of the Transient Coupled Conduction and Radiation Heat Transfer in Glass: Phonic Diffusivity Measurements by the Flash Technique. *In-*

- International Journal of Heat and Mass Transfer*, 38(18), 3401–3412. doi:10.1016/0017-9310(95)00075-K
- Angell, M. F. (1911). Thermal Conductivity at High Temperatures. *Physical Review (Series I)*, 33(5), 421–432. doi:10.1103/PhysRevSeriesI.33.421
- Ångström, A. J. (1861). Neue Methode, das Wärmeleitungsvermögen der Körper zu bestimmen. *Annalen der Physik*, 114, 513–530. doi:10.1002/andp.18621901202
- Araki, N., Makino, A., & Mihara, J. (1992). Measurement and Evaluation of the Thermal Diffusivity of Two-Layered Materials. *International Journal of Thermophysics*, 13(2), 331–349. doi:10.1007/BF00504441
- Ashton, F. W., & Wilson, R. (1927). The Preparation and Optical Properties of Calcium Hydroxide Crystals. *American Journal of Science, Series 5, Vol. 13*(75), 209–218. doi:10.2475/ajs.s5-13.75.209
- ASTM E1461. (2013). *Standard Test Method for Thermal Diffusivity by the Flash Method*. ASTM International. doi:10.1520/E1461-13
- Azumi, T., & Takahashi, Y. (1981). Novel Finite Pulse-Width Correction in Flash Thermal Diffusivity Measurement. *Review of Scientific Instruments*, 52(9), 1411–1413. doi:10.1063/1.1136793
- Baba, T., & Cezairliyan, A. (1994). Thermal Diffusivity of POCO AXM-5Q1 Graphite in the Range 1500 to 2500 K Measured by a Laser-Pulse Technique. *International Journal of Thermophysics*, 15(2), 343–364. doi:10.1007/BF01441590
- Baba, T., Kobayashi, M., Ono, A., Hong, J. H., & Suliyanti, M. M. (1993). Experimental Investigation of the Nonuniform Heating Effect in Laser Flash Thermal Diffusivity Measurements. *Thermochimica Acta*, 218, 329–339. doi:10.1016/0040-6031(93)80433-B
- Baba, T., & Ono, A. (2001). Improvement of the Laser Flash Method to Reduce Uncertainty in Thermal Diffusivity Measurements. *Measurement Science and Technology*, 12(12), 2046–2057. doi:10.1088/0957-0233/12/12/304
- Bachheimer, J. P. (1980). An Anomaly in the β Phase Near the α - β Transition of Quartz. *Journal de Physique Lettres*, 41(23), 559–561. doi:10.1051/jphyslet:019800041023055900
- Baehr, H. D., & Kabelac, S. (2016). *Thermodynamik* (16th). Berlin, Heidelberg: Springer.
- Beck, A. E., Darbha, D. M., & Schloessin, H. H. (1978). Lattice Conductivities of Single-Crystal and Polycrystalline Materials at Mantle Pressures and Temperatures. *Physics of the Earth and Planetary Interiors*, 17(1), 35–53. doi:10.1016/0031-9201(78)90008-0
- Berman, R. B. (1976). *Thermal Conduction in Solids*. Oxford: Clarendon Press.
- Berman, R. G., & Brown, T. H. (1985). Heat Capacity of Minerals in the System Na₂O-K₂O-CaO-MgO-FeO-Fe₂O₃-A₂O₃-SiO₂-TiO₂-H₂O-CO₂: Representation, Estimation, and High Temperature Extrapolation. *Contributions to Mineralogy and Petrology*, 89, 168–183.

- Bigham, J. M., Kost, D. A., Stehouwer, R. C., Beeghly, J. H., Fowler, R., Traina, S. J., Wolfe, W. E., & Dick, W. A. (2005). Mineralogical and Engineering Characteristics of Dry Flue Gas Desulfurization Products. *Fuel*, *84*(14-15), 1839–1848. doi:10.1016/j.fuel.2005.03.018
- Birch, F. (1955). Physics of the Crust. *Geological Society of America*, *62*, 101–118.
- Birchall, J. D., Howard, A. J., & Bailey, J. A. (1978). On the Hydration of Portland Cement. *Proceedings of the Royal Society of London A - Mathematical and Physical Sciences*, *360*(1702), 445–453. doi:10.1098/rspa.1978.0078
- Blakemore, J. S. (1974). *Solid State Physics* (2nd). Philadelphia: Saunders.
- Blumm, J., Lindemann, A., & Niedrig, B. (2003a). Measurement of the Thermophysical Properties of an NPL Thermal Conductivity Standard Inconel 600. *High Temperatures-High Pressures*, *35/36*(6), 621–626. doi:10.1068/htjr145
- Blumm, J., & Opfermann, J. (2002). Improvement of the Mathematical Modeling of Flash Measurements. *High Temperatures-High Pressures*, *34*(5), 515–521. doi:10.1068/htjr061
- Blumm, J., Opfermann, J., & Matsui, T. (2003b). Thermophysical Properties Characterization of Multi-Layer Systems Using the Flash Technique. In *Thermophysical Properties (Proceedings of 24th Japan Symposium on Thermophysical Properties)* (pp. 396–398). Okayama.
- Böer, K. W., & Pohl, U. W. (2018). *Semiconductor Physics*. Cham: Springer International Publishing.
- Bragg, W. L., & Gibbs, R. E. (1925). The Structure of α and β Quartz. *Proceedings of the Royal Society of London*, *109*(751), 405–427. doi:10.1098/rspa.1925.0135
- Branlund, J. M., & Hofmeister, A. M. (2007). Thermal Diffusivity of Quartz to 1,000°C: Effects of Impurities and the α - β Phase Transition. *Physics and Chemistry of Minerals*, *34*(8), 581–595. doi:10.1007/s00269-007-0173-7
- Breuer, S., & Schilling, F. R. (2019). Improving Thermal Diffusivity Measurements by Including Detector Inherent Delayed Response in Laser Flash Method. *International Journal of Thermophysics*, *40*(10), 95. doi:10.1007/s10765-019-2562-9
- Breuer, S., & Schilling, F. R. (2020). Anisotropic Thermal Transport Properties of Quartz: From -120 °C Through the α - β Phase Transition. *European Journal of Mineralogy*, (under review).
- Breuer, S., Schwotzer, M., Speziale, S., & Schilling, F. R. (2020). Thermoelectric Properties of Synthetic Single Crystal Portlandite $\text{Ca}(\text{OH})_2$ - Temperature-Dependent Thermal Diffusivity with Derived Thermal Conductivity and Elastic Constants at Ambient Conditions. *Cement and Concrete Research*, *137*, 106199. doi:10.1016/j.cemconres.2020.106199
- Brillouin, L. (1922). Diffusion de la Lumière et des Rayons X par un Corps Transparent Homogène - Influence de l'Agitation Ther-

- mique. *Annales de Physique*, 9(17), 88–122. doi:10.1051/anphys/192209170088
- Buntebarth, G. (1984). *Geothermics: An Introduction*. Berlin, Heidelberg: Springer-Verlag.
- Cahill, D. G., & Pohl, R. O. (1987). Thermal Conductivity of Amorphous Solids Above the Plateau. *Physical Review B*, 35(8), 4067–4073. doi:10.1103/PhysRevB.35.4067
- Cahill, D. G., Watson, S. K., & Pohl, R. O. (1992). Lower Limit to the Thermal Conductivity of Disordered Crystals. *Physical Review B*, 46(10), 6131–6140. doi:10.1103/PhysRevB.46.6131
- Cape, J. A., & Lehman, G. W. (1963). Temperature and Finite Pulse-Time Effects in the Flash Method for Measuring Thermal Diffusivity. *Journal of Applied Physics*, 34(7), 1909–1913. doi:10.1063/1.1729711
- Carpenter, M. A. (2006). Elastic Properties of Minerals and the Influence of Phase Transitions. *American Mineralogist*, 91(2-3), 229–246. doi:10.2138/am.2006.1979
- Carslaw, H. S., & Jaeger, J. C. (1959). *Conduction of Heat in Solids* (2nd). Oxford: Oxford University Press.
- Casimir, H. B. G. (1938). Note on the Conduction of Heat in Crystals. *Physica*, 5(6), 495–500. doi:10.1016/S0031-8914(38)80162-2
- Čermák, V. (1982). Crustal Temperature and Mantle Heat Flow in Europe. *Tectonophysics*, 83(1), 123–142. doi:10.1016/0040-1951(82)90012-9
- Čermák, V., & Haenel, R. (Eds.). (1982). *Geothermics and Geothermal Energy: Symposium Held During the Joint General Assemblies of EGS and ESC, Budapest, August 1980*. Stuttgart: E. Schweizerbart'sche Verlagsbuchhandlung.
- Cermák, V., & Rybach, L. (1982). Thermal Properties: Thermal Conductivity and Specific Heat of Minerals and Rocks. In G. Angenheister (Ed.), *Landolt-Börnstein Zahlenwerte und Funktionen aus Naturwissenschaften und Technik, Neue Serie, Physikalische Eigenschaften der Gesteine* (Vol. V(1a), pp. 305–343). Berlin, Heidelberg, New York: Springer.
- Cernuschi, F., Lorenzoni, L., Bianchi, P., & Figari, A. (2002). The Effects of Sample Surface Treatments on Laser Flash Thermal Diffusivity Measurement. *Infrared Physics and Technology*, 43(3-5), 133–138. doi:10.1016/S1350-4495(02)00131-7
- Chase, M. W. (Ed.). (1998). *NIST-JANAF Thermochemical Tables* (4th). Woodbury, New York: American Chemical Society, the American Institute of Physics for the National Institute of Standards, and Technology.
- Chen, C.-C., Lin, C.-C., Liu, L.-G., Sinogeikin, S. V., & Bass, J. D. (2001). Elasticity of Single-Crystal Calcite and Rhodochrosite by Brillouin Spectroscopy. *American Mineralogist*, 86(11-12), 1525–1529. doi:10.2138/am-2001-11-1222
- Chen, H., Yue, Z., Ren, D., Zeng, H., Wei, T., Zhao, K., Yang, R., Qiu, P., Chen, L., & Shi, X. (2018). Thermal Conductivity dur-

- ing Phase Transitions. *Advanced Materials*, 1806518. doi:10.1002/adma.201806518
- Chui, G. K., & Gardon, R. (1969). Interaction of Radiation and Conduction in Glass. *Journal of the American Ceramic Society*, 52(10), 548–553. doi:10.1111/j.1151-2916.1969.tb09162.x
- Clark III, L. M., & Taylor, R. E. (1975). Radiation Loss in the Flash Method for Thermal Diffusivity. *Journal of Applied Physics*, 46(2), 714–719. doi:10.1063/1.321635
- Clark, S. P. (1957). Radiative Transfer in the Earth's Mantle. *Transactions, American Geophys. Union*, 38(6), 931. doi:10.1029/TR038i006p00931
- Clauser, C., & Huenges, E. (1995). Thermal Conductivity of Rocks and Minerals. In T. J. Ahrens (Ed.), *Rock Physics and Phase Relations: A Handbook of Physical Constants* (pp. 105–126). American Geophysical Union.
- Clausius, R. (1879). *The Mechanical Theory of Heat*. translated by W. R. Browne. London: Macmillan and Co.
- Cohen, R. E. (1998). Thermal Conductivity of MgO at High Pressures. *The Review of High Pressure Science and Technology*, 7, 160–162. doi:10.4131/jshpreview.7.160
- Cowan, R. D. (1963). Pulse Method of Measuring Thermal Diffusivity at High Temperatures. *Journal of Applied Physics*, 34(4), 926–927. doi:10.1063/1.1729564
- Cui, Y., Xie, J., Liu, J., Wang, J., & Chen, S. (2017). A Review on Phase Change Material Application in Building. *Advances in Mechanical Engineering*, 9(6), 1–15. doi:10.1177/1687814017700828
- Cummins, H. Z., & Schoen, P. E. (1972). Linear Scattering from Thermal Fluctuations. In F. T. Arecchi & E. O. Schultz-Dubois (Eds.), *Laser Handbook* (Vol. 2, pp. 1029–1076). Amsterdam: North-Holland Publishing.
- de Haas, W. J., & Biermasz, T. (1935). The Thermal Conductivity of Quartz at Low Temperatures. *Physica*, 2(1), 673–682. doi:10.1016/S0031-8914(35)90143-4
- Deakin, M. R., & Buttry, D. A. (1989). Electrochemical Applications of the Quartz Crystal Microbalance. *Analytical Chemistry*, 61(20), 1147A–1154A. doi:10.1021/ac00195a001
- Debye, P. (1914). Vortraege Ueber die Kinetische Theorie der Materie und der Elektrizitaet: Zustandsgleichung und Quantenhypothese. Göttingen.
- Dekura, H., & Tsuchiya, T. (2017). Ab initio Lattice Thermal Conductivity of MgO from a Complete Solution of the Linearized Boltzmann Transport Equation. *Physical Review B*, 95(18), 184303. doi:10.1103/PhysRevB.95.184303
- den Toonder, J. M. J., van Dommelen, J. A. W., & Baaijens, F. P. T. (1999). The Relation Between Single Crystal Elasticity and the Effective Elastic Behaviour of Polycrystalline Materials: Theory, Measurement and Computation. *Modelling and Simulation in Ma-*

- terials Science and Engineering*, 7(6), 909–928. doi:10.1088/0965-0393/7/6/301
- Desgranges, L., Calvarin, G., & Chevrier, G. (1996). Interlayer Interactions in $M(\text{OH})_2$: A Neutron Diffraction Study of $\text{Mg}(\text{OH})_2$. *Acta Crystallographica Section B Structural Science*, 52(1), 82–86. doi:10.1107/S0108768195008275
- Desgranges, L., Grebille, D., Calvarin, G., Chevrier, G., Floquet, N., & Niepce, J.-C. (1993). Hydrogen Thermal Motion in Calcium Hydroxide: $\text{Ca}(\text{OH})_2$. *Acta Crystallographica Section B Structural Science*, 49(5), 812–817. doi:10.1107/S0108768193003556
- Desgranges, L., Grebille, D., Calvarin, G., Chhor, K., Pommier, C., Floquet, N., & Niepce, J. C. (1994). Structural and Thermodynamic Evidence of a Change in Thermal Motion of Hydrogen Atoms in $\text{Ca}(\text{OH})_2$ at Low Temperature. *Journal of Physics and Chemistry of Solids*, 55(2), 161–166. doi:10.1016/0022-3697(94)90073-6
- DIN EN/IEC 60584-1. (2013). *Thermocouples - Part 1: EMF Specifications and Tolerances*. CENELEC European Committee for Electrotechnical Standardization, CLC/TC 65X Industrial-process measurement, control and automation.
- DIN EN/IEC 60758. (2016). *Synthetic Quartz Crystal – Specifications and Guidelines for Use*. IEC International Electrotechnical Commission, IEC/TC 49 Piezoelectric devices for frequency control and selection.
- Dirac, P. A. M. (1967). *The Principles of Quantum Mechanics* (4th ed. (rev.)). Oxford: Clarendon Press.
- Dixit, U. S., Hazarika, M., & Davim, J. P. (2017). *A Brief History of Mechanical Engineering*. Cham: Springer International Publishing.
- Dolino, G. (1990). The α -Inc- β Transitions of Quartz: A Century of Research on Displacive Phase Transitions. *Phase Transitions*, 21(1), 59–72. doi:10.1080/01411599008206882
- Dolino, G., Bachheimer, J. P., & Zeyen, C. M. E. (1983). Observation of an Intermediate Phase Near the α - β Transition of Quartz by Heat Capacity and Neutron Scattering Measurements. *Solid State Communications*, 45(3), 295–299. doi:10.1016/0038-1098(83)90485-4
- Dove, M. T. (1997). Theory of Displacive Phase Transitions in Minerals. *American Mineralogist*, 82(3-4), 213–244. doi:10.2138/am-1997-3-401
- Dusza, L. (1995). Combined Solution of the Simultaneous Heat Loss and Finite Pulse Corrections with the Laser Flash Method. *High Temperatures - High Pressures*, 27-28(5), 467–473.
- Dusza, L. (1996). *Wärmetransport - Modelle zur Bestimmung der Temperaturleitfähigkeit von Werkstoffen mit der Instationären Laser-Flash Methode* (Dissertation, University Karlsruhe (TH), Karlsruhe).
- Esfarjani, K., Chen, G., & Stokes, H. T. (2011). Heat Transport in Silicon From First-Principles Calculations. *Physical Review B*, 84(8), 085204. doi:10.1103/PhysRevB.84.085204

- Eucken, A. (1911). Über die Temperaturabhängigkeit der Wärmeleitfähigkeit Fester Nichtmetalle. *Annalen der Physik*, 339(2), 185–221. doi:10.1002/andp.19113390202
- Every, A. G. (1980). General Closed-Form Expressions for Acoustic Waves in Elastically Anisotropic Solids. *Physical Review B*, 22(4), 1746–1760. doi:10.1103/PhysRevB.22.1746
- Fernández, I., Garea, A., & Irabien, A. (1998). SO₂ Reaction with Ca(OH)₂ at Medium Temperatures (300–425°C): Kinetic Behaviour. *Chemical Engineering Science*, 53(10), 1869–1881. doi:10.1016/S0009-2509(98)00029-3
- Fiquet, G., Richet, P., & Montagnac, G. (1999). High-Temperature Thermal Expansion of Lime, Periclase, Corundum and Spinel. *Physics and Chemistry of Minerals*, 27(2), 103–111. doi:10.1007/s002690050246
- Fourier, J. B. J. (1822). *Théorie Analytique de la Chaleur*. Paris: Firmin Didot.
- Fridleifsson, I. B. (2001). Geothermal Energy for the Benefit of the People. *Renewable and Sustainable Energy Reviews*, 5(3), 299–312. doi:10.1016/S1364-0321(01)00002-8
- Galwey, A. K. (2003). Dehydration of Crystalline Hydrates. In M. E. Brown & P. K. Gallagher (Eds.), *Handbook of Thermal Analysis and Calorimetry Vol. 2: Applications to Inorganic and Miscellaneous Materials* (pp. 595–656). Elsevier.
- Gammon, P. H., Kieffe, H., & Clouter, M. J. (1983). Elastic Constants of Ice Samples by Brillouin Spectroscopy. *The Journal of Physical Chemistry*, 87(21), 4025–4029. doi:10.1021/j100244a004
- Gibert, B., Schilling, F. R., Gratz, K., & Tommasi, A. (2005). Thermal Diffusivity of Olivine Single Crystals and a Dunite at High Temperature: Evidence for Heat Transfer by Radiation in the Upper Mantle. *Physics of the Earth and Planetary Interiors*, 151(1-2), 129–141. doi:10.1016/j.pepi.2005.02.003
- Giura, P., Paulatto, L., He, F., Lobo, R. P. S. M., Bosak, A., Calandrini, E., Paolasini, L., & Antonangeli, D. (2019). Multiphonon Anharmonicity of MgO. *Physical Review B*, 99(22), 220304. doi:10.1103/PhysRevB.99.220304
- Göbel, A., Hemberger, F., Ebert, H.-P., Jansen, M., & Wilfert, J. (2011). Thermophysical Properties of an Amorphous Polymer-Derived Si/B/N/C Ceramic. *Thermochimica Acta*, 520(1-2), 20–24. doi:10.1016/j.tca.2011.03.001
- Göbel, A., Hemberger, F., Vidi, S., & Ebert, H.-P. (2013). A New Method for the Determination of the Specific Heat Capacity Using Laser-Flash Calorimetry Down to 77K. *International Journal of Thermophysics*, 34(5), 883–893. doi:10.1007/s10765-012-1255-4
- Götze, J. (2009). Chemistry, Textures and Physical Properties of Quartz - Geological Interpretation and Technical Application. *Mineralogical Magazine*, 73(4), 645–671. doi:10.1180/minmag.2009.073.4.645

- Groot, H. (1989). Experiences Gained While Examining Thermophysical Properties of State-of-the-Art Materials. In D. P. H. Hasselman & J. R. Thomas (Eds.), *Thermal Conductivity 20* (pp. 357–366). Boston: Springer.
- Gross, E. (1930). Über änderung der Wellenlänge bei Lichtzerstreuung in Kristallen. *Zeitschrift für Physik*, 63(9-10), 685–687. doi:10.1007/BF01340308
- Gross, R., & Marx, A. (2014). *Festkörperphysik* (2nd). Berlin Boston: De Gruyter.
- Gurzhi, R. N. (1964). Thermal Conductivity of Dielectrics and Ferroelectrics at Low Temperatures. *Journal of Experimental and Theoretical Physics*, 46, 719–724.
- Gustafsson, S. E. (1991). Transient Plane Source Techniques for Thermal Conductivity and Thermal Diffusivity Measurements of Solid Materials. *Review of Scientific Instruments*, 62(3), 797–804. doi:10.1063/1.1142087
- Hartmann, J., Nilsson, O., & Fricke, J. (1993). Thermal Diffusivity Measurements on Two-Layered and Three-Layered Systems with the Laser-Flash Method. *High Temperatures - High Pressures*, 25, 403–410.
- Hasselman, D. P. H., & Donaldson, K. Y. (1990). Effects of Detector Non-linearity and Specimen Size on the Apparent Thermal Diffusivity of NIST 8425 Graphite. *International Journal of Thermophysics*, 11(3), 573–585. doi:10.1007/BF00500847
- Hasselman, D. P. H., & Merkel, G. A. (1989). Specimen Size Effect of the Thermal Diffusivity/Conductivity of Aluminum Nitride. *Journal of the American Ceramic Society*, 72(6), 967–971. doi:10.1111/j.1151-2916.1989.tb06253.x
- Hatton, W. E., Hildenbrand, D. L., Sinke, G. C., & Stull, D. R. (1959). The Chemical Thermodynamic Properties of Calcium Hydroxide. *Journal of the American Chemical Society*, 81(19), 5028–5030. doi:10.1021/ja01528a004
- Heckman, R. C. (1973). Finite Pulse-Time and Heat-Loss Effects in Pulse Thermal Diffusivity Measurements. *Journal of Applied Physics*, 44(4), 1455–1460. doi:10.1063/1.1662393
- Hemberger, F., Göbel, A., & Ebert, H.-P. (2010). Determination of the Thermal Diffusivity of Electrically Non-Conductive Solids in the Temperature Range from 80 K to 300 K by Laser-Flash Measurement. *International Journal of Thermophysics*, 31(11-12), 2187–2200. doi:10.1007/s10765-010-0876-8
- Hill, R. (1952). The Elastic Behaviour of a Crystalline Aggregate. *Proceedings of the Physical Society. Section A*, 65(5), 349–354. doi:10.1088/0370-1298/65/5/307
- Hoefler, J. J., & Taylor, R. E. (1990). Effects of Infrared Detector Non-linearity on Thermal Diffusivity Measurements Using the Flash Method. *International Journal of Thermophysics*, 11(6), 1099–1110. doi:10.1007/BF00500563

- Höfer, M. (2003). *Wärmetransport in Quarz und Feldspäten von 22 bis 800 °C* (Dissertation, Freie Universität Berlin, Berlin).
- Höfer, M., & Schilling, F. R. (2002). Heat Transfer in Quartz, Orthoclase, and Sanidine at Elevated Temperature. *Physics and Chemistry of Minerals*, 29(9), 571–584. doi:10.1007/s00269-002-0277-z
- Hofmeister, A. M. (1999). Mantle Values of Thermal Conductivity and the Geotherm from Phonon Lifetimes. *Science*, 283(5408), 1699–1706. doi:10.1126/science.283.5408.1699
- Hofmeister, A. M. (2004). Thermal Conductivity and Thermodynamic Properties from Infrared Spectra. In P. L. King & M. S. Ramsey (Eds.), *Infrared Spectroscopy in Geochemistry, Exploration Geochemistry, and Remote Sensing* (pp. 135–154). London, Ontario: Mineralogical Association of Canada.
- Hofmeister, A. M. (2006). Thermal Diffusivity of Garnets at High Temperature. *Physics and Chemistry of Minerals*, 33(1), 45–62. doi:10.1007/s00269-005-0056-8
- Hofmeister, A. M. (2007). Pressure Dependence of Thermal Transport Properties. *Proceedings of the National Academy of Sciences*, 104(22), 9192–9197. doi:10.1073/pnas.0610734104
- Hofmeister, A. M. (2019). *Measurements, Mechanisms, and Models of Heat Transport* (1st). Philadelphia: Elsevier.
- Hofmeister, A. M., Branlund, J. M., & Pertermann, M. (2007). 2.19 - Properties of Rocks and Minerals – Thermal Conductivity of the Earth. In G. Schubert (Ed.), *Treatise on Geophysics* (pp. 543–577). Amsterdam: Elsevier.
- Hofmeister, A. M., Dong, J., & Branlund, J. M. (2014). Thermal Diffusivity of Electrical Insulators at High Temperatures: Evidence for Diffusion of Bulk Phonon-Polaritons at Infrared Frequencies Augmenting Phonon Heat Conduction. *Journal of Applied Physics*, 115(16), 163517 1–19. doi:10.1063/1.4873295
- Holuj, F., Drozdowski, M., & Czajkowski, M. (1985). Brillouin Spectrum of Ca(OH)₂. *Solid State Communications*, 56(12), 1019–1021. doi:10.1016/0038-1098(85)90862-2
- Holuj, F., & Kwan, C. T. (1975). Polytypism and the ESR of Fe³⁺ in Ca(OH)₂. *Journal of Magnetic Resonance*, 18(1), 123–128. doi:10.1016/0022-2364(75)90230-9
- Horai, K.-I. (1971). Thermal Conductivity of Rock-Forming Minerals. *Journal of Geophysical Research*, 76(5), 1278–1308. doi:10.1029/JB076i005p01278
- Horai, K.-I., & Simmons, G. (1969). Thermal Conductivity of Rock-Forming Minerals. *Earth and Planetary Science Letters*, 6(5), 359–368. doi:10.1016/0012-821X(69)90186-1
- Hust, J. G. (1984). *A Fine-Grained, Isotropic Graphite for Use as NBS Thermophysical Property RM's from 5 to 2500K*. US Department of Commerce, National Bureau of Standards. Boulder.

- Incropera, F. P., Dewitt, D. P., Bergman, T. L., & Lavine, A. S. (Eds.). (2007). *Fundamentals of Heat and Mass Transfer* (6th). Hoboken: John Wiley.
- ISO 18755. (2005). *Fine Ceramics (Advanced Ceramics, Advanced Technical Ceramics) - Determination of Thermal Diffusivity of Monolithic Ceramics by Laser Flash Method*. ISO. Geneva.
- Issi, J.-P. (1999). Thermal Conduction Mechanisms in Solids: From Metals to Insulators. *Revue de Métallurgie*, 96, 575–584.
- Jeanloz, R., & Morris, S. (1986). Temperature Distribution in the Crust and Mantle. *Annual Review of Earth and Planetary Sciences*, 14(1), 377–415. doi:10.1146/annurev.ea.14.050186.002113
- Johnston, J. (1914). The Utilization of Diffusion Processes in the Preparation of Pure Substances. *Journal of the American Chemical Society*, 36(1), 16–19. doi:10.1021/jao2178a003
- Johnstone, J. R., & Glasser, F. P. (1992). Carbonation of Portlandite Single Crystals and Portlandite in Cement Paste. In *9th International Congress on the Chemistry of Cement* (pp. 370–376). New Delhi.
- Jozewicz, W., & Gullett, B. K. (1995). Reaction Mechanisms of Dry Ca-Based Sorbents with Gaseous HCl. *Industrial & Engineering Chemistry Research*, 34(2), 607–612. doi:10.1021/ie00041a022
- Kammer, E. W., Pardue, T. E., & Frissel, H. F. (1948). A Determination of the Elastic Constants for β -Quartz. *Journal of Applied Physics*, 19(3), 265–270. doi:10.1063/1.1715056
- Kanamori, H., Fujii, N., & Mizutani, H. (1968). Thermal Diffusivity Measurement of Rock-Forming Minerals from 300° to 1100°K. *J. Geophysical Research*, 73(2), 595–605. doi:10.1029/JB073i002p00595
- Kebblinski, P., Eastman, J. A., & Cahill, D. G. (2005). Nanofluids for Thermal Transport. *Materials Today*, 8(6), 36–44. doi:10.1016/S1369-7021(05)70936-6
- Kehoe, L., Kelly, P. V., & Crean, G. M. (1998). Application of the Laser Flash Diffusivity Method to Thin High Thermal Conductivity Materials. *Microsystem Technologies*, 5(1), 18–21. doi:10.1007/s005420050135
- Kerschbaumer, R. C., Stieger, S., Gschwandl, M., Hutterer, T., Fasching, M., Lechner, B., Meinhart, L., Hildenbrandt, J., Schritteser, B., Fuchs, P. F., Berger, G. R., & Friesenbichler, W. (2019). Comparison of Steady-State and Transient Thermal Conductivity Testing Methods Using Different Industrial Rubber Compounds. *Polymer Testing*, 80, 106121. doi:10.1016/j.polymertesting.2019.106121
- Khain, V. E., & Goncharov, M. A. (2006). Geodynamic Cycles and Geodynamic Systems of Various Ranks: Their Relationships and Evolution in the Earth's History. *Geotectonics*, 40(5), 327–344. doi:10.1134/S0016852106050013
- Kim, P., Shi, L., Majumdar, A., & McEuen, P. L. (2001). Thermal Transport Measurements of Individual Multiwalled Nanotubes. *Physical Review Letters*, 87(21), 215502. doi:10.1103/PhysRevLett.87.215502

- Kittel, C. (2005). *Introduction to Solid State Physics* (8th). Hoboken: John Wiley & Sons.
- Klumbach, S. (2015). *Elasticity and Viscoelasticity of Solid SiO₂ as a Function of Frequency and Temperature* (Dissertation, Karlsruhe Institute of Technology, Karlsruhe).
- Klumbach, S., & Schilling, F. R. (2014). Elastic and Anelastic Properties of α - and β -Quartz Single Crystals. *European Journal of Mineralogy*, 26(2), 211–220. doi:10.1127/0935-1221/2014/0026-2362
- Koski, J. A. (1981). Improved Data Reduction Methods for Laser Pulse Diffusivity Determination with the Use of Minicomputers. In *Proceedings of the Eighth Symposium on Thermophysical Properties* (Vol. 2, pp. 94–103). New York: The American Society Mechanical Engineers.
- Kruger, M. B., Williams, Q., & Jeanloz, R. (1989). Vibrational Spectra of Mg(OH)₂ and Ca(OH)₂ Under Pressure. *The Journal of Chemical Physics*, 91(10), 5910–5915. doi:10.1063/1.457460
- Lacis, A. A., & Hansen, J. (1974). A Parameterization for the Absorption of Solar Radiation in the Earth's Atmosphere. *Journal of the Atmospheric Sciences*, 31(1), 118–133.
- Lager, D., Hohenauer, W., Knoll, C., Weinberger, P., & Werner, A. (2018). Methodology to Determine the Apparent Specific Heat Capacity of Metal Hydroxides for Thermochemical Energy Storage. *Journal of Thermal Analysis and Calorimetry*, 133(1), 207–215. doi:10.1007/s10973-017-6883-2
- Larson, K. B., & Koyama, K. (1967). Correction for Finite-Pulse-Time Effects in Very Thin Samples using the Flash Method of Measuring Thermal Diffusivity. *Journal of Applied Physics*, 38(2), 465–474. doi:10.1063/1.1709360
- Laugesen, J. L. (2005). Density Functional Calculations of Elastic Properties of Portlandite, Ca(OH)₂. *Cement and Concrete Research*, 35(2), 199–202. doi:10.1016/j.cemconres.2004.07.036
- Le Chatelier, H. (1890). Sur la Dilatation du Quartz. *Bulletin de la Société française de Minéralogie*, 13(3), 112–118. doi:10.3406/bulmi.1890.2156
- Lee, H. J. (1975). *Thermal Diffusivity in Layered and Dispersed Composites* (Dissertation, Purdue University, Lafayette).
- Lee, H. L., & Hasselman, D. P. H. (1985). Comparison of Data for Thermal Diffusivity Obtained by Laser-Flash Method Using Thermocouple and Photodetector. *Journal of the American Ceramic Society*, 68(1), C–12–C–13. doi:10.1111/j.1151-2916.1985.tb15255.x
- Leibfried, G., & Schlömann, E. (1954). *Wärmeleitung in Elektrisch Isolierenden Kristallen*. Göttingen: Vandenhoeck & Ruprecht.
- Lenardic, A., & Kaula, W. M. (1995). Mantle Dynamics and the Heat Flow Into the Earth's Continents. *Nature*, 378(6558), 709–711. doi:10.1038/378709a0

- Levenberg, K. (1944). A Method for the Solution of Certain Non-Linear Problems in Least Squares. *Quarterly of Applied Mathematics*, 2(2), 164–168. doi:10.1090/qam/10666
- Li, G. G., Keener, T. C., Stein, A. W., & Khang, S. J. (1999). CO₂ Reaction with Ca(OH)₂ During SO₂ Removal with Convective Pass Sorbent Injection and High Temperature Filtration. *Environmental Engineering and Policy*, 2(1), 47–56. doi:10.1007/BF03500906
- Lim, K.-H., Kim, S.-K., & Chung, M.-K. (2009). Improvement of the Thermal Diffusivity Measurement of Thin Samples by the Flash Method. *Thermochimica Acta*, 494(1-2), 71–79. doi:10.1016/j.tca.2009.04.019
- Lindsay, L., Katre, A., Cepellotti, A., & Mingo, N. (2019). Perspective on ab initio Phonon Thermal Transport. *Journal of Applied Physics*, 126(5), 050902. doi:10.1063/1.5108651
- Liu, C.-F., & Shih, S.-M. (2006). Effects of Flue Gas Components on the Reaction of Ca(OH)₂ with SO₂. *Industrial & Engineering Chemistry Research*, 45(26), 8765–8769. doi:10.1021/ie0605534
- Loebich, O. (1972). The Optical Properties of Gold. *Gold Bulletin*, 5, 2–10.
- Lord, R. C., & Morrow, J. C. (1957). Calculation of the Heat Capacity of α Quartz and Vitreous Silica from Spectroscopic Data. *The Journal of Chemical Physics*, 26(2), 230–232. doi:10.1063/1.1743274
- Ma, Z., Xi, L., Liu, H., Zheng, F., Gao, H., Chen, Z., & Chen, H. (2017). Ferroelectric Phase transition of BaTiO₃ Single Crystal Based on a Tenth Order Landau-Devonshire Potential. *Computational Materials Science*, 135, 109–118. doi:10.1016/j.commatsci.2017.04.011
- Maciel-Camacho, A., Hernández, H. R., Hills, A. W. D., & Morales, R. D. (1997). Hydration Kinetics of Lime. *ISIJ International*, 37(5), 468–476. doi:10.2355/isijinternational.37.468
- Mandelstam, L. I. (1926). Light Scattering by Inhomogeneous Media. *Zh. Radio-Fiziko-Khimicheskogo Obshchestva*, 58, 381.
- Marek, R., & Nitsche, K. (2012). *Praxis der Wärmeübertragung* (3rd). München: Fachbuchverl. Leipzig im Carl-Hanser-Verl.
- Marquardt, D. W. (1963). An Algorithm for Least-Squares Estimation of Nonlinear Parameters. *Journal of the Society for Industrial and Applied Mathematics*, 11(2), 431–441. doi:10.1137/0111030
- McKay, J. A., & Schriempf, J. T. (1976). Corrections for Nonuniform Surface-Heating Errors in Flash-Method Thermal-Diffusivity Measurements. *Journal of Applied Physics*, 47(4), 1668–1671. doi:10.1063/1.322790
- McMasters, R. L., & Dinwiddie, R. B. (2010). Accounting for Finite Flash Duration in Diffusivity Experiments. *Journal of Thermophysics and Heat Transfer*, 24(4), 818–822. doi:10.2514/1.49047
- McMasters, R., Harth, Z. J., Taylor, R. P., & Brooke, G. M. (2017). Testing Extremely Small Samples Using the Flash Diffusivity Method.

- International Journal of Numerical Methods for Heat and Fluid Flow*, 27(3), 551–560. doi:10.1108/HFF-03-2016-0094
- Meade, C., & Jeanloz, R. (1990). Static Compression of $\text{Ca}(\text{OH})_2$ at Room Temperature: Observations of Amorphization and Equation of State Measurements to 10.7 GPa. *Geophysical Research Letters*, 17(8), 1157–1160. doi:10.1029/GL017i008p01157
- Mechie, J., Sobolev, S. V., Ratschbacher, L., Babeyko, A. Y., Bock, G., Jones, A. G., Nelson, K. D., Solon, K. D., Brown, L. D., & Zhao, W. (2004). Precise Temperature Estimation in the Tibetan Crust From Seismic Detection of the α - β Quartz Transition. *Geology*, 32(7), 601. doi:10.1130/G20367.1
- Mehling, H., Hautzinger, G., Nilsson, O., Fricke, J., Hofmann, R., & Hahn, O. (1998). Thermal Diffusivity of Semitransparent Materials Determined by the Laser-Flash Method Applying a New Analytical Model. *International Journal of Thermophysics*, 19(3).
- Minkowycz, W. J., Sparrow, E. M., & Abraham, J. P. (Eds.). (2013). *Nanoparticle Heat Transfer and Fluid Flow*. Boca Raton: CRC Press/-Taylor & Francis Group.
- Momma, K., & Izumi, F. (2011). VESTA 3 for Three-Dimensional Visualization of Crystal, Volumetric and Morphology Data. *Journal of Applied Crystallography*, 44(6), 1272–1276. doi:10.1107/S0021889811038970
- Nagai, T., Ito, T., Hattori, T., & Yamanaka, T. (2000). Compression Mechanism and Amorphization of Portlandite, $\text{Ca}(\text{OH})_2$: Structural Refinement Under Pressure. *Physics and Chemistry of Minerals*, 27(7), 462–466. doi:10.1007/s002690000084
- Nusselt, W. (1915). Das Grundgesetz des Wärmeüberganges. *Gesundheits-Ingenieur*, 38(42), 477–482.
- Nye, J. F. (1985). *Physical Properties of Crystals: Their Representation by Tensors and Matrices*. Oxford, New York: Clarendon Press; Oxford University Press.
- Ogawa, M., Mukai, K., Fukui, T., & Baba, T. (2001). The Development of a Thermal Diffusivity Reference Material Using Alumina. *Measurement Science and Technology*, 12(12), 2058–2063. doi:10.1088/0957-0233/12/12/305
- Ohno, I. (1995). Temperature Variation of Elastic Properties of α -Quartz up to the α - β Transition. *Journal of Physics of the Earth*, 43(2), 157–169. doi:10.4294/jpe1952.43.157
- Pabst, W., & Gregorová, E. (2004). Effective Elastic Properties of Alumina-Zirconia Composite Ceramics - Part 2. Micromechanical Modeling. *Ceramics - Silikáty*, 48 (1), 14–23.
- Paddock, C. A., & Eesley, G. L. (1986). Transient Thermorefectance from Thin Metal Films. *Journal of Applied Physics*, 60(1), 285–290. doi:10.1063/1.337642
- Parker, W. J., Jenkins, R. J., Butler, C. P., & Abbott, G. L. (1961). Flash Method of Determining Thermal Diffusivity, Heat Capacity, and

- Thermal Conductivity. *Journal of Applied Physics*, 32(9), 1679–1684. doi:10.1063/1.1728417
- Pavese, A., Catti, M., Ferraris, G., & Hull, S. (1997). P-V Equation of State of Portlandite, $\text{Ca}(\text{OH})_2$, from Powder Neutron Diffraction Data. *Physics and Chemistry of Minerals*, 24(2), 85–89. doi:10.1007/s002690050020
- Peierls, R. (1929). Zur Kinetischen Theorie der Wärmeleitung in Kristallen. *Ann. Phys.*, 395(8), 1055–1101. doi:10.1002/andp.19293950803
- Pertermann, M., Whittington, A. G., Hofmeister, A. M., Spera, F. J., & Zayak, J. (2008). Transport Properties of Low-Sanidine Single-Crystals, Glasses and Melts at High Temperature. *Contributions to Mineralogy and Petrology*, 155(6), 689–702. doi:10.1007/s00410-007-0265-x
- Poensgen, R. (1912). Ein Technisches Verfahren zur Ermittlung der Wärmeleitfähigkeit Plattenförmiger Stoffe. *Zeitschrift d. Vereins Deutscher Ingenieure*, 56, 1653–1658.
- Popov, Y. A., Berezin, V. V., Semenov, V. G., & Korostelev, V. M. (1985). Complex Detailed Investigations of the Thermal Properties of Rocks on the Basis of a Moving Point Source. *Earth Physics*, 21(1), 64–70.
- Ranjha, Q. A., Vahedi, N., & Oztekin, A. (2016). Numerical Study of Thermochemical Storage Using $\text{Ca}(\text{OH})_2/\text{CaO}$: High Temperature Applications. In *Proceedings of the ASME 2016 International Mechanical Engineering Congress and Exposition* volume, Vol. 6B: Energy. doi:10.1115/IMECE2016-65909
- Ray, L., Forster, H., Schilling, F. R., & Forster, A. (2006). Thermal Diffusivity of Felsic to Mafic Granulites at Elevated Temperatures. *Earth and Planetary Science Letters*, 251(3-4), 241–253. doi:10.1016/j.epsl.2006.09.010
- Raz, U., Girsperger, S., & Thompson, A. B. (2002). *Thermal Expansion, Compressibility and Volumetric Changes of Quartz Obtained by Single Crystal Dilatometry to 700°C and 3.5 Kilobars (0.35 GPa)*. ETH Zürich. doi:10.3929/ethz-a-004392716
- Reif-Acherman, S. (2014). Early and Current Experimental Methods for Determining Thermal Conductivities of Metals. *International Journal of Heat and Mass Transfer*, 77, 542–563. doi:10.1016/j.ijheatmasstransfer.2014.05.038
- Renedo, M. J., Pesquera, C., Gonzalez, F., & Fernandez, J. (2013). Use of TG-DSC-MS and Gas Analyzer Data to Investigate the Reaction of CO_2 and SO_2 with $\text{Ca}(\text{OH})_2$ at Low Temperature. *Chemical Engineering Transactions*, 35, 739–744. doi:10.3303/CET1335123
- Reuss, A. (1929). Berechnung der Fließgrenze von Mischkristallen auf Grund der Plastizitätsbedingung für Einkristalle. *Journal of Applied Mathematics and Mechanics / Zeitschrift für Angewandte Mathematik und Mechanik*, 9(1), 49–58. doi:10.1002/zamm.19290090104

- Ronov, A. B., & Yaroshevsky, A. A. (1969). Chemical Composition of the Earth's Crust. In P. J. Hart (Ed.), *Geophysical Monograph Series* (pp. 37–57). Washington, D. C.: American Geophysical Union.
- Ross, R. G., Andersson, P., Sundqvist, B., & Backstrom, G. (1984). Thermal Conductivity of Solids and Liquids Under Pressure. *Reports on Progress in Physics*, 47(10), 1347–1402. doi:10.1088/0034-4885/47/10/002
- Roufosse, M., & Klemens, P. G. (1974). Lattice Thermal Conductivity of Minerals at High Temperatures. *Journal of Geophysical Research*, 79(5), 703–705. doi:10.1029/JB079i005p00703
- Rumble, J. R., Lide, D. R., & Bruno, T. J. (Eds.). (2018). *CRC Handbook of Chemistry and Physics* (99th). Taylor & Francis Ltd.
- Salmon, D. R., Brandt, R., & Tye, R. P. (2010). Pyroceram 9606, A Certified Ceramic Reference Material For High-Temperature Thermal Transport Properties: Part 2 - Certification Measurements. *International Journal of Thermophysics*, 31(2), 355–373. doi:10.1007/s10765-010-0710-3
- Sandercock, J. R. (1982). Trends in Brillouin Scattering: Studies of Opaque Materials, Supported Films, and Central Modes. In M. Cardona & G. Güntherodt (Eds.), *Light Scattering in Solids III: Recent Results* (pp. 173–206). Berlin, Heidelberg: Springer.
- Schaube, F. (2013). *Untersuchungen zur Nutzung des CaO/Ca(OH)₂ Reaktionssystems für die Thermochemische Wärmespeicherung*. München: Dr. Hut.
- Schaube, F., Koch, L., Wörner, A., & Müller-Steinhagen, H. (2012). A Thermodynamic and Kinetic Study of the De- and Rehydration of Ca(OH)₂ at High H₂O Partial Pressures for Thermo-Chemical Heat Storage. *Thermochimica Acta*, 538, 9–20. doi:10.1016/j.tca.2012.03.003
- Schilling, F. R. (1998). *Mineralphysik - Ein Mineralogischer Ansatz* (Habilitation, Freie Universität Berlin, Berlin).
- Schilling, F. R. (1999). A Transient Technique to Measure Thermal Diffusivity at Elevated Temperatures. *European Journal of Mineralogy*, 11(6), 1115–1124. doi:10.1127/ejm/11/6/1115
- Schmidt, M. (2017). *Experimental Investigation of Ca(OH)₂ as Thermochemical Energy Storage at Process Relevant Boundary Conditions* (Dissertation, University of Stuttgart, Stuttgart).
- Schoderböck, P., Klocker, H., Sigl, L. S., & Seeber, G. (2009). Evaluation of the Thermal Diffusivity of Thin Specimens from Laser Flash Data. *International Journal of Thermophysics*, 30(2), 599–607. doi:10.1007/s10765-009-0561-y
- Schriempf, J. T. (1972). A Laser Flash Technique for Determining Thermal Diffusivity of Liquid Metals at Elevated Temperatures. *Review of Scientific Instruments*, 43(5), 781–786. doi:10.1063/1.1685757
- Schubert, G., Yuen, D. A., & Turcotte, D. L. (1975). Role of Phase Transitions in a Dynamic Mantle. *Geophysical Journal of the Royal*

- Astronomical Society*, 42(2), 705–735. doi:10.1111/j.1365-246X.1975.tb05888.x
- Seipold, U. (1992). Depth Dependence of Thermal Transport Properties for Typical Crustal Rocks. *Physics of the Earth and Planetary Interiors*, 69(3-4), 299–303. doi:10.1016/0031-9201(92)90149-P
- Seipold, U. (1998). Temperature Dependence of Thermal Transport Properties of Crystalline Rocks - a General Law. *Tectonophysics*, 291(1-4), 161–171. doi:10.1016/S0040-1951(98)00037-7
- Shankland, T. J. (1970). Pressure Shift of Infrared Absorption Bands in Minerals and the Effect on Radiative Heat Transport. *Journal of Geophysical Research*, 75(2), 409–413. doi:10.1029/JB075i002p00409
- Shankland, T., Nitsan, U., & Duba, A. (1979). Optical Absorption and Radiative Heat Transport in Olivine at High Temperature. *Journal of Geophysical Research*, 84. doi:10.1029/JB084iB04p01603
- Sheindlin, M., Halton, D., Musella, M., & Ronchi, C. (1998). Advances in the Use of Laser-Flash Techniques for Thermal Diffusivity Measurement. *Review of Scientific Instruments*, 69(3), 1426–1436. doi:10.1063/1.1148776
- Shih, S.-M., Ho, C.-S., Song, Y.-S., & Lin, J.-P. (1999). Kinetics of the Reaction of $\text{Ca}(\text{OH})_2$ with CO_2 at Low Temperature. *Industrial & Engineering Chemistry Research*, 38(4), 1316–1322. doi:10.1021/ie980508z
- Shizawa, M., & Mase, K. (1991). Principle of Superposition: A Common Computational Framework for Analysis of Multiple Motion. *Proceedings of the IEEE Workshop on Visual Motion*, 164–172.
- Siegesmund, S. (1996). *The Significance of Rock Fabrics for the Geological Interpretation of Geophysical Anisotropies: With 61 Figures and 5 Tables*. Stuttgart: E. Schweizerbart'sche Verlagsbuchhandlung.
- Slack, G. A. (1965). Thermal Conductivity of Elements with Complex Lattices: B, P, S. *Physical Review*, 139(2A), A507–A515. doi:10.1103/PhysRev.139.A507
- Slack, G. A. (1979). The Thermal Conductivity of Nonmetallic Crystals. In H. Ehrenreich, F. Seitz, & D. Turnbull (Eds.), *Solid State Physics* (Vol. 34, pp. 1–71). New York, San Francisco, London: Academic Press.
- Slack, G. A., & Oliver, D. W. (1971). Thermal Conductivity of Garnets and Phonon Scattering by Rare-Earth Ions. *Physical Review B*, 4(2), 592–609. doi:10.1103/PhysRevB.4.592
- Speziale, S., & Duffy, T. S. (2002). Single-Crystal Elastic Constants of Fluorite (CaF_2) to 9.3 GPa. *Physics and Chemistry of Minerals*, 29(7), 465–472. doi:10.1007/s00269-002-0250-x
- Speziale, S., Jiang, F., Mao, Z., Monteiro, P. J. M., Wenk, H.-R., Duffy, T. S., & Schilling, F. R. (2008a). Single-Crystal Elastic Constants of Natural Ettringite. *Cement and Concrete Research*, 38(7), 885–889. doi:10.1016/j.cemconres.2008.02.004

- Speziale, S., Marquardt, H., & Duffy, T. S. (2014). Brillouin Scattering and its Application in Geosciences. *Reviews in Mineralogy and Geochemistry*, 78(1), 543–603. doi:10.2138/rmg.2014.78.14
- Speziale, S., Reichmann, H. J., Schilling, F. R., Wenk, H. R., & Monteiro, P. J. M. (2008b). Determination of the Elastic Constants of Portlandite by Brillouin Spectroscopy. *Cement and Concrete Research*, 38(10), 1148–1153. doi:10.1016/j.cemconres.2008.05.006
- Spitzer, D. P. (1970). Lattice Thermal Conductivity of Semiconductors: A Chemical Bond Approach. *Journal of Physics and Chemistry of Solids*, 31(1), 19–40. doi:10.1016/0022-3697(70)90284-2
- Steinbach, V., & Yuen, D. A. (1992). The Effects of Multiple Phase Transitions on Venusian Mantle Convection. *Geophysical Research Letters*, 19(22), 2243–2246. doi:10.1029/92GL02319
- Stryczniewicz, W., & Panas, A. J. (2015). Numerical Data Processing From a Laser Flash Experiment on Thin Graphite Layer. *Computer Assisted Methods in Engineering and Science*, 22, 279–287.
- Stryczniewicz, W., Zmywaczyk, J., & Panas, A. J. (2017). Inverse Problem Solution for a Laser Flash Studies of a Thin Layer Coatings. *International Journal of Numerical Methods for Heat and Fluid Flow*, 27(3), 698–710. doi:10.1108/HFF-03-2016-0100
- Swank, W. D., & Windes, W. E. (2014). Specimen Size Effects in the Determination of Nuclear Grade Graphite Thermal Diffusivity. In N. Tzelepi & M. Carroll (Eds.), *Graphite Testing for Nuclear Applications: The Significance of Test Specimen Volume and Geometry and the Statistical Significance of Test Specimen Population* (Vol. STP 1578, pp. 186–198). West Conshohocken: ASTM International.
- Taylor, R. E., & Cape, J. A. (1964). Finite Pulse-Time Effects in the Flash Diffusivity Technique. *Applied Physics Letters*, 5(10), 212–213. doi:10.1063/1.1723593
- Taylor, R. E., & Clark III, L. M. (1974). Finite Pulse Time Effects in Flash Diffusivity Method. *High Temperatures - High Pressures*, 6, 65–72.
- Taylor, R. E., & Kelsic, B. H. (1986). Parameters Governing Thermal Diffusivity Measurements of Unidirectional Fiber-Reinforced Composites. *Journal of Heat Transfer*, 108(1), 161–165. doi:10.1115/1.3246881
- Tong, T. W. (Ed.). (1994). *Thermal Conductivity 22*. Lancaster: Technomic Publishing.
- Touloukian, Y. S., Powell, R. W., Ho, C. Y., & Nicolaou, M. C. (1973). *Thermal Diffusivity*. New York: Plenum Publishing Corporation.
- Turner, S. P., & Taylor, R. E. (1991). Thermophysical Properties of Aluminium Titanate. *High Temperatures-High Pressures*, 23(4), 445–453.
- Ulian, G., & Valdrè, G. (2019). Equation of State and Second-Order Elastic Constants of Portlandite $\text{Ca}(\text{OH})_2$ and Brucite $\text{Mg}(\text{OH})_2$. *Physics and Chemistry of Minerals*, 46(2), 101–117. doi:10.1007/s00269-018-0989-3

- Vacher, R., & Boyer, L. (1972). Brillouin Scattering: A Tool for the Measurement of Elastic and Photoelastic Constants. *Physical Review B*, 6(2), 639–673. doi:10.1103/PhysRevB.6.639
- Voigt, W. (1928). *Lehrbuch der Kristallphysik*. Leipzig, Berlin: B.G. Teubner.
- Vozár, L., & Hohenauer, W. (2003). Flash Method of Measuring the Thermal Diffusivity. A Review. *High Temperatures-High Pressures*, 35/36(3), 253–264. doi:10.1068/htjr119
- Vozár, L., & Hohenauer, W. (2005). Uncertainty of Thermal Diffusivity Measurements Using the Laser Flash Method. *International Journal of Thermophysics*, 26(6), 1899–1915. doi:10.1007/s10765-005-8604-5
- Wang, H., Chen, D., Li, Z., Zhang, D., Cai, N., Yang, J., & Wei, G. (2018). SO₃ Removal from Flue Gas with Ca(OH)₂ in Entrained Flow Reactors. *Energy & Fuels*, 32(4), 5364–5373. doi:10.1021/acs.energyfuels.8b00274
- Watt, D. A. (1966). Theory of Thermal Diffusivity by Pulse Technique. *British Journal of Applied Physics*, 17(2), 231–240. doi:10.1088/0508-3443/17/2/311
- Whitfield, C. H., Brody, E. M., & Bassett, W. A. (1976). Elastic Moduli of NaCl by Brillouin Scattering at High Pressure in a Diamond Anvil Cell. *Review of Scientific Instruments*, 47(8), 942–947. doi:10.1063/1.1134778
- Woodside, W., & Messmer, J. H. (1961). Thermal Conductivity of Porous Media. I. Unconsolidated Sands. *Journal of Applied Physics*, 32(9), 1688–1699. doi:10.1063/1.1728419
- Xiong, X., Ragasa, E. J., Chernatynskiy, A., Tang, D., & Phillpot, S. R. (2019). Lattice Thermal Conductivity of Quartz at High Pressure and Temperature from the Boltzmann Transport Equation. *Journal of Applied Physics*, 126(21), 215106. doi:10.1063/1.5114992
- Xu, H., Zhao, Y., Vogel, S. C., Daemen, L. L., & Hickmott, D. D. (2007). Anisotropic Thermal Expansion and Hydrogen Bonding Behavior of Portlandite: A High-Temperature Neutron Diffraction Study. *Journal of Solid State Chemistry*, 180(4), 1519–1525. doi:10.1016/j.jssc.2007.03.004
- Xue, J., Liu, X., Lian, Y., & Taylor, R. (1993). The Effects of a Finite Pulse Time in the Flash Thermal Diffusivity Method. *International Journal of Thermophysics*, 14(1), 123–133. doi:10.1007/BF00522666
- Yaroshevsky, A. A., & Bulakh, A. G. (1994). The Mineral Composition of the Earth's Crust, Mantle, Meteorites, Moon, and Planets. In A. S. Marfunin (Ed.), *Advanced Mineralogy: Volume 1 Composition, Structure, and Properties of Mineral Matter: Concepts, Results, and Problems* (pp. 27–36). Berlin, Heidelberg: Springer.
- Yur'ev, B. P., & Spirin, N. A. (2012). Thermophysical Properties of Limestone and Lime on Heating. *Steel in Translation*, 42(4), 308–311. doi:10.3103/S0967091212040195
- Zandt, G., Beck, S. L., Ruppert, S. R., Ammon, C. J., Rock, D., Minaya, E., Wallace, T. C., & Silver, P. G. (1996). Anomalous Crust of the

- Bolivian Altiplano, Central Andes: Constraints from Broadband Regional Seismic Waveforms. *Geophysical Research Letters*, 23(10), 1159–1162. doi:10.1029/96GL00967
- Zawilski, B. M., Littleton, R. T., & Tritt, T. M. (2001). Description of the Parallel Thermal Conductance Technique for the Measurement of the Thermal Conductivity of Small Diameter Samples. *Review of Scientific Instruments*, 72(3), 1770. doi:10.1063/1.1347980
- Zeller, R. C., & Pohl, R. O. (1971). Thermal Conductivity and Specific Heat of Noncrystalline Solids. *Physical Review B*, 4(6), 2029–2041. doi:10.1103/PhysRevB.4.2029
- Zha, C.-S., Duffy, T. S., Downs, R. T., Mao, H.-K., & Hemley, R. J. (1996). Sound Velocity and Elasticity of Single-Crystal Forsterite to 16 GPa. *Journal of Geophysical Research: Solid Earth*, 101(B8), 17535–17545. doi:10.1029/96JB01266
- Zhang, T., & Luo, T. (2013). High-Contrast, Reversible Thermal Conductivity Regulation Utilizing the Phase Transition of Polyethylene Nanofibers. *ACS Nano*, 7(9), 7592–7600. doi:10.1021/nn401714e
- Zhao, D., Qian, X., Gu, X., Jajja, S. A., & Yang, R. (2016). Measurement Techniques for Thermal Conductivity and Interfacial Thermal Conductance of Bulk and Thin Film Materials. *Journal of Electronic Packaging*, 138(4), 040802. doi:10.1115/1.4034605
- Ziman, J. M. (1960). *Electrons and Phonons: The Theory of Transport Phenomena in Solids*. Oxford: Oxford University Press.
- Zoth, G., & Haenel, R. (1988). Appendix. In R. Haenel, L. Stegena, & L. Rybach (Eds.), *Handbook of Terrestrial Heat-Flow Density Determination* (1st, pp. 449–466). Dordrecht, Boston, London: Kluwer Academic Publishers.
- Zubov, V. G., & Firsova, M. M. (1962). Elastic Properties of Quartz Near the α - β Transition. *Soviet Physics, Crystallography*, 7(3), 374–376.

AUTHOR'S PUBLICATIONS

PEER-REVIEWED PUBLICATIONS

- Breuer, S., & Schilling, F. R. (2019). Improving Thermal Diffusivity Measurements by Including Detector Inherent Delayed Response in Laser Flash Method. *International Journal of Thermophysics*, 40(10), 95. doi:10.1007/s10765-019-2562-9
- Breuer, S., & Schilling, F. R. (2020). Anisotropic Thermal Transport Properties of Quartz: From -120 °C Through the α - β Phase Transition. *European Journal of Mineralogy*, (under review).
- Breuer, S., Schwotzer, M., Speziale, S., & Schilling, F. R. (2020). Thermoelastic Properties of Synthetic Single Crystal Portlandite $\text{Ca}(\text{OH})_2$ - Temperature-Dependent Thermal Diffusivity with Derived Thermal Conductivity and Elastic Constants at Ambient Conditions. *Cement and Concrete Research*, 137, 106199. doi:10.1016/j.cemconres.2020.106199
- Butscher, C., Breuer, S., & Blum, P. (2018). Swelling Laws for Clay-Sulfate Rocks Revisited. *Bulletin of Engineering Geology and the Environment*, 77(1), 399–408. doi:10.1007/s10064-016-0986-z

CONFERENCE CONTRIBUTIONS

- Breuer, S., Blum, P., & Butscher, C. (2015a). Stress-Strain Relations for Swelling Anhydritic Clay Rocks – A Review. Poster. European Geoscience Union (EGU) General Assembly, Vienna (Austria).
- Breuer, S., Scheffzük, C., Müller, B. I. R., & Schilling, F. R. (2016a). An Approach to Forward-Model Time-of-Flight Neutron Diffraction Data for Uniaxial Load Conditions Using the Example of Sandstone. Poster. 24th Annual Meeting of the German Crystallographical Society (DGK), Stuttgart (Germany).
- Breuer, S., Scheffzük, C., Müller, B. I. R., & Schilling, F. R. (2016b). An Approach to Forward-Model Time-of-Flight Neutron Diffraction Data for Uniaxial Load Conditions Using the Example of Sandstone. Poster. German Conference on Neutron Scattering, Kiel (Germany).
- Breuer, S., & Schilling, F. R. (2019a). Reducing Systematic Errors in Thermal Diffusivity Laser Flash Measurements Caused by Detector Inherent Delayed Response. Presentation. 34th International Thermal Conductivity Conference (ITCC 2019), 22nd International Thermal Expansion Symposium (ITES 2019), Wilmington, Delaware (USA).

- Breuer, S., & Schilling, F. R. (2019b). Systematic Errors in Thermal Diffusivity Measurements - Delayed Detector Response, Sample Coating and Sample Size Effects in Thermal Diffusivity Measurements. Poster. 34th International Thermal Conductivity Conference (ITCC 2019), 22nd International Thermal Expansion Symposium (ITES 2019), Wilmington, Delaware (USA).
- Breuer, S., Schilling, F. R., Müller, B. I. R., & Drüppel, K. (2015b). An Approach to Model Mineral's Bulk Moduli K from their Chemical Composition and Density. Poster. American Geophysical Union (AGU) Fall Meeting, San Francisco (USA).
- Breuer, S., Schilling, F. R., Scheffzük, C., & Müller, B. I. R. (2015c). An Approach to Model Neutron Diffraction Patterns of Uniaxially Deformed Sandstone Using Elastic Properties of Quartz. American Geophysical Union (AGU) Fall Meeting, San Francisco (USA).
- Müller, B. I. R., Scheffzük, C., Breuer, S., & Schilling, F. R. (2018). Potential of In Situ Triaxial Stress Experiments Using Neutron Time-of-Flight Diffraction on Porous Rocks for Reducing the Risk of Subsidence and Induced Seismicity Through Gas Production. Poster. SNI Conference 2018, Garching (Germany).
- Müller, H. J., Schilling, F. R., Scheffzük, C., Breuer, S., & Müller, B. I. R. (2017). Measurements of Elastic and Inelastic Properties of Polycrystalline Samples under Simulated Earth's Mantle Conditions in Large Volume Apparatus. Poster. 9th High Pressure Mineral Physics Seminar, Saint Malo (France).
- Scheffzük, C., Breuer, S., Altangerel, B., Schilling, F. R., & Müller, B. I. R. (2017). The Neutron Time-of-Flight Diffractometer EPSILON for Residual and Applied Strain Analysis on Geological Samples Under Uniaxial and Triaxial Load Conditions. Poster. 25th Annual Meeting of the German Crystallographical Society (DGK), Karlsruhe (Germany).
- Scheffzük, C., Müller, B. I. R., Breuer, S., Altangerel, B., & Schilling, F. R. (2016a). Residual and Applied Strain Investigation on Sandstone Samples Using Neutron Time-of-Flight Diffraction at the Strain Diffractometer Epsilon, IBR-2M Dubna. Presentation. International Conference on Contemporary Physics (ICCP), Ulaanbaatar (Mongolia).
- Scheffzük, C., Müller, B. I. R., Breuer, S., & Schilling, F. R. (2016b). Residual and Applied Strain Investigation on Sandstone Samples Using Neutron Time-of-Flight Diffraction at the Strain Diffractometer Epsilon. Poster. German Conference on Neutron Scattering, Kiel (Germany).
- Scheffzük, C., Müller, B. I. R., Breuer, S., & Schilling, F. R. (2018). In Situ Triaxial Deformation Experiments on a Sandstone Sample for Strain Investigation at the Neutron Time-of-Flight Diffractometer EPSILON. Poster. SNI Conference 2018, Garching (Germany).
- Voigtländer, A., Leith, K., Breuer, S., Müller, B. I. R., Scheffzük, C., Schilling, F. R., & Krautblatter, M. (2018). In Situ Strain Detection

of Stress-Strain Relationships and Their Controls on Progressive Damage in Marble and Quartzite by Neutron Diffraction Experiments. Poster. European Geoscience Union (EGU) General Assembly, Vienna (Austria).

Voigtländer, A., Leith, K., Krautblatter, M., Breuer, S., Müller, B. I. R., Scheffzük, C., & Schilling, F. R. (2017). EPSILON@JINR to Understand Progressive Rock Strength Degradation by In Situ Strain Detection Using Neutron Diffraction. Poster. International Conference "Condensed Matter Research at the IBR-2", Dubna (Russia).

OTHERS

Breuer, S., & Schilling, F. R. (2020). Quartz Single Crystal Thermal Diffusivity Measurements by Laser Flash Method: From -120°C Through the α - β Phase Transition to 800°C . Type: dataset, KI-Topen Data, doi:10.5445/IR/1000119716.

ACKNOWLEDGMENTS

Even though a dissertation superficially claims to be a single-author study only, no such thesis ever was prepared without the help of numerous fantastic people.

Hereby I express my deepest gratitude to all of you, named or unnamed, for the amazing support throughout the time preparing this thesis. Thank You!

First and foremost, my thank goes to my supervisor FRANK R. SCHILLING. You agreed to employ me after my Master's thesis and you trusted me being able to write such a dissertation. It was a great inspiration to see you facing problems and working through scientific stumbling blocks with unreached stoic calm. You were always open-minded for my ideas and optimistic in everything that you worked on – all in all a great role model, not only for me! You always trusted in my abilities, even though I sometimes wasn't aware of having them. With the freedom in our group and your support I could develop my own ideas, which I think led to some outreaching results. You always encourage us to show you how things work, what the principles of our "system Earth" are. I hope that I could teach you something – but either way, I learned a whole lot from you and will never forget our time together.

Furthermore, my thank goes to the co-authors of the third study, MATTHIAS SCHWOTZER and SERGIO SPEZIALE (besides F.R. Schilling). Both of you agreed to work with me on the topic of portlandite single crystals even though I didn't have a specific plan what to do in the beginning. With our profound discussions you showed me how the scientific everyday life looks like and gave me the feeling of being part of awesome science being in progress. SERGIO, our measurements at the GFZ were wonderful. Thank you for introducing me into the field of Brillouin spectroscopy and giving me the opportunity to make my measurements on your valuable experimental setup. I'm thankful for your patient and inspiring optimistic manner working with me. MATTHIAS, you always found the time for me to discuss things around portlandite. But not only that, you always had a lot of ideas how we could go on with our single crystals and what we could do next. You gave me the freedom to realize all aims without letting me unsupported! Thank you.

In addition, there are a lot of other people that contributed to the success of this thesis. A special thank goes to my colleague and good friend MARKUS MERK. You helped me countless times with little laboratory utensils, with your advice and know-how. Your patient and helpful character deeply impressed me and got me out of some apparently hopeless situations. Another thank goes to BIRGIT MÜLLER

and JESSICA BLACKWELL for always having an open ear for my problems and supporting me wherever possible. Another thank goes to KIRSTEN DRÜPPEL and ELISABETH EICHE for the discussions and advice on how we could analyze our crystals best. Beyond that, numerous other people were part of this work and helped me to complete this thesis. Thanks to: BEATE OETZEL for numerous XRD and CSA measurements, RALF WACHTER for printing 3D models that helped a lot understanding crystal symmetries, thanks to DOMINIK GUDELIUS for many discussions and the help with gold and graphite coating and REM photographs, and thanks to KRISTIAN NIKOLOSKI for his help and advice with sample cutting and preparation. Further acknowledge goes to TORSTEN SCHERER and VANESSA WOLLERSEN for their help in cutting crystal samples, to FRANK HEMBERGER for inspiring discussions and a great time at the ITCC, and to ERNST KIEFER for proofreading.

I gratefully acknowledge the DR. M. HERRENKNECHT foundation for funding the professorship of Technical Petrophysics and thus ultimately giving me the opportunity to work in the group Technical Petrophysics and to prepare this thesis. Further thank goes to the HELMHOLTZ ASSOCIATION for their program-oriented funding (POF III, 35.14.01, "Effiziente Nutzung geothermischer Energie") and to the FEDERAL MINISTRY OF EDUCATION AND RESEARCH (BMBF) for funding of "SUBI - Sicherheit von Untertagespeichern bei zyklischer Belastung: Funktionalität, Integrität und Überwachung von Speichern und Bohrungen". Further on, I want to acknowledge my co-examiner HAUKE MARQUARDT and the DOCTORAL COMMITTEE for their time and effort in the course of this doctoral procedure. I also want to thank the open access KIT-PUBLICATION FUND of the Karlsruhe Institute of Technology (KIT) for their support.

Finally, my last thank goes to my FAMILY, to whom this thesis is dedicated. I cannot emphasize enough how important it is to have your support whenever it is needed. You always had helpful advice for me throughout my time here at KIT to get along with everything and everyone and cheered me up whenever things went badly. I could find open doors to forget everyday life at any time and I always found a hearing. Thank you for everything!

DECLARATION OF AUTHORSHIP



Chapter 2: Breuer, S., & Schilling, F. R. (2019). *Improving Thermal Diffusivity Measurements by Including Detector Inherent Delayed Response in Laser Flash Method*. International Journal of Thermophysics, 40(10), 95. doi:10.1007/s10765-019-2562-9

The concept of the study was worked out by Simon Breuer (SB) together with Frank R. Schilling (FS). Modeling approaches were developed by SB together with FS, while code writing was done by SB. All measurements including the data processing were performed by SB. Analyzing and evaluation of the data was performed by SB and FS.

The manuscript was written by SB while corrections by FS improved it significantly. SB was responsible for the submission and accompanied the manuscript through the review process.



Chapter 3: Breuer, S., & Schilling, F. R. (2020). *Anisotropic Thermal Transport Properties of Quartz: From -120 °C Through the α-β Phase Transition*. European Journal of Mineralogy, (under review)

SB and FS worked on the conceptualization of the study. The laser flash measurements were carried out with the help of J. Späthe, R. Stemmler and D. Guth as part of their bachelor and master theses, respectively. The data have been processed by SB and analyzed together with FS. The development of the underlying models was done by SB and FS, while the setup and implementation of all codes was done by SB.

Data visualization and manuscript writing was done by SB, the structure of the study was set up in close cooperation with FS. Corrections on an early version of the manuscript were made by G. de la Flor as well as by FS. SB submitted the manuscript and was responsible for the correspondence during the review process.



Chapter 4: Breuer, S., Schwotzer, M., Speziale, S., & Schilling, F. R. (2020). *Thermoelastic Properties of Synthetic Single Crystal Portlandite Ca(OH)₂ - Temperature-Dependent Thermal Diffusivity with Derived Thermal Conductivity and Elastic Constants at Ambient Conditions*. *Cement and Concrete Research*, 137, 106199. doi:10.1016/j.cemconres.2020.106199

Ideas and concept for the study were discussed by all authors: SB with FS, Matthias Schwotzer (MS) and Sergio Speziale (SS). The crystal growth experiments were carried out by SB. Crystal characterizations (ICP-MS, XRD, CSA, IC) were performed by B. Oetzel and M. Denker with the help of E. Eiche. Thermogravimetric experiments were done by MS with the help of F. Krause. Brillouin scattering experiments were performed by SB in close collaboration with SS and the help of L. Pennacchioni at the GFZ Potsdam. Brillouin spectra processing was done by SB with the support of SS. Developing a methodology for laser flash measurements was done by SB and FS, while the sample preparation and measurements were performed by SB. Data processing and investigation was done by SB with support of FS.

Manuscript concept setup, data visualization as well as writing the manuscript was performed by SB with assistance of FS. The manuscript was reviewed and improved by co-authors MS and SS before submission. The submission was prepared and conducted by SB, who also accompanied the review process.

I hereby certify that the submitted dissertation "*Thermal Transport Properties of Single Crystal Quartz and Portlandite*" is entirely my own work except where otherwise indicated. I am aware of the principles of the Karlsruhe Institute of Technology (KIT) for the assurance of good scientific practice and I am aware of the regulations concerning plagiarism, including those regulations concerning disciplinary actions that may result from plagiarism.

Karlsruhe, 2020

Simon Breuer (M.Sc.)